

EMBL



UGA
Université
Grenoble Alpes

THÈSE

Pour obtenir le grade de

DOCTEUR DE L'UNIVERSITÉ GRENOBLE ALPES

Spécialité : **NEUROSCIENCES, NEUROBIOLOGIE**

Arrêté ministériel : 25 mai 2016

Présentée par

Tom BOISSONNET

Thèse dirigée par **Karin PERNET GALLAY**, Ingénieure de recherche, Grenoble Institut des Neurosciences, et co-encadrée par **Hiroki ASARI**, Group Leader, European Molecular Biology Laboratory, Rome

préparée au sein du **European Molecular Biology Laboratory, Epigenetics and Neurobiology Unit, Rome**

dans l'**École Doctorale de Chimie & Sciences du Vivant (ED218)**

Enregistrements électrophysiologiques de fibres du tractus optique et outils de traitement pour la caractérisation *in vivo* de la dynamique de cellules ganglionnaires de la rétine chez la souris éveillée et anesthésiée

Thèse soutenue publiquement le **2 mars 2021**, devant le jury composé de :

Thomas EULER

Professor, Institute for Ophthalmic Research, Tübingen

Rapporteur

Olivier MARRE

Chargé de recherche, Institut de la Vision, Paris

Rapporteur

Rémy SADOUL

Professeur des Universités, Grenoble Institut des Neurosciences

Président

Karl FARROW

Associate Professor, Katholieke Universiteit te Leuven

Membre

Homaira NAWABI

Chargée de recherche, Grenoble Institut des Neurosciences

Invité

Santiago ROMPANI

Group Leader, European Molecular Biology Laboratory, Rome

Invité



Resumé

Le système rétinopétal est composé de neurones situés dans le cerveau qui envoient des signaux à la rétine en faisant passer leurs axones à travers le nerf optique. Chez les mammifères, il est suggéré que ces neurones résident dans des régions telles que le noyau du raphé dorsal (sérotoninergique) et l'hypothalamus postérieur (histaminergique), et certains effets physiologiques de la sérotonine et de l'histamine dans la rétine ont été démontrés au niveau de neurones isolés dans des préparations *ex vivo*. Cependant, il reste à clarifier quelles sont les origines exactes et les cibles du système rétinopétal, et comment il affecte le traitement des signaux visuels dans la rétine *in vivo*. Les enregistrements *ex vivo* de la rétine sont des standards dans le domaine ; cependant, la procédure pour obtenir de tels enregistrements nécessite de couper le nerf optique, et donc rompt les fibres rétinopétales. Pour étudier les fonctions de la rétine tout en gardant le système rétinopétal intact, j'ai mis en place une technique d'enregistrement électrophysiologique *in vivo* à partir des axones des cellules ganglionnaires de la rétine à l'intérieur du tractus optique d'une souris en réponse à un ensemble de stimuli visuels. J'ai également établi un pipeline d'analyse de ces enregistrements et d'autres, tels que les données d'imagerie calcique en bi-photons des axones de cellules ganglionnaires de la rétine dans le colliculus supérieur. En comparant les sorties de la rétine chez les souris éveillées avec celles sous anesthésie, j'ai trouvé une amélioration substantielle de la vitesse et de la sensibilité des réponses visuelles chez les souris éveillées. Ces résultats confirment l'importance d'enregistrements *in vivo* pour comprendre pleinement la fonction de la rétine et démontrent l'impact de l'anesthésie sur la rétine, conseillant ainsi la prudence avec l'utilisation d'anesthésiques pour étudier le système visuel. Ma thèse servira ainsi de jalon pour une future étude du système rétinopétal.

Mots clés : rétine, souris, *in vivo*, cellules ganglionnaires, électrophysiologie, anesthésie

Electrophysiological optic tract fibres recordings and processing tools for the *in vivo* characterisation of retinal ganglion cell dynamics in the awake and anaesthetised mouse

Summary

The retinopetal system is composed of neurons located in the brain which send signals to the retina by passing their axons through the optic nerve. In mammals, it is suggested that these neurons reside in regions such as the dorsal raphe nucleus (serotonergic) and the posterior hypothalamus (histaminergic), and some physiological effects of serotonin and histamine in the retina have been demonstrated at the single-neuron level by *ex vivo* studies. However, it remains to be clarified what the exact origins and targets of the retinopetal system are, and how it affects the visual signals processing in the retina *in vivo*. *Ex vivo* recordings of the retina are standards in the field; however, the procedure to obtain such recordings requires to cut the optic nerve, and therefore disrupt the retinopetal fibres. To study the retinal functions while keeping the retinopetal system intact, I have established an *in vivo* electrophysiological recording technique from the axons of retinal ganglion cells inside the optic tract of a mouse in response to a set of visual stimuli. I have also established an analysis pipeline of such recordings and others, such as two-photon Calcium imaging data from retinal ganglion cell axons in the superior colliculus. By comparing the retinal outputs in awake mice with those under anesthesia, I found a substantial improvement in the speed and sensitivity of the visual responses in awake mice. These results confirm the importance of *in vivo* recordings to fully understand retinal function and demonstrate the impact of anaesthesia on retinal processing, thus advising caution with the use of anaesthetics for studying the visual system. My thesis study will thus serve as a milestone for a future study of the retinopetal system.

Keywords: retina, mouse, *in vivo*, ganglion cell, electrophysiology, anaesthesia

Acknowledgements

I would like first to thank my PhD supervisor, **Dr Hiroki Asari**, for accepting me in his group and giving me such an interesting subject to work on, for our open discussions and his help throughout the years, but also for composing such a great working environment which gave me both the support and freedom I enjoyed to explore my project.

I would also like to thank **Dr Karin Pernet Gallay**, who granted me with a fantastic project for my master back in 2014 and supported me since then. I owe her my scientific journey, as she pushed when I needed it the most. I am also extremely grateful to her for being a model of a scientist and person.

I also must give credit to all my lab: **Anastasiia Vlasiuk** for her support and friendship, **Dmitry Molotkov** for teaching and helping me, **Leiron Ferrarese** for his advice and **Matteo Tripodi** for the experiments he carried for this project during the last year. I would also like to acknowledge all the students who worked in the Asari lab throughout the years, in order of appearance: **Ylva, Simone, Prajakta, Francesco, Emily, Ilaria, Jaime, Beatrice, Harsh, Grace, Georgy, Luca, Samuele, Tristan, Lily** and **Inês**.

I would also like to thank **Marco** and **Paolo** for the year we spent together during which they introduced me to Mask-RCNN and guided me throughout the learning. I also need to thank all the open-source community from which I benefited a lot, who dedicate their time to teach, explain and create to make knowledge accessible to everyone. Also, I need to thank all the people I have met at EMBL for making this place like home. I would also like to thank **Daniel** for our lunchtime discussions, all those with whom I shared the breakfast on computational Fridays morning, and the Marterdì Ubritaliano group which made the learning of Italian fun.

I also want to be extremely grateful to my friends **Max, Will** and **Jéjé** de la rue du Piot, and to all the others from Clermont-Ferrand, Grenoble and other parts of the world with who I share priceless memories.

I would also like to thank all my family: my brother **Germain** and my sister **Emma**, with whom I had great fun growing with, my mom **Marianne** for being an incredible mom and for almost never losing patience with us, and my dad **Eric**, who I wish could witness us walking in his giant footsteps.

Above all, I would like to thank you, **Stephanie**, for all your love and support.

“Poets say science takes away from the beauty of the stars — mere globs of gas atoms. I too can see the stars on a desert night, and feel them. But do I see less or more? The vastness of the heavens stretches my imagination — stuck on this carousel my little eye can catch one-million-year-old light. A vast pattern — of which I am a part... What is the pattern, or the meaning, or the why? It does not do harm to the mystery to know a little about it. For far more marvelous is the truth than any artists of the past imagined it. Why do the poets of the present not speak of it? What men are poets who can speak of Jupiter if he were a man, but if he is an immense spinning sphere of methane and ammonia must be silent?”

Richard P. Feynman

Table of contents

Resumé	3
Summary	4
Acknowledgements	5
Figure list.....	10
Abbreviations	12
1 Introduction.....	14
1.1 Retinopetal system.....	16
1.2 Photoreceptors	19
1.2.1 Phototransduction.....	19
1.2.2 Rods.....	20
1.2.3 Cones	21
1.3 Bipolar cells.....	22
1.3.1 ON bipolar cells	23
1.3.2 OFF bipolar cells.....	24
1.4 Horizontal cells.....	24
1.5 Amacrine cells	26
1.5.1 Dopaminergic amacrine cells	27
1.6 Ganglion cells	29
1.6.1 Intrinsically photosensitive RGCs.....	31
1.7 Anaesthesia.....	31
1.7.1 Principles	31
1.7.2 Midazolam.....	33
1.7.3 Isoflurane.....	33
1.8 Specific Aims	34
2 Material & Methods	36
2.1 Hardware	36
2.1.1 Devices	36
2.1.2 Setups	41
2.2 Optic tract electrophysiology.....	42
2.2.2 Key Resources Table.....	45
2.3 Visual stimuli.....	48
2.3.1 Marker cycle.....	48
2.3.2 Checkerboard optimisation	49

2.3.3	LED dome stimuli	49
2.4	Data processing.....	49
2.4.1	Spike sorting.....	49
2.4.2	The one rig, data synchronisation and processing.....	50
2.4.3	Cell response analysis	52
2.4.4	Eye-tracking	57
3	Results.....	59
3.1	RGCs <i>in vivo</i> electrophysiology	59
3.2	Reliable event detection for synchronisation.....	60
3.3	Awake RGCs respond more rapidly than under anaesthesia.....	61
3.4	Awake RGCs respond to higher frequencies than their anaesthetised counterpart ...	63
3.5	Awake RGCs have a stronger baseline activity.....	66
3.6	Chirp AM responses and model fitting.....	67
3.7	Other awake/anaesthetised data trends	68
3.8	Direction and orientation selectivity.....	70
3.9	Pupil detection with Mask-RCNN.....	71
3.10	Eye-tracking STA correction.....	73
3.11	LED dome wide field of view coverage	75
4	Discussion.....	76
4.1	<i>In vivo</i> electrophysiological retinal recordings.....	77
4.1.1	Target choice	77
4.1.2	Signal-to-noise ratio and spike sorting.....	79
4.1.3	Multiple records of identical cells and cell pairing	79
4.1.4	Future developments	80
4.1.5	Complementary calcium imaging of axon terminals	81
4.2	Visual stimulation.....	82
4.2.1	Field of view and screen shape	82
4.2.2	Light intensity	83
4.2.3	Refresh rate	84
4.2.4	Display errors, detection and correction	85
4.3	Eye-tracking.....	86
4.3.1	Pupil detection.....	86
4.3.2	STA correction	88
4.4	<i>In vivo</i> retinal properties.....	89
4.4.1	Anaesthesia in the retina	89
4.4.2	What anaesthesia tells about our data	89
4.4.3	Visual system temporal sensitivity.....	90

4.4.4	Comparison to <i>ex vivo</i> recordings	91
4.4.5	Full-field receptive fields and LED dome	92
4.4.6	Retinopetal system	93
5	Conclusion	95
6	Bibliography	96
7	Annexe 1 – LED Dome.....	117
7.1	Presentation	117
7.2	Light intensity.....	118
7.3	LED position mapping.....	118
7.4	Frame rate	119
7.5	Visual stimuli.....	120
7.5.1	White-noise checkerboard stimulus	120
7.5.2	White-noise full-field stimulus.....	120
7.5.3	Chirp stimulus frequency epoch.....	120
7.5.4	Motion stimulus.....	121
8	Annexe 2 – Database	124
8.1	Tables description.....	124
8.2	General diagram	135
8.3	Graphical interface	136
9	Annexe 3 – Cell Zoo	137
9.1	Awake cell	137
9.2	Day/Night paired cell – Day	138
9.3	Day/Night paired cell – Night	139
9.4	LED-dome/DLP paired cell – DLP	140
9.5	LED-dome/DLP paired cell - LED-dome	141
9.6	FMM cell	142
9.7	FMM cell - ON stimulus leak response.....	143
9.8	Isoflurane cell - Transient response.....	144
9.9	Isoflurane/FMM paired cell – Isoflurane.....	145
9.10	Isoflurane/FMM paired cell – FMM	146
10	Annexe 4 – The One Rig.....	147

Figure list

Figure 1 – Eye anatomy	14
Figure 2 – Retinal cell types and basic synaptic organization of the mouse retina.....	16
Figure 3 – Localization of the neurons giving rise to centrifugal visual pathways	18
Figure 4 – Activation of rhodopsin by light and the phototransduction cascade	19
Figure 5 – Rod spherule synapse with a rod bipolar and a horizontal cell	20
Figure 6 – Distribution of cones and opsin expression in mouse and human retina.....	22
Figure 7 – Cone pedicle synapse with ON and OFF bipolar and a horizontal cell	23
Figure 8 – Classification of the mouse retinal bipolar cells	24
Figure 9 – Modulation of horizontal cell coupling in monkey retina	26
Figure 10 – Organization of the main neurotransmitters in the retina	27
Figure 11 – Presumptive synaptic connection scheme between an ipRGC (M1-type), a histaminergic centrifugal fibre and a dopaminergic amacrine cell	28
Figure 12 – Basic architecture of mouse retinal ganglion cells and visual pathways	29
Figure 13 – ipRGCs differs in morphology and site of dendritic fields.....	30
Figure 14 – Schematic representation of the GABAA and GABAC receptors	33
Figure 15 – Illustration of the electrophysiology experiment	40
Figure 16 – Silicone probe implantation in the optic tract	59
Figure 17 – Event detection and classification for synchronisation of the records.....	60
Figure 18 – In vivo RGC temporal STA from the full-field flickering stimulus	62
Figure 19 – Cells temporal frequency sensitivity.....	64
Figure 20 – High frequency RGC responses.....	65
Figure 21 – Receptive fields and nonlinearities	66
Figure 22 – Chirp AM responses	67
Figure 23 – Paired plots for selected parameters of our models	68
Figure 24 – Direction and orientation selectivity	70
Figure 25 – Pupil detection with Mask-RCNN	72
Figure 26 – Eye-tracking to correct the STA	73
Figure 27 – Receptive fields of awake cells measured with the LED dome.....	75
Figure 28 – LED dome, power curve and mapping	119
Figure 29 – LED dome motion stimulus.	122
Figure 30 – Relationship diagram between the tables about the visual stimuli	126
Figure 31 – Relationship diagram between the tables about mice.....	129

Figure 32 – Relationship diagram between the tables about recording devices	131
Figure 33 – Relationship diagram between the tables about experiments	134
Figure 34 – General database diagram	135
Figure 35 – Graphical User Interface for the database.....	136

Abbreviations

AC:	amacrine cell
AM:	amplitude modulation
AMPA:	alpha-amino-3-hydroxy-5-methyl-4-isoxazolepropionic acid
AP:	antero-posterior
AUC:	area under the curve
BC:	bipolar cell
Ca ²⁺ :	calcium ion
CCD:	charge-coupled device
CNN:	convolutional neural network
COCO:	common objects in context
DAC:	dopaminergic amacrine cell
DLC:	DeepLabCut
dLGN:	lateral geniculate nucleus
DMD:	digital mirror device
DLP:	digital light processor
DNN:	deep neural network
DV:	dorso-ventral
ERG:	electroretinogram
FE:	frequency epochs
FM:	frequency modulation
FMM:	fentanyl, medetomidine, midazolam
FPS:	frame per second
GABA:	gamma-aminobutyric acid
GABA _A R:	GABA A receptor
GABA _B R:	GABA B receptor
GABA _C R:	GABA C receptor
GCaMP:	genetically encoded calcium indicator

GCL:	ganglion cell layer
HC:	horizontal cell
INL:	inner nuclear layer
IPL:	inner plexiform layer
ipRGC:	intrinsically photosensitive retinal ganglion cell
IR:	infra-red
K^+ :	potassium ion
LED:	light emitting diode
MEA:	microelectrode array
ML:	median-lateral
Na^+ :	sodium ion
NMDA:	N-methyl-D-aspartate
ONL:	outer nuclear layer
OPL:	outer plexiform layer
PCA:	principal component analysis
PFA:	paraformaldehyde
R-CNN:	region based CNN
RGC:	retinal ganglion cell
RP:	retinopetal
SNR:	signal-to-noise ratio
STA:	spike triggering average
UV:	ultra-violet
V1:	primary visual cortex

Introduction

1 Introduction

The contributions of physicists over the past century gave us a deep understanding on the nature of the world we see: An object emits or reflects from a source (e.g. the sun) light – photons – a pure form of energy traveling at the fastest speed of the universe, behaving like a wave and a particle at the same time. Among the incredibly many photons leaving an object in all possible direction at a given time, one will perceive those only who will pass through the diaphragm of an eye, the pupil. These photons then enter in the eye and will soon cross the lens that, having a reflective index about the same as that of the water (1.33) and according to the Snell's law, will deviate the photons depending on their incident angle. That deviation will focus the photons originating from a same point onto the back of the eye, the retina. Moreover, the lens can contract or relax to deviate more or less strongly the photons, adjusting the focus of objects located at different distances. The photons of the formed image will ultimately reach cells called the photoreceptor, to be absorbed by photo pigments depending on their wavelength/energy. That absorption will initiate the phototransduction cascade in the photoreceptor and later changes in downstream nerve cells' activity to convey information of an image that has reached the eye (Figure 1).

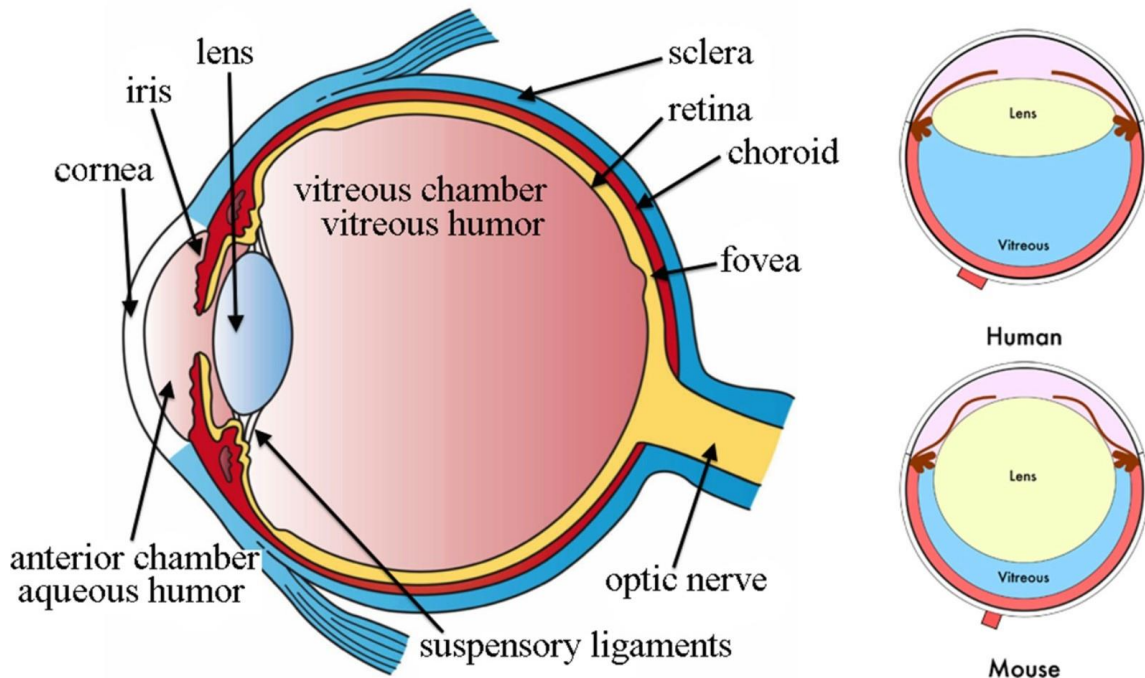


Figure 1 – Eye anatomy. The left schematic shows the basic structure of the human eye with the three main layers visible, the sclera, the choroid and the retina. The right panel displays a cross-sectional schematic of the human and mouse eye and shows the relative larger lens in the mouse eye. Mice also lack the presence of a fovea (not illustrated in this figure), the region where for humans the visual acuity is the highest. Credits: (Fisher 2013), CC BY 3.0, (Skeie et al. 2011), CC BY 2.0.

Introduction

The retina is the most accessible part of the brain and has been studied for more than a century (Cajal 1893; E Dowling 1987). It performs considerable computations with well-defined input stimuli and output responses, and the physiological functions are known in detail from the molecular to the cellular level. The retina has about 130 cell types in total (Helmstaedter et al. 2013; Sanes & Masland 2015; Seung & Sümbül 2014; Yan et al. 2020), each falling into one of five major cell types: photoreceptor, bipolar, horizontal, amacrine and ganglion cells (Berens & Euler 2017). Together they form various complex circuits of an amazing beauty¹ (Bae et al. 2018). To convey and transform light signals into multiple features before sending them to the brain, the retina benefits from its most striking feature: organization (Roska & Meister 2014) (Figure 2). Photons falling onto photoreceptors are absorbed by mixes of visual pigments – combinations of cis-retinal (derived from vitamin-A) and opsins (Baden et al. 2013b; Hecht et al. 1942; Wald 1968) – and signals are delivered to the outer plexiform layer (OPL). There, an invaginated synapse is formed by presynaptic photoreceptors and postsynaptic horizontal and bipolar cells (E Dowling 1987). When photoreceptors deliver glutamate in the synaptic cleft, at a rate inversely proportional to the light intensity (Baylor 1987), two classes of bipolar cells decode these signals into ON (bipolar cell responding after an increase of light) and OFF channels (bipolar cell responding after a decrease of light) (Borghuis et al. 2014; Euler et al. 2014; Koike et al. 2010a), while horizontal cells provide feedback to photoreceptors that can be negative (Chapot et al. 2017; Diamond 2017) or positive (Jackman et al. 2011) and perform long-range modulation through a gap junction network (Hombach et al. 2004; Janssen-Bienhold et al. 2009; Ströh et al. 2018; Vaney 1994). From the OPL, about 15 classified types of bipolar cells (Baden et al. 2013a; Euler et al. 2014; Franke et al. 2017; Ghosh et al. 2004; Mataruga et al. 2007; Seung & Sümbül 2014; Shekhar et al. 2016; Wassle et al. 2009) project to the inner plexiform layer (IPL), comprising six OFF and nine ON channels (Tsukamoto & Omi 2017).

In the IPL, a rich diversification of information occurs (Asari & Meister 2012, 2014; Grimes et al. 2010) where bipolar cells can contact a set of at least 30 ganglion (Badea & Nathans 2004; Baden et al. 2016; Bae et al. 2018; Coombs et al. 2006; Farrow & Masland 2011; Helmstaedter et al. 2013; Kong et al. 2005; Sanes & Masland 2015; Seung & Sümbül 2014) and more than 40 amacrine cell types (Anderson et al. 2011; Badea & Nathans 2004; Helmstaedter et al. 2013; Kim et al. 2014; Lin & Masland 2006; MacNeil & Masland 1998; Seung & Sümbül 2014; Zhang et al. 2007; Zhu et al. 2014). Complex interactions between bipolar, ganglion and amacrine cells discriminate features (Lettvin et al. 1959) such as looming (Münch et al. 2009),

¹ See museum.eyewire.org for 3D views of real retinal cells

Introduction

edges (Zhang et al. 2012) or motion directions (Kim et al. 2014; Vaney et al. 2012). Finally, ganglion cell axons exit the retina and project to multiple regions in the brain, including the two main targets, the lateral geniculate nucleus (dLGN) and superior colliculus (SC) (Ellis et al. 2016).

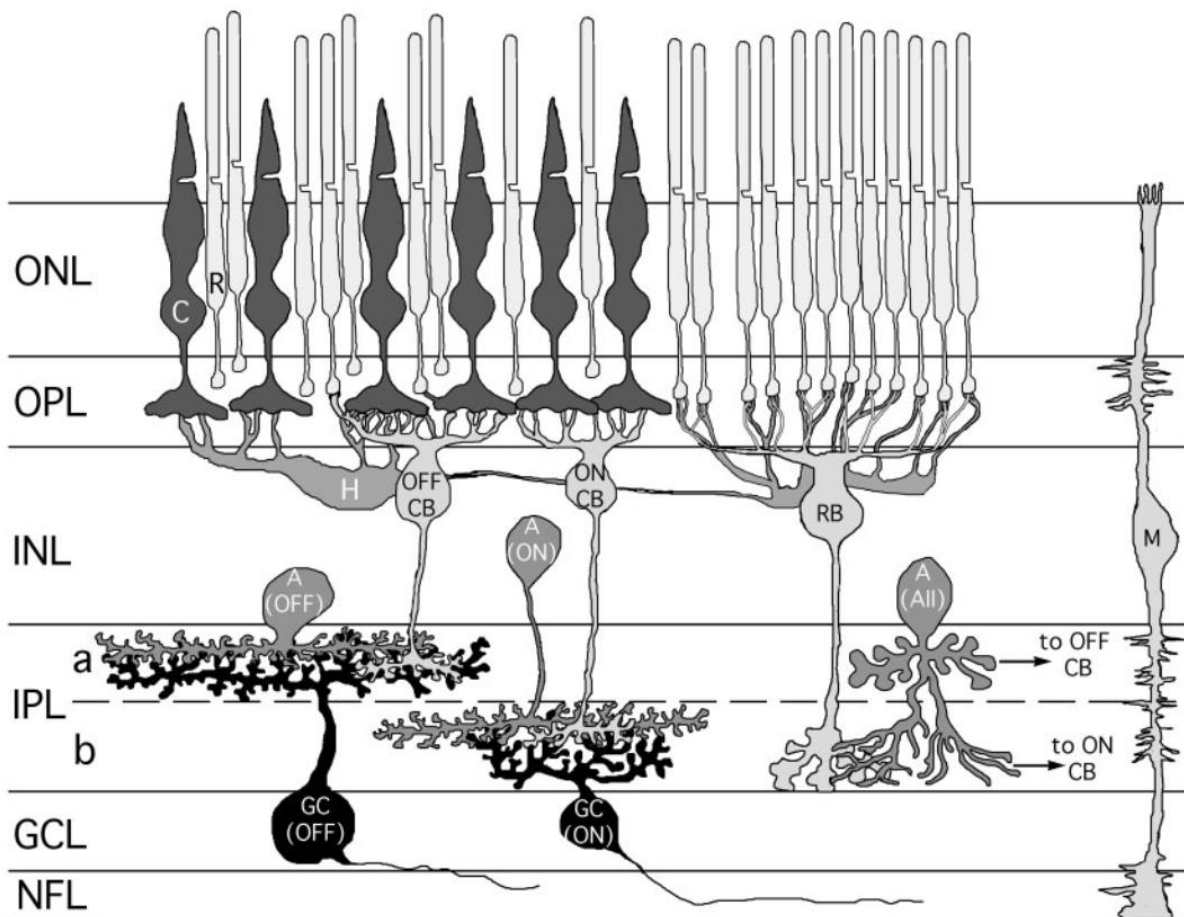


Figure 2 – Retinal cell types and basic synaptic organization of the mouse retina. *C*: cone; *R*: rod; *H*: horizontal cell; **OFF CB**: OFF cone bipolar cell; **ON CB**: ON cone bipolar cell; **RB**: rod bipolar cell; *A (OFF)*: OFF amacrine cell; *A (ON)*: ON amacrine cell; *A (All)*: All amacrine cell; **GC (OFF)**: OFF ganglion cell; **GC (ON)**: ON ganglion cell; *M*: Müller cell; **ONL**: outer nuclear layer; **OPL**: outer plexiform layer; **INL**: inner nuclear layer; **IPL**: inner plexiform layer; **GCL**: ganglion cell layer; **NFL**: nerve fibre layer. Credits: (Wang et al. 2003), Copyright © 2003 Wiley-Liss, Inc.

1.1 Retinopetal system

The retinopetal (RP) system is made of RP neurons that have cell bodies in different regions of the brain and pass their axons through the optic nerve to reach the retina (Koves et al. 2016). The RP system was first discovered by Cajal in birds (Cajal 1893; Maturana & Frenk 1965) and later in fishes, turtles, frogs and mammals. The RP system varies a lot across species: for

Introduction

example, higher vertebrates have fewer RP fibres than lower vertebrates (Repérant et al. 2006, 2007). In mammals, these neurons are suggested to reside in regions such as the dorsal raphe nucleus (serotonergic) (Frazão et al. 2008; Galambos et al. 2001; Gastinger et al. 2006a; Koves et al. 2016; Labandeira-Garcia et al. 1990; Lima & Urbina 1998; Lörincz et al. 2008; Repérant et al. 2000; Villar et al. 1987) and the posterior hypothalamus (histaminergic) (Airaksinen & Panula 1988; Bons & Petter 1986; Gastinger et al. 1999, 2006a; Koves et al. 2016; Labandeira-Garcia et al. 1990; Terubayashi et al. 1983). In complement, studies demonstrated that histamine receptors (Frazão et al. 2011; Gastinger et al. 2006a,b; Greferath et al. 2009; Sawai et al. 1988; Vila et al. 2012) and serotonergic receptors (Ehinger et al. 1981; Gastinger et al. 2006a; Jin & Brunken 1998; Pérez-León et al. 2004; Pootanakit & Brunken 2000, 2001; Pootanakit et al. 1999) were found in the retina and associated to physiological effects of histamine (Akimov et al. 2010; Frazão et al. 2011; Gastinger et al. 2004, 2006a; Horio et al. 2018; Yu et al. 2009) and serotonin (Brunken & Daw 1988; Gastinger et al. 2006a; Skrandies & Wässle 1988).

One caveat about findings on serotonin receptors and effects: the presence of serotonin-accumulating amacrine cells in the retina (Brunken et al. 1993; Li et al. 2002; Osborne & Beaton 1986; Sandell & Masland 1986; Vaney 1990). The RP system seems to be highly linked with animal behaviour. Lateral hypothalamus and dorsal raphe nucleus are both centres active when an animal is awake, following the circadian rhythm. This suggests that the RP system is used to optimize retinal functions at ambient light intensities (Galambos et al. 2001; Gastinger et al. 2006a).

Introduction

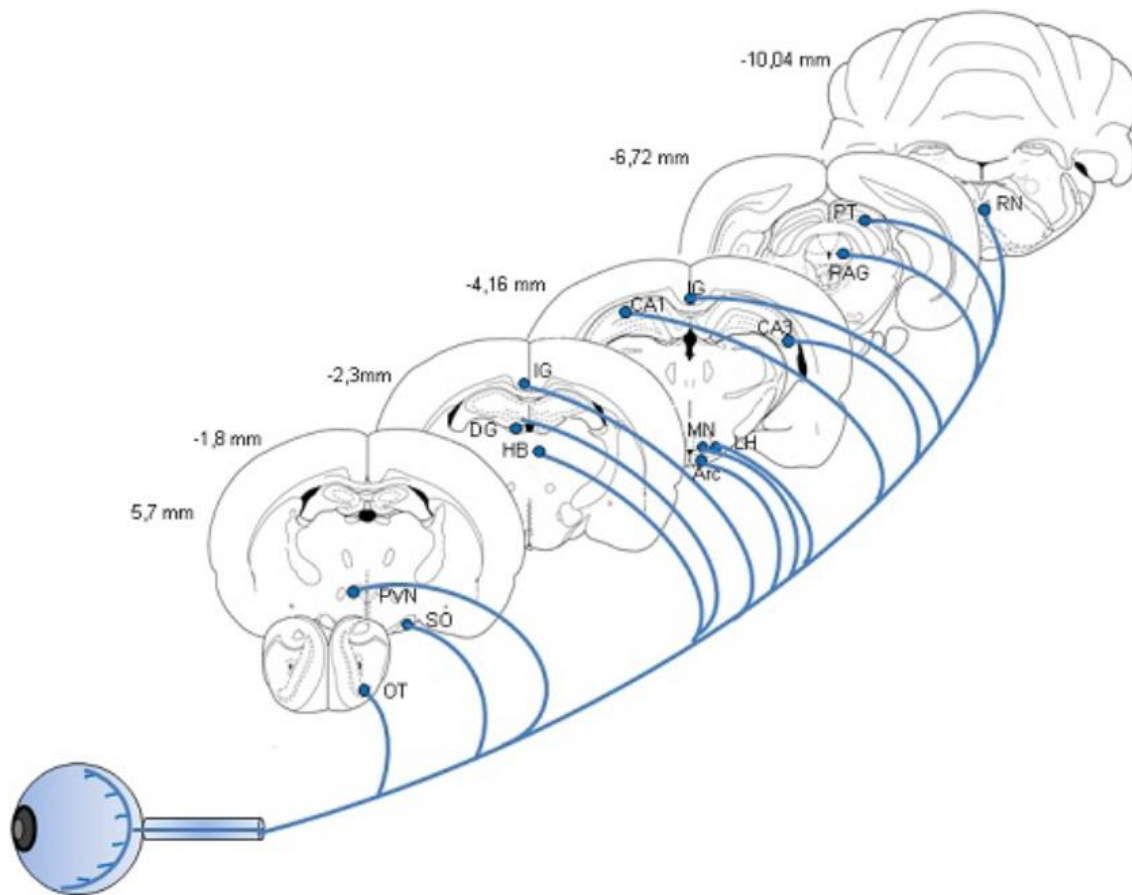


Figure 3 – Localization of the neurons giving rise to centrifugal visual pathways in mammals. *ARC: arcuate nucleus; CA1 and CA3: Regions of the Hippocampus; DG: Dentate Gyrus; HB: Habenula; IG: IndusiumGriseum; LH: Lateral Hypothalamus; MN: Mammillary Nuclei; OT: Optic Tract; PAG: Periaqueductal Gray Matter; PT: Pretectum; PVN: Paraventricular Nucleus; RN: Raphe Nuclei; SON: Supraoptic Nucleus. The numbers next to the frontal sections indicates the distance to the bregma. Credits: (Koves et al. 2016), CC BY.*

Introduction

1.2 Photoreceptors

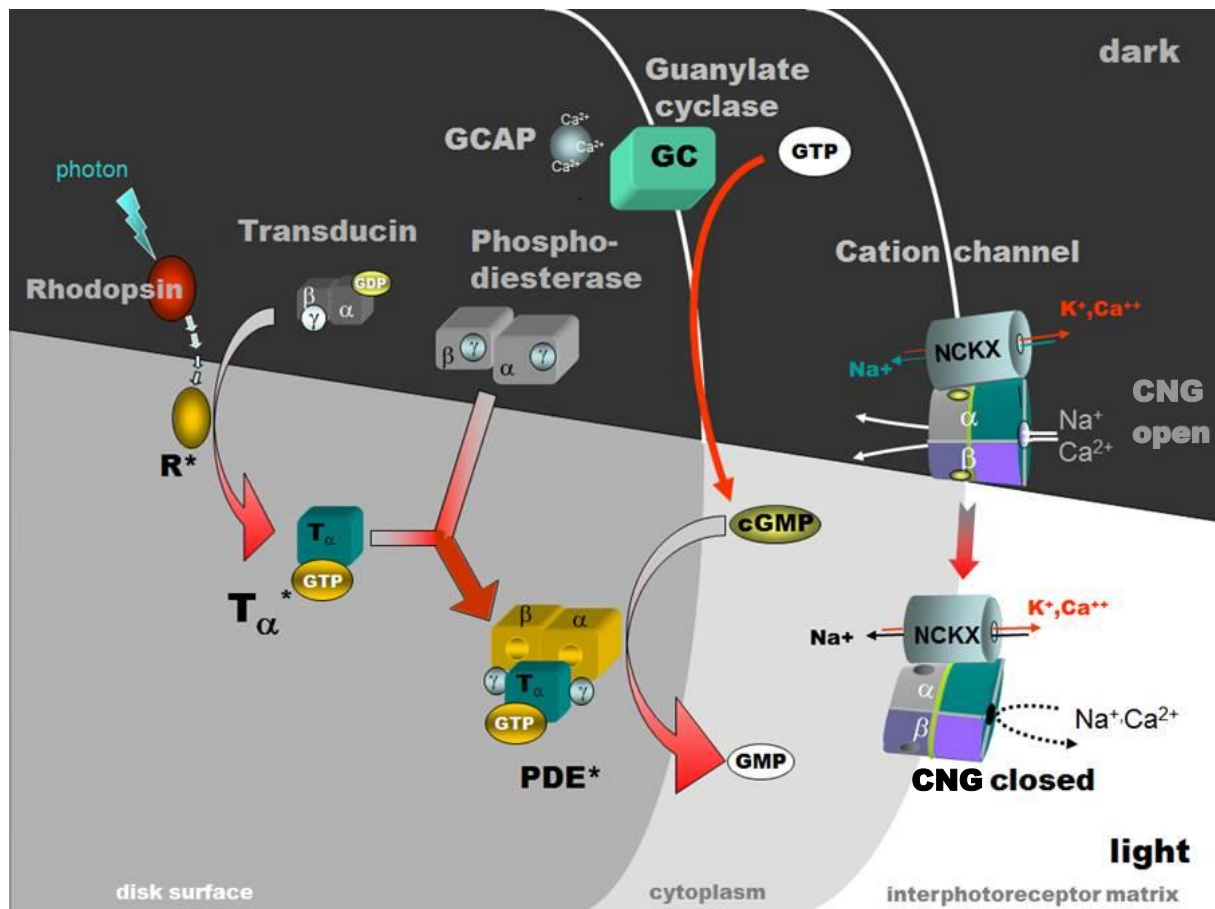


Figure 4 – Activation of rhodopsin by light and the phototransduction cascade. *R*: rhodopsin (inactive); *R**: rhodopsin (active); *T*: transducin; *PDE*: phosphodiesterase (inactive); *PDE**: phosphodiesterase (active); *NCKX*: Na/Ca,K exchanger. *CNG*: cGMP-gated channel; *IPM*: interphotoreceptor matrix. In the dark, the CNG is open and creates the dark current, depolarizing the photoreceptor. Light transduces the visual pigment (Rhodopsin) into activate rhodopsin (*R**), initiating the enzyme cascade: *R** catalyzes the activation of *T*, which in turn activate the *PDE* to *PDE**. *PDE** hydrolyze cGMP into GMP, decreasing the cytoplasmic free cGMP, leading to the closure of the CNG channel, decreasing the dark current and thus allowing the *NCKX* cation exchanger to hyperpolarize the cell. Credits: (Kolb & Baehr 2013), CC BY-NC.

1.2.1 Phototransduction

In the dark, the photoreceptors are continuously depolarized and release glutamate in the synaptic cleft. The depolarization comes from the open state of K⁺/Ca²⁺ channels in the outer segment of the photoreceptors (Baylor et al. 1980; Meister et al. 1994; Yau 1994). After crossing the retina, photons can reach the outer segment where they will be absorbed by the visual pigments of the photoreceptor (Hecht et al. 1942). The absorption will lead to an activated state of the opsin molecule, initiating a transducing cascade ending in the closing of the ion channels (Hargrave & McDowell 1992) (Figure 4). Na⁺/Ca²⁺ exchangers also present on the cellular membrane and continuously working will then be able to hyperpolarize the

Introduction

photoreceptor, leading to an interruption of the release of glutamate toward the synaptic partners of the cell (Stryer 1991; Yau 1994).

1.2.2 Rods

Rod photoreceptors are the most common photoreceptor in the human retina and have a peak sensitivity of 496 nm (Carter-Dawson & Lavail 1979; Curcio et al. 1987; Osterberg 1937). The opsin of the rods is the rhodopsin, with about $2 \cdot 10^9$ molecules per cell (Yau et al. 1979). In the OPL, the rod ending is called the spherule and contacts two synaptic partners, an horizontal cell and a rod bipolar cell (Dowling & Boycott 1966; Kolb 1970) (Figure 5). The rods are responsible for scotopic vision (night light level) because of their high sensitivity to light and can detect single photons (Hecht et al. 1942; Schneeweis & Schnapf 1995). Under day light vision, the rods were long thought to be saturated and to play no role in the retinal processing, but this view has been challenged in the past years from studies showing that rods could escape the saturation of daylight condition (Tikidji-Hamburyan et al. 2017) or act as relay cells between cones and horizontal cells (Szikra et al. 2014).

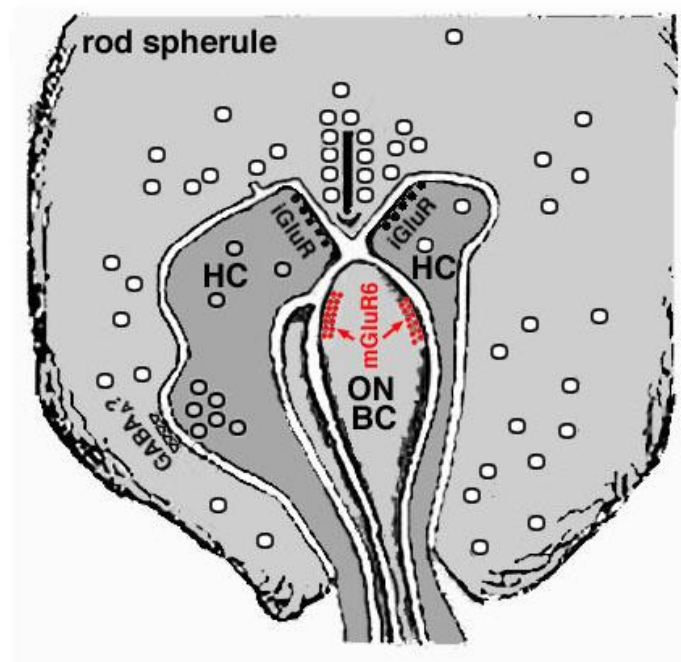


Figure 5 – Rod spherule synapse with a rod bipolar and a horizontal cell. HC: horizontal cell; ON BC: rod bipolar cell; iGluR: ionotropic glutamatergic receptor; mGluR6: metabotropic glutamate receptor. Credits: (Kolb 2011a), CC BY-NC.

Introduction

1.2.3 Cones

Cones are the photoreceptor cells responsible for photopic (day light level) vision. In humans, their density is the highest in the fovea, a central region of the eye where the image is the most resolved (Curcio et al. 1987; Osterberg 1937). The human retina contains three type of cones, each of them have one type of opsin: the L-cones (Long wavelength sensitive cones) sensitive to red light (560nm), the M-cones sensitive to green light (530nm) and the S-cones sensitive to blue light (420nm) (Bowmaker & Dartnall 1980) (Figure 6). In the mouse, there is only the S and M cone pigments, their peak sensitivity is at respectively 360 nm (ultra-violet) and 508 nm (green) (Baden et al. 2013b). There are thus the S and M cone types, as well as a cone type with a mix of both opsins, the SM-cone. Also in the mouse, there is no fovea formed with a high central density of cones. Instead the S and M cone distribution forms a gradient, with a higher concentration of M-cones in the dorsal retina, of SM-cones in the central part and of both SM and S-cones in the ventral part (Applebury et al. 2000; Baden et al. 2013b) (Figure 6). As different types of cones are sensitive to different wavelengths, they are thought to be responsible for colour vision, however a recent study suggests that rods also contribute to colour vision in mice (Szatko et al. 2020). The cone ending called the cone pedicles are large and like the rods, invaginated, and form with HCs and BCs the cone triad (Dowling & Boycott 1966; Kolb 1970).

Introduction

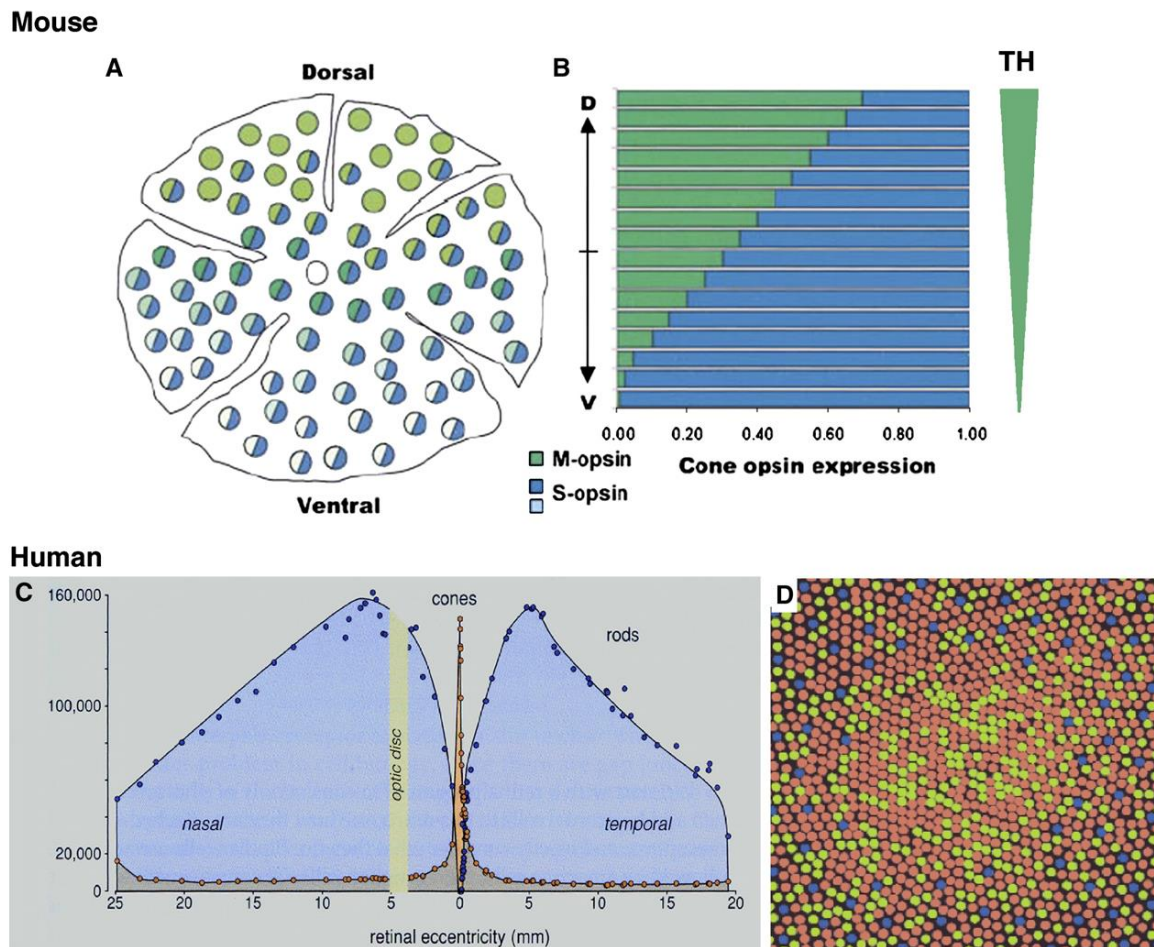


Figure 6 – Distribution of cones and opsin expression in mouse and human retina. *A, B*) In the mouse, the cones density is homogeneous across the retina, but the expression of M and S opsins follow a dorso-ventral gradient. *C*) In humans, the cone concentration peaks in the fovea and rapidly decrease in the periphery where rods predominate. *D*) Cone expression pattern of S-opsin (blue), M-opsin (green) and L-opsin (red) in the fovea. Credits : (A, B) (Applebury et al. 2000), Copyright © 2000 Cell Press, (C) (Rodieck 1999) © Oxford Publishing Limited, (D) (Cepko 2000) , Copyright © 2000, Nature Publishing Group.

1.3 Bipolar cells

Bipolar cells (BCs) are receiving their input from the photoreceptors in the OPL, and their projection to the IPL gives excitatory input to the retinal ganglion cells (RGC) and amacrine cells (AC). The cone photoreceptors contact ON and OFF BCs, that are respectively depolarized with bright and dark stimuli. Both types receive glutamatergic input from the cones (James et al. 2019; Nawy & Copenhagen 1987), but differ in the glutamate receptors displayed on the cone pedicle (Nawy & Copenhagen 1987).

Introduction

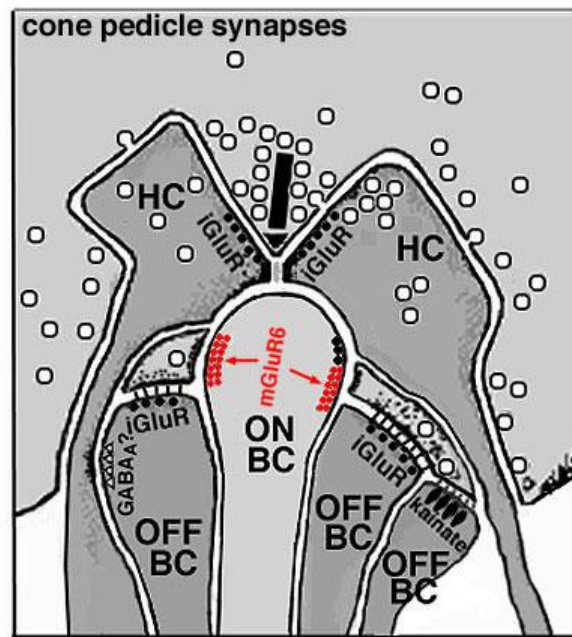


Figure 7 – Cone pedicle synapse with ON and OFF bipolar and a horizontal cell. *HC: horizontal cell; ON BC: rod bipolar cell; iGluR: ionotropic glutamatergic receptor; mGluR6: metabotropic glutamate receptor. Credits: (Kolb 2011a), CC BY-NC.*

1.3.1 ON bipolar cells

The ON BCs express metabotropic glutamate receptors (Nakajima et al. 1993; Slaughter & Miller 1981) that, when binding to a glutamate molecule, will activate a G-protein (Martemyanov & Sampath 2017; Vardi 1998) and initiate a reaction cascade ending in the closing of an ion channel, TRPM1, that will lead to an hyperpolarization of the cell (Koike et al. 2010a,b; Morgans et al. 2010; Nomura et al. 1994; Vardi & Morigiwa 1997). On the opposite, when no glutamate is released by the cones (i.e., in the light), TRPM1 will come back to an open state, depolarizing the cell (Figure 7). ON BCs project to the inner layer of the IPL (S3 to S5) (Bloomfield & Miller 1986; Nelson et al. 1978) and connect to RGCs and ACs that have dendrites in these layers. However, this paradigm is not absolute since ON BCs provide input to RGCs and receive feedback from ACs in the OFF layer (Hoshi et al. 2009; Lauritzen et al. 2013). In the mouse, the ON BCs population is divided into height sub-classes, depending on their morphology, their projection pattern and the sustainability of their response to a light stimulus (Euler et al. 2014; Ghosh et al. 2004; Tsukamoto & Omi 2017; Wassle et al. 2009) (Figure 8).

Introduction

1.3.2 OFF bipolar cells

Unlike the ON BCs, the OFF BCs express ionotropic glutamate receptors (N-Methyl-D-aspartate (NMDA) receptors and non-NMDA receptors) (Brandstätter et al. 1994; DeVries 2000; DeVries & Schwartz 1999). Following glutamate binding, these channels open and depolarize the cells (Gilbertson et al. 1991; Slaughter & Miller 1983) (Figure 7). The OFF BCs project to the outer layer of the IPL (S1 and S2) (Bloomfield & Miller 1986; Nelson et al. 1978) where they provide OFF inputs to RGCs and ACs. The OFF BCs can be divided into six subclasses in mice (Euler et al. 2014; Ghosh et al. 2004; Tsukamoto & Omi 2017; Wässle et al. 2009) (Figure 8).

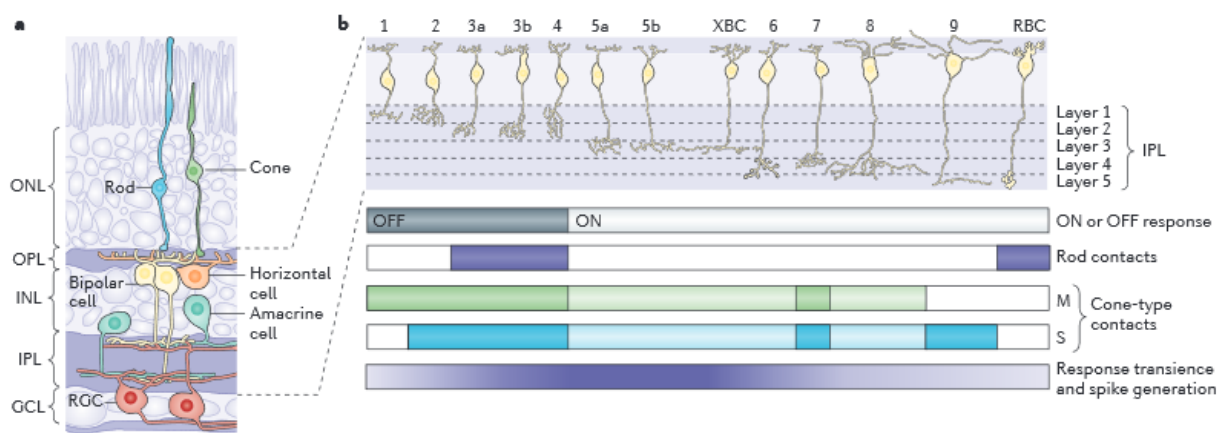


Figure 8 – Classification of the mouse retinal bipolar cells (BC). (a) Schematic of the mouse retina. (b) Classification of the BC according to their stratification pattern in the IPL, the photoreceptors they connect and the physiology of their response (ON/OFF, transient/sustained). In this figure, it shows only five of the six OFF BCs and seven of the eight ON BCs (Tsukamoto & Omi 2017). Credits: (Euler et al. 2014), Copyright © 2014, Nature Publishing Group.

1.4 Horizontal cells

Horizontal cells are located exclusively in the OPL and their hyperpolarisation is associated with a slow response to light (S-potentials) (Bloomfield & Miller 1982; Steinberg 1969; Suzuki & Pinto 1986; Svaetichin & G. 1953). Their response to light is explained by an excitatory input from the photoreceptors, which decreases under illumination (Cervetto & Piccolino 1974; Dowling & Ripps 1973; Kaneko & Shimazaki 1975). HCs provide an inhibitory feedback through GABAergic (γ -aminobutyric acid) transmission (Cuenca et al. 2000; Cueva et al. 2002; Deniz et al. 2011; Puller et al. 2014) to the photoreceptors (Beckwith-Cohen et al. 2019; Chapot et al. 2017; Diamond 2017; Drinnenberg et al. 2018; Hirano et al. 2018; Kemmler et al. 2014; Nelson et al. 1975). In the mouse, there are mainly two morphological types of HCs, the A-

Introduction

type, smaller and providing local inhibition and the B-type, larger and with axon that can provide inhibition to local and distal parts (Kolb 1974). Within the same types, the HCs form networks through gap junctions across the OPL (Dorgau et al. 2015; Hombach et al. 2004; Janssen-Bienhold et al. 2009; O'Brien et al. 2006) (Figure 9). Such a network allows HCs to have very large receptive fields (Kaneko 1971; Lamb 1976; Naka & Rushton 1967) (Figure 9) and so provide distal information to the BCs and photoreceptors which have much narrower receptive fields (Lasansky 1981; O'Bryan 1973; Ströh et al. 2018; Wu 1991). The conductivity of the gap junction is regulated by dopamine (He et al. 2000; Jackson et al. 2012; Liu et al. 2016; McMahon et al. 1989; Teranishi et al. 1983; Veruki & Wässle 1996; Witkovsky 2004; Witkovsky et al. 2008; Zhang et al. 2011) released by the dopaminergic amacrine cells (DACs). The HC seem to play a very important role in the retina; indeed, they are part of a feedback loop with the photoreceptors and they modulate large areas of the OPL, with a potential regulation coming from the IPL and mediated by the DACs. By this way the HCs may control the amount of information transmitted from the OPL to the IPL (Szikra et al. 2014). Their role has been highlighted in experiments in which targeting of the HCs did affect the RGCs centre surround receptive field (Davenport et al. 2008; Mangel 1991; Thoreson & Mangel 2012).

Introduction

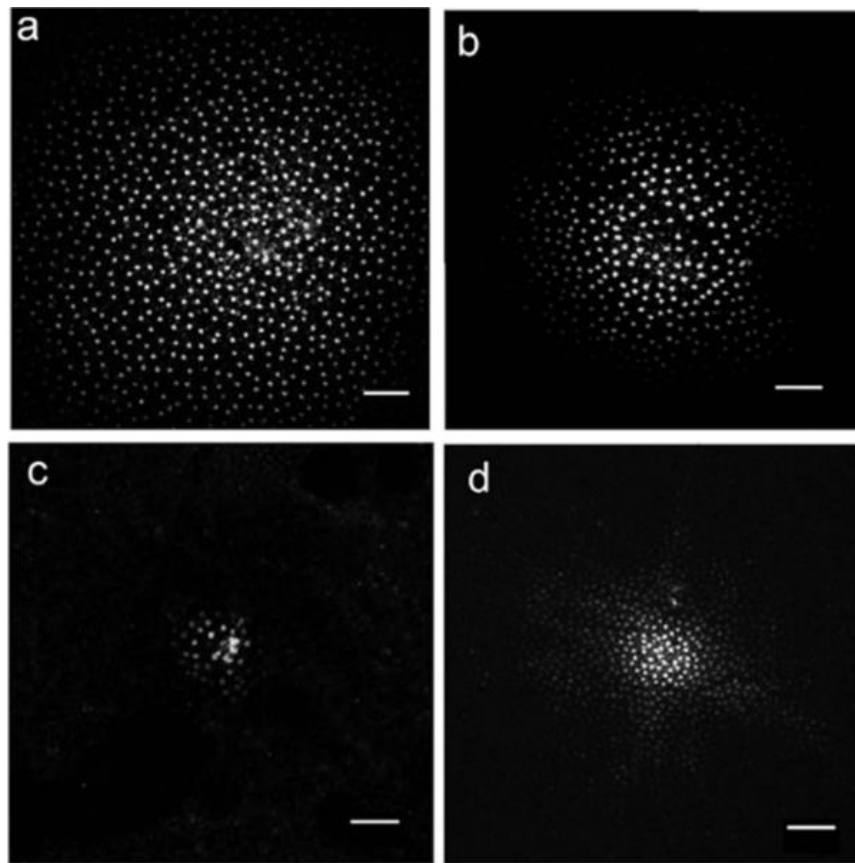


Figure 9 – Modulation of horizontal cell coupling in monkey retina. *A) Dark adapted H1 horizontal cells coupling is revealed by Neurobiotin tracer B) Mesopic light intensity decrease the coupling between HCs. C) Coupling is abolished by meclofenamic acid, a gap junction blocking agent. D) Coupling is reduced by the dopamine D1 receptor agonist SKF38393. The scale bars are 100 μm . Credits: (Zhang et al. 2011), Copyright © 2011 Wiley-Liss, Inc.*

1.5 Amacrine cells

In the IPL, the ON and OFF BCs provide input to the RGCs and the ACs (Asari & Meister 2012, 2014); the latter acts as an interneuron to modulate, split and integrate the signals (Diamond 2017; Franke & Baden 2017; Grimes et al. 2010) into the RGCs so that a thorough world representation is transmitted to the brain. Inventories of the ACs have shown that there are about 60 different AC types (Yan et al. 2020), that can be classified according to their dendritic tree size and are then called: narrow-field, small-field and wide-field ACs (Kolb et al. 1981; Lin & Masland 2006). These cells are also classified according to their dendritic tree stratification of the IPL (Kolb et al. 1992; MacNeil & Masland 1998; Mariani 1990). Some AC receive glutamatergic input from the BCs (Grünert et al. 2002) and provide negative feedback mainly with GABA and glycine (Chávez et al. 2010; Greferath et al. 1994; Grünert 2000; Wässle et al. 1998, 2009). Whereas other ACs such as the starburst amacrine cells implicated in the direction selectivity are cholinergic (Famiglietti 1983; Vaney 1990), or can use other

Introduction

neurotransmitters such as corticotropin releasing hormone (Jacoby et al. 2015; Park et al. 2018), glutamate (Della Santina et al. 2016; Lee et al. 2014) or dopamine (Figure 10).

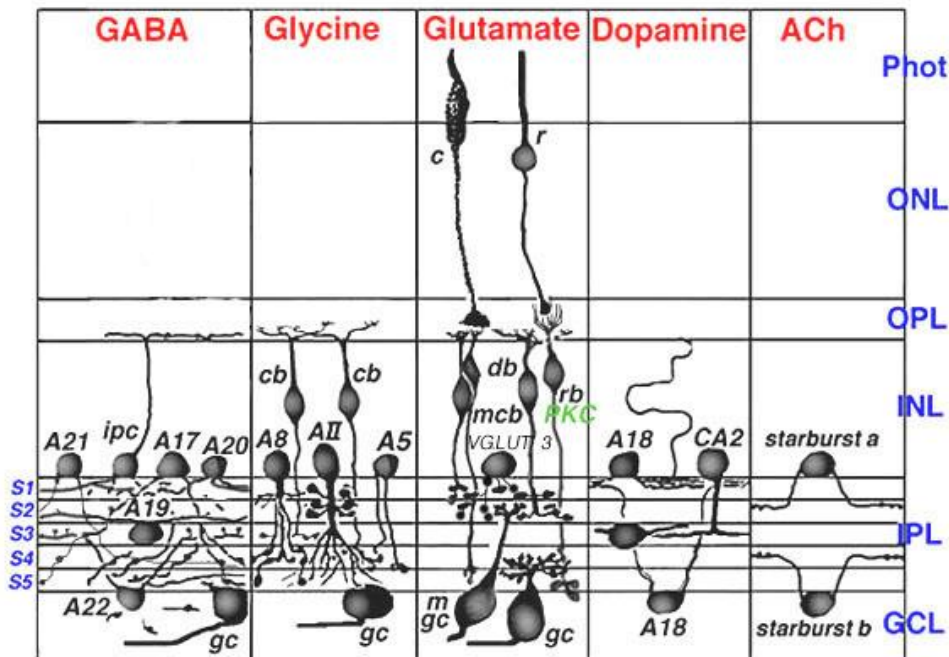


Fig. 21. Summary diagram of the organization of neurotransmitters according to cell type in the mammalian retina.

Figure 10 – Summary diagram of the organization of the main neurotransmitters in the retina. *Phot*: photoreceptor layer, *ONL*: outer nuclear layer, *OPL*: outer plexiform layer, *INL*: inner nuclear layer, *IPL*: inner plexiform layer, *GCL*: ganglion cell layer, *c*: cone, *r*: rod, *cb*: cone bipolar cell, *rb*: rod bipolar cell, *ipc*: inter-plexiform cell, *gc*: ganglion cell. This shows the diversity of neurotransmitters used in the retina and in particular by the amacrine cells. Credits: (Kolb 2011b), CC BY-NC.

1.5.1 Dopaminergic amacrine cells

The dopaminergic amacrine cells (DACs) are wide field ACs and stratify in the S1 layer of the IPL (Kolb et al. 1981, 1992; Mariani 1990). One particularity of these ACs is that their dendrites extend up to the OPL (Dacey 1990; Kolb et al. 1990), and hence they are also referred as inter-plexiform cells. In the mouse, the DACs have a small cell body, their ramifications reach the S3 layer (Contini et al. 2010; Zhang et al. 2004, 2007) and receive input from the ON BCs (Contini et al. 2010; Zhang et al. 2007) via the rod pathway (Pérez-Fernández et al. 2019; Zhao et al. 2017). DACs also release GABA like other ACs (Contini & Raviola 2003; Hirasawa et al. 2009, 2012, 2015). Dopamine receptors are found both in the OPL and IPL, respectively on HCs (Flood et al. 2018; Klaassen et al. 2011; Mazade et al. 2019; Pflug et al. 2008; Teranishi et al. 1983; Vaney 1994; Veruki & Wässle 1996), RGCs (Cui et al. 2017; Dearth et al. 1991; Ikeda et al. 1986; Jensen & Daw 1984; Thier & Alder 1984; Veruki & Wässle 1996; Wagner et al. 1993) and ACs, acting onto the gap junctions between ACs in the IPL (Hampson et al.

Introduction

1992; Vaney 1994). The communication between DACs and RGCs is bidirectional since DACs are both presynaptic (Van Hook et al. 2012; Vugler et al. 2007) and postsynaptic partners (Dkhissi-Benyahya et al. 2013; Liu et al. 2017; Qiao et al. 2016) of the intrinsically photosensitive RGCs, a type of RGCs that will be detailed in a later section (section 1.6.1). Finally, the DACs are expressing the H1 receptor and could therefore be a target of the histaminergic centrifugal fibres (Frazão et al. 2011) (Figure 11).

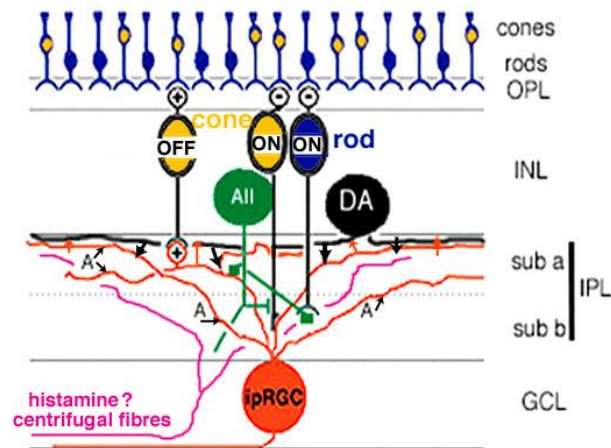


Figure 11 – Presumptive synaptic connection scheme between an ipRGC (M1-type), a histaminergic centrifugal fibre and a dopaminergic amacrine cell. ONL: outer nuclear layer; INL: inner nuclear layer; IPL: inner plexiform layer; GCL: ganglion cell layer; ipRGC: intrinsically photosensitive retinal ganglion cell; DA: dopaminergic amacrine cell; Credits: (Graham & Wong 2016), CC BY-NC.

Introduction

1.6 Ganglion cells

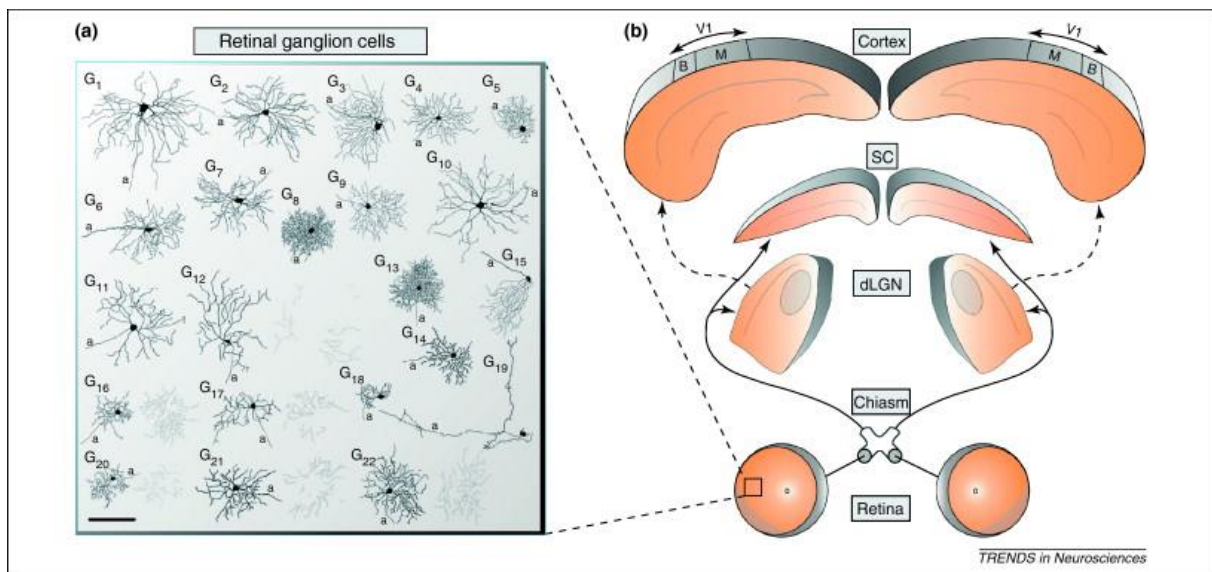


Figure 12 – Basic architecture of mouse retinal ganglion cells (RGCs) and visual pathways. **A)** This figure shows the old classification of 22 anatomically distinct subtype subtypes, termed ‘G1–G22’ (at the time of the publication in 2011), and for each a reconstruction based on dye injections is shown. Dark lines depict the somas and dendritic arbors of each cell. Lighter gray lines indicate dendritic arbors in deeper layers of the inner retina. **B)** Schematic diagram of the mouse visual pathways. The RGCs project directly to the superior colliculus (SC) and the lateral geniculate nucleus (dLGN), and this last projects to the primary visual cortex (V1). For simplicity, most of the 20-plus subcortical visual targets are not shown. Shaded portions of the retinas indicate which RGCs’ axons do not cross at the optic chiasm. Ovals in the dLGN correspond to the target of the ipsilateral-projecting RGC axons. The binocular (‘B’) and monocular (‘M’) fields in the V1 area of the cortex are shown. The lighter lines in the dLGN and SC represent the approximate boundaries between axons’ targets of different functional categories of RGCs. Credits: (Huberman & Niell 2011) Copyright © 2011 Elsevier.

The RGCs are the cells summing up (Deny et al. 2017) the complex decomposition (Asari & Meister 2012, 2014; Grimes et al. 2010) of the signal made so far in the retina and these cells send the output to the brain via the optic nerve and the optic tract (Lettvin et al. 1959). The retino-recipient brain areas are numerous (Lawrence & Studholme 2014), and among those we find that the dLGN and the SC receiving most of the retinal output (Berson 2008; Lawrence & Studholme 2014; Martersteck et al. 2017; Robles et al. 2014). Long thought to be considered as feature detectors responding to specific types of stimuli (Lettvin et al. 1959), RGCs are also capable of anticipation (Berry et al. 1999; Chalk et al. 2018; Johnston & Lagnado 2015; Palmer et al. 2015) and respond to omitted stimuli (Schwartz & Berry 2008; Werner et al. 2008). In the mouse, several attempts of classification of the RGCs have been made based upon anatomical (Badea & Nathans 2004; Bae et al. 2018; Coombs et al. 2006; Helmstaedter et al. 2013; Kong et al. 2005; Pisano et al. 2017; Sanes & Masland 2015; Seung & Sümbül 2014; Völgyi et al. 2009), molecular (Pisano et al. 2017; Sanes & Masland 2015) or physiological (Baden et al. 2016; Bae et al. 2018; Farrow & Masland 2011; Jouty et al. 2018; Pisano et al. 2017; Sanes &

Introduction

Masland 2015; Vlasits et al. 2019) criteria (Figure 12). Four of the main physiological properties exhibited by the RGCs required for the identification of a subtype are (1) the polarity, (2) the centre-surround receptive field, (3) the direction selectivity and (4) the mosaic arrangement. The polarity of an RGC is the type of light response it gives, which can be either ON, OFF or ON-OFF response (Barlow 1953; Hartline 1938; Kuffler 1953; Nelson et al. 1978; Peichl & Wässle 1981), with various degrees of sustainability in its response (Belgum et al. 1982; Cleland et al. 1971; DeVries & Baylor 1997). The centre-surround receptive field is an area where a stimulus can trigger a response of the RGC (Kuffler 1953; Rodieck 1965; Shapley & Victor 1986). On the central area, a stimulus of the polarity will trigger a response of the cell, whereas the same stimulus on the receptive field surround will be inhibitory for the cell (Peichl & Wässle 1983). The direction selectivity is a property of a population of RGCs tuned to respond strongly to stimuli moving in a specific direction while being inhibited by stimuli moving in non-preferred directions (Amthor et al. 1984; Barlow & Hill 1963; Barlow & Levick 1965; Maturana & Frenk 1963).

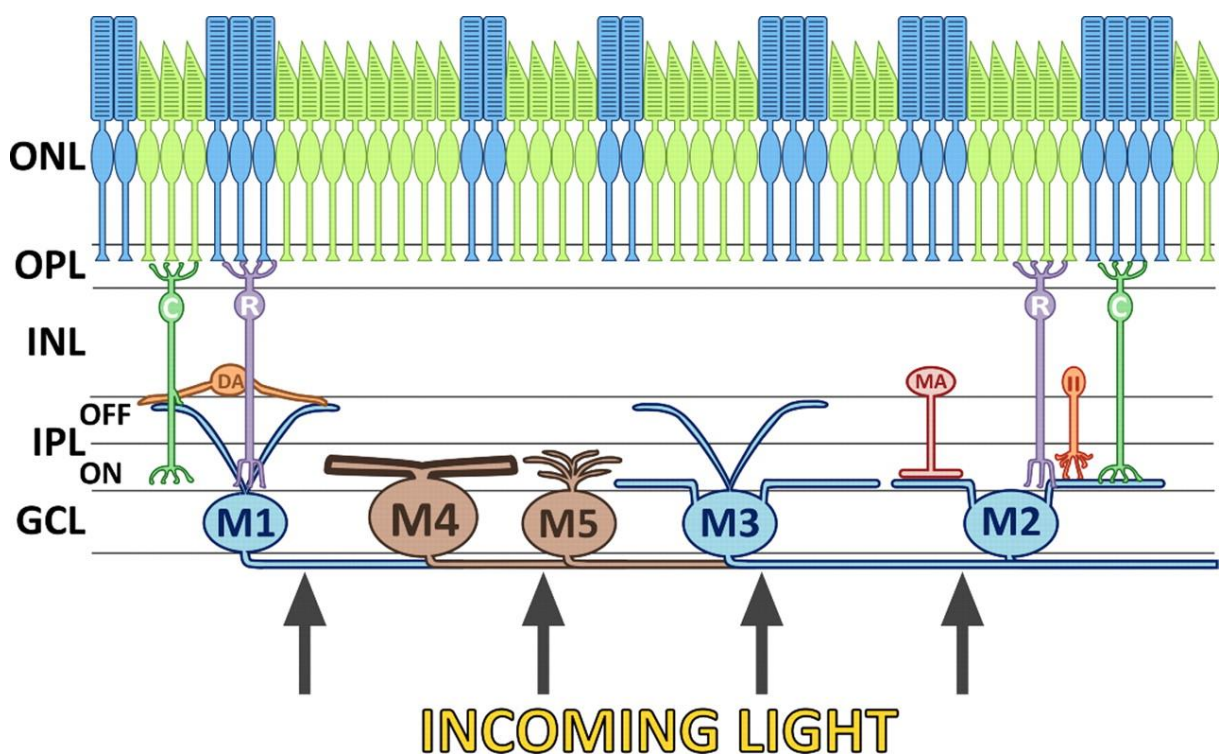


Figure 13 – ipRGCs differs in morphology and site of dendritic fields. The classification of ipRGCs (M1, M2, M3, M4 and M5) is based on morphology and somatic and dendritic localization. The M1 ipRGC connects with the dopaminergic amacrine cells. Credits (Schmidt et al. 2011), CC-BY-NC-SA.

Introduction

1.6.1 Intrinsically photosensitive RGCs

Discovered in mice lacking functional photoreceptors and still exhibiting light pupil response and circadian rhythm (Freedman et al. 1999; Keeler 1927; Lucas et al. 1999, 2003), intrinsically photosensitive RGCs (ipRGCs) are cells that express a photo pigment, the melanopsin (Provencio et al. 1998, 2000, 2002). The ipRGCs light sensitive without the need of inputs from the photoreceptors (Berson 2007; Berson et al. 2002; Graham et al. 2008). They project primarily to the supra-chiasmatic nucleus (SCN) (Gooley et al. 2001; Hannibal et al. 2002; Hattar et al. 2002, 2006; Lawrence & Studholme 2014), the central clock of the circadian rhythm (Morin 2013), and participate in different non-image-forming behaviours (Lazzerini Ospri et al. 2017; Li & Schmidt 2018; Rupp et al. 2019; Sonoda et al. 2020). Although the ipRGCs act as photoreceptors, they also receive input from the classical rod/cone input pathway (Belenky et al. 2003; Dacey et al. 2005; Perez-Leon et al. 2006; Weng et al. 2013; Wong et al. 2007; Zhao et al. 2014) (Figure 13). In addition to ON inputs (Dumitrescu et al. 2009; Hoshi et al. 2009), the ipRGCs receive modulatory input from the dopaminergic amacrine cells (DACs) (Van Hook et al. 2012; Viney et al. 2007; Vugler et al. 2007) that are involved in the light adaptation mechanisms of the retina (see section on DACs; section 1.5.1); more precisely, some of the modulatory mechanisms from the DACs to the ipRGCs could arise from histaminergic RP fibres (Frazão et al. 2011; Gastinger et al. 1999) (Figure 11) which activity is related to the circadian activities. This would then create a feedback loop for the retina involving the brain.

1.7 Anaesthesia

During the work conducted for this thesis, I recorded mice under anaesthesia, for which results are also presented and discussed in this thesis. As such, I wish to do a brief introduction of anaesthesia, and in particular on the effects of isoflurane and midazolam, the two anaesthetics I used.

1.7.1 Principles

A general anaesthesia is defined by the combination of three main components: analgesia, paralysis (Collins et al. 1995) and amnesia (Izquierdo & McGaugh 2000), and more than two hundreds millions of patients every year undergo a general anaesthesia for surgery (Weiser et al. 2008). Still, the precise mechanisms of anaesthesia remain unclear (Antkowiak 2001; Yamamoto & Schindler 2017), despite descriptions of the molecular basis of the interaction between anaesthetics and excitatory or inhibitory receptors. Indeed, many of the common anaesthetics share common target GABA receptors (Brohan & Goudra 2017; Jenkins et al. 2001; Tanelian et al. 1993; Whiting 2003), such as the families of barbiturates (Steinbach &

Introduction

Akk 2001), benzodiazepines (Alkire et al. 2008; Rudolph et al. 1999), volatile anaesthetics (John Mihic et al. 1997).

In the central nervous system, GABA is the major neurotransmitter involved in neuronal inhibition (Marsden 1977) after the development and act on three types of membrane GABA receptors: The GABA_A and GABA_C are two types of ligand-gated chloride channels (Figure 14). GABA_A receptors (GABA_AR) were identified in electrophysiology for increasing the permeability to chloride ions (Bormann 1988). While the α and β subunits are required to form the GABA_A ion channel (Connolly et al. 1996), variations in the channels subunits determine the affinity to ligands, conductance and other properties (Cossart et al. 2005). Instead of the α and β subunits, the GABA_CR are entirely composed of the ρ subunits (Enz 2001; Enz & Cutting 1998). This molecular difference induces a strong difference in affinity for ligands. Barbiturates, benzodiazepines and volatile anaesthetics all specifically modulate the GABA_AR function (Drafts & Fisher 2006; Kelly et al. 2002; Low et al. 2000; McKernan et al. 2000; Olsen & Li 2011). Each anaesthetic drug act on the GABA_AR in a specific manner, which could be the origin of specific behavioural effects to the drugs at a low dose (Tanelian et al. 1993). However, at high doses, the functional specificity is lost and all drugs potentiate the GABA_AR strongly enough for a central nervous system depression, resulting in anaesthesia (Tanelian et al. 1993). The third type of receptor, the GABA_BR, is a G-protein coupled receptor and regulates the opening of potassium channels (Bowery 1989; Chen et al. 2005).

Of all the existing anaesthetic drugs, we will present in more details the two that were used in this study. For more extensive reviews on the role of GABA_AR in anaesthesia, see (Brohan & Goudra 2017; Tanelian et al. 1993).

Introduction

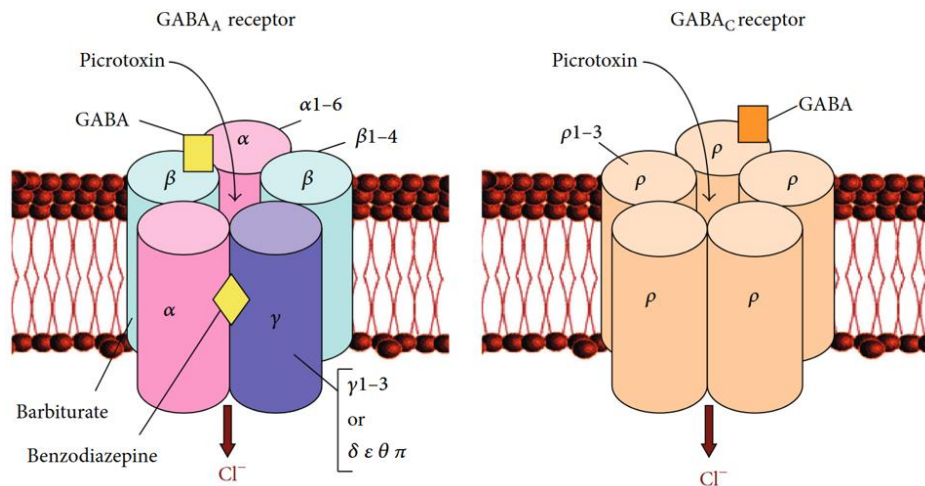


Figure 14 – Schematic representation of the GABA_A and GABA_C receptors. It shows the different subunit compositions (α , β , γ , ρ) and the binding sites of GABA, picrotoxin (antagonist), barbiturates and benzodiazepines. Five subunits are required to form each chloride channel. Credits: (Popova 2014) CC-LA.

1.7.2 Midazolam

Midazolam is a part of the family of benzodiazepine (Olkola & Ahonen 2008), for which the amnesic, anxiolytic, and sedation effects arise from their interactions with the GABA_AR (Kaufmann et al. 2003). When benzodiazepines bind to the GABA_AR, they induce a conformational change of the receptor structure, enhancing the affinity of the GABA neurotransmitter.

The benzodiazepines effects are dose-dependent, varying from a sedation at a low dose to anaesthesia with higher doses and thus the control of the depth of anaesthesia is difficult (Nilsson et al. 1988). For a better control of the anaesthesia, midazolam is often combined with other drugs, such as the fentanyl, an opioid for the analgesia, and medetomidine, an α_2 -adrenergic receptor antagonist with sedation effects (Buerkle & Yaksh 1998; Drew et al. 1977; Scheinin et al. 1989). The combination of these three drugs, fentanyl, midazolam and medetomidine is referred to as FMM.

1.7.3 Isoflurane

Isoflurane is part of the family of volatile anaesthetics, and as for others anaesthetics, they potentiate the GABA_AR chloride currents (Jones et al. 1992; Krasowski & Harrison 2000; Lin et al. 1992; Nakahiro et al. 1989). Their interaction with the GABA_AR is different from other anaesthetics, as they are calcium-dependant (MacIver et al. 1991; Mody et al. 1991). The volatile anaesthetics increase the response probability of the GABA_AR to GABA and prolongs the channel opening duration (Jones et al. 1991). The interaction between volatile anaesthetics

Introduction

and the GABA_AR is dose-dependent (Sebel et al. 2006) where high concentrations enable a direct activation of the receptor without GABA (Garcia et al. 2010). Moreover, inhibition of the excitatory N-methyl-D-aspartate (NMDA) receptor is part of the isoflurane induced depression (Brosnan 2011; De Sousa et al. 2000; Stabernack et al. 2003), together with a potentiation of the inhibitory glycine receptors (Krasowski & Harrison 2000).

1.8 Specific Aims

Despite the many studies describing the RP system, very little is known about its mechanisms. Most of the studies on the activity of retinal circuits are made with *ex vivo* preparation and therefore with disrupted RP fibres. To understand how the RP system affects the retinal computation, *in vivo* recording techniques are required. Electrophysiological recordings have been used to study diverse retinal functions in the optic tract of monkeys. (Hubel & Wiesel 1960; Marrocco 1972), cats (Andrews & Hammond 1970; Enroth-Cugell & Robson 1966; Hubel 1960) and rodents (Freeman et al. 2010; Michael 1968; Nobles et al. 2012; Sagdullaev & McCall 2005). But a caveat of these studies is that the recordings were made under anaesthesia (often even with paralyzants) and brain tissue above the optic tract was removed by suction, highly altering the brain functions. Because the RP system originates in the brain, a prerequisite is to leave the brain as close as possible to its physiological conditions during experiments.

As a model, we decided to work with mice. Despite having a poor visual acuity (Geng et al. 2011), the mouse remains a model of choice because of the many tools available to manipulate retinal circuits (Hartl et al. 2017; Huang & Zeng 2013; Huberman & Niell 2011; Siebert et al. 2009). As a group, we have been taking two approaches to record from awake head-fixed mice. The first approach is to record from RGC axons with an electrode placed in the optic tract without removing any brain parts. The second one is to use two-photon calcium imaging in the superior colliculus (SC) (Martersteck et al. 2017). Because most RGCs in mice project to the superficial layer of the SC, the axon terminals of RGCs that express calcium indicators can be imaged through a cranial window placed over the SC. Both techniques enable to record the activity of retinal output *in vivo*, with complementary temporal and population scales. This gives us an opportunity to measure the real-life retinal processing by presenting visual stimuli to a screen placed in front of the head-fixed mouse, thus enabling us to characterise the responses of the RGCs *in vivo* and compare them with the many existing *ex vivo* studies. During the preparation of this thesis, similar techniques as ours have been developed (Hong et al.

Introduction

2018a; Schröder et al. 2020) and can serve as comparison points and could, in the future, be alternatives for the recording and study of RGCs and the RP system *in vivo*.

While my colleagues have been working on determining the exact origins and targets of the RP system using viral tracing methods in mice and establishing the calcium imaging of RGCs axon terminals in the superior colliculus, I established the electrophysiological recording methods of the RGCs axons. In addition, I developed an analysis pipeline to synchronise and process the records of both techniques to fasten the analysis and ease the comparison across the data sets obtained from the two different techniques.

Ultimately, the work conducted during this thesis will enable to study the physiological effects of serotonin and histamine in the retina *in vivo* and clarify the link between the behaviour of an animal and the visual information processing in the retina. Characterizing the physiological function of the RP system and investigating the interplay of efferent and afferent pathways in the visual system will help us better understand each step of the visual information processing.

Material & Methods

2 Material & Methods

2.1 Hardware

2.1.1 Devices

2.1.1.1 DLP Projector

We used a Digital Light Processor (DLP; Texas Instruments, DLPDLCR3010EVM-LC) to project stimuli, from which we modified the light engine. The green LED was replaced by an ultra-violet (UV) LED (365 nm; LZ1-00UV00, LED Engine) and the red LED replaced by an infra-red (IR) LED (950 nm; SFH 4725S, Osram). The replacement allowed us to use the classical green channel of images to control the UV LED and so the mouse S-cone stimulation, while the inbuilt blue LED of the DLP (454 nm) was controlled by the blue channel and used to stimulate the mouse M-cones. The IR LED was controlled by the red channel and was used to send synchronisation signals to a photodiode, without being detectable by mice.

The DLP mixes the light coming from the three LEDs in the correct proportion and intensities for each pixel of a frame. A light engine alternatively turns ON the LEDs, at a frequency of four cycles per frame. The amount allocated to each LED during a cycle can be adjusted and is called the duty cycle. The three LEDs project their light onto a digital mirror device (DMD). The DMD is an array of mirrors, that can independently deviate the light. Each mirror forms a pixel of the image. When it is turned OFF, it deviates the light into a sink. When ON it adds light to that pixel. By flickering each mirror ON or OFF in the appropriate proportion, the DMD creates the image.

By projecting an image onto a photodiode (FDS200, Thorlabs), we can convert the light into an electric signal. After amplifying the signal with a current-to-voltage converter, we passed it through an analog cable and recorded it. The more the photons, the higher the signal is. Like so, by integrating the signal over time, we obtain a linear relationship between the amount of light coming out of the DLP and the area under the curve (AUC) of the analog signal. For a white image, we observe peaks at a frequency of 720Hz. This frequency corresponds to our three LEDs turning ON four times per frame, at the refresh rate of 60Hz ($3 \text{ LED} \times 4 \text{ cycles} \times 60 \text{ fps} = 720\text{Hz}$). Here we placed a long-pass filter at 950nm (Thorlabs FEL950) in front of the photodiode to detect only the IR light, corresponding to the red channel of the image. We used this red channel to transfer information about our stimulus, such as the timing of the frame from which we could detect potential errors in the display of our stimuli (frame drop, frame duplication).

Material & Methods

We also used the signal of the photodiode (without the long-pass filter) to measure the gamma curve of the device and make the proper adjustments for each channel. By measuring the area under the curve (AUC) during each frame, passing through the 256 intensities, we measured the original gamma. We rectified it in the computer display settings to obtain a linear relationship between image intensity and recorded intensity.

Finally, we increased the duty time of the UV LED to the maximum allowed while decreasing the IR LED to the minimum to maximise the intensity of the UV part of a frame. We set respectively for the IR, UV and blue channels, 14%, 55% and 31% of the duty cycle.

At maximum intensity, the measured the light power (S121C, Thorlabs) from the mouse eye position was of $1.54 \cdot 10^{-2} \text{ W} \cdot \text{m}^{-2}$ for the UV LED and $1.59 \cdot 10^{-2} \text{ W} \cdot \text{m}^{-2}$ for the blue LED. At the wavelengths of 365 nm and 454 nm, photons have respectively an energy of 3.40 eV and 2.73 eV ($E = h \cdot c / \lambda$, $h = 6.62607015 \cdot 10^{-34} \text{ J} \cdot \text{s}$, $1 \text{ eV} = 1.602176634 \cdot 10^{-19} \text{ J}$), giving for both measured light power respectively a flux of $2.82 \cdot 10^{16}$ and $3.62 \cdot 10^{16} \text{ photon} \cdot \text{s}^{-1} \cdot \text{m}^{-2}$ (F_λ). Also at maximum intensity, the mouse pupil had a diameter of 1 mm, giving an area of 0.78 mm^2 (A_{pupil}). From the mouse eye position, the image projected by the DLP covered 73° in azimuth and 44° in altitude. On the mouse retina, a distance of 1° covers $30 \mu\text{m}$ of the tissue (MouseVision 2015) and therefore the DLP image (1280 by 720 pixels) covered an area of 2.89 mm^2 (A_{retina}). At 365 nm and 454 nm, respectively 50% and 68% of the light is transmitted (T_λ) (70% transmission at 500nm (Lyubarsky et al. 2004), transmission at 365 and 454 nm derived from normalised transmission values (Jacobs & Williams 2007)). Using the previous measures and with the formula:

$$I_\lambda = \frac{F_\lambda \cdot A_{pupil} \cdot T_\lambda}{A_{retina}} \quad (1)$$

we obtain an irradiance of the retina (I_λ) for the UV and blue light of respectively $3.81 \cdot 10^3$ and $6.64 \cdot 10^3 \text{ photon} \cdot \text{s}^{-1} \cdot \mu\text{m}^{-2}$. Assuming a mouse collecting area (a_c) of $0.2 \mu\text{m}^2$ for both cones and of $0.5 \mu\text{m}^2$ for the rods (accounting for the extinction coefficient, quantum efficiency and concentration of the pigment, and the envelope volume of the outer segment) (Nikonov et al. 2006), and assuming a relative sensitivity (S_λ) of mouse rods, S and M-cones at respectively 25%, 90% and 25% for the UV light (365 nm), and 60%, 0% and 60% for the blue light (454 nm) (Jacobs & Williams 2007; Peirson et al. 2018), we obtain with the formula:

$$P^* = a_c \cdot (I_{365} \cdot S_{365} + I_{454} \cdot S_{454}) \quad (2)$$

Material & Methods

respectively $2.5 \cdot 10^3$, $0.7 \cdot 10^3$ and $1.0 \cdot 10^3$ photo-isomerization per second for rods, and S and M-cones.

2.1.1.2 LED dome

We build a custom LED array dome stimulator to cover the entire monocular visual field of an animal (see annexe 1 for details). In short, a hemisphere of 20 cm in diameter was tiled with light-emitting diode (LED) stripes and held in place with a 3D printed support. We tiled the LED stripes in the tightest pattern we thought of to minimise the space between stripes while keeping a relatively homogeneous LED density across both elevation and azimuth. The custom-made LED dome is composed of a total of 948 LEDs on 88 sub-strips. The LED dome has 90° symmetries, and each quarter is divided in two rewired LED stripes (each of nine sub-stripe wired end to end, a first for 112 LEDs and a second one for 125 LEDs). With these subdivisions, there is a total of eight individually controllable stripes. We chose to use one Arduino Uno per quarter to control the LEDs (worker), with a fifth one for synchronisation (master).

To synchronise the workers, the master Arduino sent pulses at a given frequency to signal when to begin the next frame's computation and display. Once done, each worker sent a pulse to signal that we gathered into a single analog signal.

At a distance of 10 cm, the LEDs had an angular size of 2.86° , comparable to the ganglion cells receptive field size ($2-3^\circ$). For a maximum value of 1 on an 8-bit range, we obtained a total power of $0.2 \text{ W} \cdot \text{m}^{-2}$.

Similar to the intensity of the DLP measure, we found for the LED dome at the mouse position a power of $1.34 \text{ W} \cdot \text{m}^{-2}$. The blue LEDs emit at the wavelength of 465 nm, same as that of the DLP blue LED and therefore by using the same parameters, we obtain a light power a flux of $3.17 \cdot 10^{18} \text{ photon} \cdot \text{s}^{-1} \cdot \text{m}^{-2}$ (F_λ). We did not measure the mouse pupil diameter within the LED dome, but as its intensity is a lot stronger than the intensity of the DLP projector, we will consider the half of the pupil diameter measured with the DLP projector. We then obtain a diameter of 0.5 mm, giving an area of 0.20 mm^2 (A_{pupil}). With the LED dome, the stimulus covered the entire monocular field of view, corresponding to the entire mouse retina, having an area of 18 mm^2 (A_{retina}) (Jeon et al. 1998). Using the equation 1 we obtain an irradiance of the retina (I_λ) of $6.50 \cdot 10^4 \text{ photon} \cdot \text{s}^{-1} \cdot \mu\text{m}^{-2}$. Using then the equation 2 we obtain respectively $1.9 \cdot 10^4$ and $7.8 \cdot 10^3$ photo-isomerization per second for the rods and M-cones (S-cones do not have a sensitivity for this blue light). As such, the stimulus was about eight time stronger than the stimulus of the DLP projector.

Material & Methods

2.1.1.3 Treadmill

Mice implanted with a head plate (see below for the procedure; section 2.2) were kept head-fixed above a custom-designed treadmill (by our lab technician, Dmitry Molotkov). The treadmill is made of a rotatory plate (20 cm diameter) above a suspension system (spring + counterweight) diminishing the upward forces created by the animal while pushing on its legs or moving on the plate. An optical sensor (Microsoft USB mouse) placed below the plate measured the plate rotation speed 62 mm away from the centre of rotation. A voltage of -1V in our signal corresponded to a locomotion speed of $62.5 \text{ mm}\cdot\text{s}^{-1}$, and saturated after $\pm 10\text{V}$. The sensor's sampling rate of 500Hz was considered as continuous in comparison to our other signals.

2.1.1.4 Phenotype cameras

During awake experiments, we used two complementary metal-oxide semiconductors (CMOS) cameras to record the mice. We pointed the first camera (Imaging Source DMK23UX174) to the mouse body (mouse cam) to keep a record of the mouse behaviour on the treadmill, and the second camera (Imaging Source DMK23UX174) recorded the stimulated/recorded mouse eye to perform eye-tracking later on in our analysis (eye cam). The CMOS cameras are sensitive to IR light, and after placing them behind filters and lenses, we used IR LEDs to illuminate the setup. As such, the CMOS cameras captured videos while mice were kept in the dark.

During the acquisition of data, we set the cameras to a trigger mode. In that mode, the cameras wait for pulses before acquiring a frame. The pulses were sent and recorded together with the other signals using custom software (LabView, National instruments). Like so, the pulse timings matching the video's frames were synchronised to the rest of the record. Pulses were sent at 30Hz, while the camera capture software (Imaging Source, IC capture) settings were adjusted to allow frame capture faster than 30Hz. As so the camera is supposed to be able to record at 30Hz. However, due to the computation time required by the video compression, the capture software dropped some frames, giving an average refresh rate of 29.9 Hz.

Material & Methods

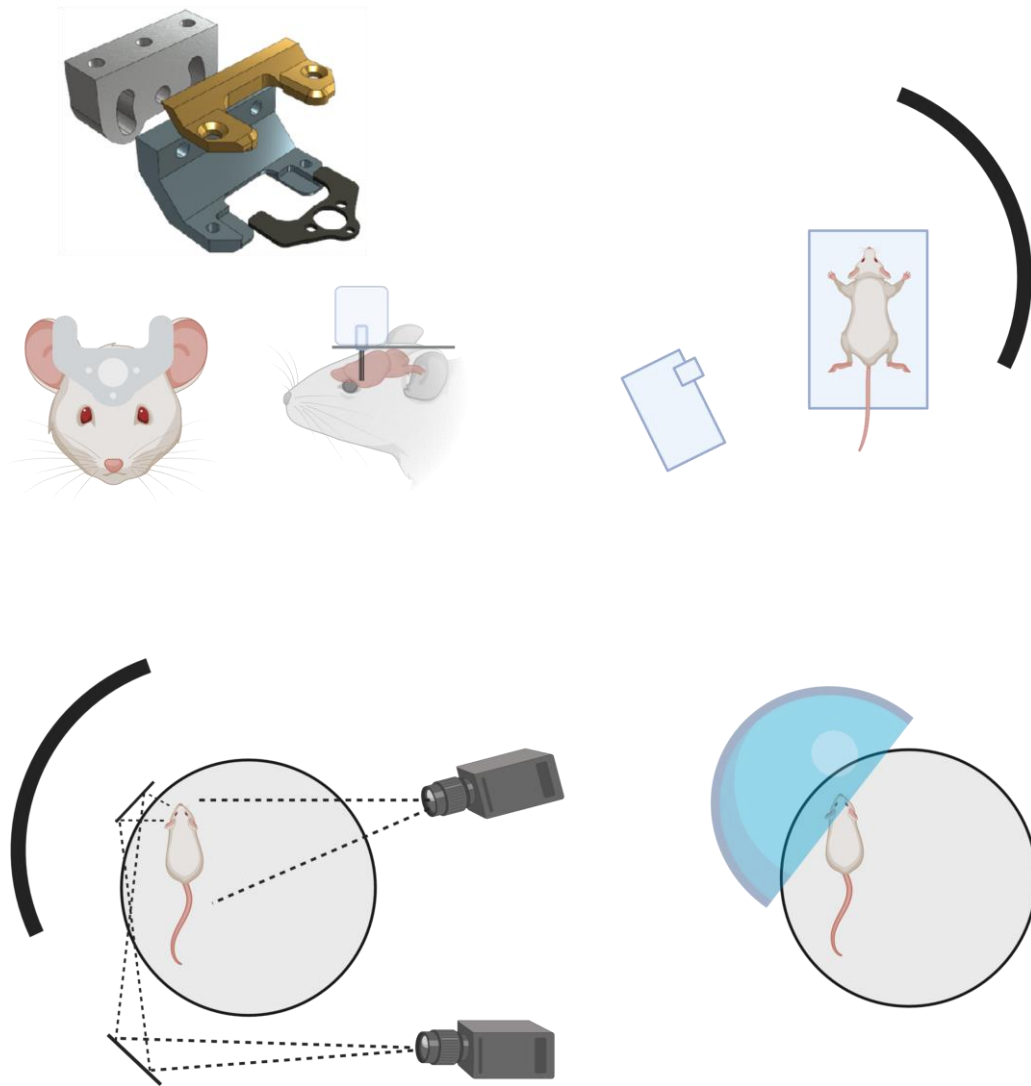


Figure 15 – Illustration of the electrophysiology experiment. **A)** Head plate holder (top) and head plate implanted on a mouse. The left mouse illustration shows the head plate without the implanted chronic electrode. The right mouse illustration shows the profile of the implant. The cap on top protects the screw used to move the electrode up and down. **B)** Anaesthetised stereotaxic electrophysiology setup. The mouse is kept under anaesthesia on top of a heating pad—the DLP projector on the left project the image to the screen on the right. The electrode is not represented here. **C)** Awake electrophysiology setup. The mouse is kept its head fixed (head plate holder not represented here), and run on the treadmill (rotating wheel) bellow—two cameras on the right capture the mouse running and the left mouse eye. The eye camera uses a mirror and a dichroic mirror to image the eye. A DLP projector (not represented) projects the image to the screen from bellow the screen with a mirror (not represented) located under the treadmill. **D)** LED dome setup. The mouse and treadmill are the same as in C. The screen is replaced by a dome covered by LEDs, whose centre is aligned to the mouse left eye. Illustration made with BioRender.

Material & Methods

2.1.2 Setups

2.1.2.1 *Anaesthetised stereotaxic electrophysiology*

The anaesthetised stereotaxic electrophysiology setup designates recordings of mouse optic tract under anaesthesia. The electrode implantation, anaesthesia and recording protocols are described in a later section (2.2). In this setup, the animal's head was secured in a stereotaxic frame (Figure 15.B). A screen covered with UV reflective paint was placed in front of the right mouse eye, onto which a DLP projected a visual stimulus. The DLP was located on the left side of the mouse to project directly onto the screen. It avoided the usage of a mirror system challenging to implement, due to repeated assemblies/disassemblies of the setup. A drawback was that the electrode holder above the mouse cast a shadow onto the screen, blocking potentially the stimulus over the recorded RGCs' receptive field. Finally, at the exit of the DLP, a dichroic mirror deviated the light's IR component onto a photodiode.

We connected the photodiode and electrophysiological data streams to a SmartBox (Neuronexus), to record both channels in a synchronised fashion. The obtained data were stored in RHD format, sampled at 30kHz.

2.1.2.2 *Awake electrophysiology*

In the awake electrophysiology setup, a mouse implanted chronically with a silicone probe in the optic tract was head-fixed over a treadmill (Figure 15.C). A screen covered with UV reflective paint was positioned on the left side of the mouse—the DLP projected from below the screen, with a mirror reflecting the image onto the screen. Lastly, a mirror in the bottom right corner of the screen reflected the image onto a photodiode. Two phenotyping cameras (the mouse cam and eye cam) with IR long-pass filters were used with IR LED illumination.

The camera trigger pulses, the optic sensor under the treadmill and the photodiode signals were all recorded by custom software written in LabView (National Instrument) at 10kHz in binary format. A second computer recorded the electrophysiology data and the photodiode signals at 30kHz (same as the anaesthetised electrophysiology setup). The photodiode data recorded twice served as a reference to synchronise both recordings.

2.1.2.3 *LED dome awake*

In the LED dome awake setup, a mouse implanted chronically with a silicone probe (Neuronexus, Buzsaki32L) in the optic tract was head-fixed over the treadmill. The LED dome was positioned next to the mouse left eye, at an angle of 40° in azimuth and 30° in altitude (Figure 15.D). Synchronisation pulses from the Arduino workers and electrophysiological data

Material & Methods

streams were given to a SmartBox (Neuronexus), to record both channels in a synchronised fashion. The obtained data are stored in RHD format, sampled at 30kHz.

2.2 Optic tract electrophysiology

All experimental procedures were conducted under the license 233/2017-PR from the Italian Ministry of Health.

2.2.1.1 Mouse

For all the experiments, a total of 21 female C57BL/6J mice were used (18 and 3 for respectively acute and chronic experiments) at around three months of age at the time of the surgery. Mice were kept on a 12-h light/12-h dark cycle and were given water and food *ad libitum*. After the chronic implantation of electrodes, mice were kept single housed.

2.2.1.2 Anaesthesia for the implantation procedure

For the implantation of silicone probes, animals were pre-anesthetised with a dose of 4% isoflurane (Zoetis Inc, IsoFlo), and later kept under isoflurane anaesthesia with a dose of 1 to 2% given through a nose mask, on top of a heating pad (Supertech Physiological) set at a temperature of 37°C. For the chronic implantation of electrodes, eye ointment (VitA-POS) was used to prevent the eyes from drying. For the anesthetised records, a contact lens (Ocuscience, 3mm) was used for the recorded eye instead of the ointment.

2.2.1.3 Silicone probe chronic implantation

After positioning the mouse head on a stereotaxic apparatus (Neurostar), the scalp skin was disinfected with Betadine and removed with scissors. The skull was meticulously cleared with a round scalpel to remove any soft tissue from the surface. Ethanol was applied to the skull, followed by acetone to disinfect and remove fat residual compounds. Finally, the skull was glazed with a drop of cyanoacrylate adhesive (Loctite 401) to secure in place the surrounding skin and to create a strong attachment.

The skull of the mouse was then registered in the stereotaxic controller software (NeuroStar). If the mouse head was too much tilted or sideways, the animal's head was repositioned. A dental drill (WPI) was used to leave three marks on the skull to indicate the entry point to target the optic tract: [-1.34, 1.87, 4.74], [-1.70, 1.87, 4.74], and [-1.82, 2.35, 4.07] in AP/ML/DV coordinates.

A hole was drilled for the reference silver wire (A-M Systems) above the cerebellum, and the wire was inserted sideways to avoid excessive brain damage. The hole and wire were covered

Material & Methods

with Vaseline before attaching the wire to the skull first with a drop of glue and later with a mix of glue and dental cement (Paladur, PALA).

Subsequently, a custom-designed titanium head-plate was attached to the skull with dental cement (Figure 15.A). The chronic silicone probe (Buzsaki32L; Neuronexus) was mounted to the stereotaxic apparatus and centred on the three marks. After taking note of the Z position, the probe was pulled up to leave space for the craniotomy.

After performing a craniotomy of 1-2mm in diameter with a drill (WPI Inc), the dura was cut with a syringe tip (Microlance, 30G). The probe was then lowered with the stereotaxic controller software at a rate of 75µm per minute up to a depth of 4.5 mm from the skull surface. After two millimetres, the probe was moved out for one millimetre to release pressure created by the initial brain entry.

After reaching the desired depth, the probe was protected with a wall of Vaseline built around it before attaching the drive mechanism with dental cement to the skull. After drying, the silicone probe was removed from its mount, to place and cement the protective cap. The cables and connectors were protected with paraffin film (Bemis, Parafilm “M”) to prevent the mouse from damaging the implant.

For the recovery after the surgery, mice were kept on a heating pad (Sera, Thermo comfort mat S). During the next four days, mice received an anti-inflammatory/antibiotic cocktail Rimadyl/Baytril (0.5 mg/mL each, 0.01mL/g). The antibiotic Baytril was given for an additional three days through drinking water (0.17 mg/mL, (Carrick et al. 2018)).

After a recovery period of five days, the mice were trained on a custom made treadmill for two hours two times a day. During these sessions, we recorded the signals and moved the electrode until visual responses were observed.

2.2.1.4 Silicone probe implantation for anaesthetised records

Similar to the chronic implantation, mice were anaesthetised and placed inside the stereotaxic apparatus. Their scalp was removed, registered in the stereotaxic software, and three entry points for targeting the optic nerve were marked with the stereotaxic drill.

The silicone probe (Buzsaki32L, Neuronexus, acute) was mounted on a micromanipulator (Sensapex, SMX), itself fixed on the stereotaxic apparatus. To prevent unwanted forces from being applied to the micromanipulator or the stereotaxic, all cables were plugged and secured with tape before the insertion of the probe.

Material & Methods

The silicone probe was then approached to the top of the skull, centred on the earlier delineated region and its coordinates were registered. After taking the probes back up, a well was made with dental cement around the marks later to hold saline solution on top of the brain. A craniotomy of 2mm of diameter was made. The silicone probe was then lowered with the micromanipulator at a rate of 100 μm per minute. Pauses and retraction of the probe, as mentioned in the chronic implantation procedure were made to let the brain move around the electrode and release pressure.

Slightly before reaching the depth of the target, the silicon probe's signals were observed while projecting a visual stimulus (ON/OFF full-field for 1 second each). In the region above our target, cells displaying intense bursts of spikes were usually found, with a high amplitude and covering most of the channels of our probe. Such activity was a sign indicating that the optic tract would soon be reached. Indeed, following this region with intense bursts, an area of silence was observed, that was interpreted as the silicon probe pushing the optic tract. After a few hundreds of micron, and also often after retracting the probe slightly, neurons responding to visual stimuli appeared.

2.2.1.5 Anaesthesia record

With the stereotaxic electrophysiology setup, the mouse was kept under anaesthesia for the total duration of the experiment. In the case of recordings under isoflurane anaesthesia, the concentration was set at around 1% isoflurane. The depth of anaesthesia was monitored with the breathing rate of the animal, kept slightly below one breath per second.

In the other set of recordings under anaesthesia, we used a cocktail of fentanyl, medetomidine, midazolam (FMM). Once that the electrode was in position and ready to record, a heart rate monitor was attached to the mouse, and the animal was injected with an FMM solution (fentanyl 0.05mg/kg, medetor 0.5mg/kg, midazolam 5mg/kg) in saline (0.9% NaCl). The heart rate was a good indicator for the depth of anaesthesia using FMM, decreasing to about 280 beat per minute (bpm) after the injection and slowly going back up to 360bpm when the anaesthesia wore off. Once the heart rate slowed down, the isoflurane dose was decreased progressively. After reaching the desired heart rate and setting the isoflurane to 0%, the isoflurane was left to wear off for 30 minutes. However, this was also the time for the fentanyl antalgic effect to stop. Therefore, after the 20 minutes' mark, the second injection with buprenorphine was performed, whose effect lasted until the end of the record.

Material & Methods

Once the 30 minutes' mark was reached, the recording session was initiated. At the end of the recording session, the electrode could be moved for a second recording session. However, at the two-hour mark from the first injection of FMM, the anaesthesia would stop. If the next records would last longer than the anaesthesia, the second dose of FMM was injected.

2.2.1.6 Histology

After acute and chronic implantation of silicon probes, the positioning of the electrodes was verified in histology. In the case of acute experiments, the probes were dipped into DiI before being inserted. In the case of chronic implantations, no dye was used because the DiI would diffuse too much into the brain with time, making it difficult to recover the electrode position.

Mice were anaesthetised with an intraperitoneal injection of Avertin 2.5% at a dose of 16 μ L/g, before being perfused with paraformaldehyde (PFA) at 4% in phosphate buffer solution. In the case of acute recordings (with DiI), the brain was extracted from the brain cavity and post-fixed overnight in PFA 4%. In the case of chronic recordings, only brain cavity's bottom was removed, while the electrode was left in position in PFA at 4% for at least four days. Like so, the brain hardened around the probe that left a visible mark after the slicing.

Harvested brains tissues were sliced with a vibratome (Leica, VT1000S), at a thickness of 150 μ m in the DV axis, and mounted on a microscopy slide (ThermoFished, Superfrost Glass) under a glass coverslip (Syntesys, Prestige). Slides were imaged with a microdissector (Leica, LMD7000) in bright field light and in fluorescence with an N2.1 filter cube (green excitation), in the acute condition to see the trace left by the DiI on the probe.

2.2.2 Key Resources Table

REAGENT or RESOURCE	SOURCE	IDENTIFIER
Anaesthesia		
Isoflurane	Zoetis Inc	IsoFlo®
Fentanyl 0.05 mg/kg	Dechra	Fentadon®
Medetomidine 0.5 mg/kg	Virbac	Medetor®
Midazolam 5 mg/kg		
Avertin (E) 2.5%		
Tabletop with Active Scavenging	VetEquip	901820

Material & Methods

Biological Temperature Controller	Supertech Physiological	TMP – 5x series
Small animal heating pad	Supertech Physiological	115*80mm, 12W (for mouse)
Thermo comfort mat S	Sera	32004
Surgery		
Eye ointment	Scope	VitA-POS®
Mini Contact Lense 3.0mm	OcuScience®	ERGACC3-30 3.0mm
Disinfectant	MEDA	Betadine®
LM-ErgoMax handle	LM-Arte Applicia	46-49XSI
Handle for scalpel blades	F·S·T	10035-12
Fine Scissor ToughCut®	F·S·T	14058-09
Dumont#55 Forceps	F·S·T	11255-20
Dumont#5 Forceps	F·S·T	11255-20
Dumont #5/45 Forceps	F·S·T	11251-35
Semken Forceps	F·S·T	11009-13
MicroDrill	WPI Inc	OmniDrill35
Ball Mill, Carbide .019” .031”	Circuit Medic®	115-6025
Hypodermic needle, 30G 0.3x13mm	Microlance™ 3	304000
Hypodermic needle, 18G 1.2x40mm	Microlance™ 3	304622
Glue	Loctite®	401
Dental cement	PALA	Paladur®
Petroleum jelly	Unilever	Vaseline®
Parafilm® “M”	Bemis	PM-992
Antibiotic	Bayer	Baytril®
Anti-inflammatory	Zoetis Petcare	Rimadyl®

Material & Methods

Electrodes		
Buzsaki32L acute	NeuroNexus™	A32 serie
Acute headstage	NeuroNexus™	SmartLink™32 Acute
Buzsaki32L chronic	NeuroNexus™	H32_21mm serie
Chronic microdrive	NeuroNexus™	dDrive-m
Chronic headstage	NeuroNexus™	SmartLink™32 Chronic
Bare silver wire	A-M Systems™	782500
Enzyme cleaner	Thomas Recording	AN000689
Electrode drive		
Stereotaxic	Neurostar	Drill & Injection Robot
Micromanipulator	Sensapex	SMX
Setup hardware		
DLP® Projector	Texas Instruments	DLP3010EVM-LC
Mouse Camera + BP740-10	The Imaging Source®	DMK33UX174
Eye Camera + FB850-40	The Imaging Source®	DMK23UV024
IR LED illumination: 850nm + FB850-40		
IR LED illumination: 750nm + FB740-10		
UV paint	Reel Wing Decoys	Bird vision UV decoy paint
Black spray paint	RS Components	136-7957
Black Nylon Fabric	Thorlabs	BK5
Light meter	RS Components	ISO-TECH ILM1335
Power meter	Thorlabs	PM100D
Photodiode power sensor	Thorlabs	S120C
Histology		
DiI Stain	Invitrogen™	D282

Material & Methods

Paraformaldehyde 4%		
Microdissector	Leica Microsystems	LMD7000
Vibratome	Leica Microsystems	VT1000
Superfrost Plus	ThermoFisher Scientific™	10149870
Cover slides 22x22mm “PRESTIGE”	SYNTESYS	372108

2.3 Visual stimuli

Our visual stimuli were made with QDSpy (Euler 2019; Franke et al. 2019) and displayed with a customised DLP projector (section 2.1.1.1). The stimulus set is comprised of a random black-and-white checkerboard stimulus (15 min; 60 Hz; 32×18 squares of 2.3° side; “checkerboard”), a random full-field black-and-white stimulus (5 min; 60 Hz; “full-field flicker”), a moving grating stimulus with square waves of spatial frequencies of 3° or 20° going at speeds of $7.5^\circ/\text{s}$ or $15^\circ/\text{s}$, in eight different directions (“moving gratings”), ten repetitions of a full-field stimulus whose intensity follows a sinusoid (1.5 Hz) with a linearly increasing amplitude (“chirp amplitude modulation (AM)”), ten repetitions of a full-field sinusoidal stimulus with an increasing frequency by 2-s-long epochs of 1.875, 3.75 and 7.5 Hz and 1-s-long epochs 15 and 30 Hz (“chirp frequency epochs (FE)”). Both chirp stimuli were preceded by an OFF-ON-OFF stimulation of two second each.

With a wrapper coded around QDSpy, some features were added to the stimuli: a marker cycle with a bigger range of values, a pre and post-stimulus background presentation, both helping with the synchronisation, and a QDSpy stimulus pickle to numpy matrix converter. Also, an optimisation algorithm for the checkerboard was included to reduce the stimulus file size as well as the number of screen printing operations.

2.3.1 Marker cycle

For an error detection purpose, the marker was given more level of intensity than the default ON-OFF implemented in QDSpy. Five levels of intensities were chosen in the red-channel, at the values 50, 100, 150, 200 and 250 (for an 8-bit range). With those additional values, it became possible to distinguish the possible errors during 60Hz stimulation, naming frame drops, frame insertions, frame replacements and a freeze.

Material & Methods

The wrapper additionally allowed the marker to be presented on the full-field, by adding the red component to the displayed object. It permitted to increase the signal-to-noise ratio of the anaesthetised stereotaxic electrophysiology setup where the photodiode was shown the entire image.

2.3.2 Checkerboard optimisation

With the checkerboard stimulus, the compiled files generated rapidly increase in size, provoking freeze of QDSpy when being loaded, and is due to the high number of display operations: 15 minutes' stimulus with 32-by-18 squares presented at 60Hz gives a total of 518400 elements to store and display.

The naïve display of each black and white square can easily be optimised by 50%, by displaying a background black (or white) and printing then only the white (or black) squares on top. The stimulus is further optimised by searching in each frame ensembles of squares forming rectangles of various shape (4×4 , 4×3 , 3×4 , ..., 2×1 , 1×2) to replace them with a single rectangle. The drawback of the technique is that the compilation time took longer, but the optimisation allowed for a reduction of 40% (observed empirically) of the file size and display operations.

2.3.3 LED dome stimuli

Stimuli for the LED dome were coded in Arduino. A set of regular stimuli is comprised of a checkerboard and full-field flicker stimuli. As for the chirp stimuli, because the LEDs' value range was limited to $[0; 1]$, the chirp AM could not work. We still used the chirp FE, but eventually made a version with more and faster frequencies: 0.5, 1, 2, 4, 8, 16, 20, 25, 33, 40 and 50Hz. More details and discussion about the stimuli were shown in the annexe 1.

2.4 Data processing

2.4.1 Spike sorting

The spike sorting (Lefebvre et al. 2016) was made with SpykingCircus (Yger et al. 2016) (v0.7.6) for the (semi)automatic detection of the clusters and phy (Rossant et al. 2020) as the graphical interface for the data curation. Following the workflow of SpykingCircus, our data underwent a Butterworth filter with a cut off of 250Hz up to half the Nyquist frequency (default value). Median from all channels was removed to decrease motion artefacts, and the signals were whitened. A threshold of 7 standard deviations was selected for the initial spike detection. The rest of the parameters were left to defaults. Once the program finished the sorting, the results were converted to phy to proceed with manual sorting. Templates were merged when

Material & Methods

appropriate, given the template location, shape and the cross-correlogram, following recommendations of the spike sorting user guide (Lenzi & Steinmetz).

This step allowed for the exclusion of most of the unwanted clusters, and others that were classified as good but that did not show visual responses were discarded in the analysis, as they did not pass the response to stimuli quality thresholds.

2.4.2 The one rig, data synchronisation and processing

2.4.2.1 *Library core*

Theonerig (read “the one rig”) is a library I developed to synchronise and process data coming from the different setups of the Asari lab. Theonerig uses a time-series as a reference and aligns onto it other data streams from various sources.

The base element is the DataChunk. It is an extension of the Numpy array, adding a few attributes to it:

- `idx`: the starting frame in a record.
- `group`: the family of data in `{sync, stim, data, cell}`.
- `fill`: a default value for when the data does not exist.

All the DataChunks of a record are stored in a single RecordMaster object. By knowing the index of each DataChunk and their shape (they are Numpy arrays), the RecordMaster figures which data exists at what time. The synchronisation of a record is done within a dedicated jupyter notebook (more details below, section 2.4.2.5). The starting index of each DataChunk is determined, and raw data undergo all required corrections and resampling to fit into the RecordMaster. After this step, a clean RecordMaster object is obtained and from this point on, data is queried with a Data_Pipe object.

The core aspects of the library are demonstrated in annexe 4. Additional details are available online (<https://tom-tbt.github.io/theonerig>).

2.4.2.2 *Event detection*

The first step of the data processing consisted of synchronising different recordings. It always included the detection of the visual stimulus frames, complemented by eye and mouse cameras in the case of awake recordings, and by the Y-galvo mirror scanning position in the case of two-photon imaging experiments (not described in this thesis).

Material & Methods

The detection of frames in the analog signal of the DLP projector was done sequentially with thresholding, frame by frame, always to include four peaks of the signal in each frame. The detection for camera triggers was done in a similar way, where each peak makes for one frame in the eye and mouse video. In the case of calcium imaging frames were detected using the function `find_peaks` (Scipy) on the Y-galvo mirror signals that have a sawtooth waveform when scanning.

For both the camera triggers and the mirror scanning position, every event is identical and only their timing had to be detected. In the case of the photodiode signal, the intensity and duration of the peaks depended on the intensity of the marker (section 2.3.1).

2.4.2.3 Frame clustering and correction

Values had to be associated with each frame of the projector to retrieve the stimulus sequence frame by frame that was displayed. The marker displaying IR light on the photodiode took five different intensities (section 2.3.1), and the height of the peaks was not enough to distinguish the intensities. Instead, the frames were clustered in five groups according to their area under the curve (AUC) and assigned a label. Stimuli authentic sequences were matched to the detected sequence, and shifts of the sequence were detected with a Needleman-Wunsch algorithm (Needleman & Wunsch 1970) custom implementation, where the similarity matrix allowed the attribution of a larger error for distant frames mismatch forcing the detection when consecutive shifts occurred: e.g. matching a zero with a two is worse than matching a zero with a one as the sequence of 0-1-2-3-4 was repeated. After the detection of the shifts, frames still mismatched were replaced by the closest frame matched. In the case of display freeze, their detection was permitted by QDSpy, and additional frames were inserted to the original sequence before performing the sequence matching.

2.4.2.4 Resampling

The DLP frame time-points were used as a reference to synchronise the other time series, as the frames were detected for the whole record and were very stable. Calcium imaging frames at 15.4Hz and videos (eye-tracking and mouse cam) at 30Hz were up-sampled to the 60Hz rate of the DLP projector. The continuous treadmill trace was down-sampled instead.

2.4.2.5 Jupyter notebook synchronisation pipeline

Each record synchronisation was done in a separate notebook, to leave a trace of every manual intervention and sanity plot made during the process. The synchronisation varied according to the setup employed, but the main steps consisted of the followings:

Material & Methods

1. Loading the raw data and connecting to the database (described in annexe 2)
2. Detecting the frames in the DLP data and assigning a value to the frames
3. (Optional) Detecting the frames in a secondary record of photodiode data.
4. Parsing of the QDSpy record
5. Creating a “record master” from the DLP frames
6. (Optional) Aligning the secondary photodiode data to the record master
7. For each stimulus
 - 7.1. Loading the marker and intensity template
 - 7.2. Template matching with the record to seek the beginning of the stimulus
 - 7.3. Detecting errors in the stimulation and correcting them
 - 7.4. Appending the stimulus to the record masters
8. Appending the cell response to the record master, one of:
 - 8.1. Electrophysiology: Loading spike sorting results and binning the spikes
 - 8.2. Calcium imaging:
 - 8.2.1. Loading the calcium activity matrix
 - 8.2.2. Detecting the two-photon frame timings and aligning it to the record master
 - 8.2.3. Inserting the calcium activity matrix in the record master
9. (Optional) Detecting the camera triggers timings and appending data like pupil position to the record master after resampling
10. (Optional) Down sampling (with averaging) the treadmill data and appending to the record master

At the end of the process, the record master contained all data streams aligned. Summary plots were generated for each cell, showing the response to the stimulus sequence.

2.4.2.6 Pairing cells across recordings

When several recording sessions were made in a single animal, the same cells could be recorded from multiple sessions. The pairing of cells was done manually, by searching across summary plots cells with similar spike template and response properties.

2.4.3 Cell response analysis

2.4.3.1 Spike Triggering Average

The spike-triggering average (STA) was calculated for the full-field flicker and the checkerboard stimuli. To this end, the spikes were binned at 60Hz, corresponding to the DLP frames and the STA was computed as:

Material & Methods

$$STA(x, y, \tau) = \frac{1}{C} \sum_{t=1}^T S(x, y, t + \tau) c(t) \quad (3)$$

where T is the number of frames in the normalised stimulus $-1 \leq S(x, y, t) \leq 1$, τ the time lag (from -483ms to 0ms, with 16.6ms steps), $c(t)$ the number of spikes at time t , and C the total number of spikes for the given cell. For the full-field flicker, x and y are equal to 1. If a cell fired spikes randomly, then for large N , the STA should follow a normal distribution with the mean value of 0 and the variance of $1/N$. It allowed the calculation of the z -score for each (x, y, t) of the STA as:

$$zscore(x, y, \tau) = \frac{STA(x, y, \tau)}{\sqrt{\frac{1}{C}}} \quad (4)$$

followed by the calculation of the p -value, double-sided:

$$pvalue(x, y, \tau) = SF(|zscore(x, y, \tau)|) \cdot 2 \quad (5)$$

where SF is the survival function. After calculating the p -values, STAs were normalised between -1 and 1.

To the checkerboard STA at the frame with the minimum p -value was fitted a difference of 2-dimensional Gaussians F_{spat} :

$$a = \left(\frac{\cos(\theta)^2}{2\sigma_x^2} + \frac{\sin(\theta)^2}{2\sigma_y^2} \right) \quad (6)$$

$$b = - \left(\frac{\sin(2\theta)}{4\sigma_x^2} + \frac{\sin(2\theta)}{4\sigma_y^2} \right) \quad (7)$$

$$c = \left(\frac{\sin(\theta)^2}{2\sigma_x^2} + \frac{\cos(\theta)^2}{2\sigma_y^2} \right) \quad (8)$$

$$2DGaussian(y, x) = amp * e^{-(a(x-x_0)^2 - b(x-x_0) \cdot (y-y_0) + c(y-y_0)^2)} \quad (9)$$

$$F_{spat}(y, x) = 2DGaussian(y, x)_{centre} - 2DGaussian(y, x)_{surround} + bias \quad (10)$$

Material & Methods

where θ are the individual angles of the two 2DGaussians, σ_x and σ_y the individual standard deviations, amp the individual amplitudes and $bias$ the bias of the 2DGaussians difference.

To estimate the time course, the full-field flicker STA was fitted with a difference of Gaussians F_{temp} :



$$Gaussian(t) = amp \cdot e^{\frac{-(t-t_0)^2}{2\sigma^2}} \quad (11)$$

$$Ftemp(t) = Gaussian(t)_1 - Gaussian(t)_2 \quad (12)$$

For both, quality indexes were calculated, QI_{spat} and QI_{temp} , as one minus the variance explained by the fit.

$$QI = 1 - \frac{var(STA - FIT)}{var(STA)} \quad (13)$$

By looking at the resulting STAs together with the p -values and QI of the fit, we found that p -value below $1 \cdot 10^{-19}$ with QI of at least 0.2 gave an acceptable trade-off between discarding noise and keeping cells of interest.

2.4.3.2 Nonlinearities

Nonlinearities of the cell's response were computed by taking the checkerboard stimulus ensemble, a grid of 18×32 squares, on a history window of 16 frames ($18 \times 32 \times 16 = 9216$ dimensions, 53984 points), and comparing it with the spike-triggered stimulus ensemble (Schwartz et al. 2006; Simoncelli et al. 2004). The spike-triggered stimulus ensemble is averaged and corresponds to the STA (eq. 3). The spike triggered stimulus ensemble and stimulus ensemble are then projected onto the STA and binned (100 bins between min and max of the projected stimulus ensemble). The nonlinearity is obtained by taking the ratio:

$$nonlin(x) = \frac{SE_{cell}(x)}{SE(x)} \quad (14)$$

Material & Methods

where x are the bins, and SE and SE_{cell} are respectively the projected and binned stimulus ensemble and spike-triggered ensemble.

2.4.3.3 ON-OFF and transiency index

The ON-OFF preference index was calculated over the ON and OFF stimulus period of the two chirp stimuli combined. It corresponded to the difference of the mean response to each condition, normalised by the sum of the two:

$$OOI = \frac{\text{mean}(R_{on}) - \text{mean}(R_{off})}{\text{mean}(R_{on}) + \text{mean}(R_{off})} \quad (15)$$

To quantify the transiency of the cells, we fitted an exponential decay over the preferred stimulus (ON or OFF):



$$\text{decay}(t) = e^{-t\lambda} \cdot (a - b) + b \quad (16)$$

where λ is the decay of the response, a the maximum amplitude of the response where the decay starts from, and b the baseline of the response (sustained component). The baseline was subtracted to the amplitude so that it corresponds to the actual amplitude of the response, independently of the baseline. Also, a quality index for the fit was calculated with equation 13, and we used a threshold of 0.35 to discard the lower quality fits.

A response quality index (QI) was also calculated as the signal-to-noise ratio over the whole ON-OFF stimulus period of the two chirp stimuli combined.:

$$QI = \frac{\text{var}(\text{mean}(C)_r)_t}{\text{mean}(\text{var}(C)_t)_r} \quad (17)$$

where C is the spike count matrix of t temporal bins by r repetitions of the stimulus, and $\text{mean}()_x$ and $\text{var}()_x$ the mean and variance across the specified dimensions. As for the threshold, we found that cells with a QI higher than 0.35 were acceptable.

Material & Methods

2.4.3.4 Contrast and frequency responses from chirp AM and FE

The contrast and frequency responses of the chirp stimuli were analysed by fitting sine-like functions to the cells mean spike responses:

$$s(t) = a \cdot \sin^p \left(\pi h t + \frac{\phi}{2} \right) \quad (18)$$

where h is the sine frequency, ϕ is the phase of the sine in radian in the interval $[0, 2\pi)$, a is the amplitude of the sine, and $p = 2n$ is the exponent of the sine with n being positive integers to fit both the sustained and transient responses of cells.

For the chirp FE, the function $s(t)$ was fitted for each of the five frequencies used in the stimulus, with the corresponding frequency parameter for the sine: 1.875, 3.75, 7.5, 15 and 30Hz.

For the chirp AM, the function $s(t)$ was weighted by a sigmoid, to fit the response to the increasing contrast:



$$g(t) = \frac{s(t)}{1 + e^{-\lambda(t-t_0)}} + b \quad (19)$$

where t_0 is the midpoint of the curve, $\lambda > 0$ the steepness of the sigmoid and $b \geq 0$ the baseline activity.

In each case, the quality index of the fit was calculated as the variance explained by the model (see eq. 13). For the analysis, the cells with a maximal mean spike count below 0.8 were discarded, and a threshold of 0.35 was used to select the good fits of the response.

2.4.3.5 Direction and orientation selectivity

The direction selectivity index was calculated by projecting the cells responses to a complex exponential:

$$DS = \frac{\sum_{k=0}^8 e^{i\alpha_k} \cdot R_k}{\sum R} \quad (20)$$

Material & Methods

where α_k is the angle of the k^{th} direction and R_k the cell response of the k^{th} direction. Orientation selectivity was calculated in the same way, but the cell's responses were grouped between opposite direction conditions by doubling the angles:

$$OS = \frac{\sum_{k=0}^8 e^{i\alpha_k \cdot 2} \cdot R_k}{\sum R} \quad (21)$$

For each condition of both indexes, a quality index was calculated by bootstrapping, consisting of randomly shuffling the conditions, with 1000 repetitions. The quality index was taken as the proportion of the original index being higher than the random indexes. We used a threshold of 0.1 for the quality indexes, and selected the cells displaying orientation or direction selectivity when the preference index was higher than 0.3.

2.4.4 Eye-tracking

2.4.4.1 *Mask-Region based convolutional neural network*

Eye-tracking was performed on the mouse eye videos, with Mask-Region based convolutional neural network (RCNN), a deep neural network performing object instance segmentation. The network weights were trained on 260 images sampled across several mice videos, on a range of qualities, pupil dilation and positions, labelled by hand. In addition, the following image augmentations of the python library imgaug were used during the training to increase further the diversity of the training set: GaussianBlur, AverageBlur, MedianBlur, ContrastNormalization, Multiply, Sharpen, ElasticTransformation, Superpixels, CropAndPad, Affine, Dropout, CoarseDropout.

A backbone of resnet50 was selected instead of the default resnet101 due to the low complexity of the task. The default learning rate of 0.001 was used.

From pre-existing weights provided with the distribution of the program (Waleed 2017), the network was fine-tuned over two days with a batch size of 1000, on two GPUs (NVIDIA GeForce RTX 1080Ti). The head layers of the network were tuned for the first 100 epochs, and the following 300 epochs trained the layers four and on. Finally, the last 200 epochs ran for the tuning of all the layers at a tenth of the learning rate.

Following the training, Mask-RCNN detected the pupil for all of our videos. The result of the detection comprises a bounding box for the object and a pixel-wise segmentation of the pupil

Material & Methods

within the bounding box. An ellipse was finally fitted to the pixel map to extract the pupil parameters for each frame.

2.4.4.2 Calibration and spatial STA correction

From a retinal cell's viewpoint, a shift of the eye to the right (in the video) corresponds to a shift of the stimulus to the left. The two shifts are proportional and are related by a transformation matrix. We obtain the stimulus shift Δx_{stim} and Δy_{stim} as such:

$$\begin{bmatrix} \Delta x_{stim} \\ \Delta y_{stim} \end{bmatrix} = \begin{bmatrix} i_x & j_x \\ i_y & j_y \end{bmatrix} \cdot \begin{bmatrix} \Delta x_{eye} \\ \Delta y_{eye} \end{bmatrix} \quad (22)$$

where Δx_{eye} and Δy_{eye} are the shift measured in the eye video, and with i and j the basis vectors of the transformation matrix.

To estimate i and j , we used two methods. The first method consisted of measuring on the setup the angular screen size at the eye of the mouse. For that, IR LEDs were shined from the corner of the screen and reflected in the mouse eye, visible in the eye cam video. The transformation matrix was measured from the size of the screen in the mouse eye video.

The second method consisted of calculating an STA for each time the eye remained still, fitting a Gaussian to evaluate the RF, and performing a multivariate linear regression between the RF and eye positions.

Once that the transformation matrix was known, the stimulus could be pre-processed to match the eye motion. Due to the division of the checkerboard stimulus in large blocks, incomplete shifts led to an up-sampling of the stimulus.

Results

3 Results

3.1 RGCs *in vivo* electrophysiology

The first goal of the project was to obtain records of mouse retinal ganglion cells axons *in vivo* to study what exactly the eye tells the brain. Our approach was to measure the action potentials at the level of the RGCs' axons, by inserting an electrode in the optic chiasm or tract (in blue in the figure 16.A). We chose as a first target the optic chiasm located at the bottom of the brain, where optic nerves of both eyes cross. During the first batch of experiments using silicon probes (Buzsaki32L), histological analysis confirmed that we reached the target (5/9). However, we obtained visual responses only from a subset of these successful implantations (2/5), that were associated with probe's shank breaking during the experiment.

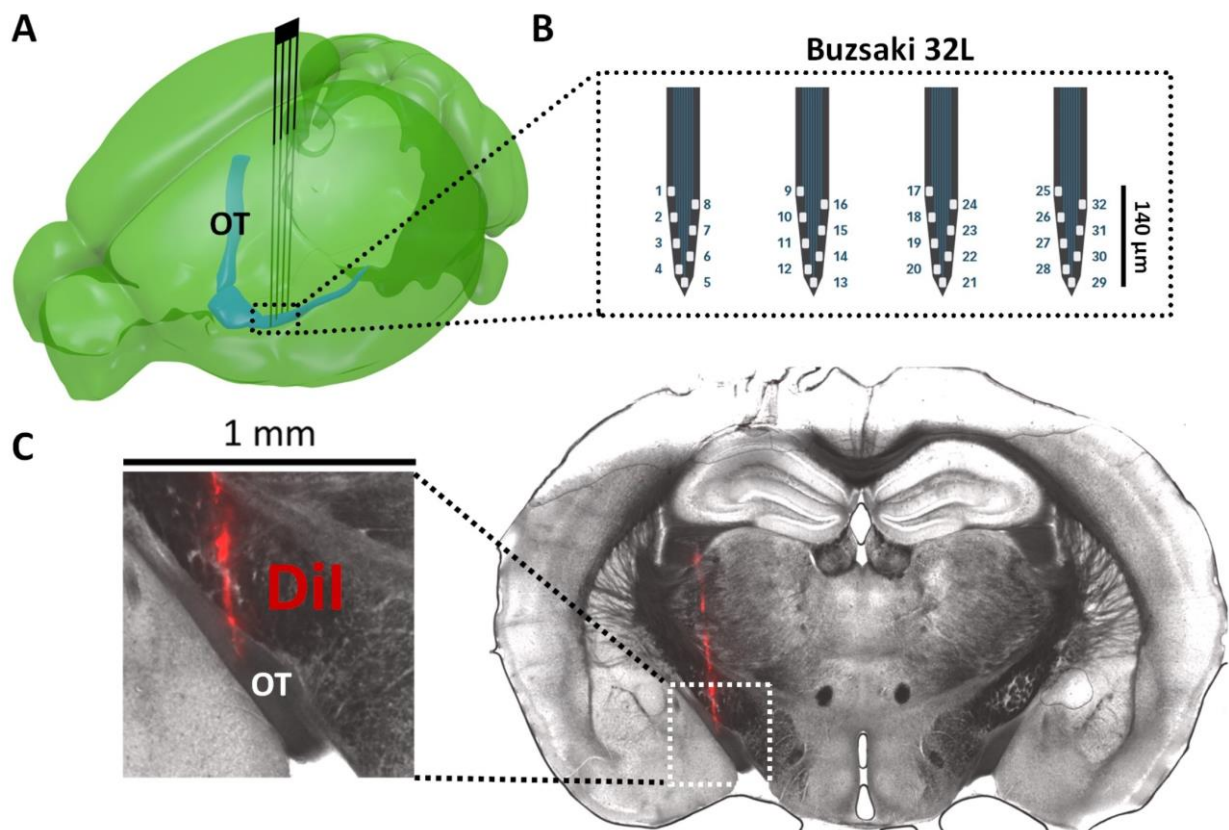


Figure 16 – Silicone probe implantation in the optic tract (OT) A) 3D model of a mouse brain in green with the optic chiasm and optic tract in blue (3D models from AllenBrainInstitute (Wang et al. 2020)), together with a Buzsaki32L probe in black, at scale. B) Layout of the silicone probe channels. C) Mouse brain slice with the fluorescent marker DiI in red.

In the second batch of experiments, we changed the target to the optic tract (as show by the probe position in figure 16.A). We found that after a time of adaptation to the new targeting protocol (1/5), we frequently obtained visual responses (29/31) associated with a histological

probe placement confirmation, as shown in the figure 16.C where the red dye (DiI) left by the electrode shows its path in the brain, down to the optic tract.

3.2 Reliable event detection for synchronisation

Following “theonerig” pipeline for synchronising the electrophysiology data with visual stimulation and video recordings, a total of 113 data sets were processed: 54 from the anaesthetised stereotaxic electrophysiology setup, 26 from the awake electrophysiology setup and 33 from the awake calcium imaging setup (not presented in this thesis). For these recordings, the events were detected as presented in figure 17.A, and the DLP projector frames marker values were reliably assigned a label based on their AUC (Figure 17.B).

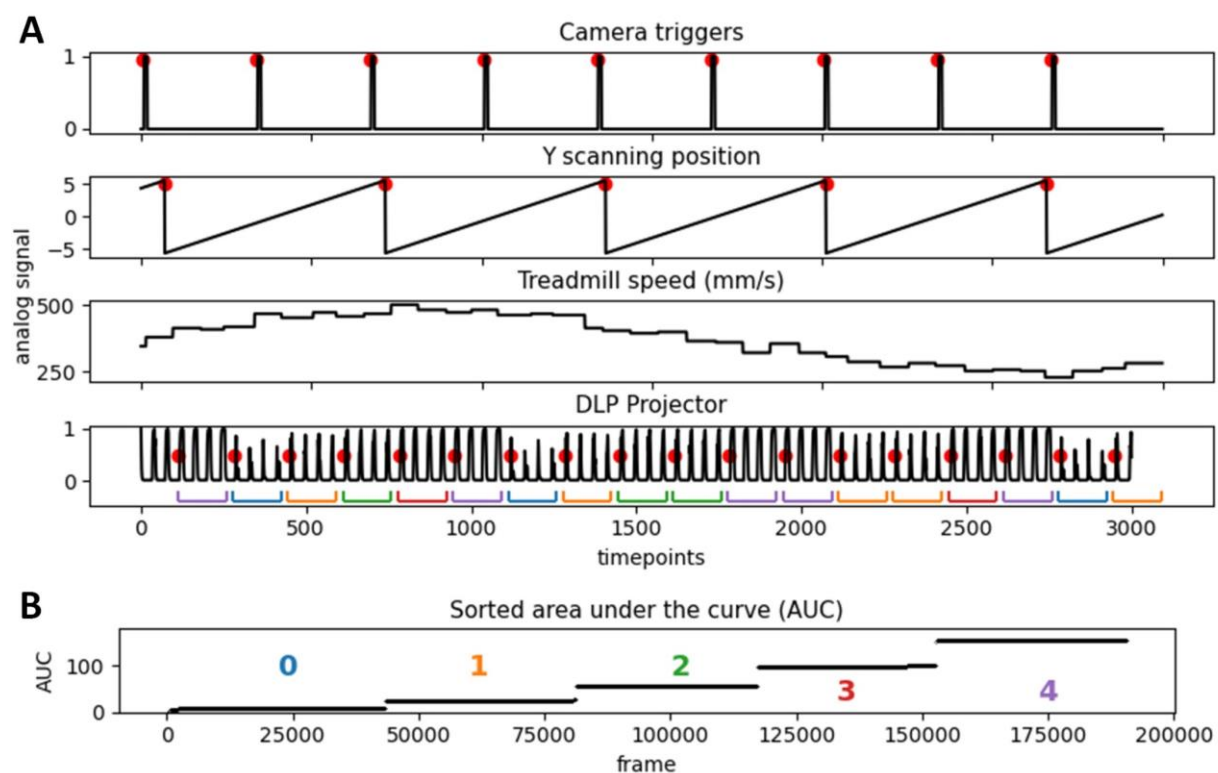


Figure 17 – Event detection and classification for synchronisation of the records. **A)** The four streams of the in vivo awake calcium imaging setup. The red dots on each plot show the automatic detection of the event. Under the DLP Projector trace, the brackets (colour coded) come from the frame clustering of the panel B. The normal sequence here should be to go from 0 to 4 and cycling, but we see that the sequence here contains multiple errors (frame substitutions). **B)** Area under the curve of each frame, sorted. Each number above or below the steps indicates the attributed cluster.

Using the Needleman-Wunsch algorithm, the detected sequences were matched to the true sequence, followed by an error detection and correction. The amount of errors in the display varied between the setup. The awake electrophysiology setup stimuli produced the most errors, ($8.7 \pm 8.0\%$; mean \pm standard deviation), followed by the calcium imaging setup stimuli ($3.7 \pm 4.0\%$, the stimulus display setup is identical to the awake electrophysiology, but the

Results

stimuli are going at a slower rate). The anaesthetised stereotaxic electrophysiology setup produced the least errors out of the three setups ($1.0 \pm 0.7\%$).

3.3 Awake RGCs respond more rapidly than under anaesthesia

In our stimulus routine, we presented a full-field flickering stimulus under three different conditions: isoflurane and FMM anaesthesia, and awake. The purpose of the stimulus was to examine the temporal dynamics of the responses by calculating the spike-triggered average of the stimuli (STA). For each condition, we sorted all the STAs by their first to principal components (PC1 and PC2) to look at the general trend (figure 18.C, F, I). We found that both anaesthetised conditions are comparable; however, the RGCs recorded in awake condition showed shorter integration time and a shorter response peak latency than in anaesthetised conditions. For quantification, we fitted a difference of Gaussian model to each STA (eq. 12) and extracted the peak latencies (figure 18.J). We found that ON cells responded faster than OFF cells in awake condition ($p=2 \cdot 10^{-4}$), but no statistical difference was found in anaesthetised conditions (iso: $p=0.13$; fmm: $p=0.98$). We also found that the difference in the STA peak latency is statistically significant between awake and isoflurane ($p=1 \cdot 10^{-20}$, independent t-test), awake and FMM ($p=1 \cdot 10^{-17}$), but not between the isoflurane and FMM ($p=0.35$). Moreover, figure 18.K shows in the Fourier transform of the principal components (PC) of each condition, where both PC1 and PC2 under anaesthesia has a power at lower frequencies than in the awake condition, in line with a longer integration of the stimulus under anaesthesia condition. To illustrate the difference, we plotted in figure 18.L a representative cell from each condition with comparable dynamics.

Results

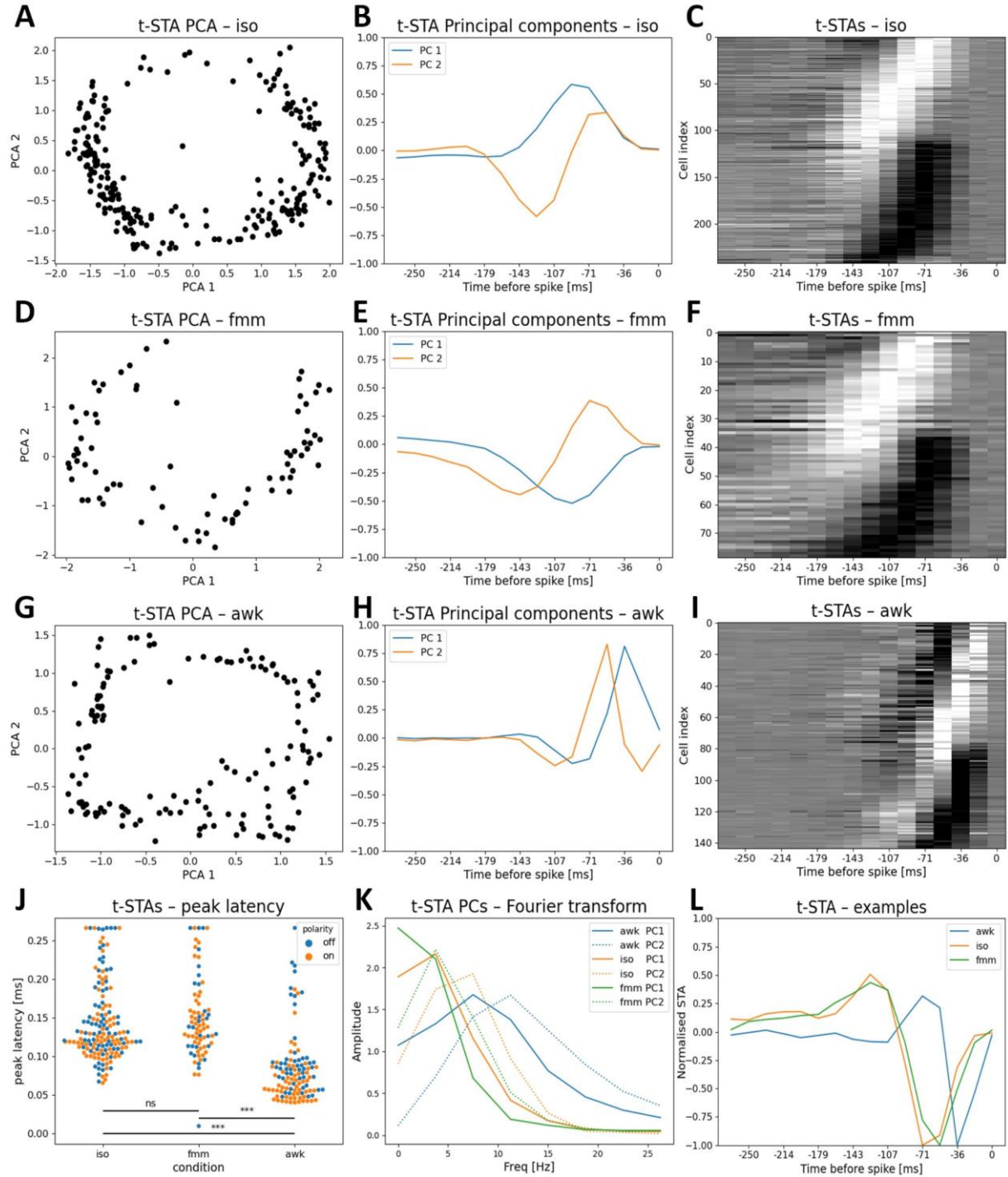


Figure 18 – In vivo RGC temporal STA from the full-field flickering stimulus. **A)** PCA of the temporal STA of cells from RGCs under isoflurane anaesthesia ($n=243$). **B)** Principal components 1 and 2 of the PCA shown in panel A. Explained variance ratio for PC1:0.59 and PC2:0.25 **C)** Temporal STA of each cell under isoflurane anaesthesia, sorted using the angle of each cell in polar coordinates with PC1 and PC2. **D) to F)** Same as A to C, under FMM anaesthesia ($n=79$). Explained variance ratio for PC1:0.56 and PC2:0.30 **G) to I)** Same as A to C, in awake mouse ($n=144$). Explained variance ratio for PC1:0.42 and PC2:0.35 **J)** STA peak latency between stimulus and response of cells in the three conditions, obtained from the difference of gaussian fit of each STA (iso; fmm; awk: $n=158$; 78; 113; mean \pm std: 140 ± 49 ms; 150 ± 52 ms; 83 ± 43 ms; ***, $p<0.001$, t-test; ns, $p>0.05$). **K)** Fourier transform of PC1 and PC2 of each condition. **L)** Selected examples of the temporal STA of cells in awake and anaesthetised conditions.

Results

3.4 Awake RGCs respond to higher temporal frequencies than their anaesthetised counterpart

From an initial batch of experiments, we noticed that the awake cells d responses to faster frequencies with a chirp stimulus modulated in frequency. However, due to the continuous increase of the frequency, it was not possible to understand up to which frequency the cells could respond stably. To palliate this, we replaced the continuous increase of the frequency by epochs of a defined frequency.

With this new stimulus, awake cells did respond to a 15Hz stimulus (see figure 19.B for an example cell). In contrast, cells recorded under isoflurane or FMM did not show such response (figure 19.A). For every frequency tested, an even power of sine function was fitted (eq. 18), and both the quality of the fit and a minimal response amplitude were an indication of the maximal frequency that a cell can reach. The plot in figure 19.C shows the fit quality for the first four frequencies. No cell responded at 30Hz; however, display errors in stimulation of the awake setup can account for the unresponsiveness of the cells.

Results

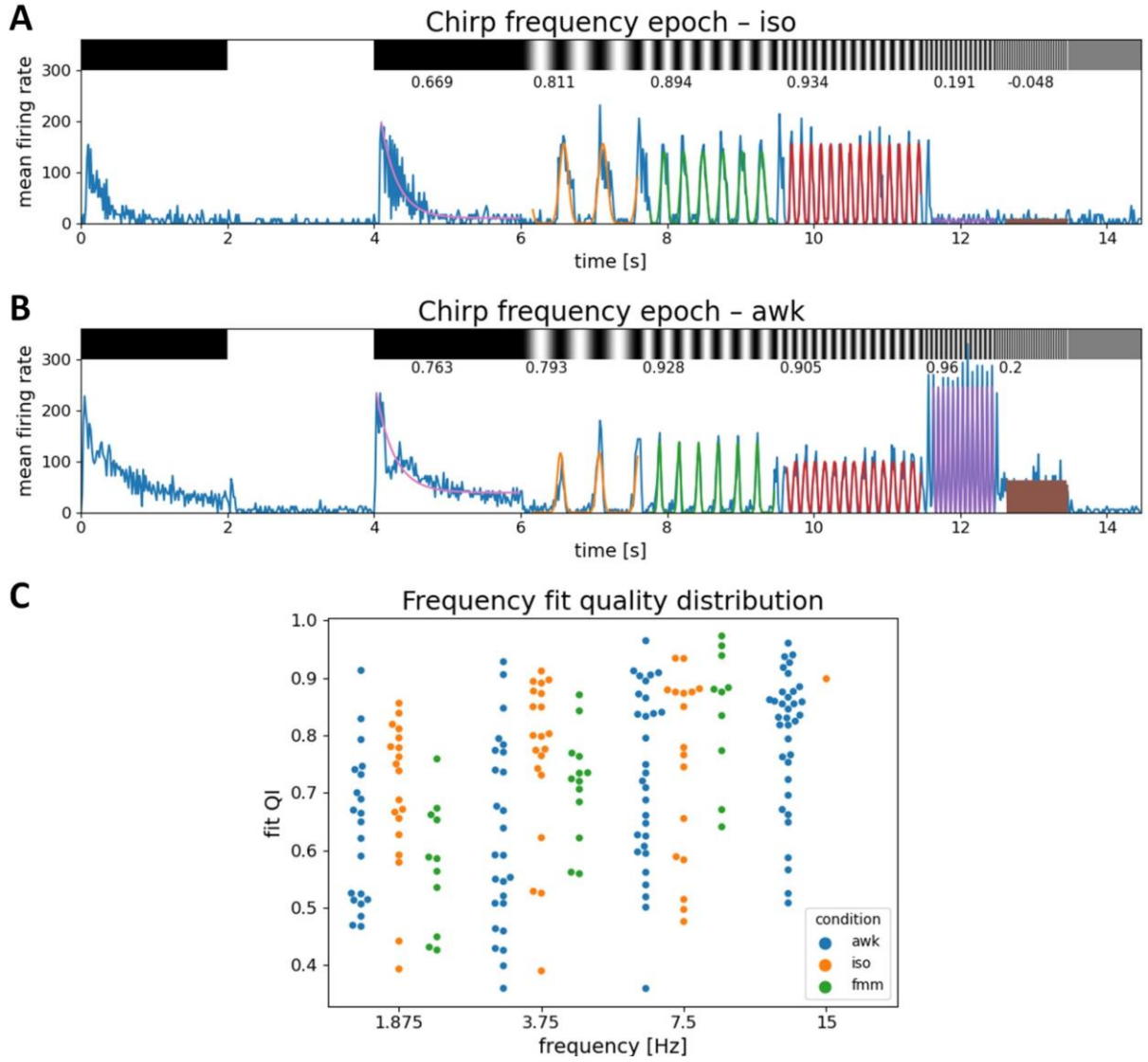


Figure 19 – Cells temporal frequency sensitivity. A) Response example of a cell response in blue in isoflurane condition to the chirp frequency epoch stimulus. In pink over the ON-OFF stimulation is the exponential decay fit (eq. 16), and in orange, green, red, violet and brown are the fit of exponentiated sine (eq. 18) at respectively frequencies of 1.875, 3.75, 7.5, 15 and 30Hz. The numbers above the fits correspond to the quality index of that fit (eq.13). B) Same as A) in awake condition. C) Quality indexes amplitude (fit QI) for the fit of increasing frequencies of the three experimental conditions.

To know whether awake cells are able or not to respond to higher frequencies, we tested the response of two cells from a single record to a set of frequencies with the LED dome (figure 20). Since the LEDs have a higher refresh rate (400Hz) than the DLP projector (60Hz), it is possible to present an ON-OFF stimulus at higher frequencies. The receptive fields of the only two recorded cells for such stimulus are shown in figure 20.A. For each cell, a raster plot to 25Hz frequency is shown in figure 20.B with an averaged response, and all other averaged responses to the rest of the frequencies are shown in figure 20.C. We see that the cells could

Results

follow the stimulus strongly up to 33Hz (fit quality in figure 20.C). At higher frequencies, the stimulus started to desynchronise between the two halves of LEDs in each quarter of the dome because the Arduino workers updates the two LED stripes they control sequentially, taking about 2ms per stripe to upload the new values. This means that the stimulus was not optimal at high frequencies, and especially for the cell 1 whose receptive field was located between desynchronised portions. However, even with a non-optimal stimulus, the cells followed up to 40Hz (fit quality in figure 20.C).

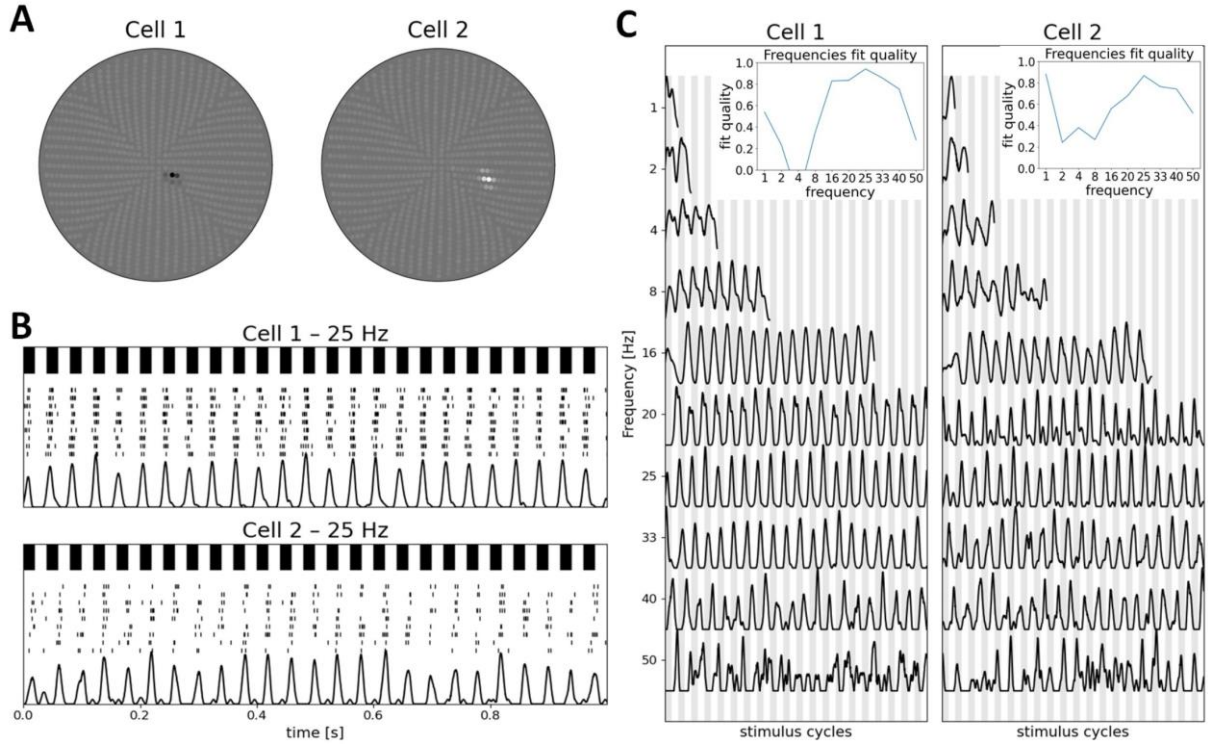


Figure 20 – High frequency RGC responses . A) Receptive field on the LED dome of the only two cells for which we displayed the high frequency stimulation. The distance of an LED to the centre correspond to the inclination of the LED ($\pi/2$ - elevation radians). **B)** Individual raster plots of the cells to the 25Hz full-field flicker. The lower trace is the sum of the spikes over the 10 repetitions, convolved with a Gaussian filter. The width of the filter was a ratio of the sampling rate (30KHz) and varied according to the stimulus frequency: $30000/(freq-4)$. **C)** Same as B, to increasing frequencies. The responses were normalised and aligned to the stimulus, shown by the grey vertical bars: clear grey correspond to OFF stimulation, and the white parts to ON stimulation. The inset plots show the fitting quality (eq. 13) of an exponentiated sine (eq. 18) to each frequency, same as presented in figure 19.

Results

3.5 Awake RGCs have a stronger baseline activity

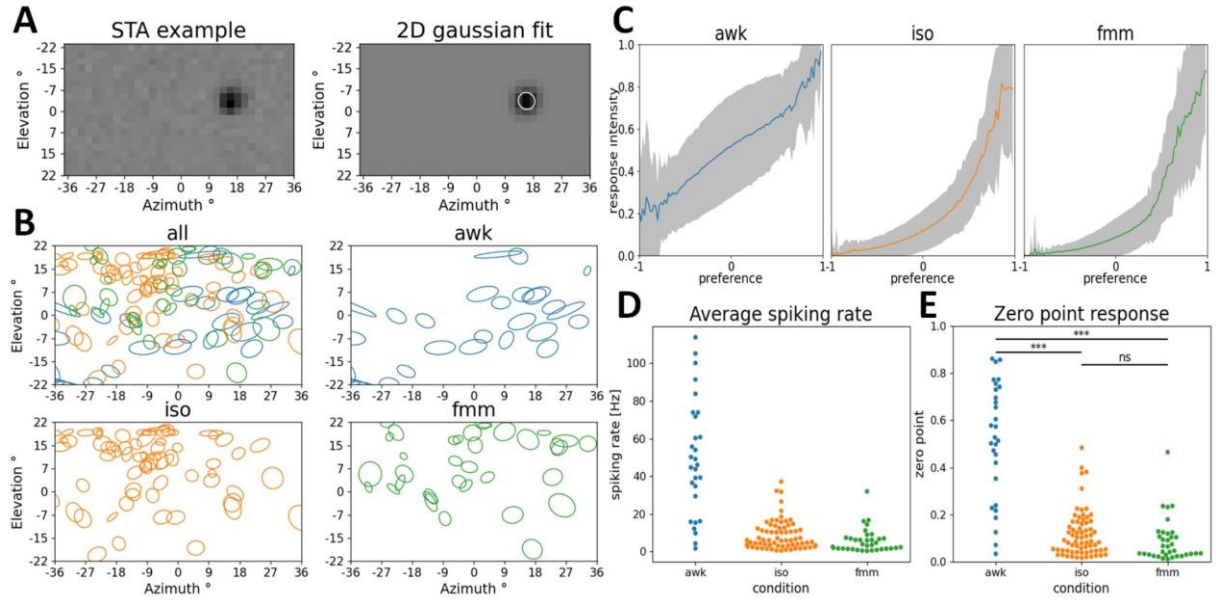


Figure 21 – Receptive fields and nonlinearities **A)** Example of a response to a checkerboard stimulus, showing the receptive field of the RGC on the left, and the difference of 2D Gaussian model on the right. The ellipse corresponds to two sigma of the Gaussian fit (eq. 10). **B)** Summary plots of all receptive fields observed across the all condition and the three separated conditions. The ellipses correspond to two sigma of the Gaussian fit (awk: $n=29$; iso: $n=69$; fmm: $n=35$) **C)** Nonlinearities estimation from the checkerboard stimulus across the condition (eq. 14). The colour line shows the average for each condition, and the grey area corresponds to one standard deviation. **D)** Spiking rate for the three conditions during the checkerboard stimulus. **E)** Zero point of the nonlinearity for the three conditions. A higher value for that metric corresponds to a cell displaying a higher baseline activity during the null stimulus presentation.

To further characterise the properties of the cells we recorded from, we presented a checkerboard stimulus, from which we calculated the STA and fitted a difference of 2D Gaussian model to estimate the receptive fields of the cells (see an example cell shown in the figure 21.A).

In figure 21.B, the most noticeable difference is in the elongated shape displayed by awake cells, due to the free eye motion of the mouse. Eye tracking correction is detailed in a later section (3.10), but since we could not do it systematically, we have not compared the size of the receptive field in more details.

We computed for this stimulus the nonlinearities associated to each cell's response and averaged them for each condition (figure 21.C). For a metric of comparison, we took from the obtained curves values at the zero point, interpreted as the null stimulus. A higher value for that metric corresponds to a cell displaying a higher baseline activity during the null stimulus presentation. Significant differences were observed between awake and isoflurane ($p=9 \cdot 10^{-15}$,

Results

independent t-test) and between awake and FMM ($p=4 \cdot 10^{-8}$) while no significant difference was observed between the two anaesthetised conditions ($p=0.74$) (Figure 21.E). Cells recorded under the awake condition therefore displayed a stronger baseline activity, that we also see in the spiking rate (Figure 21.D). A criticism to the awake curves is that they were computed from a stimulus matrix that is not corrected for the eye motion, and the curve may be different with such a correction. Due to difficulties in the eye tracking system, all cells could not be corrected. However, we show for some cells how the eye tracking correction has an effect on the curve in figure 26.F.

3.6 Chirp AM responses and model fitting

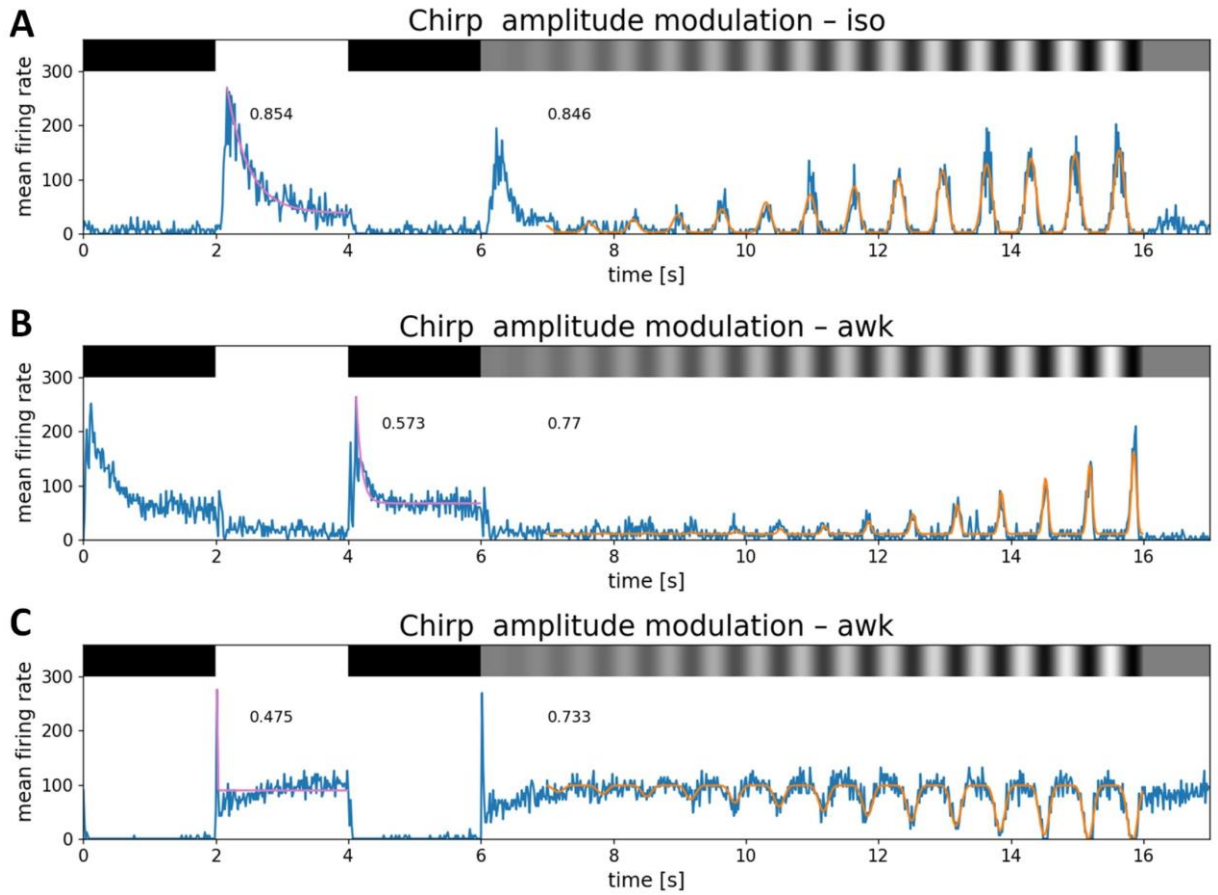


Figure 22 – Chirp AM responses. *A)* Response of a cell to a chirp modulated in amplitude under isoflurane. The blue trace corresponds to the mean response of the cell. In pink over the ON-OFF stimulation is the exponential decay fit (eq. 16), and in orange the fit to the amplitude modulation response (eq. 19). The number above the trace correspond to the fits quality (eq. 13). *B)* and *C)* Same as A for cells in awake condition. The cell in C shows a “negative” fit of the sine, where the response is explained by an inhibition from the basal activity of the cell.

In figure 22, we show examples of cells’ response to the chirp AM stimulus together with the fit of the model. By comparing the responses of the different conditions, we did not find particular features in the response, except for the timing and amplitude of the responses (figure

Results

23) as discussed in the next section. One thing to note, though, is the presence of suppressive responses in the awake data set (see, for example, figure 21.C). Such responses were found only in ON cells with a strong sustained response. To the chirp response, they did not show an increase of activity, but rather an increase of inhibition to the OFF stimulus. Their responses are thus better fitted with a negative amplitude (eq. 18) than with a positive amplitude.

3.7 Other awake/anaesthetised data trends

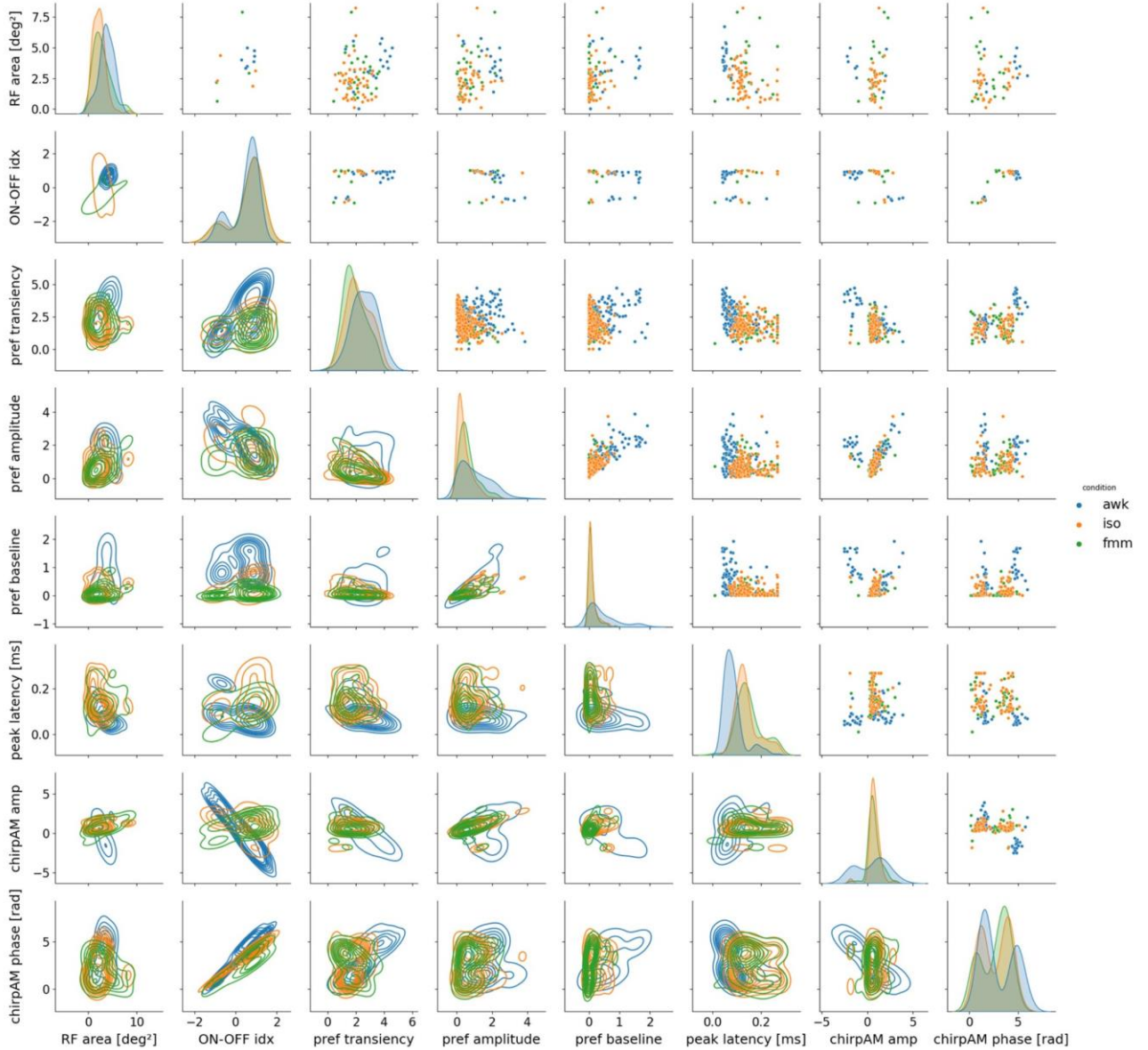


Figure 23 – Paired plots for selected parameters of our models. On the bottom axis, from left to right, we show the receptive field area (eq. 10), the on-off preference index (eq.15), the exponential decay fit parameters to the preferred (“pref”) stimulus (eq.16; $\log(\lambda)$: transiency; a : amplitude; b : baseline), the temporal STA peak latency (eq. 12), the chirp AM amplitude (eq.19), and the chirp AM phase (eq.19). The number of points varies depending on the condition pairs, as the parameters were thresholded by the quality indexes for each case. The diagonal axis shows the distribution of each condition at the corresponding parameter.

Results

We found striking differences in the ganglion cells responses properties between the awake and anaesthetised conditions (figure 23). First we observe a difference in the response speed to a stimulus. Indeed, the chirp AM phase parameter of the fit (eq. 19) shows a shift in the distributions. A higher phase indicates that the sine is shifted earlier in time. For every condition, we observe two bumps, corresponding from left to right to OFF and ON cells. The peak for the isoflurane OFF cells phase is at $\Phi=1.19\pm0.43$ (mean \pm standard deviation), whereas the awake peak is at $\Phi=1.59\pm0.21$. A phase shift of 0.40 (p-value= $4\cdot10^{-5}$, independent t-test), for a frequency of 1.5Hz (that of the chirp AM), corresponds to a temporal shift of 42ms ($=0.40/(1.5\cdot2\pi)$), which is compatible with the peak latency observed in the temporal STA (section 3.3, figure 18, peak latency awk: 84 ± 43 ms; iso: 140 ± 49 ms; fmm: 150 ± 52 ms). With the same calculation for the FMM peak at $\Phi=0.74\pm0.41$, FMM has a latency of 53ms if compared to the isoflurane (p-value= $7\cdot10^{-4}$), and 95ms if compared with the awake cells (p-value= $2\cdot10^{-11}$). Since there are no significant differences between the peak latency of FMM and isoflurane in the temporal STA, we did not expect such difference.

For the right peaks corresponding to the ON cells phase, the phase of the cells with negative chirp AM amplitude corresponded to the inhibition of the cell, and were therefore shifted by π radians to transform them into the response phase (as the cell in figure 23.C). We observe the same difference between isoflurane ($\Phi=3.85\pm0.53$) and FMM ($\Phi=3.56\pm0.63$) (p-value= $5\cdot10^{-3}$). However, the peak of awake cells ($\Phi=4.93\pm0.39$) and the isoflurane correspond to a shift of the response of 95ms (p-value= $6\cdot10^{-9}$), which is twice the shift of the first peak, but could be due to the fact that most of the awake cells have a negative amplitude in chirp AM fit. The temporal difference between the awake and FMM condition is of 146ms (p-value= $4\cdot10^{-11}$).

The second notable difference is in the chirp AM amplitude (eq. 19). When taking the absolute value of the amplitude, we observe that the awake condition (amp= 1.59 ± 0.78 , mean \pm standard deviation) have a higher amplitude than the isoflurane (amp= 0.81 ± 0.47 , p-value= $6\cdot10^{-10}$) and FMM (amp= 0.83 ± 0.61 , p-value= $3\cdot10^{-7}$), whereas we observe no difference between the two anaesthetised conditions (p-value=0.91).

Moreover, we found a consistent difference in the three parameters of the preferred stimulus fit (eq. 16): $\log(\lambda)$: “pref transiency”; a: “pref amplitude”; and b: “pref baseline”. The awake parameters (mean \pm standard deviation, respectively 2.63 ± 0.89 ; 1.05 ± 0.84 ; 0.43 ± 0.49) were significantly different to the parameters under isoflurane (respectively 2.19 ± 0.86 ; 0.43 ± 0.46 ; 0.11 ± 0.15) (p-values respectively $2\cdot10^{-6}$; $4\cdot10^{-20}$; $3\cdot10^{-22}$), and under FMM (respectively 1.92 ± 0.77 ; 0.63 ± 0.50 ; 0.09 ± 0.14) (p-values respectively $1\cdot10^{-10}$; $4\cdot10^{-6}$; $4\cdot10^{-12}$), while the two

Results

anaesthetised conditions differed on the transiency and amplitude, but not on the baseline (p-values respectively $3 \cdot 10^{-3}$; $2 \cdot 10^{-4}$; 0.33). All three differences are captured by the examples cells shown in the figures 19 and 22. The higher baseline of the awake cells is consistent with the effect reported on the non-linearities (figure 21), and the higher transiency matches the tuning of awake cells to higher frequencies than the anaesthetised cells (figure 18).

The next difference is in the ON-OFF index where we inside each condition more ON than OFF response. We found for awake, isoflurane and FMM respectively 16, 8 and 10 ON cells but only 5, 2 and 2 OFF cells (p-value=0.03, paired t-test). We observed no difference between the three conditions.

For the last two parameters, the receptive field size and the peak latency, the differences are highlighted respectively in the sections 3.5 and 3.3, and are only displayed here to be compared with the other parameters.

3.8 Direction and orientation selectivity

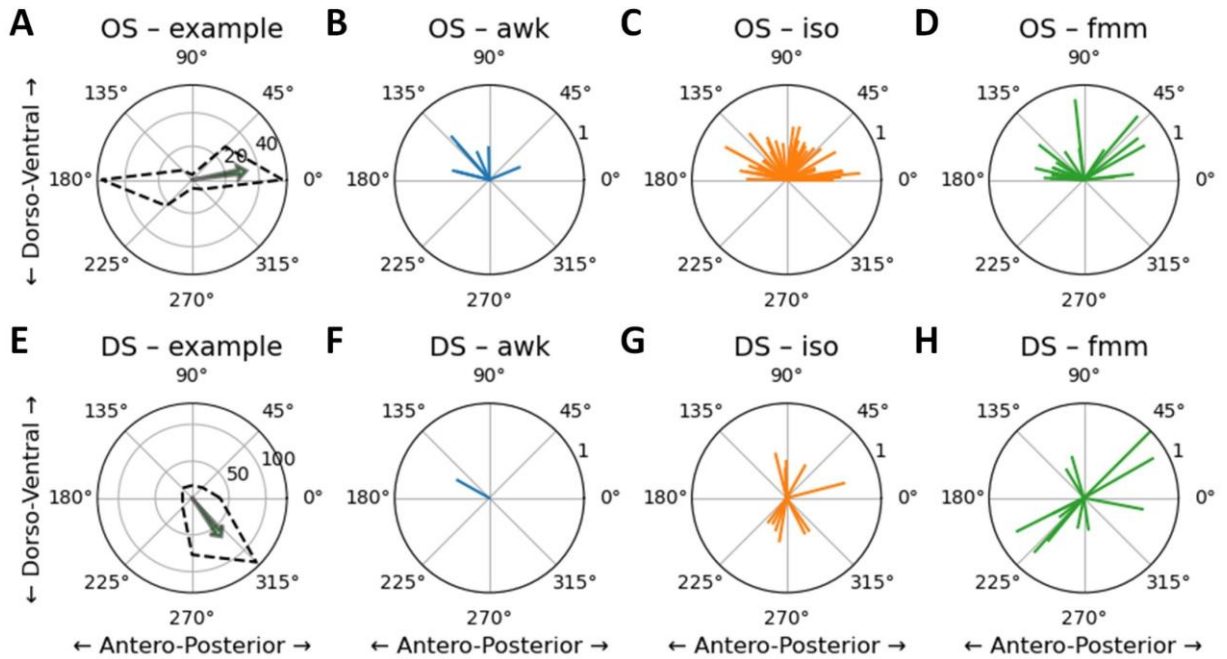


Figure 24 – Direction and orientation selectivity A) and E) Example cells with orientation (A) and direction (E) selectivity. The dashed black shows the gathered number of spikes for each of the eight angles. The green arrow indicates the preferred angle of the cell, while its amplitude encodes the preference index. B), C) and D) show the orientation selective cells gathered across the moving gratings condition, for awake ($n=7$), isoflurane ($n=38$) and FMM ($n=18$) conditions, respectively. F), G) and H) show the direction selective cells for awake ($n=1$), isoflurane ($n=11$) and FMM ($n=12$)

Direction and orientation selectivity are very well-known features of RGCs in the mouse retina. We presented a moving grating, instead of a moving bar, so that the stimulus would be

Results

homogenous and simultaneous across opposite parts of the screen while reducing the stimulus duration. We found in our records for each condition cell displaying orientation (awk/iso/fmm, $n = 7/38/18$) and direction (awk/iso/fmm, $n = 1/11/12$) preference. By comparing with the number cells for which we found a receptive field (figure 21), it corresponds for awake, isoflurane and FMM to respectively 24, 55 and 51% of the cells which were orientation selective, and 3, 16 and 34% of the cells which were direction selective. However, due to large differences in the number of animal per conditions together with duplicated records of cells (discussion section 4.1.3), the proportion difference we observe are not necessary meaningful.

3.9 Pupil detection with Mask-RCNN

After testing an existing solution for eye tracking (Jed et al. 2018), we realised that the diversity among our recordings required to tune parameters between animals or even during a session. Moreover, the diversity in the quality of the pupils and videos made the task even harder. Instead of searching for the optimal protocol and parameters to obtain a good eye-tracking, we decided to test an artificial neural network, Mask-RCNN (He et al. 2017). Starting from pre-trained weights of the network, learned from the wide Common Objects in Context dataset (Lin et al. 2014), we obtained a low and stable validation loss at the end of our 600 epochs of training (figure 25.A), and reliably detected mouse pupils (figure 25.B).

In addition, artificial neural networks provide confidence values of their predictions, which was not the case for the original solution we tested. The confidence retrieved is valuable, as it can be used to detect blinks of the eye, where no or partial pupil would be present on the image.

We plotted in figure 25.C the position in X of the pupil in the eye video. Red dots correspond to the detected epochs done as described in the methods (section 2.4.4). By looking at inter gazing events, we notice the stability of the pupil position, illustrating the reliability and consistency of Mask-RCNN in this task.

Finally, as a sanity control, figure 25.D shows the evolution of the pupil size during a chirp AM stimulus, averaged over ten repetitions. We observe the increase of the pupil size during the initial off stimulations and the rapid drop during the ON stimulation. Also, during the amplitude modulation phase, we can see the pupil following the fast 1.5Hz stimulation while the slow tendency is to decrease in size progressively due to the increase in contrast. Such fit of the pupil size to the stimulus corroborates a reliable pupil detection done by Mask-RCNN.

Results

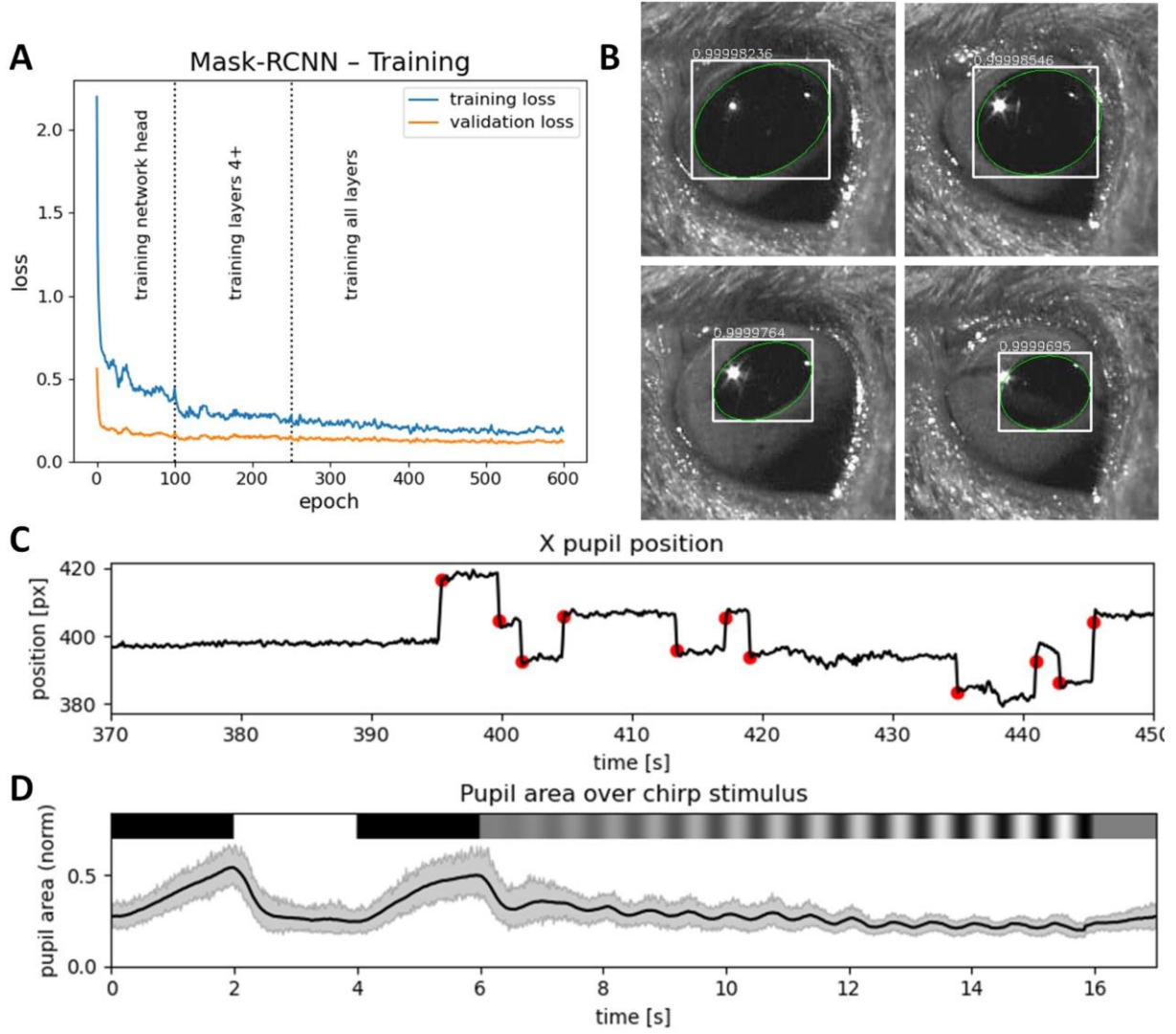


Figure 25 – Pupil detection with Mask-RCNN. **A)** Training loss and validation loss across training epochs for the fine-tuning of Mask-RCNN weights. **B)** Pupil detection by Mask-RCNN for the same mouse with four different pupil sizes and orientations. The white box represents the boundary of the object Mask-RCNN detected, and the value above is the confidence the network has in the detection. The green ellipse was fitted to the pixel mask of the pupil. **C)** Pupil X position in the eye video. Red dots mark the beginning of epochs detected with clustering. **D)** Normalised pupil area against the chirp AM stimulus, averaged over ten trials. The grey around the black trace corresponds to one standard deviation.

Results

3.10 Eye-tracking STA correction

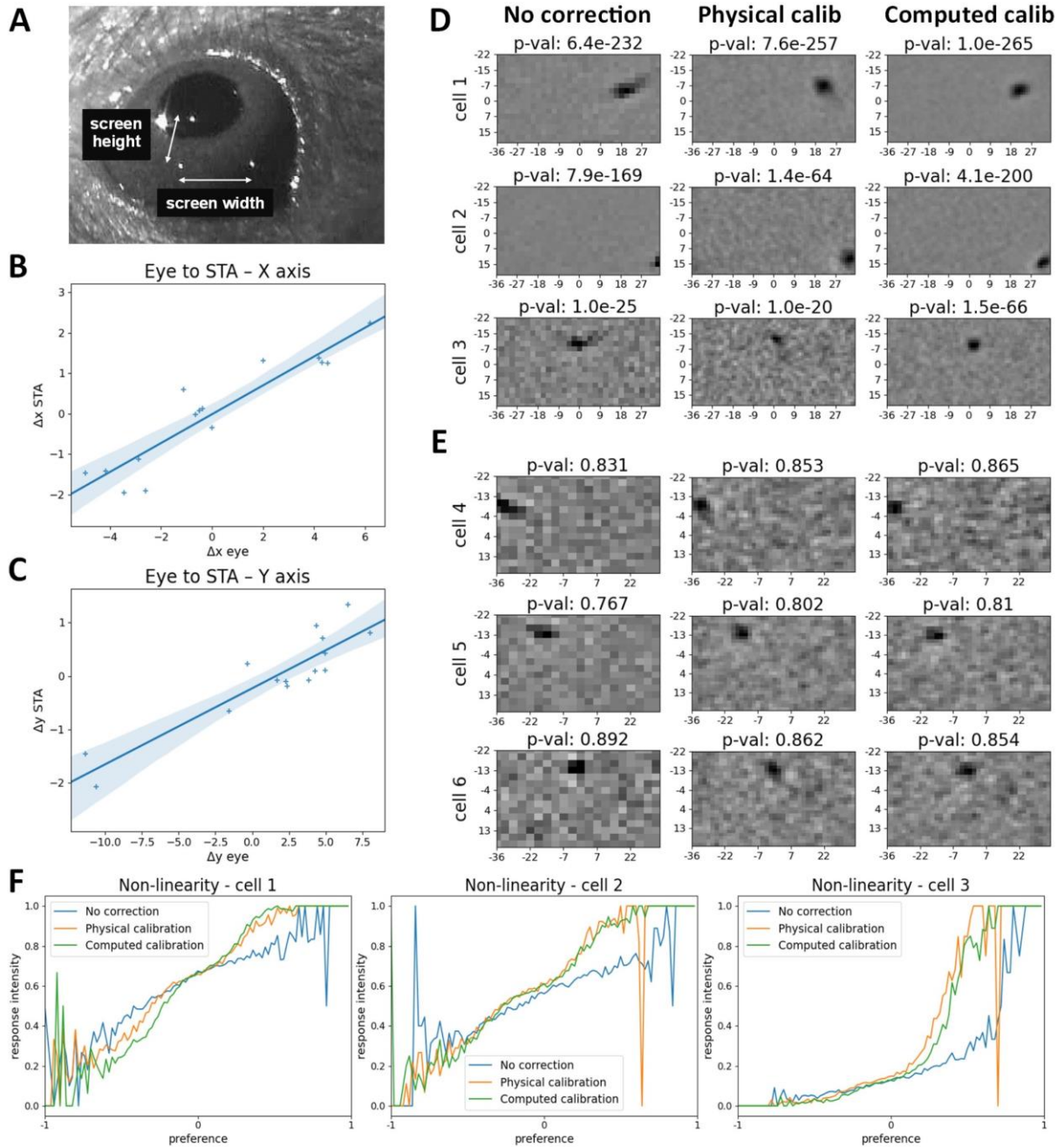


Figure 26 – Eye-tracking to correct the STA. **A)** First method, physical calibration. Infra-red LEDs were placed in the corner of the stimulus projection, visible in the eye video (three small white dots). Distances in x and y of the stimulus width and stimulus height (orange arrows) were measured in the eye video, and used to create the transformation matrix. **B)** Computed calibration. Regression fit between the eye's positions at stable epochs and the corresponding STAs positions. Values are expressed as shifts from the mean positions. **C)** Same as B but for the y axis. B and C regression fits are shown here as independent, but the fit was done on both axes at once to obtain the actual transformation matrix. **D)** Correction examples of cells obtained in electrophysiology. The computed calibration method was obtained from cell 1. **E)** Correction examples of cells obtained in calcium imaging. The computed calibration was also obtained from the cell 1 in D. **F)** Non-linearity of the cells 1, 2 and 3 in D before and after the correction of the stimulus with the two different calibrations.

Results

To test the eye-tracking performance of our system, we corrected the STA obtained from the checkerboard stimulus with two methods. Figure 26.A shows how the physical calibration was obtained. By turning on three light-emitting diodes (LEDs) in the corner of the stimulus screen (the fourth LED was hidden behind the dichroic mirror), we measured in the eye video the vectors corresponding to the width and height of the stimulus.

For the computed calibration, partial STAs at each epoch when the pupil remained stable were calculated and fitted with a 2D Gaussian. The position of the STA was then plotted against the eye position at each epoch for which the STA passed a quality threshold. From the x and y positions of the STA against those of the eye position, a regression fit was performed to obtain the transformation matrix (figure 26.B and C).

Figure 26.D shows the correction obtained from each calibration method for three cells obtained in the same electrophysiology record. The computed calibration method was obtained from cell 1 and applied to the rest of the cells (including cells in figure 26.E). For the cells 1 and 3, both methods correct the elongated shape of the STA observed without correction. However, from the p-value of each condition (eq. 5), only the computed calibration systematically improved the STA (the p-values are lower than without correction). For the cell 2, the uncorrected STA appeared at the very edge of the presented stimulus, but eye tracking allowed to restore almost completely the receptive field for that cell.

In addition, the non-linearities for the three cells are shown for each of the corrected and uncorrected STA (Figure 26.F). Nonlinearities were affected by the correction, decreasing slightly the response to non-preferred stimulus and increasing that to the preferred stimulus, while the null-point remained in position. Because this null-point was used in figure 21 to show a stronger baseline activity of the awake cells on incorrect STAs, we hypothesise that the corrected nonlinearities would produce similar results and therefore not impacting the results showed in figure 21.E.

In figure 26.E, we show the STA of cells obtained from calcium imaging experiments (not detailed in this thesis). The calibration with the second method was also taken from the cell 1 mentioned above, as the calcium response was not salient enough to obtain STAs on each epoch of the eye motion. As for electrophysiology (figure 26.D), both calibration show a visual improvement of the STA profile, with the physical calibration having lower p-values than the computed calibration, however none of them resulted in a lower p-value than the uncorrected STA.

Results

3.11 LED dome wide field of view coverage

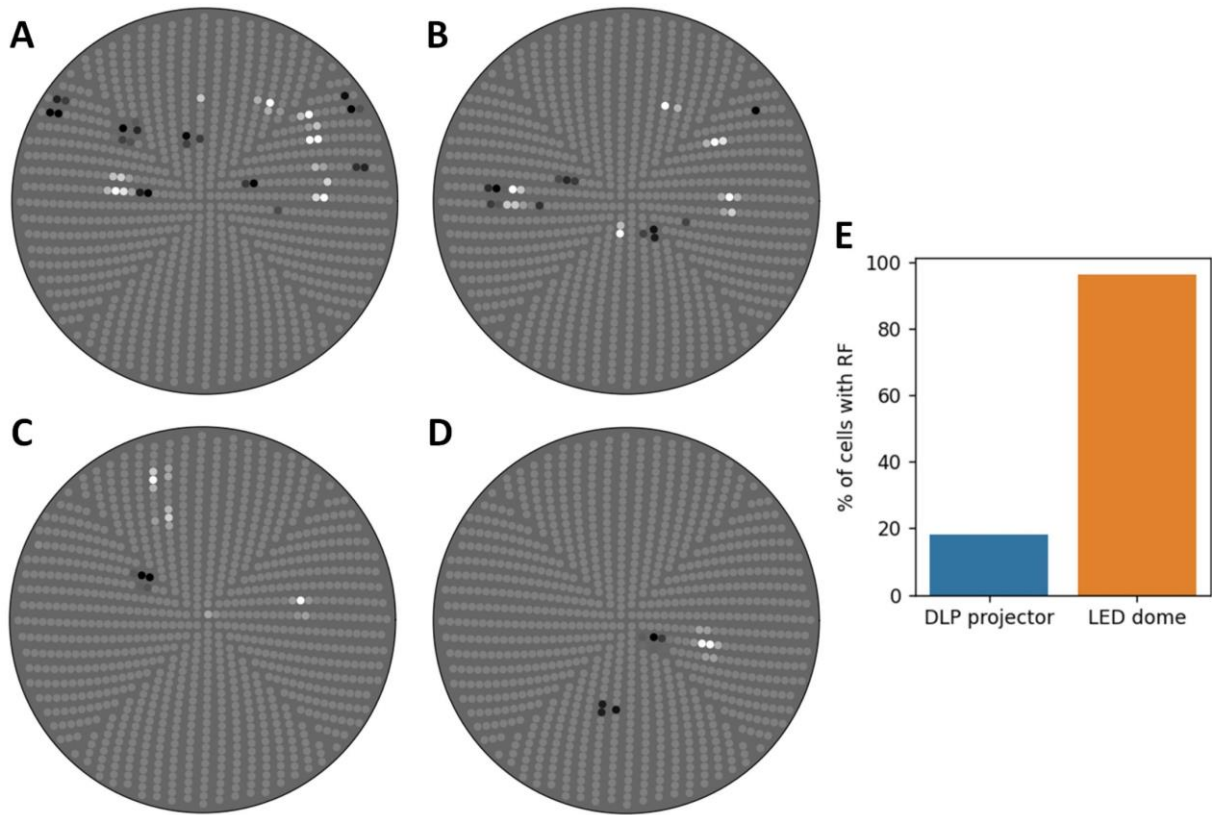


Figure 27 – Receptive fields of awake cells measured with the LED dome. A) to D) Receptive fields of cells recorded together and thresholded for the p -value and summed across the LED dome. The distance of an LED to the centre correspond to the inclination of the LED ($\pi/2$ - elevation radians). E) Proportion of cells with an STA using the full-field flicker stimulus that also have an STA using the checkerboard, for the DLP Projector and LED dome.

A test for the efficacy of the LED dome device was our ability to retrieve the receptive field of the recorded RGCs. In figure 27, all the receptive fields using the checkerboard stimulus on the LED dome are mapped to the positions of the LEDs and joined for individual recordings (four recordings with respectively from A to D 14, 11, 5 and 3 cells). On figure 27.E, we show the proportion of cells displaying an STA from the full-field flickering stimulus that also showed a receptive field using the checkerboard stimulus. Because changes in the intensity of the full-field stimulus can be reflected in the setup to outside of the screen — covering 73° by 44° in the case of the DLP — some recorded visual cells are able to pick up the changes without having their receptive field within the screen. The high proportion of cells with a receptive field using the LED dome — covering an entire monocular visual field — shows a coverage four times higher than that of the DLP projector.

Discussion

4 Discussion

In the past decades, retinal physiology has been studied extensively, dissecting the circuits that compose features computed by the retina such as direction selectivity, suppressed by contrast activity or centre-surround receptive field. The progress in our understanding of the retinal tissue has been allowed by the fast pace of technological advancement, allowing for a more extensive population acquisition together with the increase of processing power. From around twenty RGC types described ten years ago, about forty were distinguished when I started this thesis.

With the use of modern tools and technologies, we pursued an even more in-depth description of the retinal physiology for studying the poorly understood mammalian retinopetal system. To that aim, we first had to develop recording methods from the retina *in vivo*, to measure the modulations provided by the brain in the most realistic paradigm. The main goal of my thesis was to develop *in vivo* electrophysiological recordings of the mouse retinal ganglion cells (RGCs) axons, together with an analysis pipeline for the processing of both electrophysiology and calcium imaging experiments, to explore retinopetal modulations.

To set up the electrophysiological recordings, I started with anaesthetised mice to define the electrode implantation strategy, that once established allowed me to observe RGC outputs *in vivo*. After getting a sufficient amount of practice at implanting the electrodes acutely, I moved toward a chronic implantation procedure that ultimately allowed me to record what the mouse's eye tells the mouse's brain without the presence of anaesthetic drugs, meaning in more physiological conditions.

The *in vivo* awake RGCs records came with a set of challenges to solve, such as the synchronisation of behavioural data, including the eye video that we subsequently exploited to perform eye tracking. Those tasks took me more time than I anticipated, as I also developed and used the pipeline to process the *in vivo* RGCs calcium imaging experiments.

In the meantime, other projects of my research group aimed to replicate previous tracing experiments of the retinopetal connexions, using modern viral tools. However, still up to now, we were not able to confirm the origins of retinopetal neurons, nor confirm existence of the retinopetal axons in the mouse retina. Moreover, we experienced difficulties in the setting up of *ex vivo* recordings of the retina, that we had planned to use to study the effects of retinopetal neurotransmitters and complement previous studies conducted on histamine (Akimov et al.

Discussion

2010; Frazão et al. 2011; Gastinger et al. 2004, 2006a; Horio et al. 2018; Yu et al. 2009) and serotonin (Brunken & Daw 1988; Gastinger et al. 2006a; Skrandies & Wässle 1988).

Without specific brain regions to target, to up or downregulate the retinopetal activity, and without knowing the effects retinopetal neurotransmitters have on the mouse retina, we sought comparisons elsewhere. With the striking differences I observed in the retinal outputs between the awake and the anaesthetised conditions, and knowing how widespread the use of that anaesthetic is for neurobiology experiments, I realised that a more in-depth analysis of the differences could provide a new perspective on the work done under anaesthesia. To this end, I tested a second condition for anaesthesia, the combination of fentanyl, midazolam and medetomidine (FMM).

Finally, during the last year of my project, I designed and built the LED dome to investigate the cells that appeared to respond to a stimulus presented everywhere on the screen by the STA analysis. By recording a chronically implanted mouse using each stimulation device, the LED dome and the DLP projector, we eventually observed a cell present in both records and showed that it was an artefact (discussed in section 4.4.5). However, the LED dome proved useful for other measurements, such as the temporal frequency response of awake retinal cells.

4.1 *In vivo* electrophysiological retinal recordings

4.1.1 Target choice

As an initial target, I selected what I thought would be the easiest to reach systematically due to its large width: the optic chiasm (Freeman et al. 2010). One difference to note with similar recordings in rodents (Freeman et al. 2010; Michael 1968; Nobles et al. 2012; Sagdullaev & McCall 2005) is that I did not exposed the RGC fibres by removing the overhead brain tissue. Instead, I would identify the region by presenting visual stimuli to the mouse once an electrode would be located near the target in stereotaxic coordinates. While setting up the recording technique, I tried nine times this approach, from which five histological analysis showed that the target was reached. Two factors can explain the difficulties in reaching the target: the optic chiasm lies at the bottom of the brain, for the mouse at a depth of 5.5mm. With distances, small initial misplacement errors translate into larger error. The second factor is that the optic chiasm is located under the midline of the brain, where a large vein passes at the surface. For that reason, the electrode cannot be lowered vertically to the target but requires to depart from the side of the midline, diagonally.

Discussion

In those five sessions for which we confirmed the targeting, I observed visual responses only twice. How could we obtain such a low yield, despite having the silicon probe with 32 recording sites surrounded by RGC axonal fibres? To that question, I obtained the first clues of the answer during these two recordings: after looking for the target up to a far enough depth, I initiated the retraction of the probes and subsequently observed visual responses. As a final blow, it also turned out that during the successful trials, shanks of the silicone probes broke, most likely due to the probe pushing beyond the optic chiasm, against the bone.

To circumvent those difficulties, I decided to choose a different target. The RGC axon fibres go back up inside the brain after the optic chiasm to reach the dorsal part of the lateral geniculate nucleus (dLGN). To avoid confusion with dLGN visual responses, I chose as a new target the optic tract at the intermediary point between the optic chiasm and the dLGN. As I could also obtain visually responsive cells with this target, and since I was less susceptible to damage the expensive silicon probes as the optic tract climbs up in the brain, I kept it as a target.

Like for the initial optic chiasm recordings (not shown in this thesis), I noticed relationship between the probe retraction and the apparition of RGCs signals. In both cases, the electrode did not seem to penetrate the tissue easily, and pressure built up as I inserted the electrode in the optic tract. When retracting the electrode, a probable scenario was that the optic tract also followed the upward motion as the pressure was released, therefore leaving the electrode recording sites close to the RGCs axons. Because pressure can prevent the normal physiology of the axon (Keir & Rempel 2005; Wang et al. 2012), this scenario would explain why signals appeared during the retraction of the probe.

To corroborate this last point, I observed the inertia of the tissue. Given the presence of a response on a recording site, and given the distance separating two recording sites, displacing the probe of that distance should move the signal to the next recording site. However, I observed that after displacing the probe by such amount, the signal went initially unchanged. Only after about a minute and for 10 to 15 minutes, the signal moved and appeared on the next channel.

Myelin correlates with increased stiffness of the brain (Weickenmeier et al. 2016, 2017). Because the optic tract is a bundle of parallel myelinated fibres, not yet interleaved in the surrounding tissue, the penetration is difficult, resulting in a combination of displacement and pressure increase of the optic tract. By retracting the probe, we relieve the applied stress that restores the neuronal activity. Because the optic tract is not located at the bottom of the brain, the probe has enough space behind the optic tract to push without hitting the bone. As such, the

Discussion

optic tract seems to be the optimal target to obtain RGCs recordings with a conventional silicone probe.

4.1.2 Signal-to-noise ratio and spike sorting

To position the silicone probe in the optic tract for a recording, I aimed at maximizing the number and signal amplitude of clear visual responsive cells, but such cells were rare (2-3 per record). Moreover, during waiting periods after I moved the silicon probe, it happened that the signals of those cells faded over time or moved on the electrode, while other units' signal could increase over time. In addition to the clear visual responsive cells, more cells passed the seven standard deviation threshold for spike detection after filtering the noise of the signal. Among those units, some of them displayed characteristic responses to the visual stimuli and were also included in the global analysis when meeting the quality criteria.

The signal amplitude variations and the low signal-to-noise ratio (SNR) of some units impacted the spike sorting quality. During the automatic process by the SpykingCircus (Yger et al. 2018), the identified spikes are grouped in clusters automatically. Following, a manual review is done with goal to identify neurons from noise and merge clusters corresponding to the same cell. This task is, however, non-trivial and is increasingly difficult and subjective as the SNR decreases. Moreover, at low SNR, spikes of a cell are more likely to be overlooked by the algorithm (false negative), while more noise signals are likely to be detected as spikes (false positive).

A solution would be to place the bar high for accepting a cluster for further analysis, but due to the scarcity of visual cells in a record, this was not the solution I opted for. To quote the authors of the spike sorting guide (Lenzi & Steinmetz): The goal here is slightly different from "com[ing] up with the truth about the data" - instead it is to "improve the results of the automatic algorithm". To that end, I accepted clusters on the basis that the amplitude was reasonably high, so if a cell were indeed visual, its signal would not be covered by random noise. Ultimately, cells' responses to visual stimuli were averaged, and quality indexes served as criteria to distinguish the good from the bad units (still using an arbitrary threshold, but independent of the experimental condition). Ultimately, the main drawback of including low SNR clusters in the analysis was to make harder the comparison of spike counts or firing rates.

4.1.3 Multiple records of identical cells and cell pairing

In the aim of maximizing the amount of data gathered per animal, I performed several recording sessions in each mouse. The first scenario was to record a first time and then move the electrode

Discussion

to a different location to find more cells and replay the stimulus sequence, with isoflurane (18 mice; 44 different locations; min: 1; max: 4; mean \pm std: 2.4 \pm 1.0), FMM (6 mice; 10 different locations; min: 1; max: 3; mean \pm std: 1.7 \pm 0.9) and awake (3 mice; 6 different locations; min: 2; max: 2). Interesting regions could be found close to each other so that it occurred that signals of identical cells were recorded from multiple recordings. However, due to the signal shape change and varying SNR across the recordings, it remained too difficult to identify those cells during the analysis. For that reason, the same cells may appear more than once in our data, introducing a bias that must be considered.

A second scenario was to perform twice the recording in the same location, either after changing a condition such as the anaesthetic (5 isoflurane-FMM pairs in 10 recordings in 5 mice, annexe 3 cells 9 and 10) or at two different times in the case of chronically implanted mice. In those case, I purposely aimed at recording the same cells (14 day-night pairs in 13 recordings at 3 locations in 2 mice, annexe 3 cells 2 and 3). After spike sorting the records and processing the cells' response to the stimuli, summary plots of each cell were compared from paired records to identify identical cells. However, still due to SNR fluctuations and unwanted displacement of the electrodes, not all cells could be tracked across the recording sessions, while others could not be tracked due to noise fluctuations (37 \pm 28% of the cells paired in anaesthesia for 19 pairs, 47 \pm 23% of the cells paired in day-night for 25 pairs).

4.1.4 Future developments

With the present work, I demonstrated how to perform electrophysiological recordings of mouse RGC axons *in vivo* using the silicon probes, in both awake and anaesthetised conditions. Despite successfully reporting cells response properties, the technique showed its limitations in the cell units yield, in the recording stability across sessions, and in the time required to prepare the animal in the case of awake records with the use of chronic implants. Because the retina under anaesthesia does not resemble the awake one, we wish to develop further the recordings of the awake retina in several aspects: 1) reducing the implantation time and difficulty, 2) increasing the cell yield by reviewing the implantation strategy and optimising silicone probe designs, and 3) smoothing the synchronisation process to ease the experiment reproduction in other laboratories.

A recent work (Schröder et al. 2020) showed the use of a Neuropixels probe (Jun et al. 2017) to obtain recordings from the optic tract. The Neuropixels probe is a 10mm long silicon probe with 960 recording sites along the shank (384 can be recorded simultaneously), with a 70 x 20 μ m cross-section. The advantage of this probe is that it can record from several brain regions it

Discussion

crosses, that could prove useful while assessing the correlation of specific behavioural activity with the modulation of the retinal output (Schröder et al. 2020).

Despite the high density of the recording sites on that probe, it remained two times thinner than the 10mm Buzsaki32L probe we used (52 x 50 μm cross-section) (Royer et al. 2010). The advantage of the Buzsaki32L probe remained in the strategical positioning of the recording sites across its four shanks. Even without the high density of the Neuropixels probe, we were able to observe the action potentials of RGC axons across several sites of the same shank, indicating that a higher density of sites should not necessarily provide a higher yield. Moreover, if the probe is positioned accurately, each shanks could record from different areas of the optic tract (200 μm apart), which is unlikely to show identical cells. As of now, we are also looking at several other probe designs that we hope will increase our yield. After more experimenting with different recording sites layouts, we aim to design custom silicon probes specific for optic tract recordings, that would have a smaller length to obtain thinner shanks (15 μm instead of 50 μm) for better penetration of the optic tract. Finally, we have been assembling a specific awake setup for acute electrophysiology recordings, that should decrease drastically the time required for the collection of cells, in comparison to the chronic recordings we did so far.

A serious alternative to electrode implantations in the optic tract is the flexible mesh electronics (Hong et al. 2018b; Schuhmann et al. 2018). The first awake recordings of the mouse RGCs published were done using a mesh implant (Hong et al. 2018a). The mesh is injected in the vitreous humour and unwrap onto the ganglion cells body. The mesh is subsequently recorded through a cable going out of the injection hole. The technique invasiveness seems relatively low as the mouse blinking, pupil light responses and visual acuity were not impacted (Hong et al. 2018a). The technology shows many advantages such as the records' stability across weeks and potentially a higher cell yield, from a positioning next to the cellular bodies, similar to what microelectrode arrays (MEA) do. Though the technology is up-and-coming, its principal obstacle remains its accessibility and would profit of broader commercialisation.

4.1.5 Complementary calcium imaging of axon terminals

In parallel to my project was established the calcium imaging of the RGC' axon terminals in the superior colliculus, transfected with a GCaMP. The recordings are not presented here as they are not part of the work I conducted. However, I still wish to discuss the advantages and disadvantages of the technique in comparison to the electrophysiology records I made.

Discussion

On the cell yield and stability across days, the advantage is for the calcium imaging. Indeed, the calcium imaging was able to record each time a set of twenty cells or more, which is a double for most of the electrophysiology records we obtained when counting the cells without receptive field. The records were also more stable in time, as the same region could be retrieved and re-acquired across weeks. This was not the case for the electrophysiology, as recording day to day without moving the electrode did not allow to retrieve all cells. Finally, the electrophysiology signal amplitude attenuates in time, as scar tissue forms around the electrode.

Moreover, the axons terminals follow a retinotopy in their projection at the superior colliculus. In other words, the axons terminals are spatially related, and it can be seen in the receptive field mapping of the cells. This is a good advantage for the calcium imaging, as the stimulus is not required to cover the entire field of view of an eye, unlike the electrophysiology which picks the RGCs randomly in the optic tract, sampling their receptive field across the whole eye's field of view.

The advantage of the electrophysiology is in the temporal precision of the recorded response. With it, we can obtain precise timing of the RGC response against a visual stimulus. In the case of calcium imaging, the fluorescence rise, decay and SNR of GCaMP prevent the discrimination of rapid changes in the activity of the RGCs, making it difficult to use 60Hz stimuli for the receptive field mapping for example. Moreover, electrophysiological recordings can be performed multiple times during a single day, while calcium imaging is limited in acquisition time due to the bleaching of the fluorescent probes, and requires breaks of several days across recording sessions.

In conclusion, several alternatives exist to the silicon probe approach I developed. Considering each aspects of the strategies, no technique seems to be superior to the others, and instead, the choice should depend on the question asked.

4.2 Visual stimulation

4.2.1 Field of view and screen shape

In the case of *ex vivo* retinal recordings employing MEAs or calcium imaging, the retina is placed in a chamber and kept flat. To present the visual stimulus, an image from a projector or a flat monitor is directly focussed with a lens system onto the retina. The *ex vivo* preparation can therefore ignore the optics of the mouse eye and always present a focussed stimulus, no matter the region of the visual field recorded.

Discussion

In contrast, the study of the visual system *in vivo* requires the stimulus to pass through the eye's optics. Mice are known to have a low visual acuity, at around 0.5 cycles per degree (Artal et al. 1998; Geng et al. 2011; Prusky & Douglas 2004; Prusky et al. 2000). Moreover, the mouse eye is subject to optical aberrations (de la Cera et al. 2006), linked to its small size (Glickstein & Millodot 1970; Smith 2012). As such, the presentation of a stimulus with a disproportioned flat-screen leads to spherical distortions of the image at the periphery of the visual field, related to a fisheye lens distortion (Smith 2012). In an attempt of reducing the aberrations, the DLP stimulus image was shone to a spherical screen. In this configuration, the image distance to the eye remained homogeneous across the visual field. However, it did not prevent the distortion of straight lines on the projected image.

The second obstacle in presenting visual stimulation to mice is the field of view coverage. As mentioned above, large flat screens are not good at delivering homogeneous stimulation. The closer their position is to the mouse, the larger the field of view coverage is, but also the more massive the distortion is, and the less uniform the light intensity is across the visual field. In the case of our spherical screen for the awake electrophysiology and anaesthetised stereotaxic electrophysiology setups, I presented the image at a 20 cm distance, covering 70° in azimuth and 45° in elevation. Such coverage corresponded to only a fraction of the mouse visual field and accounts for the small proportion of the cells exhibiting a receptive field.

Intending to cover most of the recorded eye visual field, we designed, built and tested a LED dome. The LED dome had a diameter of 20 cm (annexe 1), which resulted in a homogenous distance of 10 cm when placing the mouse eye at the dome centre. With this device, I observed a receptive field for most of the visual cells I recorded (figure 27), and it allowed to assess the receptive field of the cells that showed full-field receptive field with the DLP projector stimulation (annexe 3, cell 4 and 5).

4.2.2 Light intensity

For retinal processing, the light level is determinant. At scotopic levels, the cones are not sensitive enough to reliably detect the image reaching the retina. Instead, the rods are involved and relay the information through the rod pathway (Soucy et al. 1998; Tsukamoto et al. 2001). At photopic levels, the rods are thought to saturate (though this has been nuanced by a recent study (Tikidji-Hamburyan et al. 2017)), and the vision is cone driven, whereas at intermediary light levels, termed mesopic, the retinal processing is a mix of the two.

Discussion

From the DLP 3010 EVM, we modified the light engine to replace the green LED by a UV LED. In that configuration, we aimed to stimulate both the S-cones (with UV light) and M-cones (with blue light). For the *ex vivo* setup we have, the stimulation intensity could easily reach photopic levels, as all the light is concentrated on a small area, directly onto the retina. However, for the *in vivo* setups, the image was indirectly presented to the mouse by projecting it on a screen (covered with UV reflective paint). Even at the highest intensity, the LEDs of the light engine could only generate mesopic light levels ($2.5 \cdot 10^3$ rods photoisomerization \cdot s $^{-1}$) and it should be taken into consideration.

With the LED dome, we faced the opposite problem. With individual LEDs making for the pixels of our image, and with direct stimulation of the mouse retina, the light level was already higher ($1.9 \cdot 10^4$ rods photoisomerization \cdot s $^{-1}$) at the smallest possible LED intensity. As such, we could not exploit the dynamic range of the LEDs to present stimuli with varying contrasts. A second drawback of the LED dome was the lack of UV components.

4.2.3 Refresh rate

A first limitation in the refresh rate that the LED dome can attain comes from the computation time for the Arduino workers to generate the frames. The speed relies first on the algorithm used and optimisations (more details in annexe 1) and should avoid jitters from random fluctuations. In the case of full-field stimuli, this computation time is negligible.

To assess the temporal sensitivity limit of RGCs, the use of a screen with a fixed refresh rate is limiting. Indeed, for balanced ON-OFF stimulation, the screen can only use a pair number of frames. As such, the DLP at 60Hz can use 2, 4, 6 or 8 frames per cycle for stimuli at 30, 15, 10, 7.5Hz and on. To access frequencies such as 20, 25, 35 or 40 Hz, a device with a higher refresh rate must be used. The LED dome was suited to display such stimuli. Indeed, the LED stripes composing the dome have a refresh rate of 400Hz. As such, it is theoretically possible to show stimuli at 200, 100, 66, 50, 40, 33, 28, 25, 20Hz and on.

To present the high-frequency ON-OFF stimulus, we overestimated the capabilities of Arduinos to control two independent LED stripes. The design was made so that the number of Arduino workers could be doubled to decrease by half the LED value loading time. However, with two stripes to control, the Arduino updates sequentially the stripes. One stripe update takes about 3.5 ms to complete, and the frequency of 400Hz indicates that there is a jitter of 0 to 2.5 ms for the stripe to refresh the newly updated values. As such, our highest stimulus frequency of 50Hz with normally a frame each 10ms, had the two stripes of each Arduino desynchronised by 1 to

Discussion

6 ms. Thus, the stimuli provided to the cells at high intensities were strongly distorted, and to further investigate the maximum temporal frequency of RGCs, the LED dome will require an upgrade to eight Arduino workers.

4.2.4 Display errors, detection and correction

With the rapid dynamics of the cells *in vivo*, precise synchronisation between the stimuli projected and the cell's response needs to be achieved to attribute the effects to changes of experimental conditions. To this end, I established a pipeline to detect events of the stimulation and acquisition for allowing the synchronisation of each recording. Moreover, display errors of the stimulus need to be accounted for, due to temporal shifts of the stimulus that would influence the measure of the cell stimulus to response lag. For that purpose, a binary marker is insufficient. Given a stimulus displayed at the frequency of the device (in our case 60Hz), the marker needs to change state at each frame to encode the stimulus change and therefore flag a display error. For example, if the sequence we want to display is [0,1,0,1,0], but we record the sequence [0,1,1,1,0], the marker indicate that an error occurred. However, it cannot solve if the frame replaced the stimulus corresponding to the missing zero before or after, as both signals are identical.

To decide between the two scenarios to later apply the correct fix, we need to know what kind of errors the setup can make. The first place where errors occur is within the software playing the stimulus (QDSpy) but it keeps tracks of the time between each frame it produces. By experimenting with it, I noticed that the errors QDSpy reports correspond to freeze of the software (computer being busy with other programs) but then resume to the normal sequence. After handling the errors logged by QDSpy, other errors remain. The error must come from the next pieces of equipment on the chain, but detecting and fixing the issues becomes much more challenging. Depending on the graphic card, its configuration, miscommunications with the DLP or the DLP itself, the error can come from many places.

Due to the difficulty of the task, and the multiple setups and configuration we use, the way I found to catalogue the errors was to increase the complexity of the marker used for synchronisation. With more information encoded in more light intensity level, we could follow up more precisely the history of errors in the display. The first requirement for that method to work is to be able to tell the difference between the intensities. Fortunately, after performing frame detection and computing the area under the curve of each frame, I noticed a strong separation between the frames of the five light level we picked (figure 17).

Discussion

With such markers, I went through recordings of our different setups with the hope to identify patterns in the errors. By then going through several records of each setup, I encountered three kinds of errors: insertion, deletion and substitution. Still, each setup was unique, in the sense that some showed little or no errors, some had periods of calm followed by bursts of error. In contrast, others produced errors continuously across the record, which corroborated with the idea that many factors were involved. A well-endowed group could consider replacing its hardware by more powerful machines; however, I noticed from our diversity of setups that a cheap computer, when left undisturbed, outperformed more expensive ones.

In conclusion, finding the ideal stimulation device turned out more difficult than expected. Many parameters need to be taken into account: a spherical shape to prevent visual aberration, a large intensity dynamic range with a UV component to match mouse vision, a high refresh rate allowing the presentation of a stimulus at high frequencies and a reliable computer to control the display. Finally, a high spatial resolution of the device is also desirable to display naturalistic stimuli, as their interest is growing (Walker et al. 2019). If such a device is not yet available, its construction is not impossible, as monitors with 240Hz refresh rate, or with 4K resolution are commercially available (but do not have UV light). In the meantime, it seems desirable to use a set of devices depending on the question asked.

4.3 Eye-tracking

4.3.1 Pupil detection

In prospects of correcting or detecting artefacts in the cell's response, we recorded a video of the mouse eye. To extract the pupil position from the image, we tried first a program based on an edge detection algorithm (Jed et al. 2018), fine-tuned from a set of parameters. After a user provides a region of interest (ROI), the program locates the minimum in the image, that should correspond to the pupil. Then, from this detected point, the program traces straight lines in a different direction and locates the edge of the pupil as a sudden increase of pixel intensity. Following the edge detection, the points are fitted with an ellipse with a Random Sample Consensus algorithm (RANSAC) (Fischler & Bolles 1981), resilient to noise in the points to be fitted.

The approach is valid and works for many practical cases, but proved unable to process the videos we acquired. For a whole recording session, the light stimulation varied the size of the mouse pupil. Combined with variation in the illumination due to the mouse body casting a

Discussion

shadow from our infra-red (IR) source, and sometimes other irregularities of the eye, a set of parameters could not process a whole video.

During the time we aimed to solve the pupil detection, I witnessed the capabilities of a deep neural network (DNN) at detecting scissors, hairs, combs, hairdryer and other things you find at a hairdresser, that was part of my flatmates' master project. They used a DNN called Mask-RCNN (He et al. 2017), part of a family of DNN called the region-based convolutional neural networks (R-CNN). The original goal of R-CNNs was to detect a bounding box for objects of interest, but Mask-RCNN added a masking component to it, which detects inside the bounding box the pixels belonging to the item.

After its publication, the network was implemented for Tensorflow in python (Waleed 2017) and made available together with trained weight against the Common Object in Context (COCO) dataset (Tsung-Yi Lin et al. 2018). From those weights, the network was fine-tuned (Yosinski et al. 2014) against a set of labelled mouse pupil.

With an initial dataset made of 500 manual segmentation of mouse eye, I trained the network over a weekend, and the results were satisfying. However, the eye video quality needed to be further improved, and modifications of the setup changed the angle of the video. To avoid overfitting, the training set needs to be highly diverse, but the manual segmentation of numerous images is time-consuming. To prevent overfitting to such a small dataset, we used image augmentation (Shorten & Khoshgoftaar 2019) to diversify the training set artificially.

Ultimately, Mask-RCNN allowed us to detect mouse pupils from our videos reliably, as shown in figure 25. However, in retrospective, Mask-RCNN is an overkill for this task. Compared to the COCO dataset challenge, pupil detection is trivial. Once trained, the image processing speed does not depend on the detection difficulty but on the size of the DNN, which is about five frames per second for Mask-RCNN. Other lighter networks could perform as well at this task while requiring less processing. Such a solution, a now popular framework called DeepLabCut (DLC) (Mathis et al. 2018), came out the next year. DLC is based on DeeperCut (Insafutdinov et al. 2016) which performs multi-person pose estimation, specialised in recognizing points of an object, like the shoulders, knees, feet of a mouse or the cardinal points of a mouse pupil. Therefore, DLC seems to be more suited for the task of pupil detection and should be considered instead of Mask-RCNN. However, both networks perform the detection on single frames, not accounting for the sequence that makes it a video. If a sequential neural network came in play,

Discussion

with an interface as ergonomic as the DeepLabCut one, it could outperform both networks in tasks such as blinks detection.

4.3.2 STA correction

To compensate the eye motion for the spike-triggering average (STA) of the checkerboard stimulus, we employed two different kinds of strategy. A first one was to measure after a record the physical dimension of the screen in the mouse eye video. As such, we estimated the transformation matrix needed to pass from an eye shift to a stimulus shift. The second approach was to measure the displacement of the STA calculated over epochs, where the eye stayed still and fit the transformation matrix directly to these measurements. We aimed to show with both methods that the eye-tracking can lead to improvement of the STA; however, it suffers from several problems.

The first significant issue is that the two methods are not leading to similar results. If the eye-tracking calibration was valid with both approaches, the corrected STA should show more comparable results. An issue of this dataset is that we could not use both methods on a single record: none of the mice recorded in electrophysiology was calibrated for the first method, and the calcium imaging responses are not strong enough to calculate the calibration with the second method.

A second problem we encountered that lowers the valid data to test the eye tracking performance is in the synchronisation of the video frames with the recorded triggers. During past analysis, I realised a discrepancy between the number of triggers and the number of frames in the video. Both should be equal, however, the video missed some of the frames. After doing a few tests with the acquisition software, it seemed that the missing frames were spread across the record, and were coming from the capture software being busy at compressing the video. Like so, with an interpolation of the data between the first and last frame, the shift should be gradually compensated. However, only later, while looking at the pupil size variation from the chirp AM stimulus (same as in figure 25.D), I noticed that for some records, the pupil was not synchronised with the stimulus, and seemed to come from a large shift of the video at once. If such large shift exists and occurred before or during the checkerboard stimulus, the STA correction with eye tracking cannot work. More investigation is needed to understand why the acquisition failed and what kind of error happened. However, it seems unlikely that the impacted records can be repaired.

Discussion

The next issue with the eye-tracking we performed is in the measure of the pupil displacement. We took it as a shift in pixels of the video and fitted a linear relationship with the stimulus displacement. But the eye rotates, and the angle of displacement does not follow the displacement linearly in pixels. If the eye rotations are small, and if the eye is not acquired from a strong angle, the approximation of using a shift in pixels could suffice. However, the mouse to mouse variability due to the head plate implantations, and adjustments of the dichroic mirror placed in front of the eye are sources of changes of calibration. Measuring the eye rotation angles instead could help at finding a common calibration setting of our setup, similarly to what was done previously (Sakatani & Isa 2004).

4.4 In vivo retinal properties

4.4.1 Anaesthesia in the retina

To explain how the anaesthesia affected the retina, we must identify putative affected processing mechanisms. As presented in the introduction (section 1.7), isoflurane and midazolam (part of FMM cocktail) potentiate the GABA_A receptor, an inhibitory chloride channel. Those receptors are mainly located on the axon terminals of the three major BC type, naming the ON, OFF (Eggers & Lukasiewicz 2011) and rod BCs (Chávez et al. 2010; Eggers & Lukasiewicz 2006), and on the RGCs dendrites (Wässle et al. 1998) where amacrine cells (AC) provide feedback by the release of GABA (Crooks & Kolb 1992). In addition to the GABA_A receptors, GABA_C receptors also play a role in the feedback modulation of the BC. The two receptors have different dynamic: the GABA_AR provide a fast and short inhibition, while the onset of the GABA_CR is slower but last longer (Popova 2014). Only the GABA_AR is affected by either anaesthetic drugs, but because the ratio between GABA_CR and GABA_AR varies from BC subtypes (Eggers et al. 2007; Euler & Wässle 1998), anaesthesia should not affect equally all the BCs types. With the BCs signals being inhibited, ACs and RGCs will receive less excitatory inputs. Since AC have a retroactive inhibition on the BCs, it could just be that the negative feedback loop compensates itself. But it could also be that the lateral inhibition of ACs and the more intricate networks they form between AC types are affected in unexpected ways.

4.4.2 What anaesthesia tells about our data

By recording the mouse retina output *in vivo*, in both anaesthetised and awake animals, I showed that the temporal properties of the RGCs were substantially affected by anaesthesia. Indeed, to the response of the full-field flickering stimulus (figure 18), we obtained the spike-triggered average (STA) showing an increased peak latency between the stimulus and the

Discussion

response, together with a longer integration of the signal (the STAs are broader) in the case of anaesthetised records. These two critical components of the anaesthesia effects on RGC' responses are also seen in the response to the chirp stimuli. Firstly, with the chirp AM stimulus (figure 22), the fit to the sinusoidal response showed a shift of phase between the two anaesthetised conditions and the awake (figure 23), that corresponds to the long peak latency measured in the STA. Secondly, the chirp modulated on the frequency shows that anaesthetised cells are not capable of responding to 15Hz frequency (figure 19), matching with a longer signal integration in anaesthetised condition, and thus cannot respond to fast-changing stimuli (also shown as lower frequencies in the Fourier space of the STA of anaesthetised cells, figure 18.L).

With a potentiation of the GABA_AR by anaesthesia, small excitatory signals of the BC may not pass through. More excitatory signals would need to be summed to then excite the downstream RGC, thus causing a long peak latency in the response as it must integrate more signals. It could also account for the broader temporal filter (i.e, preference to lower frequency), as the BC response to a single frame would not suffice to excite the RGC.

In addition to these two observation on the RGCs temporal properties, one feature we saw from the awake retinal output was high baseline response (figure 22 and 23) in comparison to the anaesthetised cells. From the recording, of awake and anaesthetised cells in the dLGN, Durand et al. (2016) show similar results (they report a higher sustainability of awake cells, which in their metric, it corresponds the most to our baseline parameter). One difference though is that they used urethane instead of isoflurane or FMM, which potentiate the GABA_A and glycine receptors while inhibiting the NMDA and AMPA receptors (Hara & Harris 2002). With a potentiation of GABA_AR due to the anaesthesia, the presynaptic inhibition of the bipolar cells is stronger, thus a sustained response from that cell has less chances to occur, therefore leading to the lower baseline we observed.

4.4.3 Visual system temporal sensitivity

From previous studies, the mouse visual system was reported to have a maximal temporal sensitivity of about 10Hz *in vivo* in the dLGN (Grubb & Thompson 2003, 2005), the superior colliculus (Wang et al. 2010) and V1 (Niell & Stryker 2008; Porciatti et al. 1999). This temporal sensitivity resembles what we observed with the anaesthetised retina, and in fact, those studies were also conducted in animals under anaesthesia. Also, the light levels they used were in the range of photopic levels, whereas our DLP projector is in the range of mesopic levels, and higher light levels are correlated with faster visual responses (Fortenbach et al. 2015; Rider et al. 2019) .

Discussion

However, we observe something very different with the awake retina. At least up to the 30Hz stimulus we displayed, RGCs showed robust responses (figure 19 and 20). The high frequency stimulus experiment with the LED dome was conducted only once, however, both cells showed a receptive field (figure 20.A), have an opposite polarity (one ON and one OFF cell) and their responses to other stimuli are similar to previously recorded cells, which tend to show that the two cells are not outliers.

In conclusion, it seems that the temporal sensitivity of the retina and downstream visual areas has been underestimated, due to observation conducted under the influence of anaesthetics. From the comparisons between awake and anaesthetised recordings, I showed that anaesthesia affects signal processing in the retina. Thus, the use of anaesthesia should be avoided when studying physiological brain functions, or the interpretation of an effect should always be paired with a discussion on the impact of anaesthesia on the measure.

4.4.4 Comparison to *ex vivo* recordings

The main highlight of the present work is on the temporal sensitivity of the awake retina, but how does it compare to the *ex vivo* recordings? From cone electroretinogram (ERG), Krishna et al. (2002) showed that the mouse cones amplitude in the ERG diminished with an increase of the stimulus frequency, and had a significant response up to 30Hz. However, the presence of a response to a 30Hz stimulus in the cones was not preserved in the electrophysiological recordings of BCs showing a maximal frequency to 10Hz stimuli (Ichinose et al. 2014), and in RGCs recordings where the response peaked at 10Hz and decreased rapidly to higher temporal frequencies (Wang et al. 2011). Note that the authors reported substantial responsiveness up to ~30Hz. However, the response amplitude at these frequencies for the wild type mouse seems much lower than the one we observed for 30Hz stimuli in the *in vivo* retina (figure 20). Therefore, it tends to show that the *in vivo* retina has a higher temporal sensitivity.

Studying more in depth the different features of the retina *in vivo* could provide new insights on the computations performed by the retina. Also, it gives an ultimate test to assess features that were observed so far using *ex vivo* recordings. Indeed, we know little about the impact of the preparation to obtain such records, which requires the cutting of the optic nerve, the maintenance of the tissue in an artificial media (Ames' medium, (Ames & Nesbett 1981)) and detaches the retinal pigment epithelium that plays numerous roles in the maintenance of the retinal physiology (Strauss 2005). These perturbations of the retina could affect the processing in tangled ways.

Discussion

One of the aims of this project was to classify the RGCs into subtypes, similarly to what has been done previously with *ex vivo* preparations in the mouse using calcium imaging (Baden et al. 2016) or electrophysiology (Jouty et al. 2018). However, the dataset we acquired present several flaws. First, the recorded cells often present a partial response to the set of stimuli (figure 23), which is problematic for a complete classification of the cells. Second, the yield of the technique is tiny in comparison to the records of hundreds of cells that *ex vivo* preparations can achieve (Jouty et al. 2018; Marre et al. 2012). As such, in the awake condition, the dataset contains fewer cells responding to all stimuli than there are RGC subtypes (and even less when considering the duplicated recordings of identical cells). To perform such comparison, the recording technique requires further improvement and optimisations (as detailed in section 4.1.4), that will allow a higher yield and a quicker collection of *in vivo* RGC recordings. As such, with the accumulation of enough experiments, one could achieve response comparison between *ex vivo* and *in vivo* retina at the RGC subtype level. The functional classification *in vivo* is highly desirable (Vlasits et al. 2019), as it would tell us what the real inputs of retino-recipient areas such as the superior colliculus and the lateral geniculate nucleus are.

4.4.5 Full-field receptive fields and LED dome

During early recordings of the *in vivo* retina output, we obtained several cells which exhibited in their STA to the checkerboard stimulus a receptive field spanning on the entirety of our image, on about 70° (annexe 3, cell 4). This phenomenon was highly unusual, as the receptive field of the cells in the retina usually span on several degrees at maximum. To produce such outcome in the STA, the cells need to selectively respond to frames with a bias in the squares' proportions. Since the squares' polarity followed a binomial distribution with equal outcome chances, with a total of 576 samples per frames (18 by 32 squares), we obtain for the stimulus a standard deviation of 8.3% of the light intensity. Given a 60Hz stimulation, long enough brightness deviations occur rarely. However, one explanation for this phenomenon could still be that a cell with receptive field located outside of the screen could see the global light intensity changes from the reflection of the stimulus in the setup, and respond accordingly.

To test whether this was the case or not, we built the LED dome to cover the monocular visual field of the recorded eye (figure 27). Following the analysis of recordings made in the same mouse and at the same location with a chronic implant, we identified a cell present in both records (annexe 3, cell 5), which showed a full-field receptive field with the DLP projector and a conventional confined receptive field using the LED dome. As such, this indicates that the full-field receptive field was an artefact of the stimulation. This effect nonetheless contributes

Discussion

to the demonstration that the *in vivo* retina is very sensitive. This phenomenon was also observed in cells recorded under anaesthesia; however, the effect was less pronounced than in awake cells, as anaesthetised cells have a longer integration time (figure 18).

4.4.6 Retinopetal system

The original question that drove the project was to study the effects of the retinopetal (RP) on the retinal processing. Our group started with two approaches. The first consisted of transfecting the retina with GCaMP, a calcium-sensitive probe, together with an implantation of a cranial window above the superior colliculus, where RGCs send their projections. As such, we could measure the fluorescence in that region, that translates into the measure of RGC activity. This strategy worked, and we could acquire a visual response to our set of stimuli, providing the calcium-transient-triggered average (equivalent to the STA of electrophysiology) presented at figure 26.E.

The second strategy, which is the one described in the present work, performs electrophysiological recordings of the RGC axons. Both techniques have their flaws and advantages, which depends on their practicality to identify effects of the RP system. Indeed, depending on the temporal scale and intensity at which the brain provides feedback to the brain, the calcium imaging may not be able to distinguish a small modulation from noise variations, or the electrophysiology may not have the stability to follow slow fluctuations.

How does an animal's internal state affect the RP system and hence the retinal visual responses? Few studies about the RP system (Frazão et al. 2011; Koves et al. 2016) in mice seem to indicate that histaminergic RP fibres could target the DACs or the ipRGCs, two cell types that seem to interact a lot and implicated in the regulation of the retinal sensitivity, by for example modulating the HCs gap junction network in the OPL. If one of the RP system's role were to regulate the retinal sensitivity to light or other types of computation, targeting these cells in the retina would be a very efficient way of modulating the retinal processing given the previously reported few numbers of RP fibres in mammals.

As a start for the investigation, we recorded the activity of RGCs at day time and night time, to eventually see an effect from the circadian rhythm. Such an outcome would not prove that the RP system was the cause, as other circadian mechanisms exist in the retina independently of the brain, controlling its physiology (Ko 2020). However, we hoped to obtain preliminary data that could later be confirmed with an active stimulation of retinopetal neurons.

Discussion

To identify how we could modulate the RP system actively, a parallel project of our group was to replicate with recent tracing technologies the identification of the RP regions, and their type (histaminergic, serotonergic or something else). Like so, we could insert optogenetic fibres to activate those regions while recording the RGC activity. Also, with the identification of the neurotransmitters released by RP projections, we could block the corresponding system systemically (e.g. with anti-histaminergic drugs). However, we so far could not reproduce the retinopetal tracing experiments in our mouse model.

The existence of a retinopetal system in the mouse is thus challenged by the absence of results in our tracing project. However, a recent study (Schröder et al. 2020) showed that the retinal output was modulated by arousal and could be attributed to the retinopetal system. Using the two techniques we developed, future objectives will therefore to confirm the existence of such modulation, and to assess if the retinal output can be modulated differently by driving the activity of previously reported retinopetal centres, in order to provide direct evidence for the retinopetal system.

Conclusion

5 Conclusion

As the first student of a new research group, my role was to assemble the computational tools necessary for the different stages of the *in vivo* the retina study. As such, I set up the stimulation, spike sorting, data organization, pupil detection and eye tracking to later synchronize and analyze the responses of RGCs within a processing pipeline. Additionally, I designed and built a new stimulation device to meet the challenges posed by the recordings of *in vivo* mouse retinal ganglion cells axons. While establishing this technique, I recorded the RGC responses with and without anaesthesia, and by relying on a precise synchronisation and error correction system, I could show how anaesthesia both increase the stimulus to response peak latency and the signal integration time, abolishing responses to fast stimuli and decreasing its sensitivity. Such impact of the anaesthesia as early as the retina in the visual system suggests that the use of anaesthetic should be avoided when investigating the neurobiology of vision. This work represents a step towards the study of the *in vivo* retinal physiology and of the enigmatic retinopetal system.

Bibliography

6 Bibliography

- Airaksinen MS, Panula P. 1988. The histaminergic system in the guinea pig central nervous system: An immunocytochemical mapping study using an antiserum against histamine. *J. Comp. Neurol.*
- Akimov NP, Marshak DW, Frishman LJ, Glickman RD, Yusupov RG. 2010. Histamine reduces flash sensitivity of ON ganglion cells in the primate retina. *Investig. Ophthalmol. Vis. Sci.*
- Alkire MT, Hudetz AG, Tononi G. 2008. Consciousness and anesthesia
- Ames A, Nesbett FB. 1981. In Vitro Retina as an Experimental Model of the Central Nervous System. *J. Neurochem.*
- Amthor FR, Oyster CW, Takahashi ES. 1984. Morphology of on-off direction-selective ganglion cells in the rabbit retina. *Brain Res.*
- Anderson JR, Jones BW, Watt CB, Shaw M V, Yang JH, et al. 2011. Exploring the retinal connectome. *Mol Vis*
- Andrews DP, Hammond P. 1970. Suprathreshold spectral properties of single optic tract fibres in cat, under mesopic adaptation; cone-rod interaction. *J. Physiol.*
- Antkowiak B. 2001. How do general anaesthetics work?
- Applebury ML, Antoch MP, Baxter LC, Chun LLY, Falk JD, et al. 2000. The murine cone photoreceptor: A single cone type expresses both S and M opsins with retinal spatial patterning. *Neuron*
- Artal P, De Tejada PH, Tedó CM, Green DG. 1998. Retinal image quality in the rodent eye. *Vis. Neurosci.* 15(4):597–605
- Asari H, Meister M. 2012. Divergence of visual channels in the inner retina. *Nat. Neurosci.*
- Asari H, Meister M. 2014. The Projective Field of Retinal Bipolar Cells and Its Modulation by Visual Context. *Neuron*
- Badea TC, Nathans J. 2004. Quantitative analysis of neuronal morphologies in the mouse retina visualized by using a genetically directed reporter. *J. Comp. Neurol.*
- Baden T, Berens P, Bethge M, Euler T. 2013a. Spikes in mammalian bipolar cells support temporal layering of the inner retina. *Curr. Biol.*
- Baden T, Berens P, Franke K, Román Rosón M, Bethge M, Euler T. 2016. The functional diversity of retinal ganglion cells in the mouse. *Nature.* 529(7586):
- Baden T, Schubert T, Chang L, Wei T, Zaichuk M, et al. 2013b. A Tale of Two Retinal Domains: Near-Optimal Sampling of Achromatic Contrasts in Natural Scenes through Asymmetric Photoreceptor Distribution. *Neuron.* 80(5):1206–17
- Bae JA, Mu S, Kim JS, Turner NL, Tartavull I, et al. 2018. Digital Museum of Retinal Ganglion Cells with Dense Anatomy and Physiology. *Cell.* 173(5):1293-1306.e19
- Barlow H. 1953. Summation and inhibition in the frog's retina. *J. Physiol.* 69–88
- Barlow HB, Hill RM. 1963. Selective Sensitivity to Direction of Movement in Ganglion Cells of the Rabbit Retina. *Science* (80-.).

Bibliography

- Barlow HB, Levick WR. 1965. The mechanism of directionally selective units in rabbit's retina. *J. Physiol.*
- Baylor DA. 1987. Photoreceptor signals and vision: Proctor lecture
- Baylor DA, Matthews G, Yau KW. 1980. Two components of electrical dark noise in toad retinal rod outer segments. *J. Physiol.* 309(1):591–621
- Beckwith-Cohen B, Holzhausen LC, Wang T-M, Rajappa R, Kramer RH. 2019. Localizing Proton-Mediated Inhibitory Feedback at the Retinal Horizontal Cell–Cone Synapse with Genetically-Encoded pH Probes. *J. Neurosci.*
- Belenky MA, Smeraski CA, Provencio I, Sollars PJ, Pickard GE. 2003. Melanopsin retinal ganglion cells receive bipolar and amacrine cell synapses. *J. Comp. Neurol.*
- Belgum JH, Dvorak DR, McReynolds JS. 1982. Sustained synaptic input to ganglion cells of mudpuppy retina. *J. Physiol.*
- Berens P, Euler T. 2017. Neuronal Diversity In The Retina. *e-Neuroforum.* 23(2):93–101
- Berry MJ, Brivanlou IH, Jordan TA, Meister M. 1999. Anticipation of moving stimuli by the retina. *Nature*
- Berson DM. 2007. Phototransduction in ganglion-cell photoreceptors
- Berson DM. 2008. Retinal Ganglion Cell Types and Their Central Projections. In *The Senses: A Comprehensive Reference*
- Berson DM, Dunn FA, Takao M. 2002. Phototransduction by retinal ganglion cells that set the circadian clock. *Science* (80-.).
- Bloomfield SA, Miller RF. 1982. A physiological and morphological study of the horizontal cell types of the rabbit retina. *J. Comp. Neurol.*
- Bloomfield SA, Miller RF. 1986. A functional organization on ON and OFF pathways in the rabbit retina. *J. Neurosci.*
- Bons N, Petter A. 1986. Retinal afferents of hypothalamic origin in a prosimian primate: *Microcebus murinus*. Study using retrograde fluorescent tracers. *C. R. Acad. Sci. III.*
- Borghuis BG, Looger LL, Tomita S, Demb JB. 2014. Kainate Receptors Mediate Signaling in Both Transient and Sustained OFF Bipolar Cell Pathways in Mouse Retina. *J. Neurosci.*
- Bormann J. 1988. Electrophysiology of GABAA and GABAB receptor subtypes
- Bowery N. 1989. GABAB receptors and their significance in mammalian pharmacology
- Bowmaker JK, Dartnall HJ. 1980. Visual pigments of rods and cones in a human retina. *J. Physiol.*
- Brandstätter JH, Hartveit E, Sassoè-Pognetto M, Wässle H. 1994. Expression of NMDA and High-affinity Kainate Receptor Subunit mRNAs in the Adult Rat Retina. *Eur. J. Neurosci.*
- Brohan J, Goudra BG. 2017. The Role of GABA Receptor Agonists in Anesthesia and Sedation
- Brosnan RJ. 2011. GABAA receptor antagonism increases NMDA receptor inhibition by isoflurane at a minimum alveolar concentration. *Vet. Anaesth. Analg.*
- Brunken WJ, Daw NW. 1988. The effects of serotonin agonists and antagonists on the response

Bibliography

- properties of complex ganglion cells in the rabbit's retina. *Vis. Neurosci.* 1(02):181–88
- Brunken WJ, Jin XT, Pis-Lopez AM. 1993. Chapter 4 The properties of the serotonergic system in the retina. *Prog. Retin. Res.* 12:75–99
- Buerkle H, Yaksh TL. 1998. Pharmacological evidence for different α_2 -adrenergic receptor sites mediating analgesia and sedation in the rat. *Br. J. Anaesth.*
- Cajal SR. 1893. La retine des vertebres. In *The Vertebrate Retina*
- Carter-Dawson LD, Lavail MM. 1979. Rods and cones in the mouse retina. I. Structural analysis using light and electron microscopy. *J. Comp. Neurol.*
- Cepko C. 2000. Giving in to the blues
- Cervetto L, Piccolino M. 1974. Synaptic transmission between photoreceptors and horizontal cells in the turtle retina. *Science* (80-.).
- Chalk M, Marre O, Tkačik G. 2018. Toward a unified theory of efficient, predictive, and sparse coding. *Proc. Natl. Acad. Sci. U. S. A.*
- Chapot CA, Behrens C, Rogerson LE, Baden T, Pop S, et al. 2017. Local Signals in Mouse Horizontal Cell Dendrites
- Chávez AE, Grimes WN, Diamond JS. 2010. Mechanisms underlying lateral GABAergic feedback onto rod bipolar cells in rat retina. *J. Neurosci.*
- Chen K, Li HZ, Ye N, Zhang J, Wang JJ. 2005. Role of GABAB receptors in GABA and baclofen-induced inhibition of adult rat cerebellar interpositus nucleus neurons in vitro. *Brain Res. Bull.*
- Cleland BG, Dubin MW, Levick WR. 1971. Sustained and transient neurones in the cat's retina and lateral geniculate nucleus. *J. Physiol.*
- Collins JG, Kendig JJ, Mason P. 1995. Anesthetic actions within the spinal cord: contributions to the state of general anesthesia
- Connolly CN, Krishek BJ, McDonald BJ, Smart TG, Moss SJ. 1996. Assembly and cell surface expression of heteromeric and homomeric γ -aminobutyric acid type A receptors. *J. Biol. Chem.*
- Contini M, Lin B, Kobayashi K, Okano H, Masland RH, Raviola E. 2010. Synaptic input of ON-bipolar cells onto the dopaminergic neurons of the mouse retina. *J. Comp. Neurol.*
- Contini M, Raviola E. 2003. GABAergic synapses made by a retinal dopaminergic neuron. *Proc. Natl. Acad. Sci. U. S. A.*
- Coombs J, van der List D, Wang GY, Chalupa LM. 2006. Morphological properties of mouse retinal ganglion cells. *Neuroscience*
- Cossart R, Bernard C, Ben-Ari Y. 2005. Multiple facets of GABAergic neurons and synapses: Multiple fates of GABA signalling in epilepsies
- Crooks J, Kolb H. 1992. Localization of GABA, glycine, glutamate and tyrosine hydroxylase in the human retina. *J. Comp. Neurol.*
- Cuenca N, Haverkamp S, Kolb H. 2000. Choline acetyltransferase is found in terminals of horizontal cells that label with GABA, nitric oxide synthase and calcium binding proteins

Bibliography

- in the turtle retina. *Brain Res.*
- Cueva JG, Haverkamp S, Reimer RJ, Edwards R, Wässle H, Brecha NC. 2002. Vesicular γ -aminobutyric acid transporter expression in amacrine and horizontal cells. *J. Comp. Neurol.*
- Cui P, Li X-Y, Zhao Y, Li Q, Gao F, et al. 2017. Activation of dopamine D1 receptors enhances the temporal summation and excitability of rat retinal ganglion cells. *Neuroscience*
- Curcio CA, Sloan KR, Packer O, Hendrickson AE, Kalina RE. 1987. Distribution of cones in human and monkey retina: Individual variability and radial asymmetry. *Science* (80-.).
- Dacey DM. 1990. The dopaminergic amacrine cell. *J. Comp. Neurol.*
- Dacey DM, Liao HW, Peterson BB, Robinson FR, Smith VC, et al. 2005. Melanopsin-expressing ganglion cells in primate retina signal colour and irradiance and project to the LGN. *Nature*
- Davenport CM, Detwiler PB, Dacey DM. 2008. Effects of pH buffering on horizontal and ganglion cell light responses in primate retina: Evidence for the proton hypothesis of surround formation. *J. Neurosci.*
- de la Cera EG, Rodríguez G, Llorente L, Schaeffel F, Marcos S. 2006. Optical aberrations in the mouse eye. *Vision Res.*
- De Sousa SLM, Dickinson R, Lieb WR, Franks NP. 2000. Contrasting synaptic actions of the inhalational general anesthetics isoflurane and xenon. *Anesthesiology*
- Dearry A, Falardeau P, Shores C, Caron MG. 1991. D2 dopamine receptors in the human retina: Cloning of cDNA and localization of mRNA. *Cell. Mol. Neurobiol.*
- Della Santina L, Kuo SP, Yoshimatsu T, Okawa H, Suzuki SC, et al. 2016. Glutamatergic Monopolar Interneurons Provide a Novel Pathway of Excitation in the Mouse Retina. *Curr. Biol.*
- Deniz S, Wersinger E, Schwab Y, Mura C, Erdelyi F, et al. 2011. Mammalian retinal horizontal cells are unconventional GABAergic neurons. *J. Neurochem.*
- Deny S, Ferrari U, Macé E, Yger P, Caplette R, et al. 2017. Multiplexed computations in retinal ganglion cells of a single type. *Nat. Commun.* 8(1):1964
- Deserno M. 2004. How to generate equidistributed points on the surface of a sphere. *If Polym.* 99
- DeVries SH. 2000. Bipolar cells use kainate and AMPA receptors to filter visual information into separate channels. *Neuron*
- DeVries SH, Baylor DA. 1997. Mosaic arrangement of ganglion cell receptive fields in rabbit retina. *J. Neurophysiol.*
- DeVries SH, Schwartz EA. 1999. Kainate receptors mediate synaptic transmission between cones and “Off” bipolar cells in a mammalian retina. *Nature*
- Diamond JS. 2017. Inhibitory Interneurons in the Retina: Types, Circuitry, and Function. *Annu. Rev. Vis. Sci.*
- Dkhissi-Benyahya O, Coutanson C, Knoblauch K, Lahouaoui H, Leviel V, et al. 2013. The absence of melanopsin alters retinal clock function and dopamine regulation by light. *Cell.*

Bibliography

Mol. Life Sci.

- Dorgau B, Herrling R, Schultz K, Greb H, Segelken J, et al. 2015. Connexin50 couples axon terminals of mouse horizontal cells by homotypic gap junctions. *J. Comp. Neurol.* 523(14):2062–81
- Dowling JE, Boycott BB. 1966. Organization of the primate retina: electron microscopy. *Proc. R. Soc. London. Ser. B. Biol. Sci.*
- Dowling JE, Ripps H. 1973. Effect of magnesium on horizontal cell activity in the skate retina. *Nature*
- Drafts BC, Fisher JL. 2006. Identification of structures within GABAA receptor α subunits that regulate the agonist action of pentobarbital. *J. Pharmacol. Exp. Ther.*
- Drew GM, Gower AJ, Marriott AS. 1977. Pharmacological characterization of α -adrenoceptors which mediate clonidine-induced sedation. *Br. J. Pharmacol.*
- Drinnenberg A, Franke F, Morikawa RK, Jüttner J, Hillier D, et al. 2018. How Diverse Retinal Functions Arise from Feedback at the First Visual Synapse. *Neuron*
- Dumitrescu ON, Pucci FG, Wong KY, Berson DM. 2009. Ectopic retinal ON bipolar cell synapses in the OFF inner plexiform layer: Contacts with dopaminergic amacrine cells and melanopsin ganglion cells. *J. Comp. Neurol.*
- Durand S, Iyer R, Mizuseki K, De Vries S, Mihalas S, Reid RC. 2016. A comparison of visual response properties in the lateral geniculate nucleus and primary visual cortex of awake and anesthetized mice. *J. Neurosci.*
- E Dowling J. 1987. The retina: an approachable part of the brain. *Cambridge Harvard Univ. Press.* 282
- Eggers ED, Lukasiewicz PD. 2006. GABAA, GABAC and glycine receptor-mediated inhibition differentially affects light-evoked signalling from mouse retinal rod bipolar cells. *J. Physiol.*
- Eggers ED, Lukasiewicz PD. 2011. Multiple pathways of inhibition shape bipolar cell responses in the retina
- Eggers ED, McCall MA, Lukasiewicz PD. 2007. Presynaptic inhibition differentially shapes transmission in distinct circuits in the mouse retina. *J. Physiol.*
- Ehinger B, Hansson C, Tornqvist K. 1981. 5-Hydroxytryptamine in the retina of some mammals. *Exp. Eye Res.* 33(6):663–72
- Ellis EM, Gauvain G, Sivyer B, Murphy GJ. 2016. Shared and distinct retinal input to the mouse superior colliculus and dorsal lateral geniculate nucleus. *J. Neurophysiol.* 116(2):602–10
- Enroth-Cugell C, Robson JG. 1966. The contrast sensitivity of retinal ganglion cells of the cat. *J. Physiol.*
- Enz R. 2001. GABAC receptors: A molecular view
- Enz R, Cutting GR. 1998. Molecular composition of GABA(C) receptors. *Vision Res.*
- Euler T. 2019. QDSpy
- Euler T, Haverkamp S, Schubert T, Baden T. 2014. Retinal bipolar cells: Elementary building

Bibliography

blocks of vision

- Euler T, Wässle H. 1998. Different contributions of GABA(A) and GABA(C) receptors to rod and cone bipolar cells in a rat retinal slice preparation. *J. Neurophysiol.*
- Famiglietti E V. 1983. “Starburst” amacrine cells and cholinergic neurons: mirror-symmetric ON and OFF amacrine cells of rabbit retina. *Brain Res.*
- Farrow K, Masland RH. 2011. Physiological clustering of visual channels in the mouse retina. *J. Neurophysiol.*
- Fischler MA, Bolles RC. 1981. Random sample consensus: A Paradigm for Model Fitting with Applications to Image Analysis and Automated Cartography. *Commun. ACM*
- Fisher H. 2013. *Three Main Layers of the Eye.png* - *Wikimedia Commons*. https://commons.wikimedia.org/wiki/File:Three_Main_Layers_of_the_Eye.png
- Flood MD, Moore-Dotson JM, Eggers ED. 2018. Dopamine D1 receptor activation contributes to light-adapted changes in retinal inhibition to rod bipolar cells. *J. Neurophysiol.*
- Fortenbach CR, Kessler C, Peinado Allina G, Burns ME. 2015. Speeding rod recovery improves temporal resolution in the retina. *Vision Res.*
- Franke K, Baden T. 2017. General features of inhibition in the inner retina. *J. Physiol.* 595(16):
- Franke K, Berens P, Schubert T, Bethge M, Euler T, Baden T. 2017. Inhibition decorrelates visual feature representations in the inner retina. *Nature*
- Franke K, Chagas AM, Zhao Z, Zimmermann MJY, Bartel P, et al. 2019. An arbitrary-spectrum spatial visual stimulator for vision research. *Elife*
- Frazão R, McMahon DG, Schunack W, Datta P, Heidelberger R, Marshak DW. 2011. Histamine elevates free intracellular calcium in mouse retinal dopaminergic cells via H1-receptors. *Investig. Ophthalmol. Vis. Sci.*
- Frazão R, Pinato L, da Silva A V., Britto LRG, Oliveira JA, Nogueira MI. 2008. Evidence of reciprocal connections between the dorsal raphe nucleus and the retina in the monkey *Cebus apella*. *Neurosci. Lett.*
- Freedman MS, Lucas RJ, Soni B, Von Schantz M, Muñoz M, et al. 1999. Regulation of mammalian circadian behavior by non-rod, non-cone, ocular photoreceptors. *Science* (80- .).
- Freeman DK, Heine WF, Passaglia CL. 2010. Single-unit in vivo recordings from the optic chiasm of rat. *J. Vis. Exp.*
- Galambos R, Szabó-Salfay O, Szatmári E, Szilágyi N, Juhász G. 2001. Sleep modifies retinal ganglion cell responses in the normal rat. *Proc. Natl. Acad. Sci. U. S. A.*
- Garcia P, Kolesky S, Jenkins A. 2010. General Anesthetic Actions on GABAA Receptors. *Curr. Neuropharmacol.*
- Gastinger M, Tian N, Horvath T, Marshak D. 2006a. Retinopetal axons in mammals: Emphasis on histamine and serotonin. *Curr. Eye Res.*
- Gastinger MJ, Barber AJ, Vardi N, Marshak DW. 2006b. Histamine receptors in mammalian retinas. *J. Comp. Neurol.* 495(6):658–67

Bibliography

- Gastinger MJ, O'Brien JJ, Larsen JNB, Marshak DW. 1999. Histamine immunoreactive axons in the macaque retina. *Investig. Ophthalmol. Vis. Sci.*
- Gastinger MJ, Yusupov RG, Glickman RD, Marshak DW. 2004. The effects of histamine on rat and monkey retinal ganglion cells. *Vis. Neurosci.* 21(6):935–43
- Geng Y, Schery LA, Sharma R, Dubra A, Ahmad K, et al. 2011. Optical properties of the mouse eye. *Biomed. Opt. Express*
- Ghosh KK, Bujan S, Haverkamp S, Feigenspan A, Wässle H. 2004. Types of bipolar cells in the mouse retina. *J Comp Neurol*
- Gilbertson TA, Scobey R, Wilson M. 1991. Permeation of calcium ions through non-NMDA glutamate channels in retinal bipolar cells. *Science* (80-.).
- Glickstein M, Millodot M. 1970. Retinoscopy and eye size. *Science* (80-.). 168(3931):605–6
- González Á. 2010. Measurement of Areas on a Sphere Using Fibonacci and Latitude-Longitude Lattices. *Math. Geosci.*
- Gooley JJ, Lu J, Chou TC, Scammell TE, Saper CB. 2001. Melanopsin in cells of origin of the retinohypothalamic tract. *Nat. Neurosci.*
- Graham DM, Wong KY. 2016. *Webvision – Melanopsin-expressing, Intrinsically Photosensitive Retinal Ganglion Cells (ipRGCs)*. <https://webvision.med.utah.edu/book/part-ii-anatomy-and-physiology-of-the-retina/melanopsin-expressing-intrinsically-photosensitive-retinal-ganglion-cells/>
- Graham DM, Wong KY, Shapiro P, Frederick C, Pattabiraman K, Berson DM. 2008. Melanopsin ganglion cells use a membrane-associated rhabdomeric phototransduction cascade. *J. Neurophysiol.*
- Greferath U, Grünert U, Müller F, Wässle H. 1994. Localization of GABAA receptors in the rabbit retina. *Cell Tissue Res.*
- Greferath U, Kambourakis M, Barth C, Fletcher EL, Murphy M. 2009. Characterization of histamine projections and their potential cellular targets in the mouse retina. *Neuroscience.* 158(2):932–44
- Grimes WN, Zhang J, Graydon CW, Kachar B, Diamond JS. 2010. Retinal Parallel Processors: More than 100 Independent Microcircuits Operate within a Single Interneuron. *Neuron*
- Grubb MS, Thompson ID. 2003. Quantitative Characterization of Visual Response Properties in the Mouse Dorsal Lateral Geniculate Nucleus. *J. Neurophysiol.*
- Grubb MS, Thompson ID. 2005. Visual response properties of burst and tonic firing in the mouse dorsal lateral geniculate nucleus. *J. Neurophysiol.*
- Grünert U. 2000. Distribution of GABA and glycine receptors on bipolar and ganglion cells in the mammalian retina. *Microsc. Res. Tech.*
- Grünert U, Haverkamp S, Fletcher EL, Wässle H. 2002. Synaptic distribution of ionotropic glutamate receptors in the inner plexiform layer of the primate retina. *J. Comp. Neurol.*
- Hampson ECGM, Vaney DI, Weiler R. 1992. Dopaminergic modulation of gap junction permeability between amacrine cells in mammalian retina. *J. Neurosci.*
- Hannibal J, Hindersson P, Knudsen SM, Georg B, Fahrenkrug J. 2002. The photopigment

Bibliography

- melanopsin is exclusively present in pituitary adenylate cyclase-activating polypeptide-containing retinal ganglion cells of the retinohypothalamic tract. *J. Neurosci.*
- Hara K, Harris RA. 2002. The anesthetic mechanism of urethane: The effects on neurotransmitter-gated ion channels. *Anesth. Analg.*
- Hargrave PA, McDowell JH. 1992. Rhodopsin and phototransduction: A model system for G protein-linked receptors
- Hartl D, Krebs AR, Jüttner J, Roska B, Schübeler D. 2017. Cis-regulatory landscapes of four cell types of the retina. *Nucleic Acids Res.* 45(20):11607–21
- Hartline HK. 1938. THE RESPONSE OF SINGLE OPTIC NERVE FIBERS OF THE VERTEBRATE EYE TO ILLUMINATION OF THE RETINA. *Am. J. Physiol. Content*
- Hattar S, Kumar M, Park A, Tong P, Tung J, et al. 2006. Central projections of melanopsin-expressing retinal ganglion cells in the mouse. *J. Comp. Neurol.*
- Hattar S, Liao HW, Takao M, Berson DM, Yau KW. 2002. Melanopsin-containing retinal ganglion cells: Architecture, projections, and intrinsic photosensitivity. *Science* (80-.).
- He K, Gkioxari G, Dollar P, Girshick R. 2017. Mask R-CNN. *Proc. IEEE Int. Conf. Comput. Vis.*
- He S, Weiler R, Vaney DI. 2000. Endogenous dopaminergic regulation of horizontal cell coupling in the mammalian retina. *J. Comp. Neurol.*
- Hecht S, Shlaer S, Pirenne MH. 1942. ENERGY, QUANTA, AND VISION. *J. Gen. Physiol.* 25(6):819–40
- Helmstaedter M, Briggman KL, Turaga SC, Jain V, Seung HS, Denk W. 2013. Connectomic reconstruction of the inner plexiform layer in the mouse retina. *Nature.* 500(7461):
- Hirano AA, Liu X, Brecha NC, Barnes S. 2018. Analysis of Feedback Signaling from Horizontal Cells to Photoreceptors in Mice. In *Methods in Molecular Biology (Clifton, N.J.)*, Vol. 1753, pp. 179–89
- Hirasawa H, Betensky RA, Raviola E. 2012. Corelease of Dopamine and GABA by a Retinal Dopaminergic Neuron. *J. Neurosci.*
- Hirasawa H, Contini M, Raviola E. 2015. Extrasynaptic release of GABA and dopamine by retinal dopaminergic neurons. *Philos. Trans. R. Soc. B Biol. Sci.*
- Hirasawa H, Puopolo M, Raviola E. 2009. Extrasynaptic release of GABA by retinal dopaminergic neurons. *J. Neurophysiol.*
- Hombach S, Janssen-Bienhold U, Sohl G, Schubert T, Bussow H, et al. 2004. Functional expression of connexin57 in horizontal cells of the mouse retina. *Eur J Neurosci*
- Hong G, Fu T-M, Qiao M, Viveros RD, Yang X, et al. 2018a. A method for single-neuron chronic recording from the retina in awake mice. *Science.* 360(6396):1447–51
- Hong G, Yang X, Zhou T, Lieber CM. 2018b. Mesh electronics: a new paradigm for tissue-like brain probes
- Horio K, Ohkuma M, Miyachi E ichi. 2018. The Effect of Histamine on Inward and Outward Currents in Mouse Retinal Amacrine Cells. *Cell. Mol. Neurobiol.* 38(3):757–67

Bibliography

- Hoshi H, Liu W-L, Massey SC, Mills SL. 2009. ON Inputs to the OFF Layer: Bipolar Cells That Break the Stratification Rules of the Retina. *J. Neurosci.*
- Huang JZ, Zeng H. 2013. Genetic Approaches to Neural Circuits in the Mouse. *Annu. Rev. Neurosci.*
- Hubel DH. 1960. Single unit activity in lateral geniculate body and optic tract of unrestrained cats. *J. Physiol.*
- Hubel DH, Wiesel TN. 1960. Receptive fields of optic nerve fibres in the spider monkey. *J. Physiol.*
- Huberman AD, Niell CM. 2011. What can mice tell us about how vision works? *Trends Neurosci.* 34(9):464–73
- Ichinose T, Fyk-Kolodziej B, Cohn J. 2014. Roles of ON Cone Bipolar Cell Subtypes in Temporal Coding in the Mouse Retina. *J. Neurosci.*
- Ikeda H, Priest TD, Robbins J, Wakakuwa K. 1986. Silent dopaminergic synapse at feline retinal ganglion cells? *Clin. Vis. Sci.*
- Insafutdinov E, Pishchulin L, Andres B, Andriluka M, Schiele B. 2016. Deepercut: A deeper, stronger, and faster multi-person pose estimation model. *Lect. Notes Comput. Sci. (Including Subser. Lect. Notes Artif. Intell. Lect. Notes Bioinformatics)*
- Izquierdo I, McGaugh JL. 2000. Behavioural pharmacology and its contribution to the molecular basis of memory consolidation
- Jackman SL, Babai N, Chambers JJ, Thoreson WB, Kramer RH. 2011. A Positive Feedback Synapse from Retinal Horizontal Cells to Cone Photoreceptors. *PLoS Biol.* 9(5):e1001057
- Jackson CR, Ruan G-X, Aseem F, Abey J, Gamble K, et al. 2012. Retinal Dopamine Mediates Multiple Dimensions of Light-Adapted Vision. *J. Neurosci.*
- Jacobs GH, Williams GA. 2007. Contributions of the mouse UV photopigment to the ERG and to vision. *Doc. Ophthalmol.*
- Jacoby J, Zhu Y, DeVries SH, Schwartz GW. 2015. An Amacrine Cell Circuit for Signaling Steady Illumination in the Retina. *Cell Rep.*
- James B, Darnet L, Moya-Díaz J, Seibel S-H, Lagnado L. 2019. An amplitude code transmits information at a visual synapse. *Nat. Neurosci.*
- Janssen-Bienhold U, Trümpler J, Hilgen G, Schultz K, De Sevilla Muller LP, et al. 2009. Connexin57 is expressed in dendro-dendritic and axo-axonal gap junctions of mouse horizontal cells and its distribution is modulated by light. *J. Comp. Neurol.*
- Jed P, Feng D, Buice M. 2018. *AllenSDK Eye Tracking documentation*. https://alleninstitute.github.io/allensdk.eye_tracking/index.html
- Jenkins A, Greenblatt EP, Faulkner HJ, Bertaccini E, Light A, et al. 2001. Evidence for a common binding cavity for three general anesthetics within the GABAA receptor. *J. Neurosci.*
- Jensen RJ, Daw NW. 1984. Effects of dopamine antagonists on receptive fields of brisk cells and directionally selective cells in the rabbit retina. *J. Neurosci.*
- Jeon CJ, Strettoi E, Masland RH. 1998. The major cell populations of the mouse retina. *J.*

Bibliography

Neurosci.

- Jin XT, Brunken WJ. 1998. Serotonin receptors modulate rod signals: A neuropharmacological comparison of light- and dark-adapted retinas. *Vis. Neurosci.*
- John Mihic S, Ye Q, Wick MJ, Koltchine V V., Krasowski MD, et al. 1997. Sites of alcohol and volatile anaesthetic action on GABA(A) and glycine receptors. *Nature*
- Johnston J, Lagnado L. 2015. General features of the retinal connectome determine the computation of motion anticipation. *Elife*
- Jones M V., Brooks PA, Harrison NL. 1992. Enhancement of gamma-aminobutyric acid-activated Cl⁻ currents in cultured rat hippocampal neurones by three volatile anaesthetics. *J. Physiol.*
- Jones M V., Hornberger LA, Harrison NL. 1991. Clinical concentrations of three volatile anesthetics prolong gaba-mediated inhibitory postsynaptic currents at synapses between cultured rat hippocampal neurons. *Anesthesiology*
- Jouty J, Hilgen G, Sernagor E, Hennig MH. 2018. Non-parametric Physiological Classification of Retinal Ganglion Cells in the Mouse Retina. *Front. Cell. Neurosci.*
- Jun JJ, Steinmetz NA, Siegle JH, Denman DJ, Bauza M, et al. 2017. Fully integrated silicon probes for high-density recording of neural activity. *Nature*
- Kaneko A. 1971. Electrical connexions between horizontal cells in the dogfish retina. *J. Physiol.*
- Kaneko A, Shimazaki H. 1975. Effects of external ions on the synaptic transmission from photoreceptors to horizontal cells in the carp retina. *J. Physiol.*
- Kaufmann WA, Humpel C, Alheid GF, Marksteiner J. 2003. Compartmentation of alpha 1 and alpha 2 GABAA receptor subunits within rat extended amygdala: Implications for benzodiazepine action. *Brain Res.*
- Keeler CE. 1927. IRIS MOVEMENTS IN BLIND MICE. *Am. J. Physiol. Content*
- Keir PJ, Rempel DM. 2005. Pathomechanics of peripheral nerve loading: Evidence in carpal tunnel syndrome. *J. Hand Ther.*
- Kelly MD, Smith A, Banks G, Wingrove P, Whiting PW, et al. 2002. Role of the histidine residue at position 105 in the human $\alpha 5$ containing GABA_A receptor on the affinity and efficacy of benzodiazepine site ligands. *Br. J. Pharmacol.*
- Kemmler R, Schultz K, Dedek K, Euler T, Schubert T. 2014. Differential regulation of cone calcium signals by different horizontal cell feedback mechanisms in the mouse retina. *J. Neurosci.*
- Kim JS, Greene MJ, Zlateski A, Lee K, Richardson M, et al. 2014. Space-time wiring specificity supports direction selectivity in the retina. *Nature*
- Klaassen LJ, Sun Z, Steijaert MN, Bolte P, Fahrenfort I, et al. 2011. Synaptic transmission from horizontal cells to cones is impaired by loss of connexin hemichannels. *PLoS Biol.*
- Ko GYP. 2020. Circadian regulation in the retina: From molecules to network
- Koike C, Numata T, Ueda H, Mori Y, Furukawa T. 2010a. TRPM1: A vertebrate TRP channel responsible for retinal ON bipolar function

Bibliography

- Koike C, Obara T, Uriu Y, Numata T, Sanuki R, et al. 2010b. TRPM1 is a component of the retinal ON bipolar cell transduction channel in the mGluR6 cascade. *Proc. Natl. Acad. Sci. U. S. A.*
- Kolb H. 1970. Organization of the outer plexiform layer of the primate retina: electron microscopy of Golgi-impregnated cells. *Philos. Trans. R. Soc. Lond. B. Biol. Sci.*
- Kolb H. 1974. The connections between horizontal cells and photoreceptors in the retina of the cat: Electron microscopy of Golgi preparations. *J. Comp. Neurol.*
- Kolb H. 2011a. *Webvision - Circuitry for Rod Signals Through The Retina*. <https://webvision.med.utah.edu/book/part-iii-retinal-circuits/circuitry-for-rod-cells-through-the-retina/>
- Kolb H. 2011b. *Webvision – Neurotransmitters in the Retina*. <https://webvision.med.utah.edu/book/part-iv-neurotransmitters-in-the-retina-2/part-iv-neurotransmitters-in-the-retina/>
- Kolb H, Baehr W. 2013. *Webvision: Phototransduction in Rods and Cones*. <https://www.ncbi.nlm.nih.gov/books/NBK52768/>
- Kolb H, Cuenca N, Wang HH, Dekorver L. 1990. The synaptic organization of the dopaminergic amacrine cell in the cat retina. *J. Neurocytol.*
- Kolb H, Linberg KA, Fisher SK. 1992. Neurons of the human retina: A Golgi study. *J. Comp. Neurol.*
- Kolb H, Nelson R, Mariani A. 1981. Amacrine cells, bipolar cells and ganglion cells of the cat retina: A Golgi study. *Vision Res.*
- Kong JH, Fish DR, Rockhill RL, Masland RH. 2005. Diversity of ganglion cells in the mouse retina: Unsupervised morphological classification and its limits. *J. Comp. Neurol.*
- Koves K, Csaki A, Vereczki V. 2016. Recent Research on the Centrifugal Visual System in Mammalian Species. *Anat. Physiol.* 06(03):
- Krasowski MD, Harrison NL. 2000. The actions of ether, alcohol and alkane general anaesthetics on GABA(A) and glycine receptors and the effects of TM2 and TM3 mutations. *Br. J. Pharmacol.*
- Krishna VR, Alexander KR, Peachey NS. 2002. Temporal properties of the mouse cone electroretinogram. *J. Neurophysiol.*
- Kuffler S. 1953. Discharge patterns and functional organization of mammalian retina. *J. Neurophysiol.*
- Labandeira-Garcia JL, Guerra-Seijas MJ, Gonzalez F, Perez R, Acuña C. 1990. Location of neurons projecting to the retina in mammals. *Neurosci. Res.*
- Lamb TD. 1976. Spatial properties of horizontal cell responses in the turtle retina. *J. Physiol.*
- Lasansky A. 1981. Synaptic action mediating cone responses to annular illumination in the retina of the larval tiger salamander. *J. Physiol.*
- Lauritzen JS, Anderson JR, Jones BW, Watt CB, Mohammed S, et al. 2013. ON cone bipolar cell axonal synapses in the OFF inner plexiform layer of the rabbit retina. *J. Comp. Neurol.*
- Lawrence PM, Studholme KM. 2014. Retinofugal projections in the mouse. *J. Comp. Neurol.*

Bibliography

- Lazzerini Ospri L, Prusky G, Hattar S. 2017. Mood, the Circadian System, and Melanopsin Retinal Ganglion Cells. *Annu. Rev. Neurosci.*
- Lee S, Chen L, Chen M, Ye M, Seal RP, Zhou J. 2014. An unconventional glutamatergic circuit in the retina formed by vGluT3 amacrine cells. *Neuron*
- Lefebvre B, Yger P, Marre O. 2016. Recent progress in multi-electrode spike sorting methods
- Lenzi S, Steinmetz N. *Manual Clustering Practical Guide - phy*.
https://phy.readthedocs.io/en/latest/sorting_user_guide/
- Lettvin JY, Maturana HR, Maturana HR, McCulloch WS, Pitts WH. 1959. What the Frog's Eye Tells the Frog's Brain. *Proc. IRE.* 47(11):1940–51
- Li JY, Schmidt TM. 2018. Divergent projection patterns of M1 ipRGC subtypes. *J. Comp. Neurol.*
- Li W, Zhang J, Massey SC. 2002. Coupling pattern of S1 and S2 amacrine cells in the rabbit retina. *Vis. Neurosci.* 19(2):119–31
- Lima L, Urbina M. 1998. Serotonergic projections to the retina of rat and goldfish. *Neurochem. Int.* 32(2):133–41
- Lin B, Masland RH. 2006. Populations of wide-field amacrine cells in the mouse retina. *J Comp Neurol*
- Lin LH, Chen LL, Zirrolli JA, Harris RA. 1992. General anesthetics potentiate γ -aminobutyric acid actions on γ -aminobutyric acid(A) receptors expressed by *Xenopus* oocytes: Lack of involvement of intracellular calcium. *J. Pharmacol. Exp. Ther.*
- Lin TY, Maire M, Belongie S, Hays J, Perona P, et al. 2014. Microsoft COCO: Common objects in context. *Lect. Notes Comput. Sci. (Including Subser. Lect. Notes Artif. Intell. Lect. Notes Bioinformatics)*
- Liu L-L, Spix NJ, Zhang D-Q. 2017. NMDA Receptors Contribute to Retrograde Synaptic Transmission from Ganglion Cell Photoreceptors to Dopaminergic Amacrine Cells. *Front. Cell. Neurosci.*
- Liu X, Grove JCR, Hirano AA, Brecha NC, Barnes S. 2016. Dopamine D1 receptor modulation of calcium channel currents in horizontal cells of mouse retina. *J. Neurophysiol.* 116(2):686–97
- Lörincz ML, Oláh M, Juhász G. 2008. Functional Consequences of Retinopetal Fibers Originating in the Dorsal Raphe Nucleus. *Int. J. Neurosci.* 118(10):1374–83
- Low K, Crestani F, Keist R, Benke D, Brunig I, et al. 2000. Molecular and neuronal substrate for the selective attenuation of anxiety. *Science* (80-.).
- Lucas RJ, Freedman MS, Muñoz M, Garcia-Fernández JM, Foster RG. 1999. Regulation of the mammalian pineal by non-rod, non-cone, ocular photoreceptors. *Science* (80-.).
- Lucas RJ, Hattar S, Takao M, Berson DM, Foster RG, Yau KW. 2003. Diminished pupillary light reflex at high irradiances in melanopsin-knockout mice. *Science* (80-.).
- Lyubarsky AL, Daniele LL, Pugh EN. 2004. From candelas to photoisomerizations in the mouse eye by rhodopsin bleaching in situ and the light-rearing dependence of the major components of the mouse ERG. *Vision Res.*

Bibliography

- MacIver MB, Tanelian DL, Mody I. 1991. Two Mechanisms for Anesthetic-Induced Enhancement of GABAA-Mediated Neuronal Inhibition. *Ann. N. Y. Acad. Sci.*
- MacNeil M a, Masland RH. 1998. Extreme diversity among amacrine cells: implications for function. *Neuron*
- Mangel SC. 1991. Analysis of the horizontal cell contribution to the receptive field surround of ganglion cells in the rabbit retina. *J. Physiol.*
- Mariani AP. 1990. Amacrine cells of the rhesus monkey retina. *J. Comp. Neurol.*
- Marre O, Amodei D, Deshmukh N, Sadeghi K, Soo F, et al. 2012. Mapping a complete neural population in the retina. *J. Neurosci.*
- Marrocco RT. 1972. Responses of monkey optic tract fibers to monochromatic lights. *Vision Res.*
- Marsden CD. 1977. GABA in Nervous System Function. *J. Neurol. Neurosurg. Psychiatry*
- Martemyanov KA, Sampath AP. 2017. The Transduction Cascade in Retinal ON-Bipolar Cells: Signal Processing and Disease. *Annu. Rev. Vis. Sci.*
- Martersteck EM, Hirokawa KE, Evarts M, Bernard A, Duan X, et al. 2017. Diverse Central Projection Patterns of Retinal Ganglion Cells. *Cell Rep.* 18(8):
- Mataruga A, Kremmer E, Müller F. 2007. Type 3a and type 3b off cone bipolar cells provide for the alternative rod pathway in the mouse retina. *J. Comp. Neurol.*
- Mathis A, Mamidanna P, Cury KM, Abe T, Murthy VN, et al. 2018. DeepLabCut: markerless pose estimation of user-defined body parts with deep learning. *Nat. Neurosci.*
- Maturana HR, Frenk S. 1963. Directional movement and horizontal edge detectors in the pigeon retina. *Science* (80-.).
- Maturana HR, Frenk S. 1965. Synaptic connections of the centrifugal fibers in the pigeon retina. *Science* (80-.).
- Mazade R, Jin J, Pons C, Alonso J, Mazade R, et al. 2019. Functional Specialization of ON and OFF Cortical Pathways for Global-Slow and Local-Fast Vision Article Functional Specialization of ON and OFF Cortical Pathways. *CellReports.* 27(10):2881-2894.e5
- McKernan RM, Rosahl TW, Reynolds DS, Sur C, Wafford KA, et al. 2000. Sedative but not anxiolytic properties of benzodiazepines are mediated by the GABA(A) receptor $\alpha 1$ subtype. *Nat. Neurosci.*
- McMahon DG, Knapp AG, Dowling JE. 1989. Horizontal cell gap junctions: Single-channel conductance and modulation by dopamine. *Proc. Natl. Acad. Sci. U. S. A.*
- Meister M, Pine J, Baylor DA. 1994. Multi-neuronal signals from the retina: acquisition and analysis. *J. Neurosci. Methods*
- Michael C. 1968. Receptive Fields of Single With Optic Nerve Fibers in a Mammal with an all cone retina. II : Directionally selective units. *J. Neurophysiol.*
- Mody I, Tanelian DL, Bruce MacIver M. 1991. Halothane enhances tonic neuronal inhibition of elevating intracellular calcium. *Brain Res.*
- Morgans CW, Brown RL, Duvoisin RM. 2010. TRPM1: The endpoint of the mGluR6 signal

Bibliography

transduction cascade in retinal ON-bipolar cells

Morin LP. 2013. Neuroanatomy of the extended circadian rhythm system

MouseVision. 2015. *Mouse vision - VISTA LAB WIKI*.
https://web.stanford.edu/group/vista/cgi-bin/wiki/index.php/Mouse_vision

Münch TA, Da Silveira RA, Siebert S, Viney TJ, Awatramani GB, Roska B. 2009. Approach sensitivity in the retina processed by a multifunctional neural circuit. *Nat. Neurosci.*

Naka KI, Rushton WAH. 1967. The generation and spread of S-potentials in fish (Cyprinidae). *J. Physiol.*

Nakahiro M, Yeh JZ, Brunner E, Narahashi T. 1989. General anesthetics modulate GABA receptor channel complex in rat dorsal root ganglion neurons. *FASEB J.*

Nakajima Y, Iwakabe H, Akazawa C, Nawa H, Shigemoto R, et al. 1993. Molecular characterization of a novel retinal metabotropic glutamate receptor mGluR6 with a high agonist selectivity for L-2-amino-4-phosphonobutyrate. *J. Biol. Chem.*

Nawy S, Copenhagen DR. 1987. Multiple classes of glutamate receptor on depolarizing bipolar cells in retina. *Nature*

Needleman SB, Wunsch CD. 1970. A general method applicable to the search for similarities in the amino acid sequence of two proteins. *J. Mol. Biol.*

Nelson R, Famiglietti E V., Kolb H. 1978. Intracellular staining reveals different levels of stratification for on- and off-center ganglion cells in cat retina. *J. Neurophysiol.*

Nelson R, von Litzow A, Kolb H, Gouras P. 1975. Horizontal cells in cat retina with independent dendritic systems. *Science* (80-.).

Niell CM, Stryker MP. 2008. Highly selective receptive fields in mouse visual cortex. *J. Neurosci.*

Nikonov SS, Kholodenko R, Lem J, Pugh EN. 2006. Physiological features of the S- and M-cone photoreceptors of wild-type mice from single-cell recordings. *J. Gen. Physiol.*

Nilsson A, Persson MP, Hartvig P. 1988. Effects of the benzodiazepine antagonist flumazenil on postoperative performance following total intravenous anaesthesia with midazolam and alfentanil. *Acta Anaesthesiol. Scand.*

Nobles RD, Zhang C, Muller U, Betz H, McCall MA. 2012. Selective Glycine Receptor 2 Subunit Control of Crossover Inhibition between the On and Off Retinal Pathways. *J. Neurosci.*

Nomura A, Shigemoto R, Nakamura Y, Okamoto N, Mizuno N, Nakanishi S. 1994. Developmentally regulated postsynaptic localization of a metabotropic glutamate receptor in rat rod bipolar cells. *Cell*

O'Brien JJ, Li W, Pan F, Keung J, O'Brien J, Massey SC. 2006. Coupling between A-Type horizontal cells is mediated by connexin 50 gap junctions in the rabbit retina. *J. Neurosci.*

O'Bryan PM. 1973. Properties of the depolarizing synaptic potential evoked by peripheral illumination in cones of the turtle retina. *J. Physiol.*

Olkola KT, Ahonen J. 2008. Midazolam and Other Benzodiazepines. In *Modern Anesthetics*

Bibliography

- Olsen RW, Li GD. 2011. GABA A receptors as molecular targets of general anesthetics: Identification of binding sites provides clues to allosteric modulation
- Osborne NN, Beaton DW. 1986. Direct histochemical localisation of 5,7-dihydroxytryptamine and the uptake of serotonin by a subpopulation of GABA neurones in the rabbit retina. *Brain Res.* 382(1):158–62
- Osterberg. 1937. Topography of the Layer of Rods and Cones in the Human Retina. *J. Am. Med. Assoc.*
- Palmer SE, Marre O, Berry MJ, Bialek W. 2015. Predictive information in a sensory population. *Proc. Natl. Acad. Sci. U. S. A.*
- Park SJH, Pottackal J, Ke J-B, Jun NY, Rahmani P, et al. 2018. Convergence and Divergence of CRH Amacrine Cells in Mouse Retinal Circuitry. *J. Neurosci.*
- Peichl L, Wässle H. 1981. Morphological identification of on- and off-centre brisk transient (Y) cells in the cat retina. *Proc. R. Soc. London - Biol. Sci.*
- Peichl L, Wässle H. 1983. The structural correlate of the receptive field centre of alpha ganglion cells in the cat retina. *J. Physiol.*
- Peirson SN, Brown LA, Potheary CA, Benson LA, Fisk AS. 2018. Light and the laboratory mouse. *J. Neurosci. Methods*
- Pérez-Fernández V, Milosavljevic N, Allen AE, Vessey KA, Jobling AI, et al. 2019. Rod Photoreceptor Activation Alone Defines the Release of Dopamine in the Retina. *Curr. Biol.*
- Perez-Leon JA, Warren EJ, Allen CN, Robinson DW, Lane Brown R. 2006. Synaptic inputs to retinal ganglion cells that set the circadian clock. *Eur. J. Neurosci.*
- Pérez-León JA, Sarabia G, Miledi R, García-Alcocer G. 2004. Distribution of 5-hydroxytryptamine_{2C} receptor mRNA in rat retina. *Mol. Brain Res.* 125(1–2):140–42
- Pflug R, Nelson R, Huber S, Reitsamer H. 2008. Modulation of horizontal cell function by dopaminergic ligands in mammalian retina. *Vision Res.*
- Pisano F, Zampaglione E, McAlinden N, Roebber J, Dawson MD, et al. 2017. Large scale matching of function to the genetic identity of retinal ganglion cells. *Sci. Rep.*
- Pootanakit K, Brunken WJ. 2000. 5-HT_{1A} and 5-HT₇ receptor expression in the mammalian retina. *Brain Res.*
- Pootanakit K, Brunken WJ. 2001. Identification of 5-HT_{3A} and 5-HT_{3B} receptor subunits in mammalian retinae: Potential pre-synaptic modulators of photoreceptors. *Brain Res.*
- Pootanakit K, Prior KJ, Hunter DD, Brunken WJ. 1999. 5-HT_{2a} receptors in the rabbit retina: Potential presynaptic modulators. *Vis. Neurosci.* 16(2):221–30
- Popova E. 2014. Ionotropic GABA Receptors and Distal Retinal ON and OFF Responses. *Scientifica (Cairo).*
- Porciatti V, Pizzorusso T, Maffei L. 1999. The visual physiology of the wild type mouse determined with pattern VEPs. *Vision Res.*
- Provencio I, Jiang G, De Grip WJ, Pär Hayes W, Rollag MD. 1998. Melanopsin: An opsin in melanophores, brain, and eye. *Proc. Natl. Acad. Sci. U. S. A.*

Bibliography

- Provencio I, Rodriguez IR, Jiang G, Hayes WP, Moreira EF, Rollag MD. 2000. A Novel Human Opsin in the Inner Retina. *J. Neurosci.* 20(2):600–605
- Provencio I, Rollag MD, Castrucci AM. 2002. Photoreceptive net in the mammalian retina. This mesh of cells may explain how some blind mice can still tell day from night. *Nature*
- Prusky GT, Douglas RM. 2004. Characterization of mouse cortical spatial vision. *Vision Res.* 44(28 SPEC.ISS.):3411–18
- Prusky GT, West PWR, Douglas RM. 2000. Behavioral assessment of visual acuity in mice and rats. *Vision Res.* 40(16):2201–9
- Puller C, Haverkamp S, Neitz M, Neitz J. 2014. Synaptic elements for GABAergic feed-forward signaling between HII horizontal cells and blue cone bipolar cells are enriched beneath primate S-cones. *PLoS One*
- Qiao SN, Zhang Z, Ribelayga CP, Zhong YM, Zhang DQ. 2016. Multiple cone pathways are involved in photic regulation of retinal dopamine. *Sci. Rep.*
- Repérant J, Araneda S, Miceli D, Medina M, Rio JP. 2000. Serotonergic retinopetal projections from the dorsal raphe nucleus in the mouse demonstrated by combined [3H] 5-HT retrograde tracing and immunolabeling of endogenous 5-HT. *Brain Res.* 878(1–2):213–17
- Repérant J, Médina M, Ward R, Miceli D, Kenigfest NB, et al. 2007. The evolution of the centrifugal visual system of vertebrates. A cladistic analysis and new hypotheses
- Repérant J, Ward R, Miceli D, Rio JP, Médina M, et al. 2006. The centrifugal visual system of vertebrates: A comparative analysis of its functional anatomical organization. *Brain Res. Rev.* 52(1):1–57
- Rider AT, Bruce Henning G, Stockman A. 2019. Light adaptation controls visual sensitivity by adjusting the speed and gain of the response to light. *PLoS One*
- Ridley JN. 1982. Packing efficiency in sunflower heads. *Math. Biosci.*
- Robles E, Laurell E, Baier H. 2014. The retinal projectome reveals brain-area-specific visual representations generated by ganglion cell diversity. *Curr. Biol.*
- Rodieck RW. 1965. Quantitative analysis of cat retinal ganglion cell response to visual stimuli. *Vision Res.*
- Rodieck RW. 1999. The first steps in seeing. *Arch. Ophthalmol.*
- Roska B, Meister M. 2014. *The Retina Dissects the Visual Scene into Distinct Features*. Cambridge, MA: MIT Press
- Rossant C, Buccino A, Economo M, Gestes C, Goodman D, et al. 2020. phy: interactive visualization and manual spike sorting of large-scale ephys data. <https://phy.readthedocs.io/en/latest/>
- Royer S, Zemelman B V., Barbic M, Losonczy A, Buzsáki G, Magee JC. 2010. Multi-array silicon probes with integrated optical fibers: Light-assisted perturbation and recording of local neural circuits in the behaving animal. *Eur. J. Neurosci.*
- Rudolph U, Crestani F, Benke D, Brünig I, Benson JA, et al. 1999. Benzodiazepine actions mediated by specific γ -aminobutyric acid(A) receptor subtypes. *Nature*
- Rupp AC, Ren M, Altimus CM, Fernandez DC, Richardson M, et al. 2019. Distinct ipRGC

Bibliography

- subpopulations mediate light's acute and circadian effects on body temperature and sleep. *Elife*
- Sagdullaev BT, McCall MA. 2005. Stimulus size and intensity alter fundamental receptive-field properties of mouse retinal ganglion cells in vivo. *Vis. Neurosci.*
- Sakatani T, Isa T. 2004. PC-based high-speed video-oculography for measuring rapid eye movements in mice. *Neurosci. Res.*
- Sandell JH, Masland RH. 1986. A system of indoleamine-accumulating neurons in the rabbit retina. *J. Neurosci.* 6(11):3331–47
- Sanes JR, Masland RH. 2015. The Types of Retinal Ganglion Cells: Current Status and Implications for Neuronal Classification. *Annu. Rev. Neurosci.*
- Sawai S, Wang NP, Fukui H, Fukuda M, Manabe R, Wada H. 1988. Histamine H1-receptor in the retina: Species differences. *Biochem. Biophys. Res. Commun.* 150(1):316–22
- Scheinin H, Virtanen R, Macdonald E, Lammintausta R, Scheinin M. 1989. Medetomidine - a novel α_2 -adrenoceptor agonist: A review of its pharmacodynamic effects. *Prog. Neuropsychopharmacol. Biol. Psychiatry*
- Schmidt TM, Do MTH, Dacey D, Lucas R, Hattar S, Matynia A. 2011. Melanopsin-positive intrinsically photosensitive retinal ganglion cells: From form to function. *J. Neurosci.*
- Schneeweis DM, Schnapf JL. 1995. Photovoltage of rods and cones in the macaque retina. *Science* (80-.).
- Schröder S, Steinmetz NA, Krumin M, Pachitariu M, Rizzi M, et al. 2020. Arousal Modulates Retinal Output. *Neuron*
- Schuhmann TG, Zhou T, Hong G, Lee JM, Fu TM, et al. 2018. Syringe-injectable mesh electronics for stable chronic rodent electrophysiology. *J. Vis. Exp.*
- Schwartz G, Berry MJ. 2008. Sophisticated temporal pattern recognition in retinal ganglion cells. *J. Neurophysiol.*
- Schwartz O, Pillow JW, Rust NC, Simoncelli EP. 2006. Spike-triggered neural characterization. *J. Vis.*
- Sebel LE, Richardson JE, Singh SP, Bell S V., Jenkins A. 2006. Additive effects of sevoflurane and propofol on γ -aminobutyric acid receptor function. *Anesthesiology*
- Seung HS, Sümbül U. 2014. Neuronal cell types and connectivity: Lessons from the retina
- Shapley R, Victor J. 1986. Hyperacuity in cat retinal ganglion cells. *Science* (80-.).
- Shekhar K, Lapan SW, Whitney IE, Tran NM, Macosko EZ, et al. 2016. Comprehensive Classification of Retinal Bipolar Neurons by Single-Cell Transcriptomics. *Cell*
- Shorten C, Khoshgoftaar TM. 2019. A survey on Image Data Augmentation for Deep Learning. *J. Big Data*
- Siebert S, Scherf BG, Del Punta K, Didkovsky N, Heintz N, Roska B. 2009. Genetic address book for retinal cell types. *Nat. Neurosci.*
- Simoncelli EP, Paninski L, Pillow JW, Schwartz O. 2004. Characterization of Neural Responses with Stochastic Stimuli. In *The Cognitive Neurosciences III*

Bibliography

- Skeie JM, Tsang SH, Mahajan VB. 2011. Evisceration of mouse vitreous and retina for proteomic analyses. *J. Vis. Exp.* (50):
- Skrandies W, Wässle H. 1988. Dopamine and serotonin in cat retina: electroretinography and histology. *Exp. Brain Res.*
- Slaughter MM, Miller RF. 1981. 2-Amino-4-phosphonobutyric acid: A new pharmacological tool for retina research. *Science* (80-.).
- Slaughter MM, Miller RF. 1983. An excitatory amino acid antagonist blocks cone input to sign-conserving second-order retinal neurons. *Science* (80-.).
- Smith SL. 2012. *Visual stimuli for mice* – Labrigger. <https://labrigger.com/blog/2012/03/06/mouse-visual-stim/>
- Sonoda T, Li JY, Hayes NW, Chan JC, Okabe Y, et al. 2020. A noncanonical inhibitory circuit dampens behavioral sensitivity to light. *Science* (80-.).
- Soucy E, Wang Y, Nirenberg S, Nathans J, Meister M. 1998. A novel signaling pathway from rod photoreceptors to ganglion cells in mammalian retina. *Neuron*
- Stabernack C, Sonner JM, Laster M, Zhang Y, Xing Y, et al. 2003. Spinal N-methyl-D-aspartate receptors may contribute to the immobilizing action of isoflurane. *Anesth. Analg.*
- Steinbach JH, Akk G. 2001. Modulation of GABAA receptor channel gating by pentobarbital. *J. Physiol.*
- Steinberg RH. 1969. Rod-cone interaction in S-potentials from the cat retina. *Vision Res.*
- Strauss O. 2005. The retinal pigment epithelium in visual function
- Ströh S, Puller C, Swirski S, Hölzel M-B, van der Linde LIS, et al. 2018. Eliminating Glutamatergic Input onto Horizontal Cells Changes the Dynamic Range and Receptive Field Organization of Mouse Retinal Ganglion Cells. *J. Neurosci.* 0141–17
- Stryer L. 1991. Visual excitation and recovery
- Suzuki H, Pinto LH. 1986. Response properties of horizontal cells in the isolated retina of wild-type and pearl mutant mice. *J. Neurosci.*
- Svaetichin, G. 1953. The cone action potential. *Acta Physiol.Scand.* 29:565–600
- Szatko KP, Korympidou MM, Ran Y, Berens P, Dalkara D, et al. 2020. Neural circuits in the mouse retina support color vision in the upper visual field. *Nat. Commun.*
- Szikra T, Trenholm S, Drinnenberg A, Jüttner J, Raics Z, et al. 2014. Rods in daylight act as relay cells for cone-driven horizontal cell-mediated surround inhibition. *Nat. Neurosci.*
- Tanelian DL, Kosek P, Mody I, MacIver MB. 1993. The role of the GABA(A) receptor/chloride channel complex in anesthesia
- Teranishi T, Negishi K, Kato S. 1983. Dopamine modulates S-potential amplitude and dye-coupling between external horizontal cells in carp retina. *Nature*
- Terubayashi H, Fujisawa H, Itoi M, Ibata Y. 1983. Hypothalamo-retinal centrifugal projection in the dog. *Neurosci. Lett.* 40(1):1–6
- Thier P, Alder V. 1984. Action of iontophoretically applied dopamine on cat retinal ganglion cells. *Brain Res.*

Bibliography

- Thoreson WB, Mangel SC. 2012. Lateral interactions in the outer retina
- Tikidji-Hamburyan A, Reinhard K, Storch R, Dietter J, Seitter H, et al. 2017. Rods progressively escape saturation to drive visual responses in daylight conditions. *Nat. Commun.*
- Tsukamoto Y, Morigiwa K, Ueda M, Sterling P. 2001. Microcircuits for night vision in mouse retina. *J. Neurosci.*
- Tsukamoto Y, Omi N. 2017. Classification of Mouse Retinal Bipolar Cells: Type-Specific Connectivity with Special Reference to Rod-Driven AII Amacrine Pathways. *Front. Neuroanat.* 11:92
- Tsung-Yi Lin, Genevieve Patterson, Matteo R. Ronchi, Yin Cui, Michael Maire, et al. 2018. COCO - Common Objects in Context. *COCO Dataset*
- Van Hook MJ, Wong KY, Berson DM. 2012. Dopaminergic modulation of ganglion-cell photoreceptors in rat. *Eur. J. Neurosci.*
- Vaney DI. 1990. Chapter 2 The mosaic of amacrine cells in the mammalian retina. *Prog. Retin. Res.* 9:49–100
- Vaney DI. 1994. Patterns of neuronal coupling in the retina. *Prog. Retin. Eye Res.* 13(1):301–55
- Vaney DI, Sivyer B, Taylor WR. 2012. Direction selectivity in the retina: Symmetry and asymmetry in structure and function
- Vardi N. 1998. Alpha subunit of G(o) localizes in the dendritic tips of ON bipolar cells. *J. Comp. Neurol.*
- Vardi N, Morigiwa K. 1997. ON cone bipolar cells in rat express the metabotropic receptor mGluR6. *Vis. Neurosci.*
- Veruki ML, Wässle H. 1996. Immunohistochemical localization of dopamine D1 receptors in rat retina. *Eur. J. Neurosci.*
- Vila A, Satoh H, Rangel C, Mills SL, Hoshi H, et al. 2012. Histamine receptors of cones and horizontal cells in Old World monkey retinas. *J. Comp. Neurol.*
- Villar MJ, Vitale ML, Parisi MN. 1987. Dorsal raphe serotonergic projection to the retina. A combined peroxidase tracing-neurochemical/high-performance liquid chromatography study in the rat. *Neuroscience.* 22(2):681–86
- Viney TJ, Balint K, Hillier D, Siebert S, Boldogkoi Z, et al. 2007. Local Retinal Circuits of Melanopsin-Containing Ganglion Cells Identified by Transsynaptic Viral Tracing. *Curr. Biol.*
- Vlasits AL, Euler T, Franke K. 2019. Function first: classifying cell types and circuits of the retina
- Vogel H. 1979. A better way to construct the sunflower head. *Math. Biosci.*
- Völgyi B, Chheda S, Bloomfield SA. 2009. Tracer coupling patterns of the ganglion cell subtypes in the mouse retina. *J. Comp. Neurol.*
- Vugler AA, Redgrave P, Semo M, Lawrence J, Greenwood J, Coffey PJ. 2007. Dopamine neurones form a discrete plexus with melanopsin cells in normal and degenerating retina.

Bibliography

Exp. Neurol.

- Wagner H -J, Luo B -G, Ariano MA, Sibley DR, Stell WK. 1993. Localization of D2 dopamine receptors in vertebrate retinæ with anti-peptide antibodies. *J. Comp. Neurol.*
- Wald G. 1968. Molecular basis of visual excitation
- Waleed A. 2017. Mask R-CNN for object detection and instance segmentation on Keras and TensorFlow
- Walker EY, Sinz FH, Cobos E, Muhammad T, Froudarakis E, et al. 2019. Inception loops discover what excites neurons most using deep predictive models. *Nat. Neurosci.*
- Wang L, Sarnaik R, Rangarajan K, Liu X, Cang J. 2010. Visual receptive field properties of neurons in the superficial superior colliculus of the mouse. *J. Neurosci.* 30(49):16573–84
- Wang MM, Janz R, Belizaire R, Frishman LJ, Sherry DM. 2003. Differential distribution and developmental expression of synaptic vesicle protein 2 isoforms in the mouse retina. *J. Comp. Neurol.* 460(1):106–22
- Wang Q, Ding SL, Li Y, Royall J, Feng D, et al. 2020. The Allen Mouse Brain Common Coordinate Framework: A 3D Reference Atlas. *Cell*
- Wang Y V., Weick M, Demb JB. 2011. Spectral and temporal sensitivity of cone-mediated responses in mouse retinal ganglion cells. *J. Neurosci.*
- Wang W, Tan W, Luo D, Lin J, Yu Y, et al. 2012. Acute pressure on the sciatic nerve results in rapid inhibition of the wide dynamic range neuronal response. *BMC Neurosci.*
- Wassle H, Puller C, Muller F, Haverkamp S. 2009. Cone Contacts, Mosaics, and Territories of Bipolar Cells in the Mouse Retina. *J. Neurosci.*
- Wässle H, Heinze L, Ivanova E, Majumdar S, Weiss J, et al. 2009. Glycinergic transmission in the mammalian retina
- Wässle H, Koulen P, Brandstätter JH, Fletcher EL, Becker CM. 1998. Glycine and GABA receptors in the mammalian retina. *Vision Res.*
- Weickenmeier J, de Rooij R, Budday S, Ovaert TC, Kuhl E. 2017. The mechanical importance of myelination in the central nervous system. *J. Mech. Behav. Biomed. Mater.*
- Weickenmeier J, de Rooij R, Budday S, Steinmann P, Ovaert TC, Kuhl E. 2016. Brain stiffness increases with myelin content. *Acta Biomater.*
- Weiser TG, Regenbogen SE, Thompson KD, Haynes AB, Lipsitz SR, et al. 2008. An estimation of the global volume of surgery: a modelling strategy based on available data. *Lancet*
- Weng S, Estevez ME, Berson DM. 2013. Mouse Ganglion-Cell Photoreceptors Are Driven by the Most Sensitive Rod Pathway and by Both Types of Cones. *PLoS One*
- Werner B, Cook PB, Passaglia CL. 2008. Complex temporal response patterns with a simple retinal circuit. *J. Neurophysiol.*
- Whiting PJ. 2003. GABA-A receptor subtypes in the brain: A paradigm for CNS drug discovery?
- Witkovsky P. 2004. Dopamine and retinal function
- Witkovsky P, Gábel R, Križaj D. 2008. Anatomical and neurochemical characterization of

- dopaminergic interplexiform processes in mouse and rat retinas. *J. Comp. Neurol.*
- Wong KY, Dunn FA, Graham DM, Berson DM. 2007. Synaptic influences on rat ganglion-cell photoreceptors. *J. Physiol.*
- Wu SM. 1991. Input-output relations of the feedback synapse between horizontal cells and cones in the tiger salamander retina. *J. Neurophysiol.*
- Yamamoto T, Schindler E. 2017. Where and how do anaesthetics act? Mechanisms of action in the central nervous system
- Yan W, Laboulaye MA, Tran NM, Whitney IE, Benhar I, Sanes JR. 2020. Mouse Retinal Cell Atlas: Molecular Identification of over Sixty Amacrine Cell Types. *J. Neurosci.*
- Yau KW. 1994. Phototransduction mechanism in retinal rods and cones. *Investig. Ophthalmol. Vis. Sci.*
- Yau KW, Matthews G, Baylor DA. 1979. Thermal activation of the visual transduction mechanism in retinal rods [16]
- Yger P, Spampinato G, Esposito E, Lefebvre B, Deny S, et al. 2016. Fast and accurate spike sorting in vitro and in vivo for up to thousands of electrodes. *bioRxiv*
- Yger P, Spampinato GLB, Esposito E, Lefebvre B, Deny S, et al. 2018. A spike sorting toolbox for up to thousands of electrodes validated with ground truth recordings in vitro and in vivo. *Elife*
- Yosinski J, Clune J, Bengio Y, Lipson H. 2014. How transferable are features in deep neural networks? *Adv. Neural Inf. Process. Syst.*
- Yu YC, Satoh H, Wu SM, Marshak DW. 2009. Histamine enhances voltage-gated potassium currents of on bipolar cells in macaque retina. *Investig. Ophthalmol. Vis. Sci.*
- Zhang AJ, Jacoby R, Wu SM. 2011. Light- and dopamine-regulated receptive field plasticity in primate horizontal cells. *J. Comp. Neurol.*
- Zhang D-Q, Zhou T-R, McMahon DG. 2007. Functional Heterogeneity of Retinal Dopaminergic Neurons Underlying Their Multiple Roles in Vision. *J. Neurosci.*
- Zhang DQ, Stone JF, Zhou T, Ohta H, McMahon DG. 2004. Characterization of genetically labeled catecholamine neurons in the mouse retina. *Neuroreport*
- Zhang Y, Kim I-J, Sanes JR, Meister M. 2012. The most numerous ganglion cell type of the mouse retina is a selective feature detector. *Proc. Natl. Acad. Sci.*
- Zhao X, Stafford BK, Godin AL, King WM, Wong KY. 2014. Photoresponse diversity among the five types of intrinsically photosensitive retinal ganglion cells. *J. Physiol.*
- Zhao X, Wong KY, Zhang DQ. 2017. Mapping physiological inputs from multiple photoreceptor systems to dopaminergic amacrine cells in the mouse retina. *Sci. Rep.*
- Zhu Y, Xu J, Hauswirth WW, DeVries SH. 2014. Genetically Targeted Binary Labeling of Retinal Neurons. *J. Neurosci.*

Annexe 1 – LED Dome

7 Annexe 1 – LED Dome

7.1 Presentation

The physiology of the retina has been studied mostly in an *ex vivo* condition where the retinal tissue is dissected from an animal and placed in an oxygenated medium to be kept alive and functional. One can then record the neuronal responses using various opto- or electrophysiological methods, such as multi-electrode array and patch clamp recordings, while displaying visual stimuli directly onto the isolated retina. In this experimental paradigm, the presented visual stimulus can easily cover the whole portion of the retina.

In *in vivo* studies on higher visual areas, in contrast, visual stimuli are presented to an animal from one or multiple computer screens (e.g., liquid crystal displays; LCDs). In such cases, the presented visual stimulus covers only a fraction of the animal's visual field. Nevertheless, thanks to the retinotopy in the visual system, one can still record the visual responses of a set of local neurons that all have the receptive fields on the screens. Recent technological advances, however, start to allow for recording from much larger populations of neurons spanning the entire brain region of interest, such as the primary visual cortex. Moreover, recordings of retinal ganglion cells from the optic tract randomly selects cells, with receptive fields sampled on the entire field of view. It is then critical to stimulate as large visual field as possible to study the visual processing by the neural populations, or to account for the distance between receptive fields of optic tract recordings.

With the primary goal of covering the entire visual field of a mouse eye, we assembled light-emitting diodes (LEDs) on a dome of 20cm in diameter, achieving a spatial resolution of 2.86° comparable to the receptive field centre size of mouse retinal ganglion cells (2-3 degrees). This LED-based device is superior to commonly used LCD screens in that 1) the LEDs have a higher refresh rate; and 2) the spherical arrangement equalises the distance to the eye for any point in the visual field.

LED stripes are mounted on a 3D printed support (inner diameter, 20cm) with a slit arrangement. A total of 948 LEDs (a total of 72 stripes of different lengths) were packed in four quarters with 90° symmetries. The stripes are wired end to end to form sequences of 125 and 112 LEDs, which taken together cover a quarter of the dome. While there are eight stripes to control, we chose to use four Arduino to control the LEDs, one per quarter of the dome. A fifth Arduino (master) synchronises the four Arduinos (workers).

Annexe 1 – LED Dome

The device was mounted on a gimbal-like support to allow for an easy angular placement over an eye of a head-fixed mouse on a treadmill. All the electronics were shielded with a copper mesh to prevent any electric noise perturbation of the electrophysiological recordings. The copper mesh is sandwiched between the LED support and a frosted plastic dome also used to blur the LED, reducing strong direct illumination.

To facilitate the upload of the different stimuli to the five Arduino during a recording session, we connected all boards to a RaspberryPi. We exported for each stimulus the compiled Arduino codes (In Arduino GUI: Sketch->Export compiled binary, pick the file ending in `ino.standard.hex`). We then wrote bash scripts to update all boards automatically with the binary files using `avrdude`. The bash scripts also include logging to keep a trace for later analysis. Finally, to avoid plugging a dedicated screen, mouse and keyboard to the RaspberryPi, we enable the VNC connection through SSH so we could remotely connect and control everything from a laptop with no additional cables attached to the device.

7.2 Light intensity

The light intensity was measure using a PM100D from Thorlabs connected with a S121C sensor. We placed the sensor bellow the LED dome while turning ON the four centremost LED to make the measurements (the sensor was at a distance of 10cm from the LEDs). The power curve, extrapolated to the entirety of the hemisphere, is presented in figure 28.B.

7.3 LED position mapping

To map the position of each LED on the surface of the dome, we used the 3D model of the LED stripes support to estimate the position of the first and last LED of a stripe. Knowing then the position of both ends and the number of LED on each stripe, we interpolated the position of the remaining LEDs. This operation was repeated for the 18 stripes composing a quarter, and the three other quarters LED positions were obtained with 90° rotations. We validated the accuracy of the mapping by looking at moving stimuli, for which the effect looked convincing. The LEDs positions were also used to map the receptive fields of cells during analysis.

Annexe 1 – LED Dome

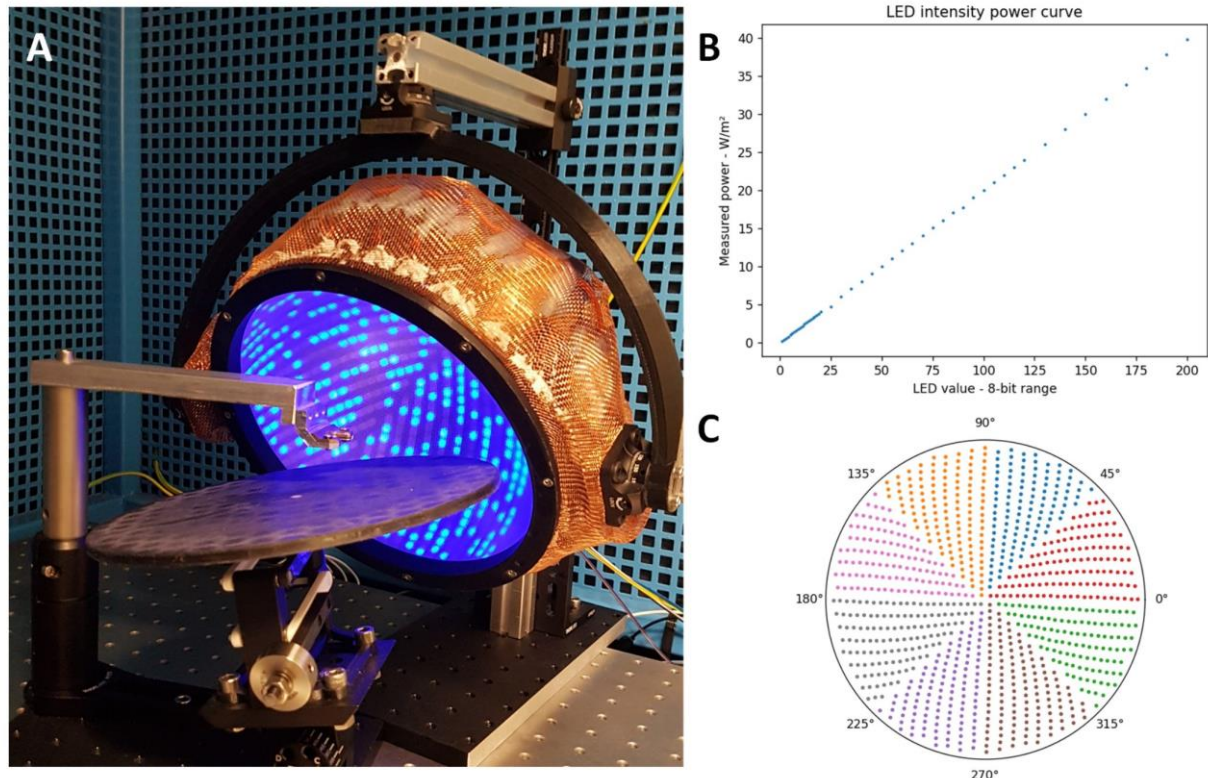


Figure 28 – LED dome, power curve and mapping. *A) LED dome showing a frame of the checkerboard stimulus. The treadmill and head plate holder are showed on the foreground. The LED dome is supported by an arch from two manual rotation stage, while the arch hangs also attached from a rotation stage. The electronics are covered by a copper mesh to prevent electric noise in electrophysiology recordings. B) Power curve of all LEDs measured for increasing LED values. C) Polar mapping of the LEDs. The distance to the centre is given by $(\pi/2 - \text{elevation})$. The colours show how the LED stripes are combined to form 8 portions.*

7.4 Frame rate

With a four worker Arduino configuration, the maximal attainable frame rate is at around 100Hz. However, at this frequency, the stripes of 112 and 125 LED start to loose synchrony. In that configuration, we recommend using a frequency of 60Hz. The asynchrony arises due to the sequential update of the two stripes. From our measurement, the upload lasts about 3.6ms per stripe. Increasing the boards to height workers with minimal modifications of the hardware, the memory available per LED is doubled. At the same time, the computation load of a frame and data transfer time to the stripes is halved. In such configuration, 100Hz and beyond becomes reachable. However, despite theoretically not dropping frames, asynchrony for the stripes can arise at higher frequencies due to the properties of the Neopixel.

The Neopixel stripes work at a frequency of 400Hz. Once an Arduino finishes passing the values to the LED, they will wait for the next cycle to refresh their display. There is, therefore, a jitter ranging from 0 to 2.5ms. A proposed solution is to replace the Neopixel to the newer

Annexe 1 – LED Dome

DotStar stripes with their 19.2KHz refresh rate (but make sure that the support fit those stripe or else the model has to be adjusted).

Another limitation for the frame rate was the code execution time to generate a frame. Upgrading to faster boards than Arduino Uno is a possibility, however, for the stimuli presented here, we could reach our goals. As INO code is apparent to C, having experience with the later helps to debug and optimise the code.

7.5 Visual stimuli

7.5.1 White-noise checkerboard stimulus

We presented a white noise checkerboard stimulus for 15 min at a frequency of 60Hz. To attain this frequency, we optimised the use of the pseudorandom generator implemented in the Arduino library (Lehmer random number generator). The generator returns 32-bit numbers, from which only 31-bits are random (the sign bit is not used). We employed each bit of the random 31-bit numbers as an independent random Boolean to signal which LED to turn ON. This optimisation resulted in a critical speed-up due to a 96% reduction of calls to the random number generator. However, this strategy comes with the risk of using bad seeds for the four workers. In the first round of recordings, we used the seeds 100, 200, 300, 400. The sequences produced by each generator were different, but the devil is in the details. Multiplication by two in base two corresponds to a bit rotation, and unexpectedly, the similarity is preserved even after passing through the generator. In the second version of the stimuli, we selected different seeds, derived from universal constants: 161803398 (ϕ), 271828182 (e), 314159265 (π) and 299792458 (c).

7.5.2 White-noise full-field stimulus

The white noise full-field stimulus is similar to the white noise checkerboard, excepting that all LEDs are attributed for each frame the same value. The stimulus has a refresh rate of 60Hz and is presented for five minutes. We used a seed of 100 for the number generator.

7.5.3 Chirp stimulus frequency epoch

For a chirp stimulus modulated in frequency, we made a total of 13 epochs going at 0.5, 1, 2, 4, 8, 16, 20, 25, 33, 40 and 50Hz lasting one second each, at the exception of the 0.5Hz epoch which lasted two seconds. Contrarily to the other stimuli, the master Arduino did not keep a fixed rhythm at 60Hz but instead sent pulses corresponding to the frequencies. As so, the workers only switched the LEDs values every time they received a pulse from the master.

Annexe 1 – LED Dome

7.5.4 Motion stimulus

Before obtaining a satisfying motion stimulus, we came up with several non-optimal solutions that we find relevant to describe here. The first solution would be to make a grating rotating around an axis passing at the base of the dome, sampled at height angles. The problem here is that the grating spatial frequency and its edges displacement speed varies with the distance to the rotation axis. As such, the stimulus is not homogenous on the dome. To limit this effect, we ought to assign to the LEDs a position along the direction axis. Like so, the speed would be homogenous along the edge (figure 29.A). However, this stimulus also had a drawback as it distorts the gratings at the dome sides.

Ultimately, we found a third way of displaying a motion stimulus, which from the elegant pieces of math it combines produced a satisfying result. The stimulus consists of a band parallel to the dome's base, starting at the top of the dome and moving down (figure 29.B). A fixed angle sets the band thickness, while it moves according to its elevation, going from π to $-\pi$. As such, both the size and speed of the band remains identical across the sphere. The LEDs are then turned ON or OFF, depending on their elevation and on the position of the band. With this method, we obtain a stimulus that can go from top to bottom or the other way around, sampling two opposite directions for the cells to respond.

Annexe 1 – LED Dome

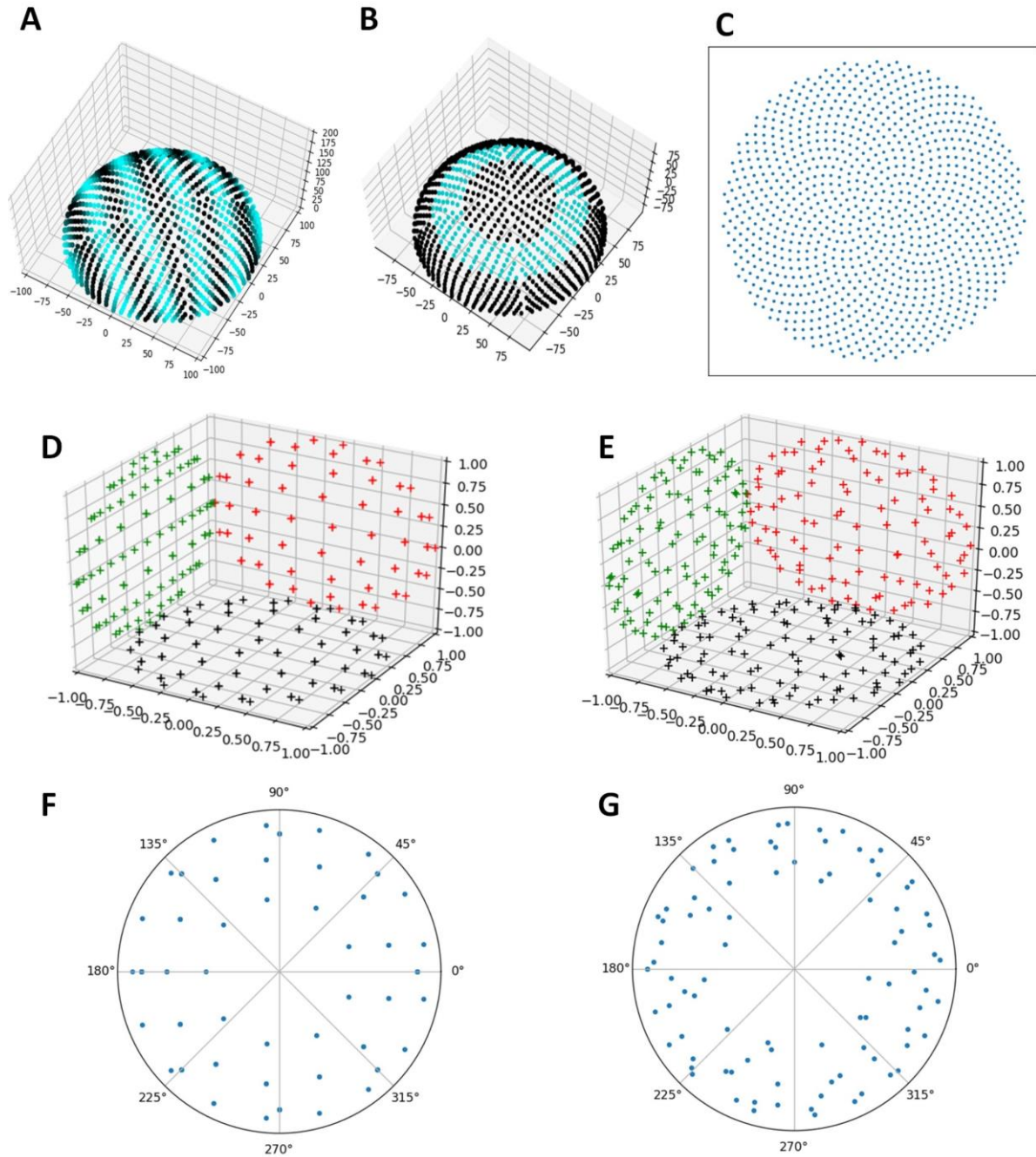


Figure 29 – LED dome motion stimulus. **A)** Un-optimal grating stimulus **B)** Band stimulus. **C)** Golden spiral obtained with 1000 points. **D)** Projection in XYZ of the points obtained with homogenous sampling for 100 points **E)** Projection in XYZ of the points obtained with 3D version of the golden angle for 100 points. **F)** Origin of motion for 100 bands sampled homogeneously, viewed from the top of the LED dome. Origins too close to the centre were excluded. **G)** Same as F for 100 bands sampled with the 3D golden angle sampling.

To increase the number of direction sampled, the wave needs to have a different origin. However, doing so would increase by a lot the complexity of the algorithm, on how to set the position of the wave and which LEDs to turn ON. Instead, we can virtually rotate positions of the LEDs and assigning them a new virtual elevation. The 3D rotations require the use of

Annexe 1 – LED Dome

quaternions, which is also computationally expansive. However, the computation can be done during the inter-stimulus-interval and results in a single elevation value per LED. As such, any other origin for the band can be sampled. The last remaining problem consist in finding which origins should be choosing so that the stimulus direction would be sampled homogeneously, irrelevantly of a cell's receptive field position.

A way to sample homogeneously position on the sphere is to take the vertices of a platonic solid as origins of the band. However, the regularity of such structure leads to an inhomogeneous sampling of directions, depending if the cell's RF is located on an edge, face or vertex. A second solution proposed by (Deserno 2004) samples points homogeneously on a sphere by choosing circles of elevation at constant intervals d_θ , and on each circle choose points with distance d_ϕ such that $d_\theta \approx d_\phi$ and $d_\theta d_\phi$ equals the average area per point (figure 29.D). This method provides more satisfying results; however, regularity once again emerge from the sampling onto a fixed circle (figure 29.F). Ultimately, we found a third way of sampling origins homogeneously, without creating any sort of regularity. This method uses a 3D variant (González 2010) (figure 29.E) of the 2D golden angle (Ridley 1982; Vogel 1979) (figure 29.C) to distribute a set numbers of points on the sphere.

To analyse the response to that stimulus, one needs to know the receptive field (RF) position of a cell. From that position, we then project to the RF's normal plane all the origins. The resulting points are distributed on a disk with centre the receptive field of the cell, showing from what direction each band approached the receptive field (figure 29.G). Using the angles of each origin, the direction (DS) can be calculated as:

$$\phi_k = e^{i\alpha_k}$$

where α_k is the direction of the k^{th} direction.

Finally, one last precaution needs to be taken. When a band originates or end too close to the receptive field, the stimulus would resemble a looming stimulus. Therefore, when gathering the response to calculate the DS, points too close to the disk centre must be excluded, or eventually used to calculate the response to looming stimuli.

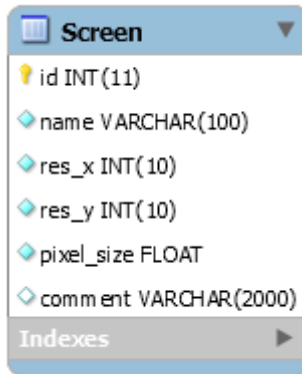
For our implementation of this stimulus, we used a total of 100 origins for the band, with a width of 40° and a speed of $40^\circ \cdot \text{s}^{-1}$.

Annexe 2 – Database

8 Annexe 2 – Database

8.1 Tables description

8.1.1.1 Visual stimulus



Screen	
id	INT(11)
name	VARCHAR(100)
res_x	INT(10)
res_y	INT(10)
pixel_size	FLOAT
comment	VARCHAR(2000)
Indexes	

Screen

A screen represents a physical device, such as a LCD screen or a DLP projector.

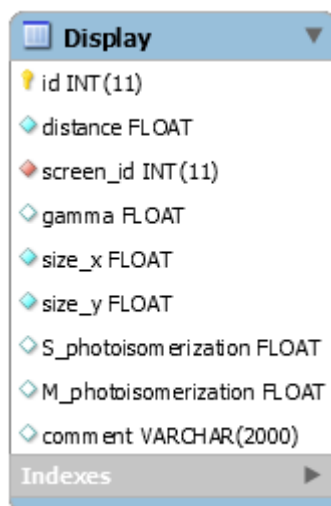
name: Name of the screen to identify it in the database

res_x: Resolution of the screen in X

res_y: Resolution of the screen in Y

pixel_size: Angular size of a pixel from the mouse point of view

comment: Relevant comment for the screen



Display	
id	INT(11)
distance	FLOAT
screen_id	INT(11)
gamma	FLOAT
size_x	FLOAT
size_y	FLOAT
S_photoisomerization	FLOAT
M_photoisomerization	FLOAT
comment	VARCHAR(2000)
Indexes	

Display

A display summarises the settings for a particular screen.

distance: Distance of the screen to the mouse

screen_id: ID of the screen this display applies to

gamma: Gamma calibration of the display

size_x: Size of the display in visual degree in X

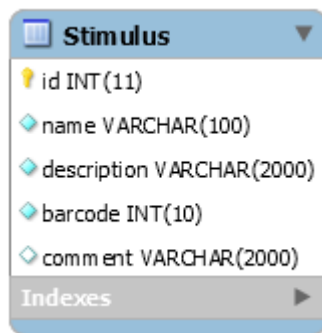
size_y: Size of a display in visual degree in Y

S_photoisomerization: P* per second of S-cone

M_photoisomerization: P* per second of M-cone

comment: Relevant comment for the display

Annexe 2 – Database



Stimulus	
id	INT(11)
name	VARCHAR(100)
description	VARCHAR(2000)
barcode	INT(10)
comment	VARCHAR(2000)
Indexes	

Stimulus

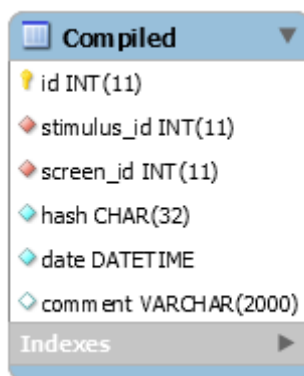
A stimulus represents a family of similar visual stimulation, such as checkerboards or moving gratings.

name: Name of the stimulus

description: General description of the stimulus

barcode: Barcode presented before of the stimulus

comment: Relevant comment for the stimulus



Compiled	
id	INT(11)
stimulus_id	INT(11)
screen_id	INT(11)
hash	CHAR(32)
date	DATETIME
comment	VARCHAR(2000)
Indexes	

Compiled

Compiled instance of a stimulus.

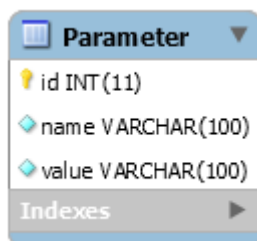
stimulus_id: Stimulus family of the compiled stimulus

screen_id: Screen for which the stimulus is designed

hash: MD5 hash of the compiled file

date: Date at which the stimulus was created. Helps identification.

comment: Relevant comment for the compiled stimulus



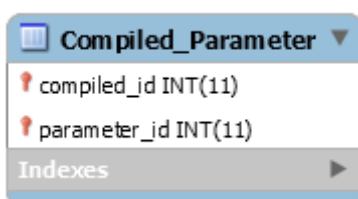
Parameter	
id	INT(11)
name	VARCHAR(100)
value	VARCHAR(100)
Indexes	

Parameter

Parameter used for a compiled instance of a stimulus.

name: Name of the parameter

value: value of the parameter



Compiled_Parameter	
compiled_id	INT(11)
parameter_id	INT(11)
Indexes	

Compiled_Parameter

Link table between compiled and parameter to make a N to N relationship

compiled_id: ID of the compiled stimulus

parameter_id: ID of the parameter

Annexe 2 – Database

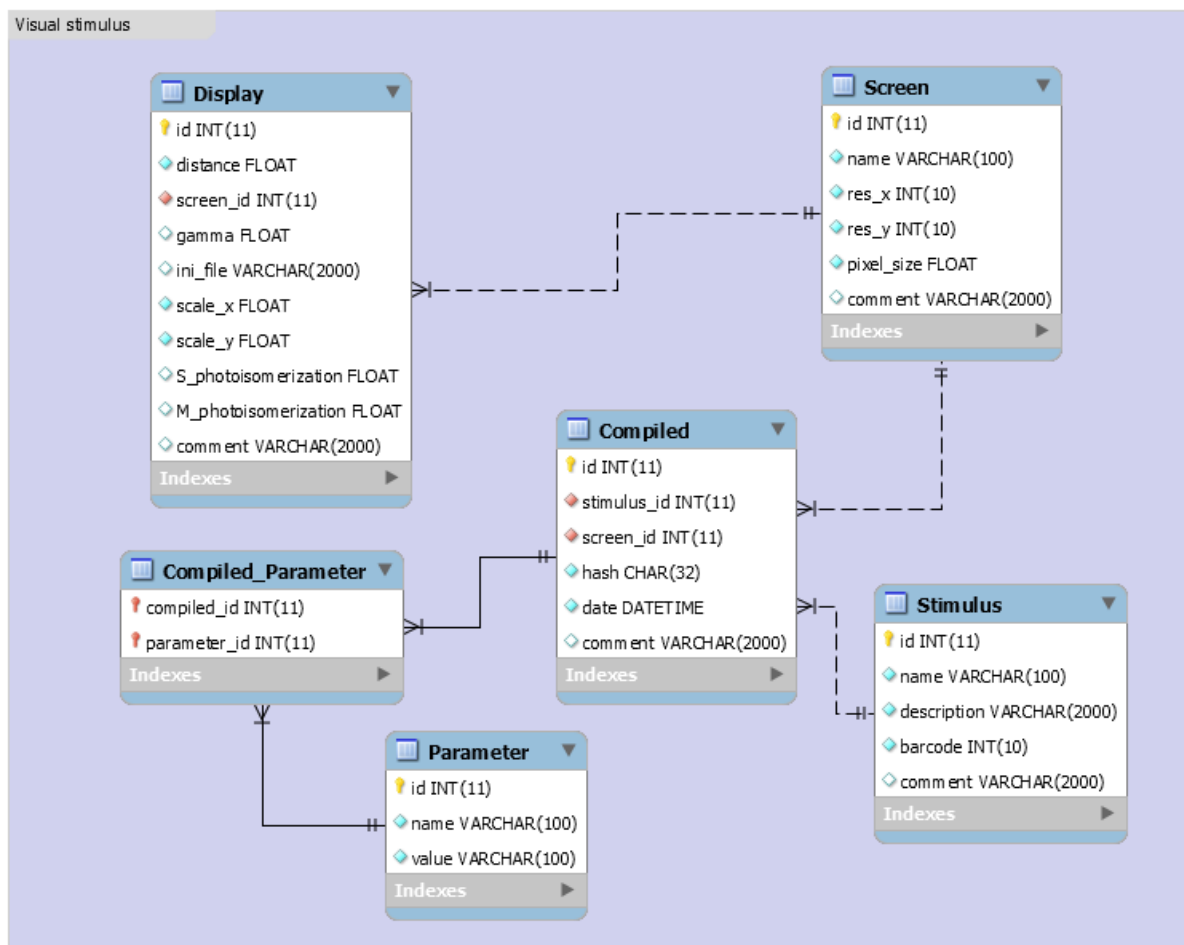
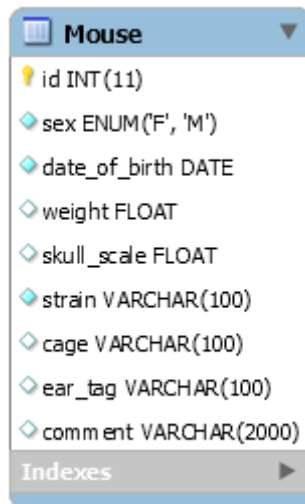


Figure 30 – Relationship diagram between the tables about the visual stimuli

Annexe 2 – Database

8.1.1.2 Mouse



Mouse
id INT(11)
sex ENUM('F', 'M')
date_of_birth DATE
weight FLOAT
skull_scale FLOAT
strain VARCHAR(100)
cage VARCHAR(100)
ear_tag VARCHAR(100)
comment VARCHAR(2000)
Indexes

Mouse

A mouse individual.

sex: Sex of the mouse

date_of_birth: Mouse date of birth

weight: weight of the mouse. Also exists in Handling.

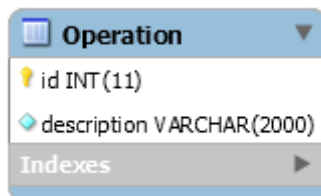
skull_scale: Skull scale given by the stereotaxic registration.

strain: Strain of the mouse

cage: Label of the cage where the mouse is kept

ear_tag: Way of identification of a mouse in a cage

comment: Relevant comment for the mouse

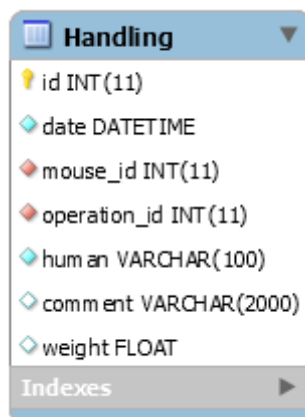


Operation
id INT(11)
description VARCHAR(2000)
Indexes

Operation

An operation or procedure description.

description: Description of the operation



Handling
id INT(11)
date DATETIME
mouse_id INT(11)
operation_id INT(11)
human VARCHAR(100)
comment VARCHAR(2000)
weight FLOAT
Indexes

Handling

Instance of an operation performed on a mouse

date: Date of the handling

mouse_id: ID of the mouse handled

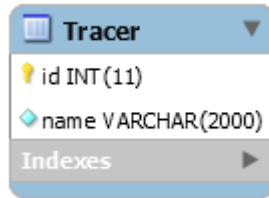
operation_id: ID of the operation performed

human: Name of the experimenter who performed the handling

comment: Relevant comment for the handling

weight: Weight of the mouse the day of the handling

Annexe 2 – Database

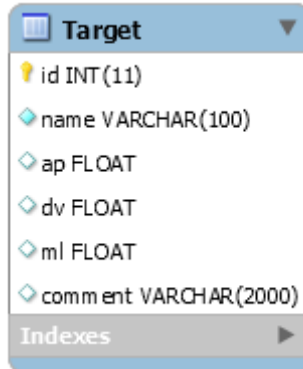


Tracer	
id	INT(11)
name	VARCHAR(2000)
Indexes	

Tracer

Tracer, virus or other injectable solution.

name: Name of the tracer



Target	
id	INT(11)
name	VARCHAR(100)
ap	FLOAT
dv	FLOAT
ml	FLOAT
comment	VARCHAR(2000)
Indexes	

Target

Brain target in stereotaxic coordinates.

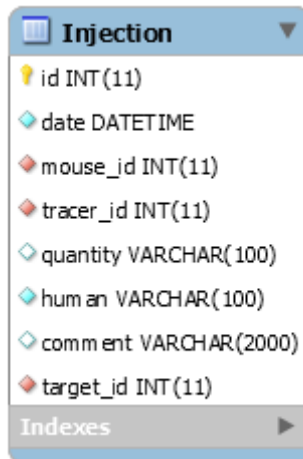
name: Name of the target

ap: Antero-posterior position of the target

dv: Dorso-ventral position of the target

ml: Medio-lateral position of the target

comment: Relevant comment for the target



Injection	
id	INT(11)
date	DATETIME
mouse_id	INT(11)
tracer_id	INT(11)
quantity	VARCHAR(100)
human	VARCHAR(100)
comment	VARCHAR(2000)
target_id	INT(11)
Indexes	

Injection

Injection procedure of a tracer.

date: Date of the injection

mouse_id: ID of the mouse who received the injection

tracer_id: ID of the injected tracer

quantity: Quantity of the tracer injected

human: Name of the experimenter who performed the injection

comment: Relevant comment for the injection

target_id: ID of the target of injection

Annexe 2 – Database

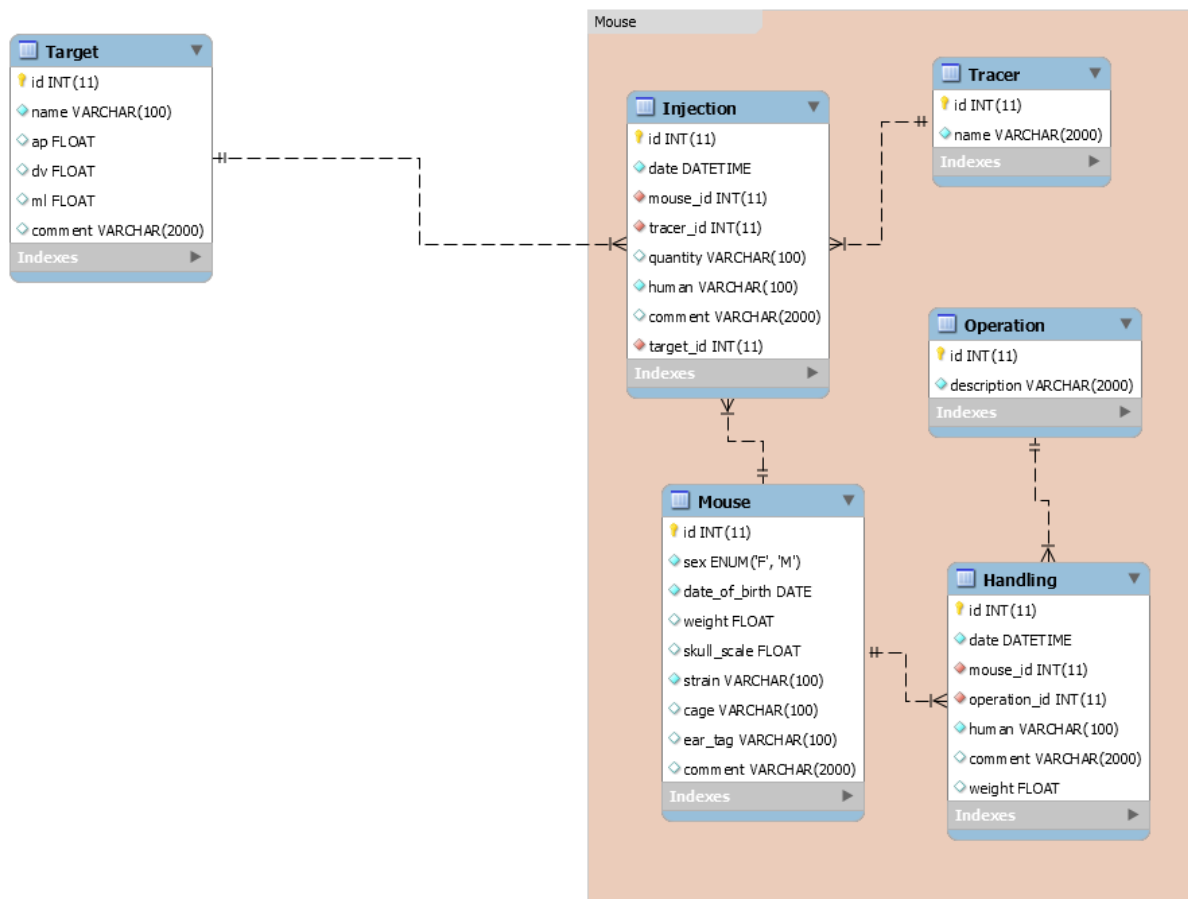
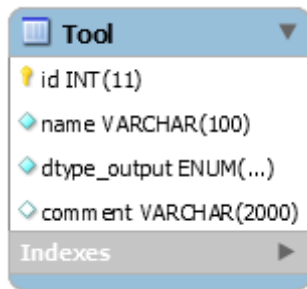


Figure 31 – Relationship diagram between the tables about mice

Annexe 2 – Database

8.1.1.3 Recording tool



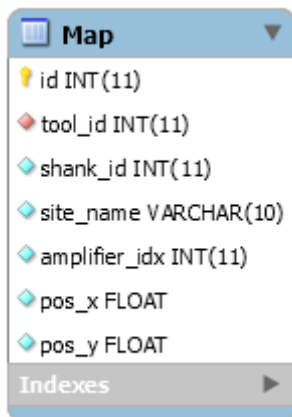
Tool

Recording device description for recording data, such as silicon probes, MEA or two-photon microscope.

name: Name of the tool

dtype_output: Output data file extension

comment: Relevant comment for the tool



Map

Mapping of recording site for an electrode kind of tool. Useful for generation of probe_map for SpykingCircus and other sanity plots.

tool_id: ID of the tool

shank_id: ID of the shank of the electrode site

site_name: Name of the site on the tool documentation

amplifier_idx: Index of the electrode site in a normal data file

pos_x: X coordinate of the electrode site

pos_y: Y coordinate of the electrode site

Annexe 2 – Database

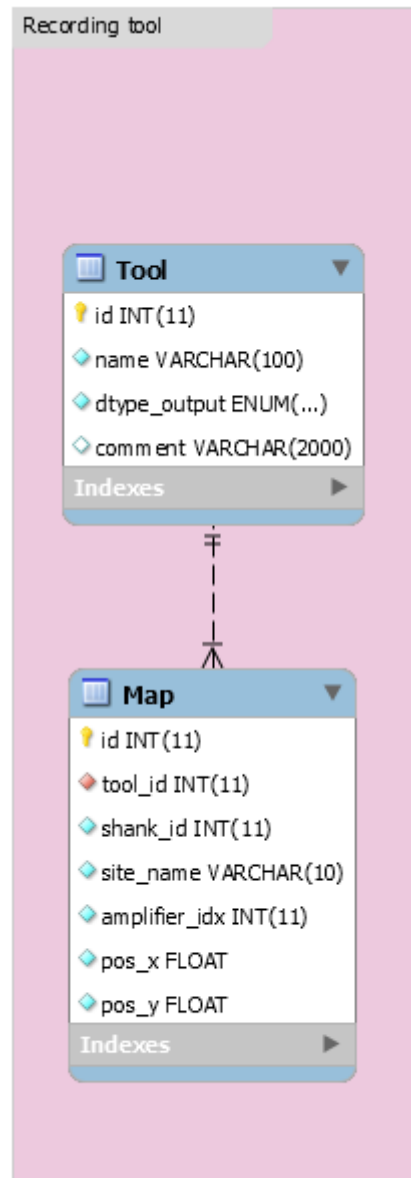
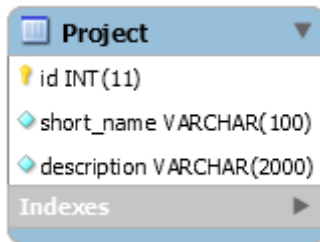


Figure 32 – Relationship diagram between the tables about recording devices

Annexe 2 – Database

8.1.1.4 Experimental data

Project



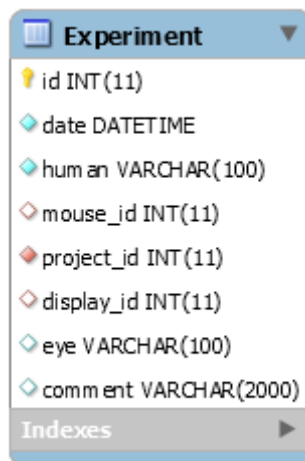
Project	
id	INT(11)
short_name	VARCHAR(100)
description	VARCHAR(2000)
Indexes	

A project describes the question under which experiments are conducted.

short_name: Short name of the project to quickly identify it

description: Additional details on the project and its aims

Experiment



Experiment	
id	INT(11)
date	DATETIME
human	VARCHAR(100)
mouse_id	INT(11)
project_id	INT(11)
display_id	INT(11)
eye	VARCHAR(100)
comment	VARCHAR(2000)
Indexes	

A single experiment conducted for a project. Not to be confused with a record.

date: Date of the experiment

human: Name of the experimenter who performed the experiment

mouse_id: ID of the mouse used for the experiment

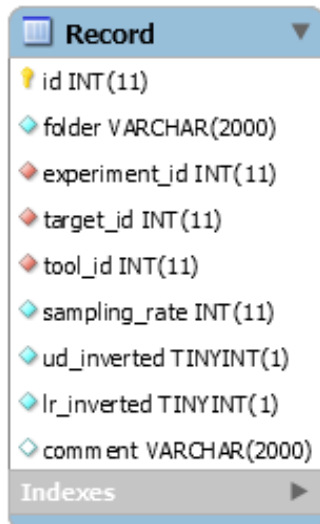
project_id: ID of the project of the experiment

display_id: Display used for the experiment

eye: Eye used for the experiment in {left, right, both}

comment: Relevant comment for the experiment

Record



Record	
id	INT(11)
folder	VARCHAR(2000)
experiment_id	INT(11)
target_id	INT(11)
tool_id	INT(11)
sampling_rate	INT(11)
ud_inverted	TINYINT(1)
lr_inverted	TINYINT(1)
comment	VARCHAR(2000)
Indexes	

A contiguous data recording of an experiment. An experiment often has several records.

folder: Folder path of the data on the shared drive

experiment_id: ID of the experiment

target_id: Target of the recorded brain region

tool_id: ID of the tool used for the record

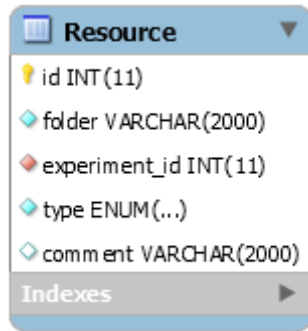
sampling_rate: Sampling rate of the data acquisition

ud_inverted: Flag for up down inversion of the visual stimulus

lr_inverted: Flag for left right inversion of the visual stimulus

comment: Relevant comment for the record

Annexe 2 – Database



Resource	
id	INT(11)
folder	VARCHAR(2000)
experiment_id	INT(11)
type	ENUM(...)
comment	VARCHAR(2000)
Indexes	

Resource

Link to a resource on the shared drive relevant for an experiment, such as histology images.

folder: Folder path of the data on the shared drive

experiment_id: ID of the experiment

type: Type of resource

comment: Relevant comment for the resource

Annexe 2 – Database

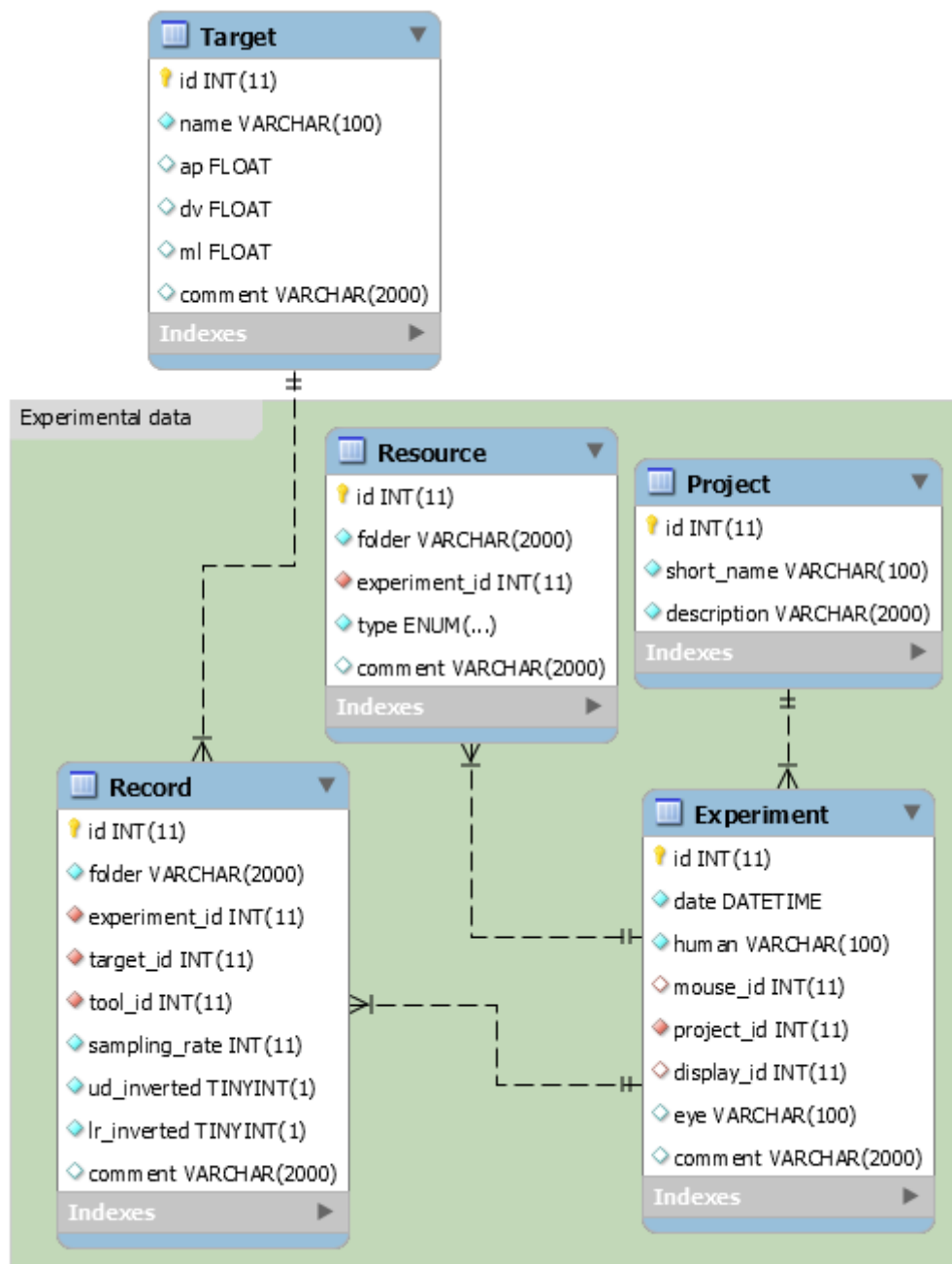


Figure 33 – Relationship diagram between the tables about experiments

Annexe 2 – Database

8.2 General diagram

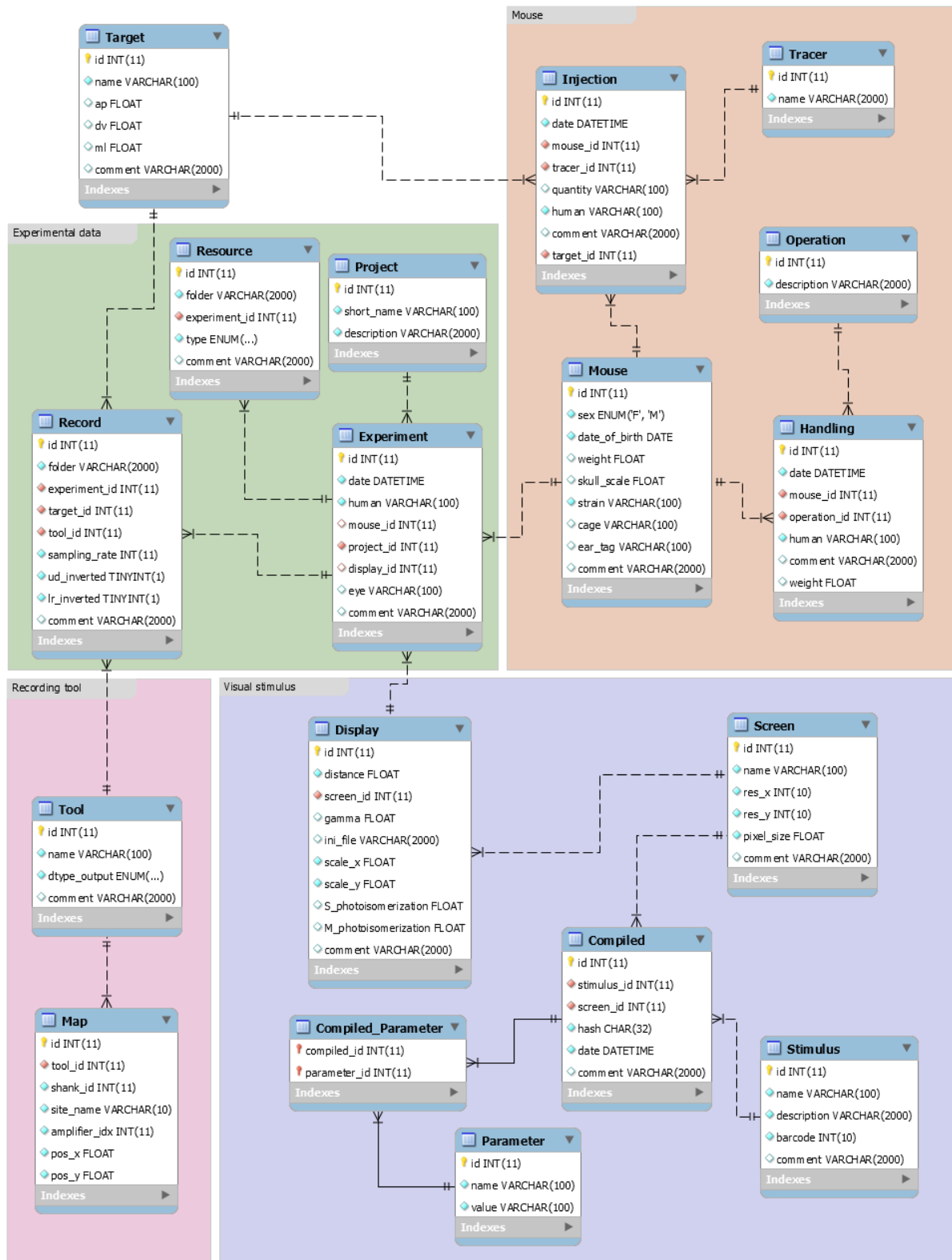


Figure 34 — General database diagram

Annexe 2 – Database

8.3 Graphical interface

A graphical user interface (GUI) was designed with QtCreator and coded in Python using the QtPy library. It implements convenient features to interact with the database:

- Insertion tabs for each table allow easy insertion, modification or deletion of the data.
- Display button for each table to access the data quickly.
- Free query tab to write SQL for selection.
- Common query tab for pre-made SQL queries, with or without parameters, written in the config file of the GUI.

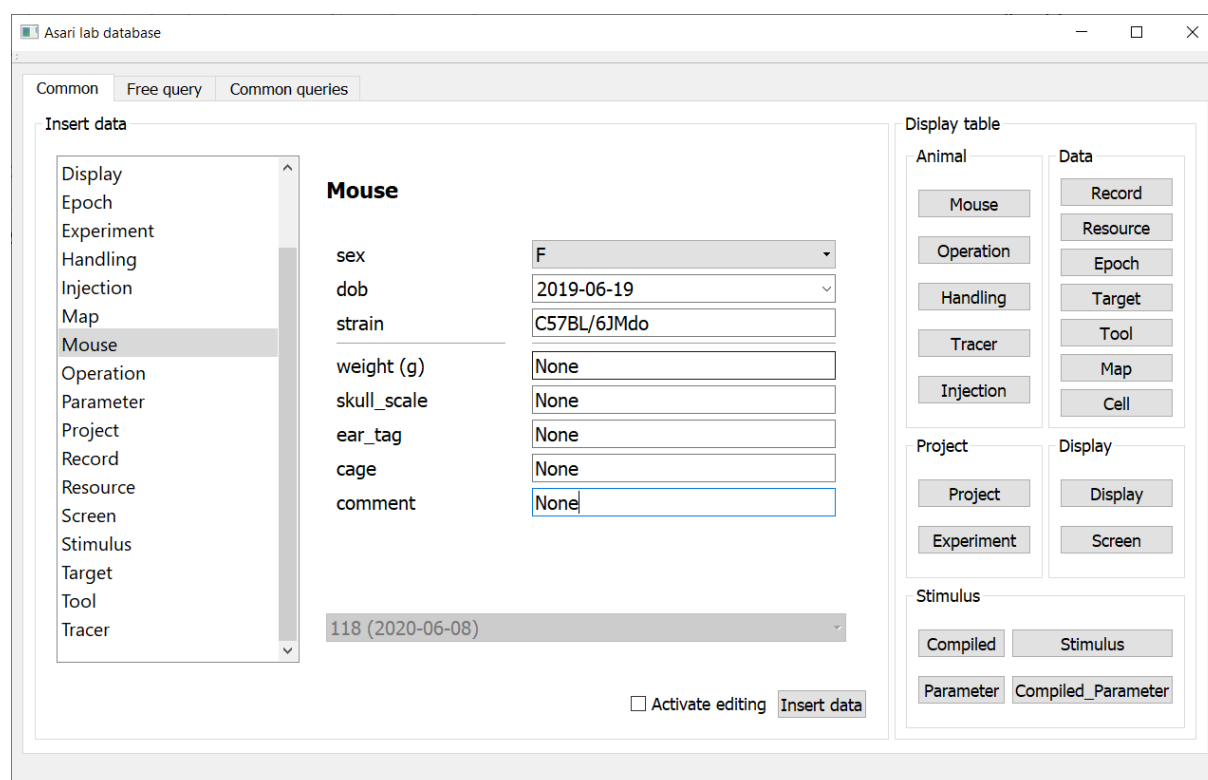
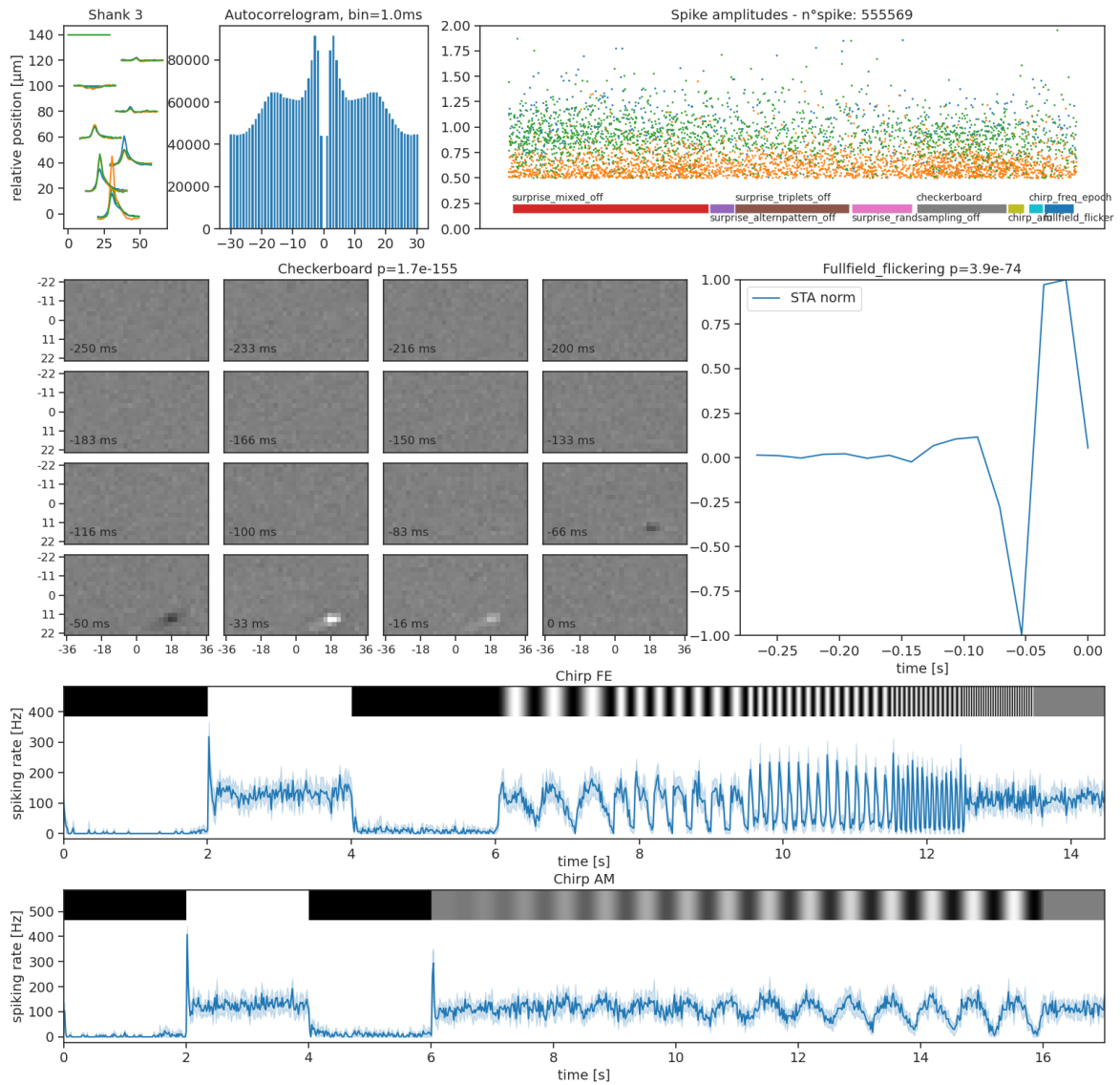


Figure 35 – Graphical User Interface for the database. The list on the left allow to choose which table to modify. Fields are completed in the centre and data submitted to the database with the 'Insert Data' button. Activate editing checkbox switch the central panel to edition mode, where existing data are selected from the drop-down menu (disabled here but showing “118 (2020-06-06)”). Tables can be fully displayed by using the corresponding buttons on the right. The two other tabs to do free SQL query or select from pre-made queries are located on top.

Annexe 3 – Cell Zoo

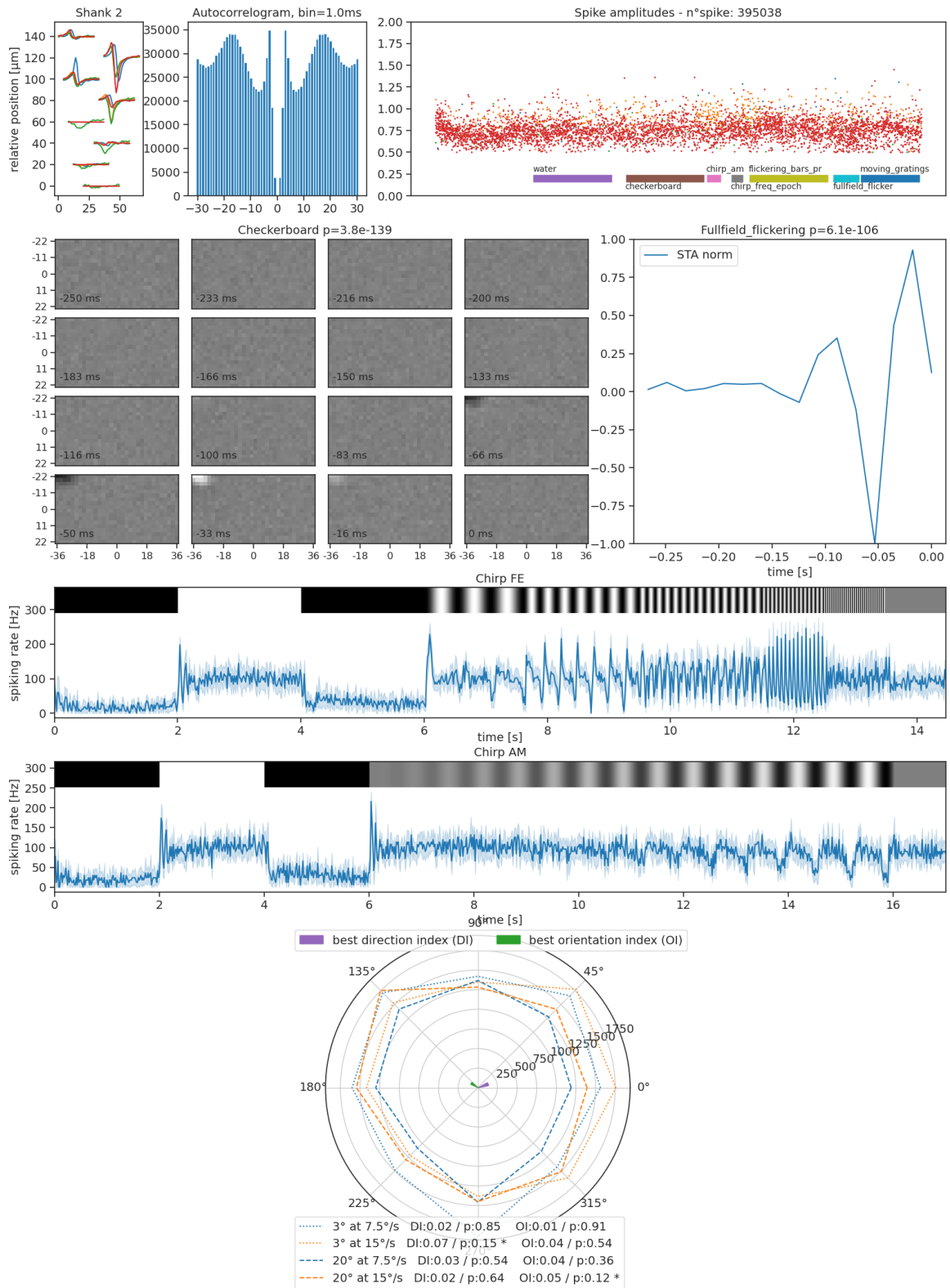
9 Annexe 3 – Cell Zoo

9.1 Awake cell



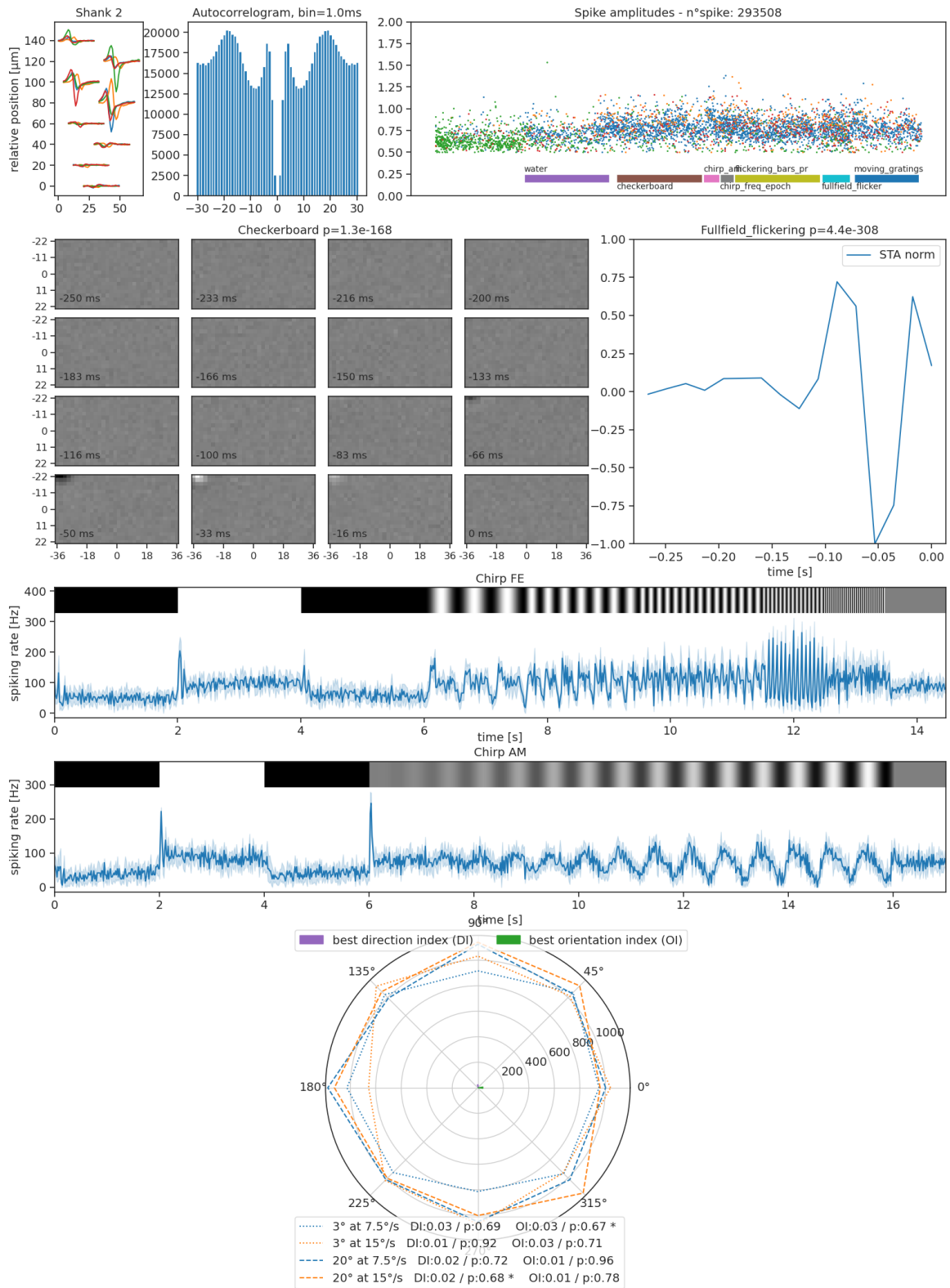
Annexe 3 – Cell Zoo

9.2 Day/Night paired cell – Day



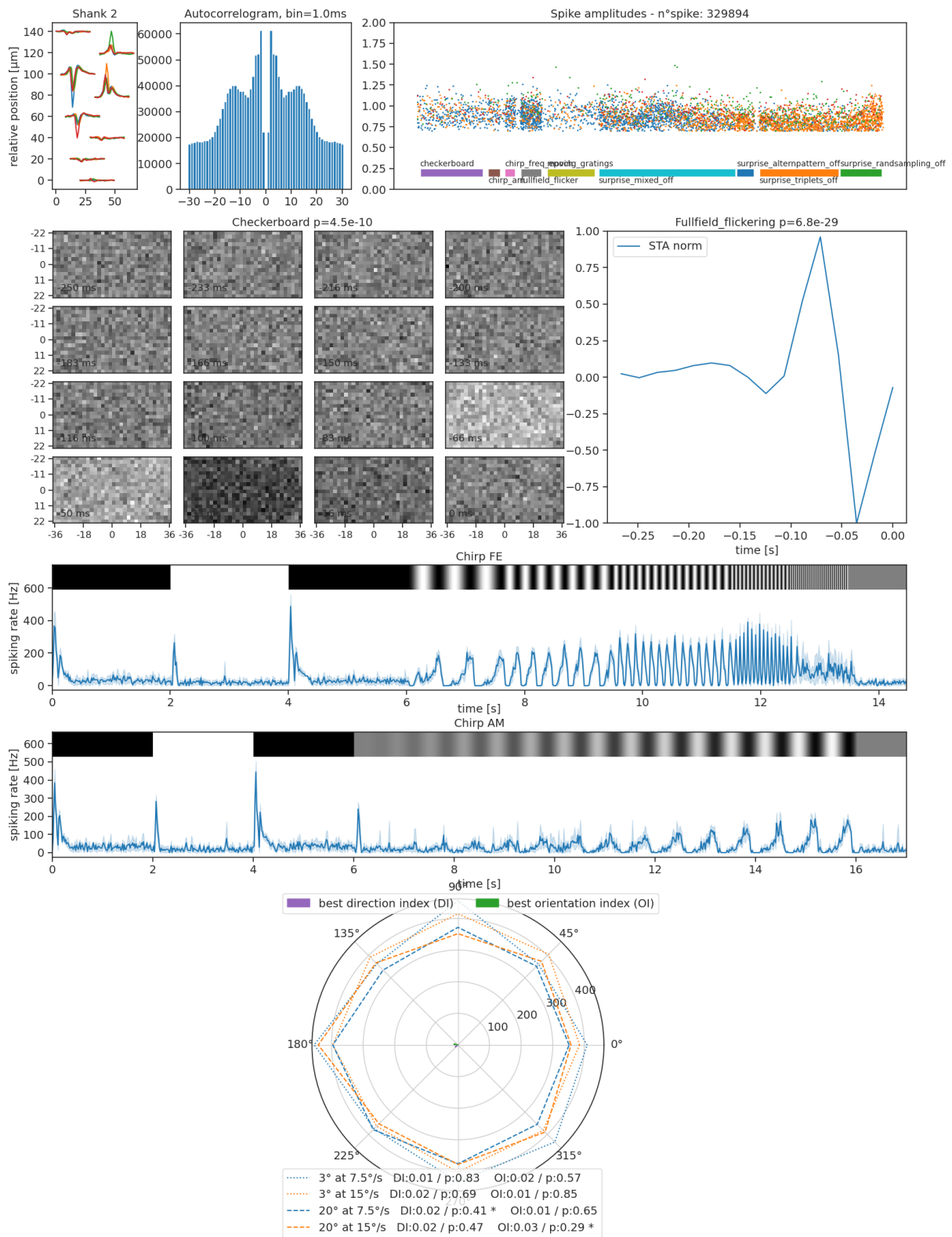
Annexe 3 – Cell Zoo

9.3 Day/Night paired cell – Night



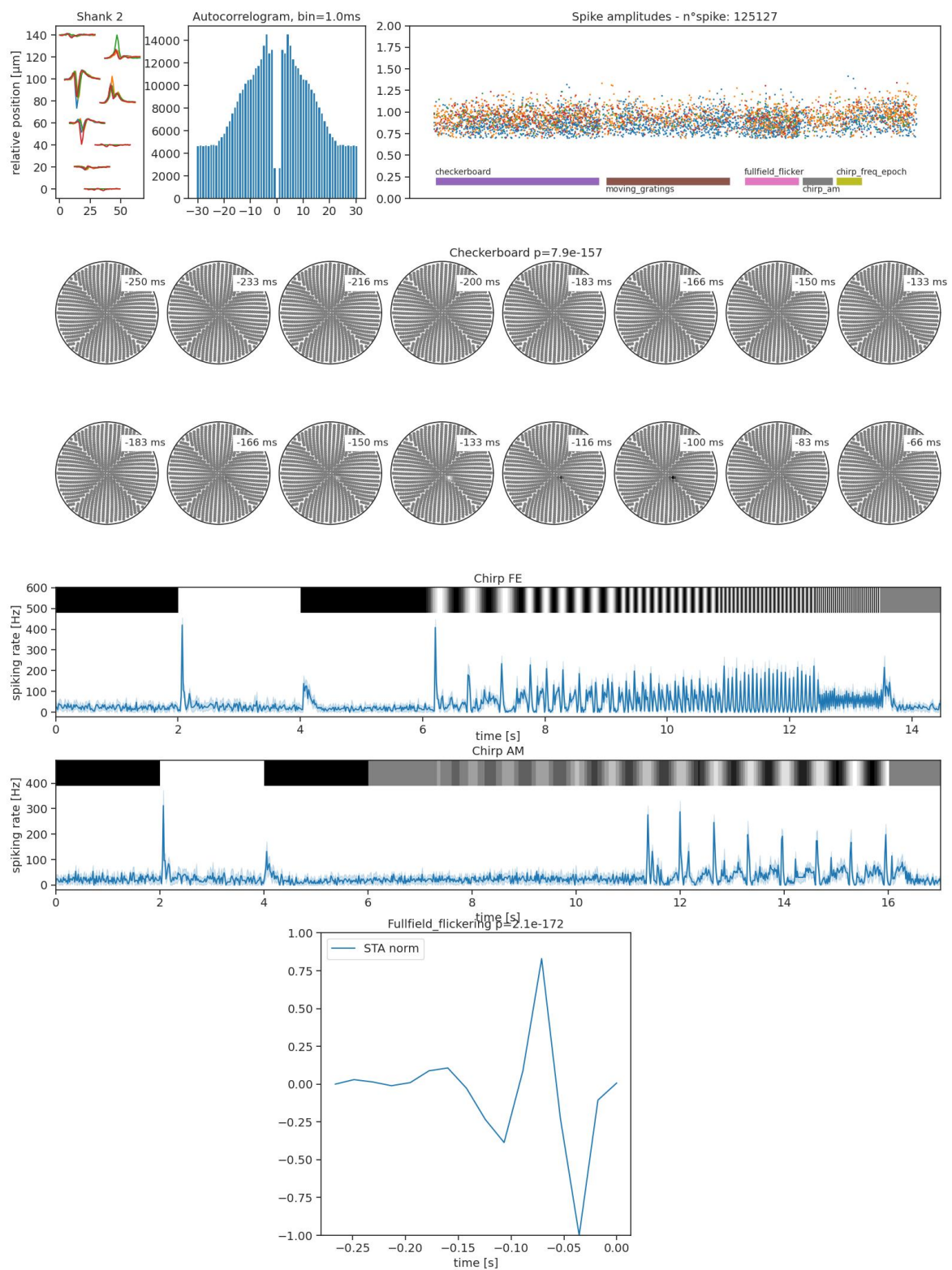
Annexe 3 – Cell Zoo

9.4 LED-dome/DLP paired cell – DLP



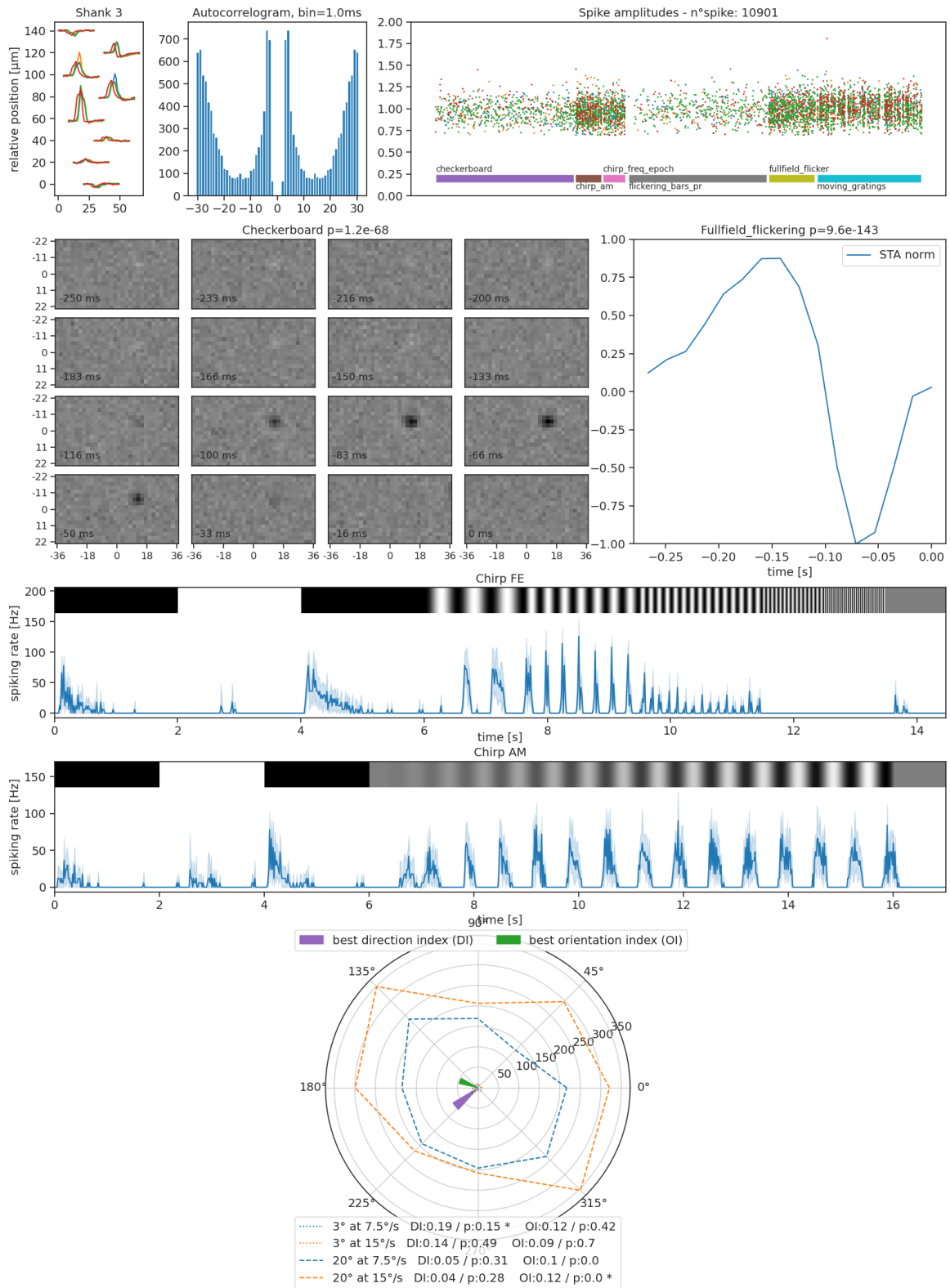
Annexe 3 – Cell Zoo

9.5 LED-dome/DLP paired cell - LED-dome



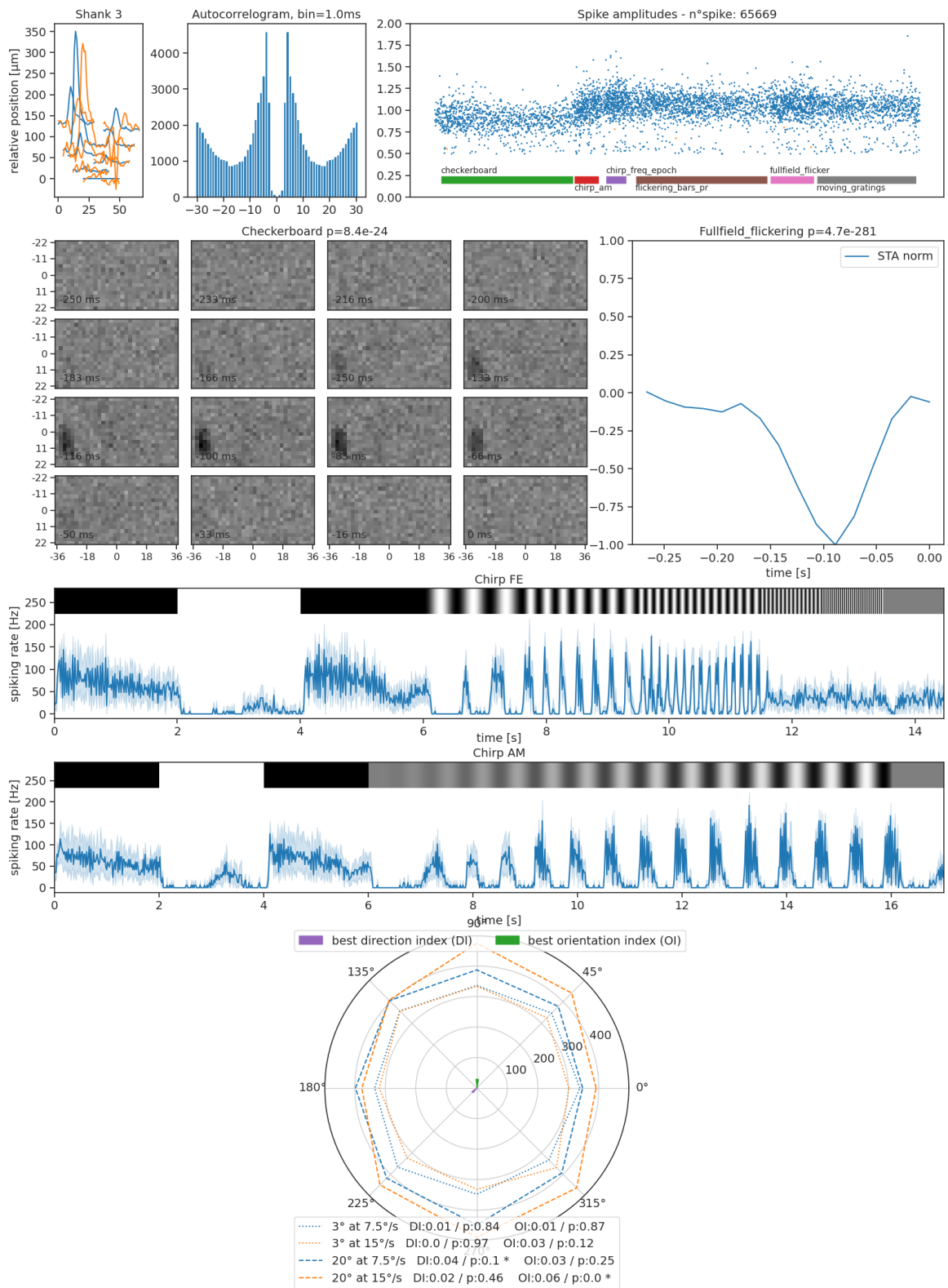
Annexe 3 – Cell Zoo

9.6 FMM cell



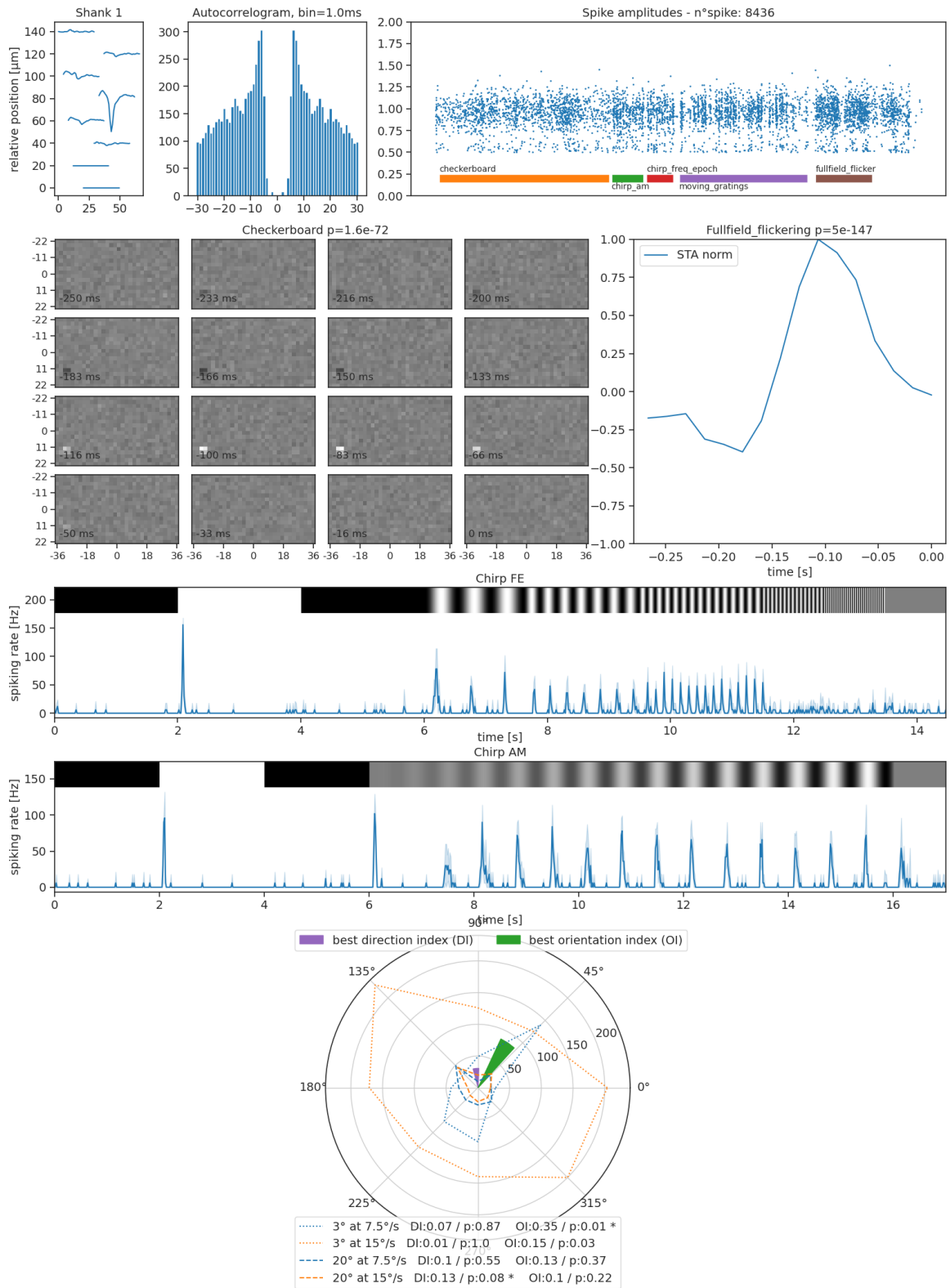
Annexe 3 – Cell Zoo

9.7 FMM cell - ON stimulus leak response



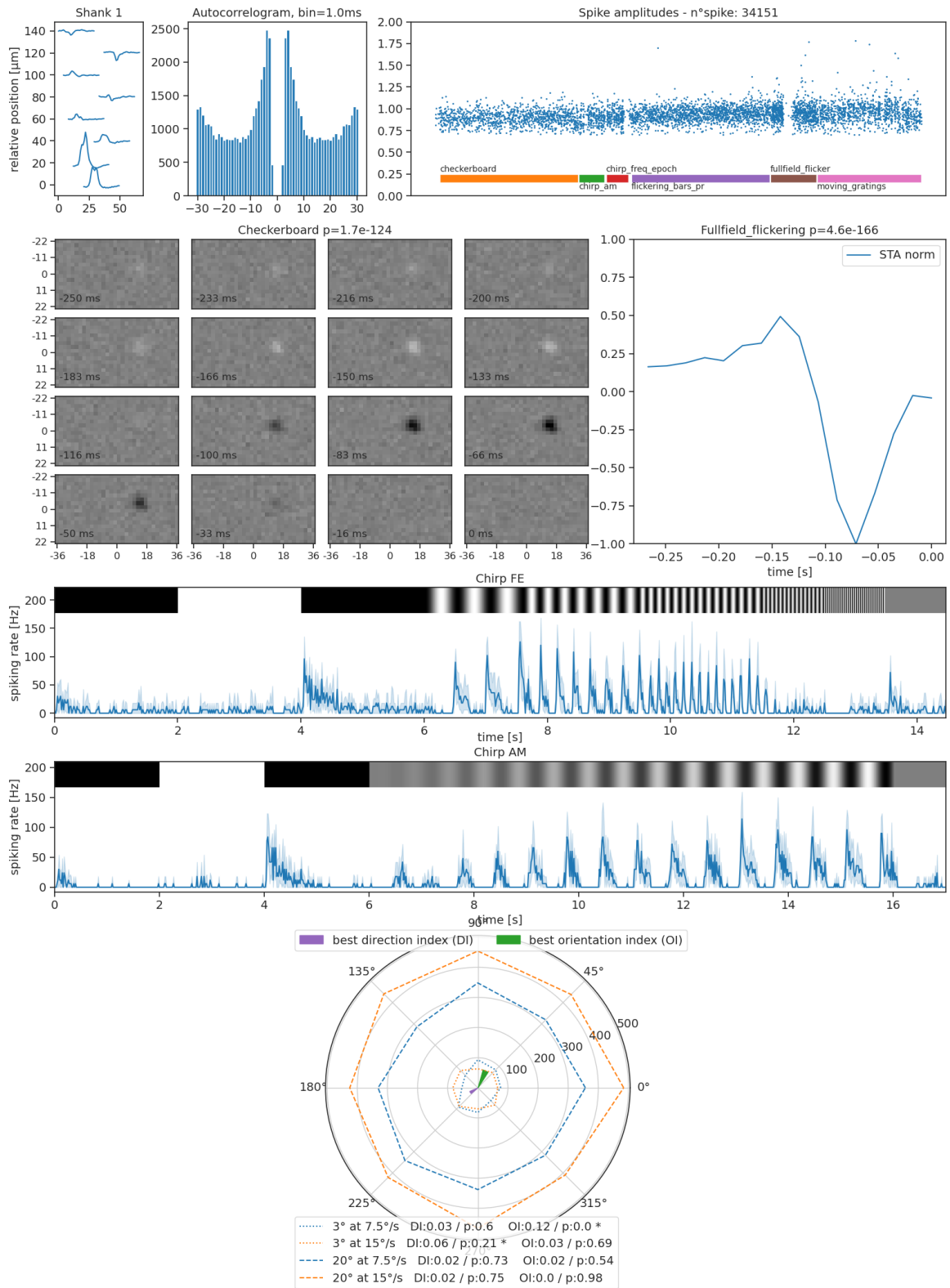
Annexe 3 – Cell Zoo

9.8 Isoflurane cell - Transient response



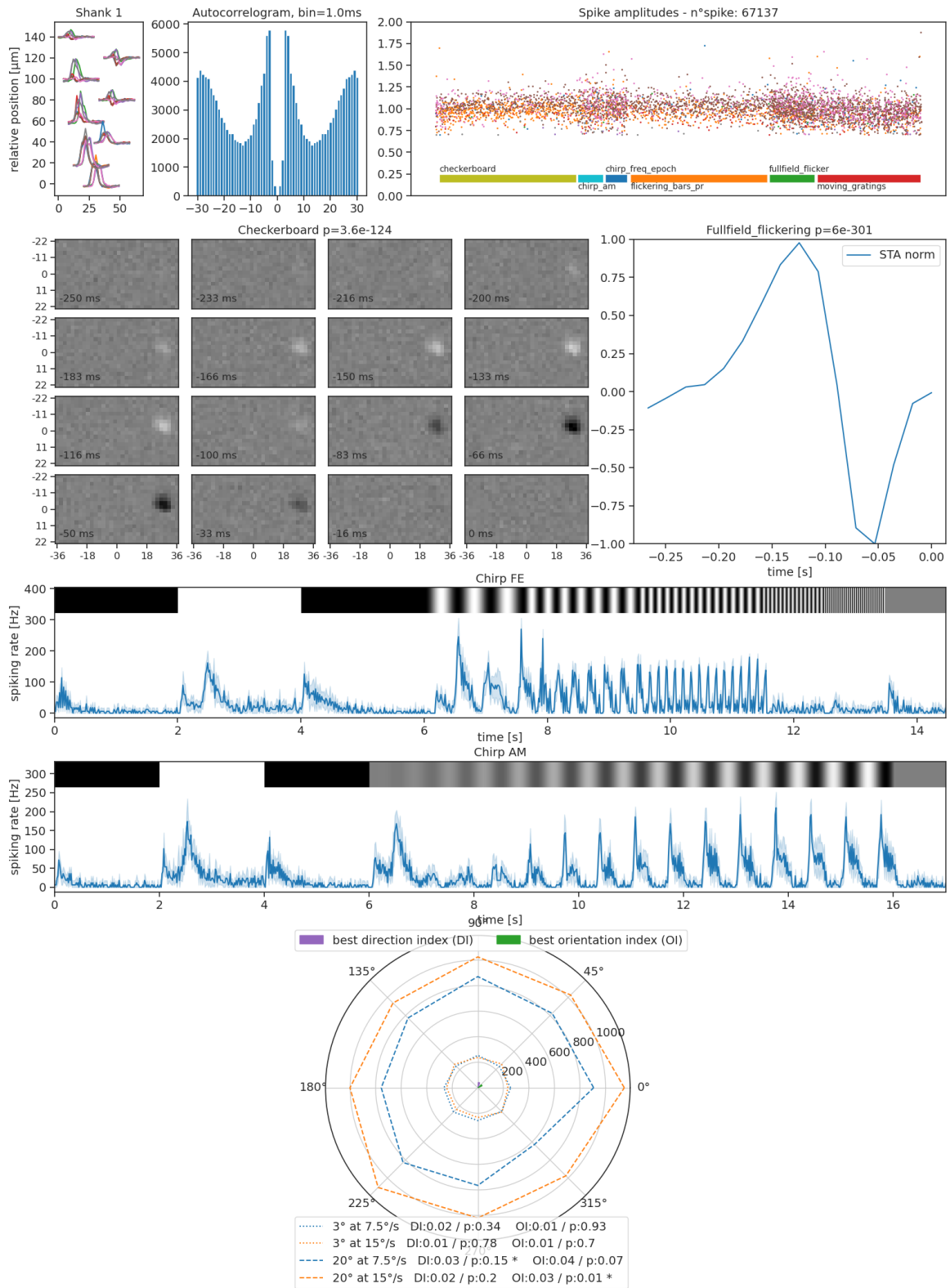
Annexe 3 – Cell Zoo

9.9 Isoflurane/FMM paired cell – Isoflurane



Annexe 3 – Cell Zoo

9.10 Isoflurane/FMM paired cell – FMM



Annexe 4 – The One Rig

10 Annexe 4 – The One Rig

The following annexe is the demonstration of the pipeline I used to synchronise and process the data presented throughout this thesis. The different format comes from a direct conversion of a Jupyter notebook containing python code.

Annexe 4 - The One Rig

March 26, 2021

One time series to rule them all, One time series to find them
One time series to bring them all and in the darkness bind them

1 Installation

So far there the only way to install tor is to download the github repository from github.com/TomTBT/theonerig and to run the following commands in the downloaded folder:

```
conda create -n tor python=3.6
activate tor for windows or source activate tor for linux/mac
pip install packaging
pip install -e .
```

2 General Presentation

Theonerig (read “the one rig”), or abbreviated as tor, is a package to synchronise and process neuronal records and their response to visual stimuli. By aligning all the time series to a master time serie, tor simplifies the slicing of the data with its intuitive masking strategy. The synchronised records are exported to the HDF5 format, and can be reimported as such:

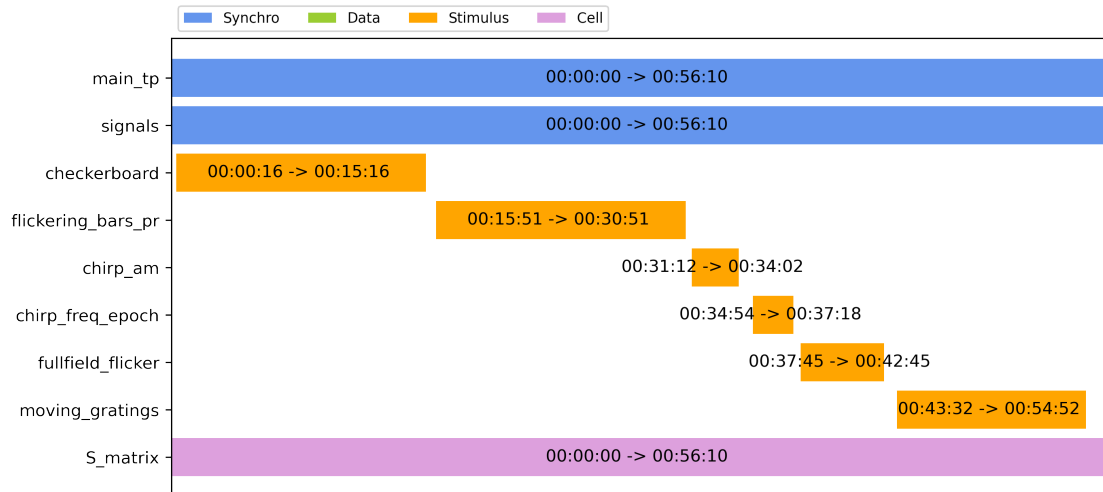
```
[6]: %matplotlib inline
import matplotlib as mpl
mpl.rcParams['figure.dpi'] = 300
import theonerig.core as core

reM = core.import_record("reM.h5")
```

Importing the record master

reM stands for RecordMaster. It’s the object that contained each of the synchronised data streams. Moreover, it has some convenient features, like the method `plot()`:

```
[7]: reM.plot()
```



We see that our record has many stimuli inside. Let's try to get some data from it by using a `Data_Pipe` object

```
[8]: pipe = core.Data_Pipe(reM, data_names=["checkerboard", "S_matrix"])
```

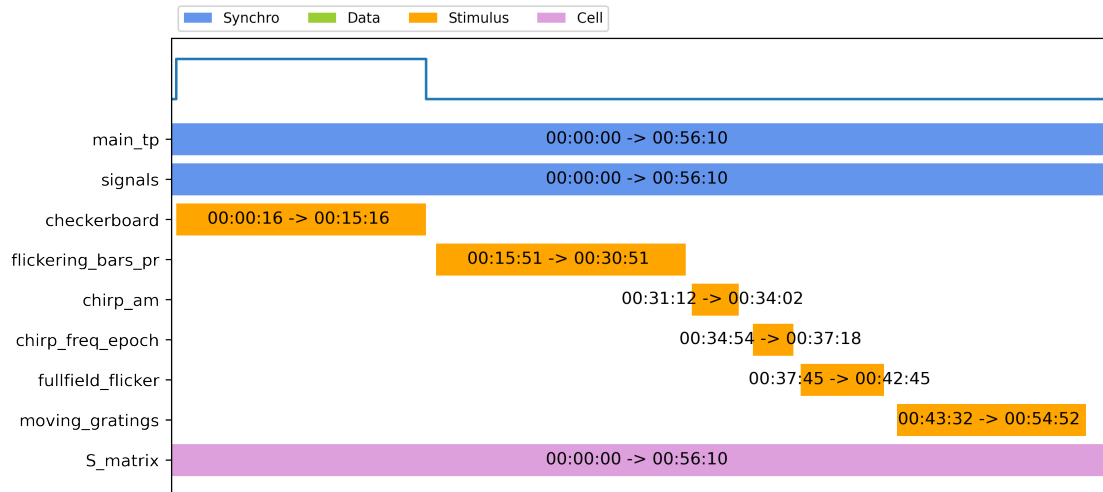
At this point, the pipe is empty. It knows it should get data of from the checkerboard stimulus and from the spikes matrix, but it doesn't know where to get it from (it knows the rows but not the columns).

To fix that, we can use some mathematical and logical operations: add, sub, and, not

```
[9]: pipe += "checkerboard"
```

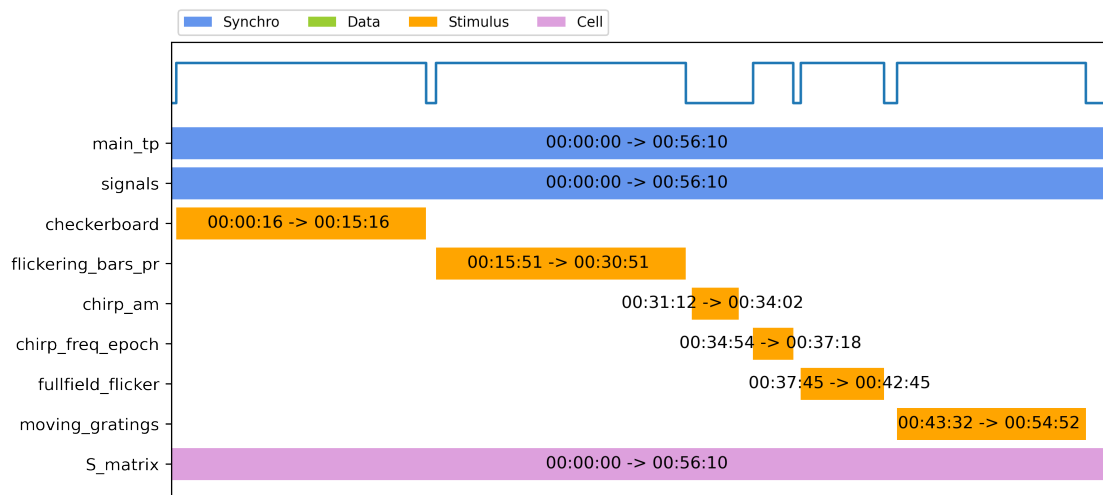
Now our pipe should contain the data of the checkerboard and spike matrix around the region where the checkerboard exists !

```
[10]: reM.plot()
       pipe.plot()
```



Additionally, each row of data belongs to a type: sync, data, stim, cell We can use that instead of the data name for the slicing

```
[11]: pipe += "stim"
      pipe -= "chirp_am"
      reM.plot()
      pipe.plot()
```



As you can see, we have now multiples epochs. This is why the pipe objects contains a list as a result of the masking, and when iterated (or indexed), it retrieves a dictionary with the data names as keys.


```
[12]: print("Pipe lenght:", len(pipe))
      print("Pipe keys  :", pipe[0].keys())
```

Pipe lenght: 5

Pipe keys : dict_keys(['checkerboard', 'S_matrix'])

3 Creating a record master

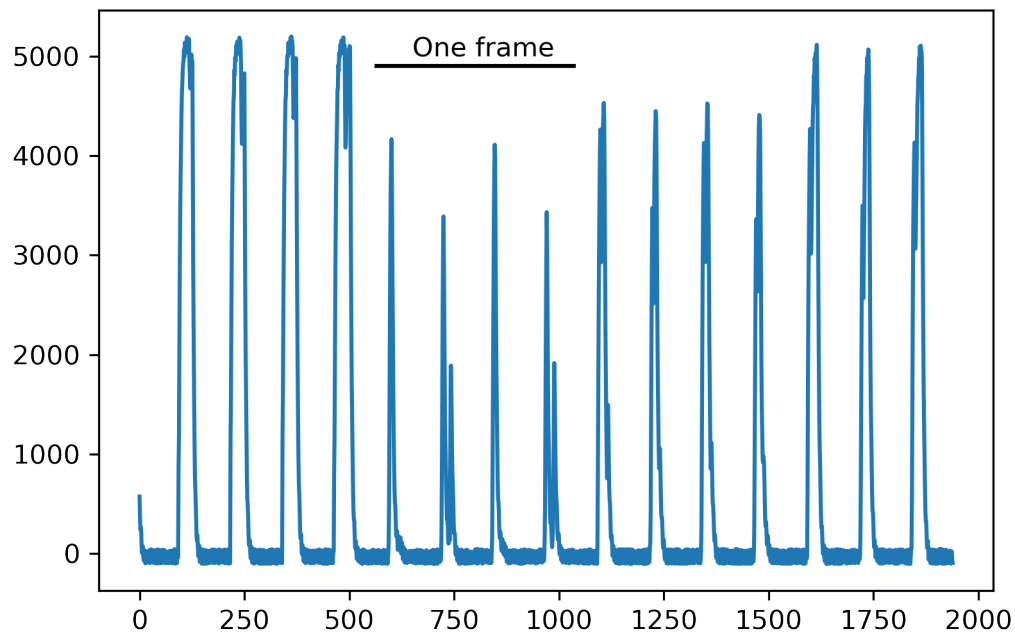
First of all, in order to process the response of cells in our record, we need to create the record master. Let's start simply by loading the raw data of our experiment.

```
[13]: import theonerig.synchro.io as io
      photodiode_data = io.load_adc_raw("./photodiode.data", sampling_rate=30000)
```

Loading the data... 100%

The photodiode receives light intensity from a DLP projector. A complete frame is made of four peaks in our record.

```
[14]: import matplotlib.pyplot as plt
      plt.figure()
      plt.plot(photodiode_data[999260:1001200])
      plt.hlines(4900, 560, 1040)
      _ = plt.text(650, 5000, "One frame")
```

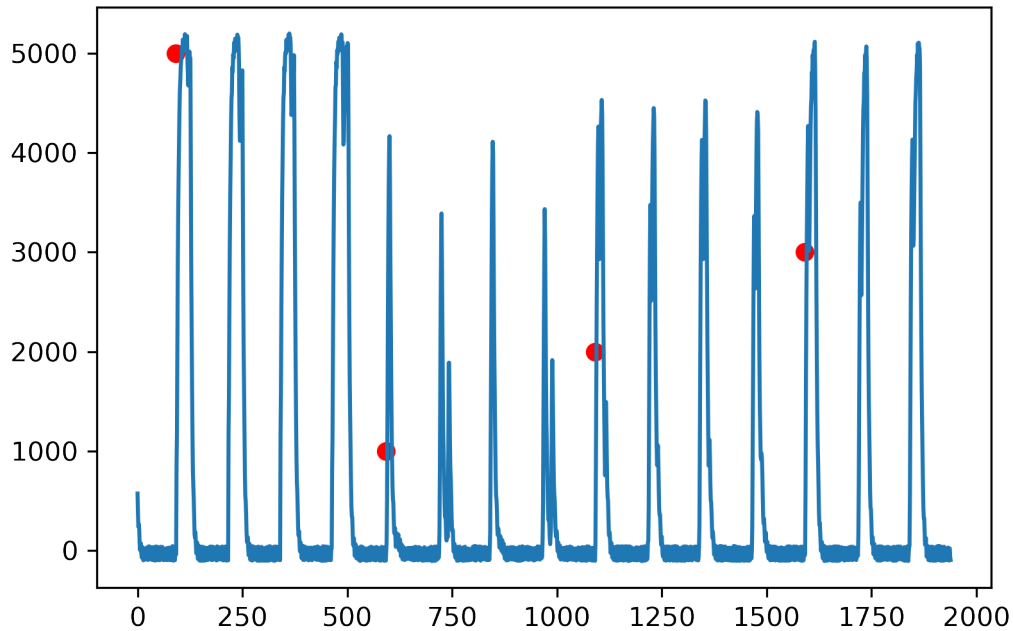


Frames are detected with `detect_frames` from **synchro.processing**, which is basically performing some smart thresholding. Then each frame is given a value from their AUC.

```
[15]: import theonerig.synchro.processing as syncproc
low_th, high_th = 1000, 4800
frame_tp, _ = syncproc.detect_frames(photodiode_data, low_th, high_th,
    ↪increment=500)
#Increment correspond to sampling_rate/freq: 30000/60

frame_sig = syncproc.cluster_frame_signals(photodiode_data, frame_tp,
    ↪n_cluster=5)

start, stop = 999260, 1001200
mask_frames = (frame_tp > start) & (frame_tp < stop)
plt.figure()
plt.plot(photodiode_data[start:stop])
_ = plt.scatter(frame_tp[mask_frames]-start, frame_sig[mask_frames]*1000+1000,
    ↪c="r")
```



From here, we can create a record master from the DLP timepoints, that will serve as the master timeserie. Both `frame_tp` and `frame_sig` have to be converted to `DataChunk` objects. For that, I use **`extend_sync_timepoints`** that takes both arrays and interpolate the timepoints to both sides of the record, in case no frames were found there.

```
[16]: import theonerig.utils as utils
ref_timepoints, ref_signals = utils.extend_sync_timepoints(frame_tp, frame_sig,
    ↪up_bound=len(photodiode_data))
reM = core.RecordMaster([(ref_timepoints, ref_signals)])
```

4 Synchronising stimuli with the record master

Now we want to add the stimuli to the record. I first read the log from the stimulation software (QDSpy) to find out the stimuli I used.

```
[17]: import theonerig.synchro.extracting as extract
log = extract.get_QDSpy_logs("./")[0]
log
```

NoName WARNING dt of frame #1 was 86.707 m

```
[17]: NoName          0a3053a663e357056b5b3c55856f8c88 at 2019-06-27 15:00:38
set_background      3e93aba4e4b7bee28aaeb6c6294d9dfe at 2019-06-27 15:02:00
checkerboard        eed21bda540934a428e93897908d049e at 2019-06-27 15:03:57
flickeringBars_pr   0049591cdf7aa379a458230e84cc3eec at 2019-06-27 15:19:33
chirp_am            31ca901daf66fcc4a832ed489d37de31 at 2019-06-27 15:34:54
chirp_freq_epoch    89c7c36d0071f4f4bef2643086ae9b95 at 2019-06-27 15:38:35
fullfield_flicker   1424ca0ff1e33a87d9072a8dd42a628a at 2019-06-27 15:41:27
moving_gratings     4e9001c1674d1851e7748b37bd1b81a4 at 2019-06-27 15:47:13
```

With this list and knowing when the record started, I can do a first estimation of what timepoint the stimulus started

```
[18]: import datetime
#record_time obtained from record filename
record_time = datetime.datetime.strptime("190627_150342", "%Y%m%d_%H%M%S")
#checker_time obtained from QDSpy log
checker_time = datetime.datetime.strptime("190627_150357", "%Y%m%d_%H%M%S")

estimate_start = syncproc.get_position_estimate(checker_time, record_time,
↪sampling_rate=30000)
print(estimate_start)
```

450000

Then we need to open the stimulus template. In my case I use the function `unpack_stim_npy`, but the end goal is to have two matrix, one containing the signal value for each frame, and the other the stimulus values for each frame

```
[19]: # The hash are obtained from the QDSpy log.
stim, signals, _ = extract.unpack_stim_npy("./stim",
↪md5_hash="eed21bda540934a428e93897908d049e")
print("Stimulus shape:", stim.shape)
print("Signals shape:", signals.shape)
```

Stimulus shape: (54039, 1, 18, 32)

Signals shape: (54039,)

My stimulus has 54039 frames. Now I want to match the stimulus signals with the signals I recorded with the photodiode.

```
[20]: starting_pos = syncproc.match_starting_position(ref_timepoints, ref_signals,
↳ signals, estimate_start)
print(starting_pos)
```

951

It seems that the stimulus started at the frame 951, but let's check it:

```
[21]: syncproc.display_match(starting_pos, signals, ref_signals, len_line=34)
```

```
REF [0]  0 0 0 0 0 0 4 0 4 4 4 0 4 4 4 0 4 0 4 0 0 0 0 0 4 0 1 2 3 4 0
REC [0]  0 0 0 0 0 0 4 0 4 4 4 0 4 0 4 4 4 0 4 0 4 0 0 0 0 0 4 0 1 2 3 4 0

REF [27019]  1 2 3 4 0 1 2 3 4 0 1 2 3 4 0 1 2 3 4 0 1 2 3 4 0 1 2 3 4 0 1 2 3 4
REC [27019]  0 1 2 3 4 0 1 2 3 4 0 1 2 3 4 0 1 2 3 4 0 1 2 3 4 0 1 2 3 4 0 1 2 3

REF [54005]  2 3 4 0 1 2 3 4 0 1 2 3 4 0 1 2 3 4 4 4 4 4 4 0 0 0 0 0 0
REC [54005]  1 2 3 4 0 1 2 3 4 0 1 2 3 4 0 1 2 3 4 4 4 4 4 4 0 0 0 0 0
```

The beginning matches, however it seems that something happens in the middle. To correct errors while handling those shift that can be dangerous, we use **frame_error_correction**

```
[22]: sub_fr_signals = ref_signals[starting_pos : starting_pos+len(signals)]
stim_tup_corr, shift_log, frame_replacement = syncproc.
↳ frame_error_correction(sub_fr_signals, (stim, signals, None), algo="nw")
(stim_corr, signals_corr, _) = stim_tup_corr
```

The frame error correction gave us three thing, the stimulus arrays corrected, a list of shifts and a list of which frames were replaced.

```
[23]: print("The few first shifts", shift_log[:4])
print("Some frames replaced (dest, orig)", frame_replacement[:4])
```

```
The few first shifts [(2120, 'ins'), (4498, 'del'), (5032, 'ins'), (7633,
'del')]
Some frames replaced (dest, orig) [(1542, 1541), (1786, 1785), (1816, 1815),
(1842, 1841)]
```

Let's have a look to the new match, with the corrected values. The corrected values match the recorded, but also correspond now to the correction on the stim matrix.

```
[24]: syncproc.display_match(starting_pos, signals, ref_signals, signals_corr,
↳ len_line=34)
```

```
REF [0]  0 0 0 0 0 0 4 0 4 4 4 0 4 4 4 0 4 0 4 0 0 0 0 0 4 0 1 2 3 4 0
REC [0]  0 0 0 0 0 0 4 0 4 4 4 0 4 4 4 0 4 0 4 0 0 0 0 0 4 0 1 2 3 4 0
COR [0]  0 0 0 0 0 0 4 0 4 4 4 0 4 4 4 0 4 0 4 0 0 0 0 0 4 0 1 2 3 4 0

REF [27019]  1 2 3 4 0 1 2 3 4 0 1 2 3 4 0 1 2 3 4 0 1 2 3 4 0 1 2 3 4 0 1 2 3 4
REC [27019]  0 1 2 3 4 0 1 2 3 4 0 1 2 3 4 0 1 2 3 4 0 1 2 3 4 0 1 2 3 4 0 1 2 3
```

```

COR [27019]  0 1 2 3 4 0 1 2 3 4 0 1 2 3 4 0 1 2 3 4 0 1 2 3 4 0 1 2 3 4 0 1 2 3
REF [54005]  2 3 4 0 1 2 3 4 0 1 2 3 4 0 1 2 3 4 4 4 4 4 4 0 0 0 0 0 0
REC [54005]  1 2 3 4 0 1 2 3 4 0 1 2 3 4 0 1 2 3 4 4 4 4 4 4 0 0 0 0 0
COR [54005]  1 2 3 4 0 1 2 3 4 0 1 2 3 4 0 1 2 3 4 4 4 4 4 4 0 0 0 0 0

```

Now that we have the starting position and the correct stimulus matrix, we can put it all together in a DataChunk and add it to our record master.

```

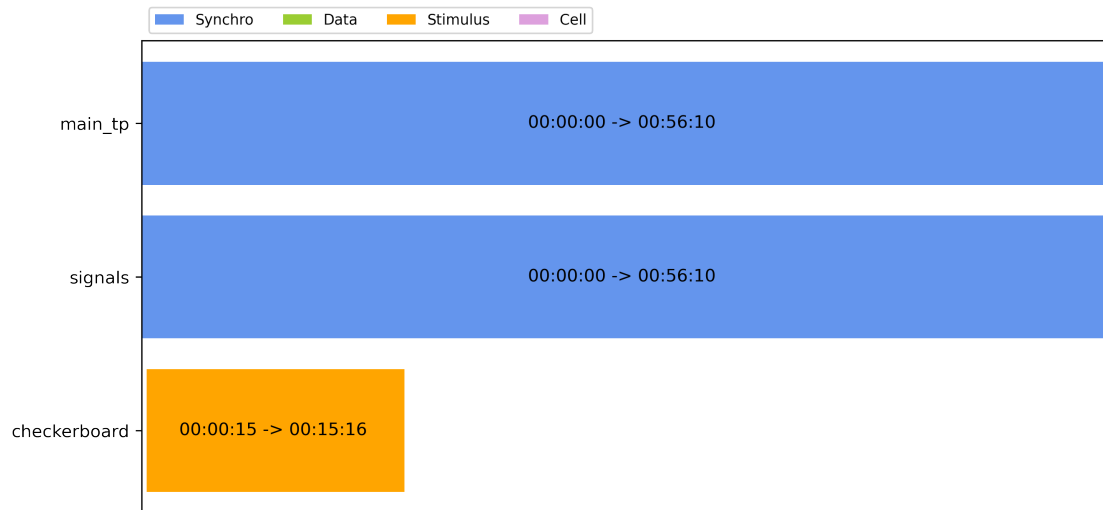
[25]: stim_datachunk      = utils.stim_to_dataChunk(stim_corr, starting_pos,
        ↪ref_signals)
reM["checkerboard"] = stim_datachunk

```

```

[26]: reM.plot()

```



5 Adding the electrophysiology data

Let's also add the electrophysiology data, after sorting with SpykingCircus and manually curated with phy

```

[27]: import os, csv
import numpy as np
phy_dir = "./phy"
phy_dict = utils.phy_results_dict(phy_dir)
good_clusters = []
with open(os.path.join(phy_dir, 'cluster_group.tsv'), 'r') as tsvfile:
    clusters = csv.reader(tsvfile, delimiter='\t', quotechar='|')
    for i, cluster in enumerate(clusters):

```

```

        if cluster[1] == "good":
            good_clusters.append(int(cluster[0]))
    good_clusters = np.array(good_clusters)
    phy_dict["good_clusters"] = good_clusters

```

And after opening the result, we convert them to a DataChunk and appened them to the record master.

```

[28]: spike_tp_dict = {}
      for good_clust in phy_dict['good_clusters']:
          cluster_mask = phy_dict["spike_clusters"]==good_clust
          spike_times = phy_dict["spike_times"][cluster_mask]
          spike_tp_dict[good_clust] = spike_times

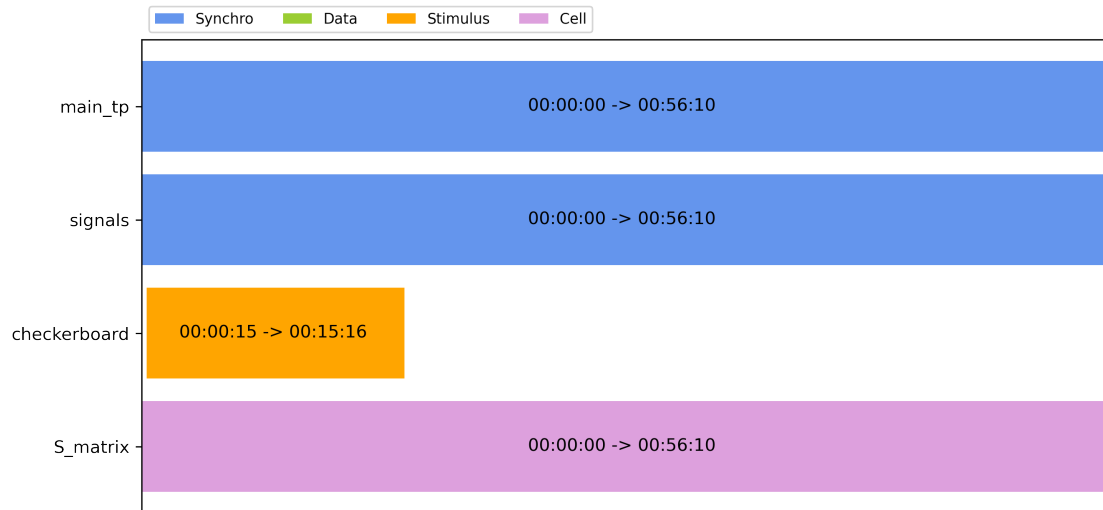
      reM["S_matrix"] = utils.spike_to_dataChunk(spike_tp_dict, ref_timepoints)

```

```

[29]: reM.plot()

```



From there, we will skip the rest of the stimuli synchronisation and load the premade record master, for the sake of the demonstration

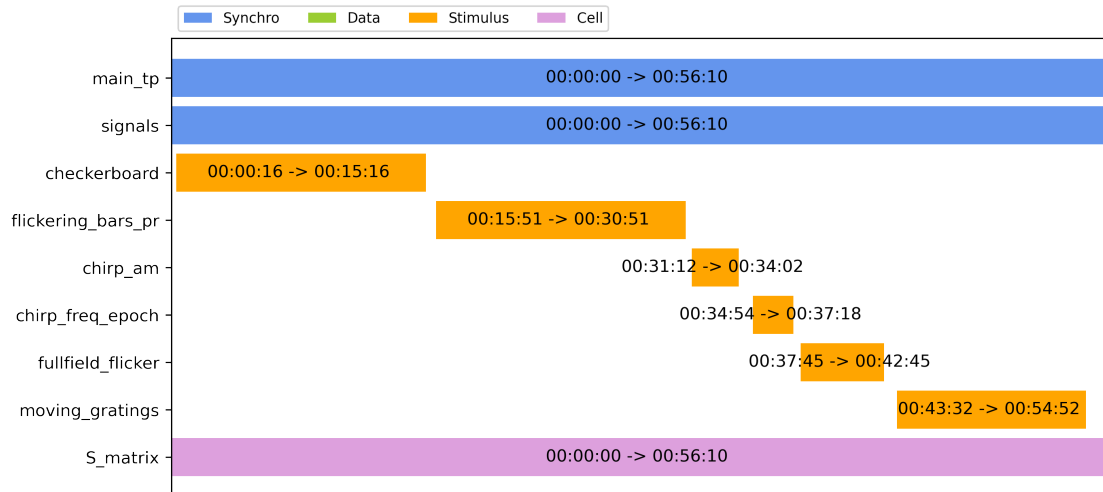
6 Processing and modelling the cells response

```

[30]: reM = core.import_record("./reM.h5")
      reM.plot()

```

Importing the record master



To process the response to the different stimuli, we will first select the region and the data by using the Data_Pipe shown in introduction

6.1 Receptive field

```
[31]: import theonerig.processing as processing
import theonerig.modelling as modelling
import theonerig.plotting as plotting

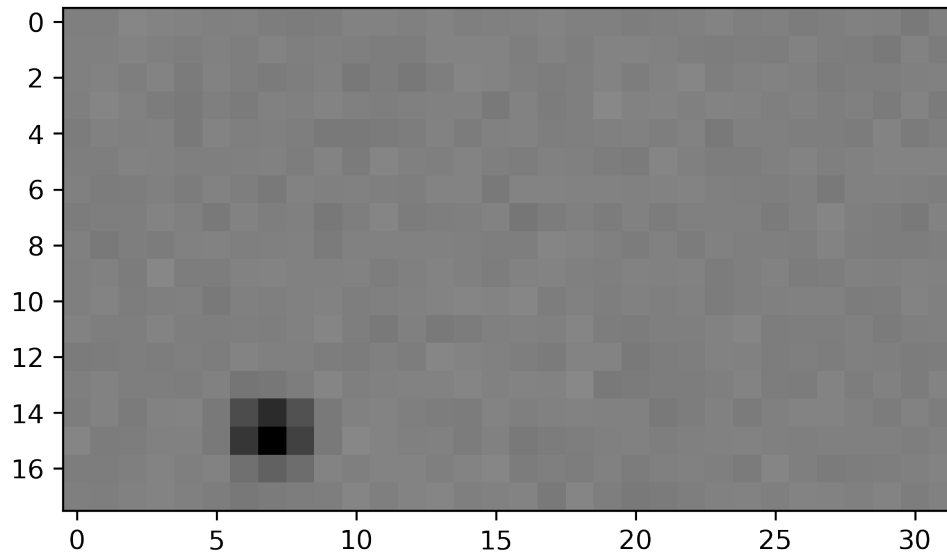
pipe = core.Data_Pipe(reM, ["checkerboard", "S_matrix"]) # Getting checkerboard_
↪and S_matrix
pipe += "checkerboard" #Selecting the region where checkerboard exists

stas = processing.process_sta_batch(stim_inten=pipe[0]["checkerboard"],
                                   spike_counts=pipe[0]["S_matrix"], Hw=16, Fw=0)
print(stas.shape)
```

(27, 16, 18, 32)

We have a total of 27 cells, a history window of 16 for checkerboard of 32*18 blocks. Let's check the cell at index 24, it's a good one

```
[36]: sta = stas[24, -6]
_ = plt.imshow(sta, vmin=-1, vmax=1, cmap="gray")
```



We can now model the receptive field, by fitting a sum of 2D gaussian. The function `fit_spatial_sta` returns a dictionary of the fit parameters, and a quality index (explained variance).

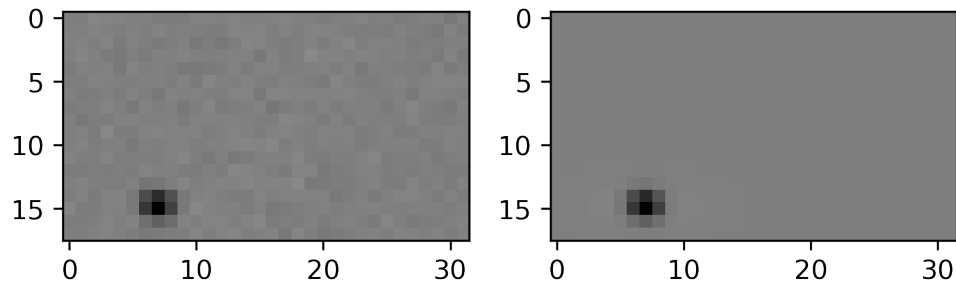
```
[37]: fit, qual_idx = modelling.fit_spatial_sta(sta)
      print(fit)

{'sigma_x_1': 0.7613322126772869, 'sigma_z_1': 0.9588988114312847, 'amp_1':
-1.194715791562662, 'theta_1': 4.659879259019961, 'x0_1': 6.943010556115394,
'z0_1': 14.712026661259749, 'sigma_x_2': 2.007906527431578, 'sigma_z_2':
0.842522470524976, 'amp_2': 0.13161667398526836, 'theta_2': 72.20916210561327,
'x0_2': 6.943010556115394, 'z0_2': 14.712027662730947, 'y0':
-7.936732427113643e-05}
```

But the fit looks better when we look at the actual image

```
[38]: y_, x_ = sta.shape
      xy = np.meshgrid(range(x_), range(y_))
      fit_img = modelling.sum_of_2D_gaussian(xy, **fit).reshape(sta.shape)

      plt.subplot(1,2,1)
      plt.imshow(sta, vmin=-1, vmax=1, cmap="gray")
      plt.subplot(1,2,2)
      _ = plt.imshow(fit_img, vmin=-1, vmax=1, cmap="gray")
```

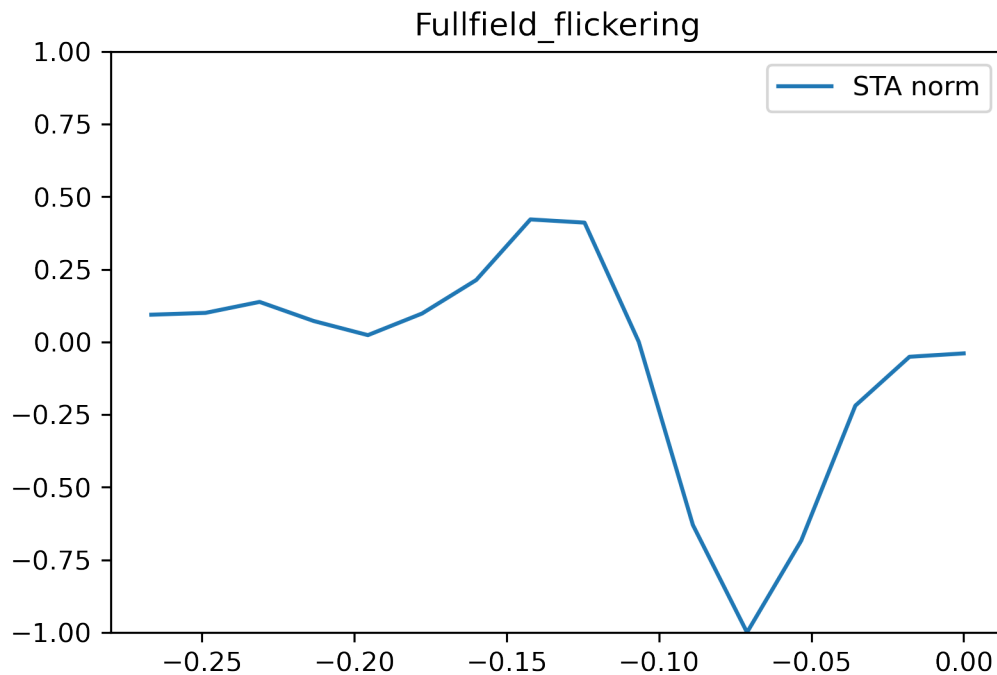



6.2 Temporal STA

After finding the receptive field of the cell, we can look at the temporal STA calculated with a full field white noise stimulus.

```
[39]: pipe = core.Data_Pipe(reM, ["fullfield_flicker", "S_matrix"],
                                ["stim_inten", "spike_counts"]) # pro tip, we can rename
                                ↳ the dataset
pipe += "fullfield_flicker"
sta = processing.process_sta_batch(**pipe[0], Hw=16, Fw=0)      # and pass them
                                ↳ to the function with **

ax = plt.axes()
plotting.plot_t_sta(ax, sta[24])
```

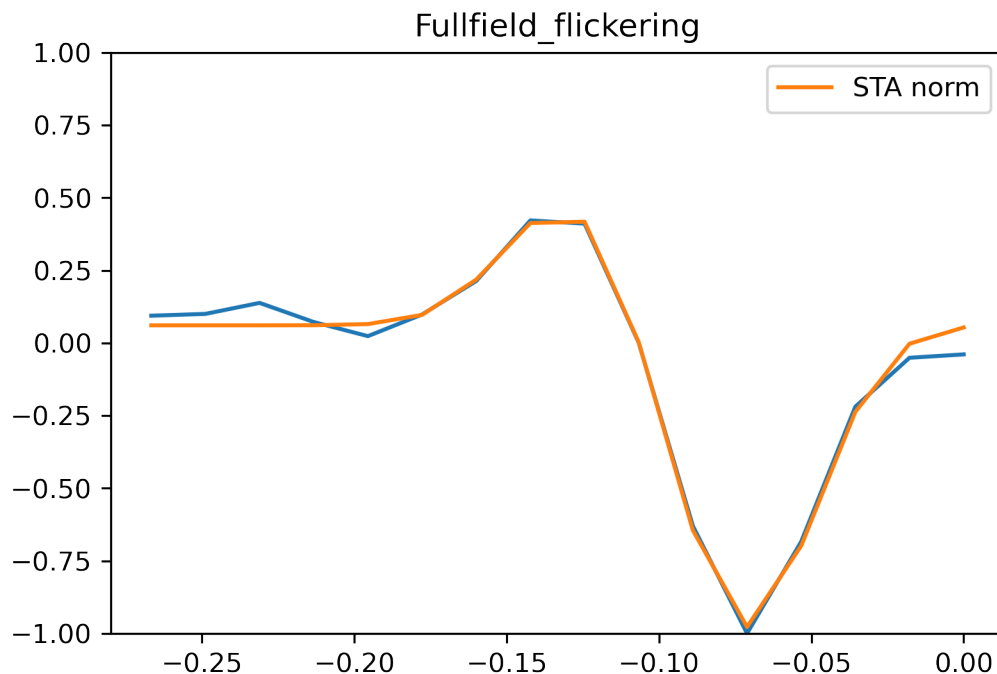


And like the receptive field, we can model it and look at the result

```
[40]: fit, qual_idx = modelling.fit_temporal_sta(sta[24])
      print(fit)

{'sigma_1': 0.020595173015770237, 'amp_1': 0.4358606906123172, 'x0_1':
-0.12065731431700889, 'sigma_2': 0.021303174675577463, 'amp_2':
-1.0529472499113097, 'x0_2': -0.0671875196718975, 'y0': 0.06075183273492472}

[41]: x = np.linspace(-15/60, 0, 16)
      ax = plt.axes()
      plotting.plot_t_sta(ax, sta[24])
      plotting.plot_t_sta(ax, modelling.sum_of_gaussian(x, **fit))
```



6.3 Frequency sensitivity

We are now gonna average the cell response to the stimulus `chirp_freq_epoch`, and then fit a model to the cell response. The model is a sine raised to an exponent, that have for effect to narrow the sine, as the exponent goes higher.

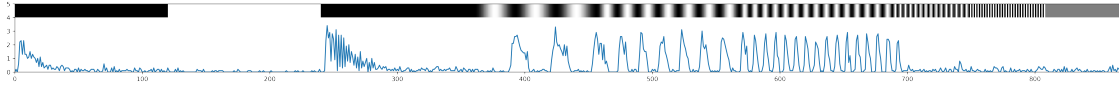
```
[42]: pipe = core.Data_Pipe(reM, ["S_matrix", "chirp_freq_epoch"], ["spike_counts",
    ↪ "stim_inten"])
      pipe += "chirp_freq_epoch"
```

```

cell_mean = np.mean(pipe[0]["spike_counts"][:,24].reshape(10,-1), axis=0) #10
↳ repetitions of the stimulus

plt.figure(figsize=(32,2))
plt.plot(cell_mean)
stim_to_plot = [pipe[0]["stim_inten"][:len(cell_mean)]]
plt.imshow(stim_to_plot, aspect='auto', cmap="gray", extent=(0,len(cell_mean),
↳ 5,4))
_ = plt.ylim(0,5)

```



We see that the cell only responded up to a certain frequency, but better fit a model for quantification

```

[43]: fit, qual_idx = modelling.fit_chirp_freq_epoch(cell_mean)
print(fit)

```

```

[{'amp': 2.2347451869716837, 'phi': 4.557354925782518, 'freq': 1.875, 'exp':
4.0}, {'amp': 2.3351841547921586, 'phi': 5.367567681921071, 'freq': 3.75, 'exp':
4.0}, {'amp': 2.5176267318433485, 'phi': 0.8697042360073766, 'freq': 7.5, 'exp':
4.0}, {'amp': 0.2494619163831114, 'phi': 3.964885693399168, 'freq': 15, 'exp':
2.0}, {'amp': 0.17149768100112495, 'phi': 5.95678696919102, 'freq': 30, 'exp':
2.0}]

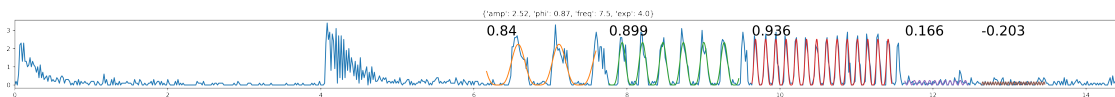
```

The fit of the chirp epoch contains one fit per frequency. Let's have a look if our fit worked well

```

[35]: plotting.plot_chirp_freq_epoch_fit(cell_mean, fit, qual_idx, figsize=(32,2))

```



6.4 Contrast sensitivity

We are now gonna average the cell response to the stimulus chirp_am, and then fit a model to the cell response. The model also fits the sine exponent, but also weights it with a sigmoid, that represent the increase in response.

```

[50]: pipe = core.Data_Pipe(reM, ["S_matrix", "chirp_am"], ["spike_counts",
↳ "stim_inten"])
pipe += "chirp_am"

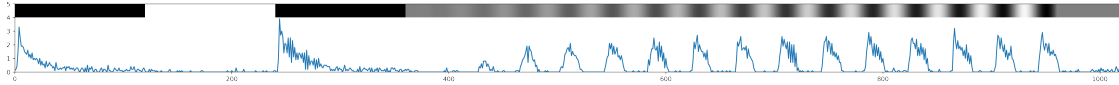
```

```

cell_mean = np.array(np.mean(pipe[0]["spike_counts"][:,24].reshape(10,-1),
    ↪axis=0)) #10 repetitions of the stimulus

plt.figure(figsize=(32,2))
plt.plot(cell_mean)
stim_to_plot = [pipe[0]["stim_inten"][:len(cell_mean)]]
plt.imshow(stim_to_plot, aspect='auto', cmap="gray", extent=(0,len(cell_mean),
    ↪5,4))
_ = plt.ylim(0,5)

```



```

[51]: fit, qual_idx = modelling.fit_chirp_am(cell_mean)
      print(fit)

```

```

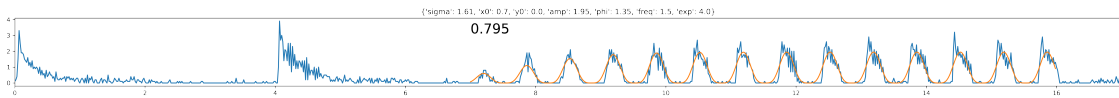
{'sigma': 1.6066674200748399, 'x0': 0.6979907523843563, 'y0':
9.157735323996803e-37, 'amp': 1.9499197494461324, 'phi': 1.3515310129506126,
'freq': 1.5, 'exp': 4.0}

```

```

[52]: plotting.plot_chirpam_fit(cell_mean, fit, qual_idx, figsize=(32,2))

```



To further explain what the model is, find below the two function that were combined to obtain the fit

```

[55]: plt.figure(figsize=(16,2))

# A sine exponent
sine_exp = modelling.sin_exponent(np.linspace(0,9,9*60), amp=fit["amp"],
    ↪phi=fit["phi"],
                                freq=fit["freq"],
                                ↪exp=fit["exp"])
# and a sigmoid
sigmo = modelling.sigmoid(np.linspace(0,9,9*60), sigma=fit["sigma"], amp=1,
    ↪x0=fit["x0"], y0=0)

plt.subplot(1,3,1)
plt.plot(sine_exp)
plt.title("Sine exponent")

```

```
plt.subplot(1,3,2)
plt.plot(sigmo)
plt.title("Sigmoid")
plt.ylim(0, None)

plt.subplot(1,3,3)
plt.plot(sine_exp*sigmo)
_ = plt.title("Sine exponent * Sigmoid")
```

